



UNIVERSITÉ DE
STRASBOURG



ÉCOLE DOCTORALE DES SCIENCES DE LA VIE ET DE LA SANTÉ
Institut de Génétique et de Biologie Moléculaire et Cellulaire

THÈSE présentée par :
Clémence ELLY

soutenue le: 6 mai 2025

pour obtenir le grade de :

Docteur de l'Université de Strasbourg

Discipline (Spécialité) : Science de la Vie et de la Santé - Génétique

**Consequences of XPD mutations on DNA repair,
transcription and cell division, leading to the
development of rare genetic diseases**

THÈSE dirigée par :

COIN Frédéric

COMPE Emmanuel

DR, CNRS, IGBMC, Illkirch

CR, CNRS, IGBMC, Illkirch

RAPPORTEURS :

TIRODE Franck

GIGLIA-MARI Ambra

DR, Centre de recherche en Cancérologie de Lyon

DR, CNRS, Laboratoire Physiopathologie et Génétique du
Neurone et du Muscle- Université Claude Bernard Lyon 1

AUTRES MEMBRES DU JURY :

PRIOETTI DDE SANTIS Luca

ORIOLO Donata

CR, Département du DEB - Département des Sciences
Écologiques et Biologiques de Toscane

CR, Institut de génétique moléculaire "Luigi Luca
Cavalli-Sforza" – CNR- Pavie

Avertissement au lecteur / Warning to the reader

Ce document est le fruit d'un long travail approuvé par le jury de soutenance et mis à disposition des membres de la communauté universitaire. Il est soumis à la propriété intellectuelle de l'auteur. Cela implique une obligation de citation et de référencement lors de l'utilisation de ce document. D'autre part, toute contrefaçon, plagiat, reproduction ou représentation illicite encourt une poursuite pénale.

This document is the result of a long process approved by the jury and made available to members of the university community. It is subject to the intellectual property rights of its author. This implies an obligation to quote and reference when using this document. Furthermore, any infringement, plagiarism, unlawful reproduction or representation will be prosecuted.

Code de la Propriété Intellectuelle

Article L122-4 :

Toute représentation ou reproduction intégrale ou partielle faite sans le consentement de l'auteur ou de ses ayants droit ou ayants cause est illicite. Il en est de même pour la traduction, l'adaptation ou la transformation, l'arrangement ou la reproduction par un art ou un procédé quelconque.

Any representation or reproduction in whole or in part without the consent of the author or his successors in title or assigns is unlawful. The same applies to translation, adaptation or transformation, arrangement or reproduction by any art or process whatsoever.

Articles L335-1 à L335-9 : Dispositions pénales / Penal provisions.

Licence attribuée par l'auteur / Licence attributed by the author



<https://creativecommons.org/licenses/?lang=fr-FR>

Corrected using AI

À mes parents,

« Dans la vie, rien n'est à craindre tout est à comprendre »

Marie Curie

Tables

ACKNOWLEDGMENTS	8
PUBLICATIONS AND ORAL COMMUNICATIONS	9
RÉSUMÉ EN FRANÇAIS	10
LIST OF FIGURES	14
GENERAL INTRODUCTION	16
SECTION 1: TFIIH AND ITS SUBUNITS XPD	18
1. THE TFIIH COMPLEX	19
1.1. <i>Composition</i>	19
1.2. <i>Structure of TFIIH</i>	21
2. STRUCTURE AND FUNCTIONAL DOMAIN OF XPD	23
2.1. <i>XPD overview</i>	23
2.2. <i>XPD structure</i>	24
SECTION 2: XPD'S ROLE IN MAJOR CELLULAR PROCESSES	25
1. LOCALIZATION, STRUCTURE AND ORGANIZATION OF THE GENOME	26
2. TRANSCRIPTION MECHANISM	27
2.1. <i>RNA polymerase</i>	28
2.2. <i>Promoters</i>	29
2.3. <i>Enhancer</i>	31
2.4. <i>Silencer</i>	32
2.5. <i>Mediator</i>	32
2.6. <i>Cohesin</i>	32
2.7. <i>Transcription steps</i>	33
3. NUCLEOTIDE EXCISION REPAIR	39
3.1. <i>DNA Damage</i>	40
3.2. <i>NER mechanism</i>	42
4. CELL CYCLE AND CHECKPOINTS	47
4.1. <i>Interphase</i>	48
4.2. <i>Mitosis</i>	50
SECTION 3: XPD MUTATIONS INDUCING VARIOUS PATHOLOGIES	56
1. XPD MUTATIONS	57
1.1. <i>XPD/R683W</i>	57
1.2. <i>XPD/G47R</i>	58

1.3.	<i>XPB/G602D</i>	59
1.4.	<i>XPB/K48R</i>	59
2.	PATHOLOGIES ASSOCIATED WITH XPB'S MUTATIONS	60
2.1.	<i>Xeroderma Pigmentosum (XP)</i>	60
2.2.	<i>Cockayne syndrome (CS) and XP/CS</i>	62
2.3.	<i>Trichothiodystrophy</i>	64
	RESULTS	67
	ARTICLE 1: PHOSPHORYLATION OF XPB DRIVES ITS MITOTIC ROLE INDEPENDENTLY OF ITS DNA REPAIR AND TRANSCRIPTION FUNCTIONS – SCIENCE ADVANCES	68
	ARTICLE 2: MUTATIONS IN XPB DIFFERENTLY AFFECT TRANSCRIPTION, NUCLEOTIDE EXCISION REPAIR AND MITOSIS.	86
	CONCLUSION/PERSPECTIVES	115
	ANNEXES	120
	BIBLIOGRAPHY	155
	ABSTRACT	186

Acknowledgments

I would like to express my profound gratitude to Emmanuel COMPE and Frédéric COIN for accepting me in their team. Your expertise and dedication have played a crucial role in shaping the direction of my research and helping me navigate challenges along the way. Thank you for your benevolent and patience.

I would like to thank La Région Réunion and la Fondation pour la Recherche Medical for accompanying over these 4 years.

Thanks to my colleagues and friends that supported me throughout my journey. Jeremy, Amélie, Max I would never have gone that far without your friendship. I cannot thank you enough for your support, advice and kindness. To Clara MARECHAL, I loved working and singing by your side. To Clara CAPELLI, I had so much fun working with you and I am very proud of the project we have built from scratch together.

Thank you Léane, your light and positivity are truly exemplary. Your friendship really means a lot to me.

I genuinely appreciated to experiment my hypothesis in the lab, and I hope to have transmitted it to my incredible interns, Larissa and Alexis. I loved sharing my project with you and I wish you the best for your future projects.

Mon bon Philippe CATEZ, je te remercie pour tous tes conseils et tous ces moments où nous avons refait le monde. Tu as toujours été là pour moi et je te serai infiniment reconnaissante. Tu es le Bienvenue à La Réunion !

To Maguelone, I would like to thank you for supporting me through the ups and downs. I am very lucky to be your friend.

To Guillaume DAVIDSON, your kindness and determination over the years were truly an example. Thank you for allways supporting me.

Un immense merci à mes parents, votre amour et vos encouragements ont été essentiels dans l'accomplissement de ce projet. *Mi aime à zot*

Publications and oral communications

Publications :

Compe, E. *et al.* (2022) ‘Phosphorylation of XPD drives its mitotic role independently of its DNA repair and transcription functions’, *Science Advances*, 8(33), p. eabp9457. <https://doi.org/10.1126/sciadv.abp9457>.

Sandoz, J. *et al.* (2023) ‘Active mRNA degradation by EXD2 nuclease elicits recovery of transcription after genotoxic stress’, *Nature Communications*, 14(1), p. 341. <https://doi.org/10.1038/s41467-023-35922-5>.

Cigrang, M. *et al.* (2025) ‘Pan-inhibition of super-enhancer-driven oncogenic transcription by next-generation synthetic ecteinascidins yields potent anti-cancer activity’, *Nature Communications*, 16(1), p. 512. <https://doi.org/10.1038/s41467-024-55667-z>.

Seminary :

2nd World Congress on Rare Skin Diseases du 12 au 14 juin 2024 – Maison Internationale- Cité Internationale Universitaire de Paris.

- Poster: XPD mutations related to rare skin disorders differentially affect DNA repair, mitosis and transcription. *Elly Clémence, COIN Frédéric, COMPE Emmanuel*

Résumé en français

Le Xeroderma Pigmentosum group D (XPD) codée par le gène *ERCC2* est une hélicase 5'-3' ATP-dépendante connue pour être l'une des sous-unités du facteur général de transcription TFIIH. Ce complexe, composé de dix sous-unités réparties en deux sous-groupes, le CAK (Cycline H, CDK7, MAT1) relié par XPD au cœur (XPB, p62, p52, p44, p34, p8) participe à la transcription de gènes codant pour des protéines. Durant la transcription, XPB ouvre la double hélice d'ADN conduisant à l'avancée de l'ARN polymérase II et à la synthèse de l'ARN naissant. La sous-unité XPD participe au maintien de la stabilité du complexe TFIIH au niveau des promoteurs des gènes codant pour des protéines mais aucun rôle enzymatique durant ce mécanisme n'a encore été décrit.

XPD est principalement connue pour son rôle dans la réparation de dommages à l'ADN par excision de nucléotides (NER). L'ADN est exposé à de nombreuses attaques génotoxiques endogènes et exogènes qui génèrent des lésions tels que les Cyclobutane Pyrimidine Dimère (CPD) et les 6-4 pyrimidine primidone (6-4 PP). Après reconnaissance de ces dommages, TFIIH est recruté sur l'ADN. L'activité hélicase de XPD permet l'ouverture de la double hélice au niveau de la lésion et conduit au recrutement d'exonucléases ainsi que de l'ADN polymérase afin de couper autour de la lésion et de resynthétiser le brin endommagé. Ce mécanisme veille au maintien de l'intégrité du génome. Mais XPD ne se cantonne pas qu'à sa présence au sein de TFIIH. En effet, de récentes études ont révélé que cette sous-unité peut également se retrouver associée à d'autres facteurs comme la kinésine Eg5, avec laquelle XPD participe à la ségrégation des chromosomes durant la mitose.

Des mutations dans la protéine XPD sont associées à des maladies autosomales récessives rares, comme la Trichothiodystrophie (TTD) pour laquelle les patients présentent une ichtyose, des anomalies neurologiques ainsi que des ongles et des cheveux cassants. XPD mutée peut également induire l'apparition de la pathologie du Xeroderma Pigmentosum (XP), qui se révèle par une forte sensibilité aux UV et une prédisposition à développer des cancers de la peau. XP peut également être associé au Syndrome de Cockayne (XP/CS) qui se caractérise par une forte sensibilité au UV, un retard de croissance et de sévères anomalies neurologiques. Pendant longtemps, ces maladies ne furent expliquées que par des défauts de réparation de l'ADN. Or les divers rôles joués par XPD laissent entendre que d'autres mécanismes cellulaires pourraient être affectés. C'est dans ce cadre que s'inscrit mon projet de thèse, dont l'objectif est de mieux appréhender les conséquences de

mutations dans XPD sur les mécanismes de réparation de l'ADN, de la transcription et de la division cellulaire, afin de mieux comprendre l'étiologie de ces pathologies.

I- XPD est principalement connue pour son rôle dans la NER. Cependant, il a été révélé que cette protéine participait aussi à la ségrégation des chromosomes lors de la mitose. En revanche, son rôle dans ce dernier mécanisme n'est pas très bien défini. Des analyses ont été conduites sur des cellules de patients atteints du XP-D arborant la mutation XPD/R683W qui présentent une hypersensibilité aux UV. De manière surprenante elles présentent également des défauts d'alignements et de ségrégation des chromosomes durant la mitose conduisant à une accélération de la progression mitotique. J'ai dans un premier temps participé à un projet permettant de comprendre les conséquences d'une telle mutation dans XPD et ces partenaires mitotiques dans l'objectif de mieux caractériser la fonction de la protéine lors la mitose. Des études approfondis révèlent un partenariat entre la kinésine Eg5 et XPD qui se trouve fragilisé en présence de la protéine mutée. De plus, la mutation semble impacter la localisation de la kinésine lors de la mitose, affectant son rôle dans la séparation des chromosomes. De plus, des approches de spectrométrie de masse ont permis de mettre en évidence qu'une phosphorylation de XPD sur la thréonine en position 425 était importante pour la pleine activité de XPD durant la mitose. Compte tenu du rôle de XPD lors de la réparation et de la transcription, j'ai vérifié si cette phosphorylation pouvait aussi influencer l'activité de XPD dans ces deux mécanismes. Nos travaux suggèrent que l'état de phosphorylation de XPD n'influence ni la survie cellulaire après irradiation aux UV ni l'activation de la transcription. Cette phosphorylation semble donc uniquement requise pour la division cellulaire. Ces résultats ont fait l'objet d'un article publié en 2022 dans la revue 'Science Advances' dans lequel je suis co-auteur.

II- Par la suite, afin de mieux comprendre le rôle de XPD durant la réparation de l'ADN, la transcription et la division cellulaire, nous avons analysé l'effet de différentes mutations de XPD sur ces trois mécanismes. Pour ce faire, nous avons réalisé de l'édition génomique par la méthode CRISPR Cas9 afin de générer des lignées cellulaires exprimant un XPD endogène portant une étiquette fluorescente GFP et arborant différentes mutations connues pour affecter son activité hélicase/ATPase: la mutation XPD/G47R (mutation retrouvée chez des patients XP/CS) touche à l'activité ATPasique de XPD en déformant la poche d'accueil de l'ATP. La mutation XPD/G602D (mutation XP/CS) affecte l'un des domaines hélicases de la protéine et conduit à la perte de son

activité enzymatique. Enfin, la mutation XPD/K48R (mutation artificielle) induit la perte de son activité ATPasique en empêchant la reconnaissance de lysine 48 par l'ATP. Ces différentes lignées partagent le même fond génétique et ne diffèrent que par la mutation introduite dans XPD.

Compte tenu, du rôle de la protéine XPD dans la NER, nous avons évalué les conséquences de ces différentes mutations sur la réparation des lésions après expositions aux rayons UV. De manière étonnante toutes les lignées mutantes, présentent une hypersensibilité similaire aux rayons UV. De plus, des études de dynamique du recrutement de XPD sur les lésions ont été effectuées et dévoilent une diminution du recrutement des protéines mutantes aux niveaux des dommages. Un suivi du niveau de réparation des lésions a été opéré et dévoile un maintien du nombre de lésions au cours du temps. En somme, les mutations XPD/G47R, XPD/G602D et XPD/K48R semblent affecter la NER de manière similaire. En perspective, des analyses centrées sur l'interaction des protéines mutantes avec l'ADN lésée seront réalisées.

Au regard du rôle de la protéine XPD pendant la mitose, nous souhaitons évaluer les conséquences de la perte de l'activité enzymatique de la protéine sur la ségrégation chromosomique. Des analyses de la localisation de XPD durant la mitose ont été effectuées. Elles mettent en évidence que les mutations induisant une perte de l'activité hélicase de XPD n'affectent pas sa localisation au niveau des fuseaux mitotiques lors de la métaphase, au niveau de la zone centrale des fuseaux mitotiques lors de l'anaphase et des corps centraux durant la télophase. De plus, la vitesse de progression des lignées mutantes durant les phases de division cellulaire a été analysée et ne semble pas être affectée par les différentes mutations de XPD, suggérant que les activités enzymatiques de XPD n'influent pas sur la progression mitotique. Nous avons ensuite évalué la capacité des cellules à respecter les points de contrôle mitotique en traitant les lignées au Taxol. De manière surprenante, nous constatons que la lignée XPD /G602D, outrepassa le blocage (slippage) du traitement et progresse en anaphase. En perspectives, des études d'interaction entre les protéines mutantes et leur partenaires mitotiques seront réalisées. Ces données nous amènent à penser que pendant la mitose, les mutations G47R et K48R n'affectent pas la localisation de XPD, ni la ségrégation de chromosomes. Cependant, la mutation G602D induit le slippage des points de contrôle et l'apparition de défauts mitotiques.

Compte tenu du rôle structural de XPD lors de la transcription, nous nous sommes intéressés à l'effet des mutations affectant l'activité enzymatique de XPD sur la transcription par une analyse de séquençage d'ARN haut débit. De manière remarquable, ces défauts transcriptionnels diffèrent

selon la nature de la mutation. En effet, la mutation G47R ne provoque que des légers changements d'expression de gènes par rapport aux cellules non-mutées. Cependant, les mutations G602D et K48R induisent la dérégulation d'expression de centaines de gènes, et de manière surprenante, beaucoup de ces gènes sont partagés entre les cellules mutantes G602D et K48R. Afin d'étudier les conséquences des mutations XPD sur l'induction forcée de l'expression de gènes, les cellules ont été traitées ou non à l'acide rétinoïque (AR), connu pour induire l'expression de gènes cibles spécifiques. Alors que les effets de la mutation G47R étaient négligeables, nous avons constaté que les mutations G602D et K48R perturbent l'induction des gènes AR-dépendant. Ces résultats suggèrent que la transcription peut être affectée par une déficience de l'activité de XPD, mais montrent aussi des divergences en fonction des mutations.

Des mutations dans la protéine XPD conduisent au développement de pathologies tels que le TTD, le XP et XP/CS. Historiquement, ces pathologies n'étaient attribuées qu'à un mécanisme de NER défectueux provenant de l'incapacité de XPD à ouvrir la double hélice d'ADN. XPD est également impliqué dans la division cellulaire et la transcription. Nous mettons en évidence dans cette étude que l'hélicase XPD est une protéine pluri-mécanistique dont des mutations distinctes peuvent affecter ces processus cellulaires de manière différentielle. Alors que les effets sur la réparation de l'ADN des trois mutations étudiées sont similaires, leurs conséquences sur la transcription divergent fortement. Pendant longtemps, le fait que des mutations différentes dans la même protéine pouvaient provoquer des pathologies aussi phénotypiquement distinctes que le XP, TTD ou CS était difficile à expliquer. Nos résultats permettent de mieux comprendre le rôle complexe de XPD et les effets différentiels de ses mutations, et nous aident ainsi à mieux appréhender les pathologies associées.

List of figures

FIGURE 1 : SUBUNITS OF THE GENERAL TRANSCRIPTION FACTOR TFIID.	20
FIGURE 2 : CRYO-EM STRUCTURE OF THE HUMAN APO-TFIID COMPLEX-SIDE VIEW (A) AND TOP VIEW (B).	22
FIGURE 3 CRYO-EM OF THE CAK FROM THE APO-TFIID.	23
FIGURE 4 : STRUCTURE OF XPD/ERCC2.	24
FIGURE 5: 3D STRUCTURE OF THE XPD PROTEIN.	24
FIGURE 6: STRUCTURE AND ORGANIZATION OF GENOMIC DNA.	27
FIGURE 7 : RNA POL II CORE PROMOTER COMPOSITION.	30
FIGURE 8: EUKARYOTIC CORE ENHANCERS	31
FIGURE 9 : PRE-INITIATION-COMPLEX (PIC).	34
FIGURE 10: PHOSPHORYLATION PATTERN OF THE RNA POL II HEPTAPEPTIDE DURING THE TRANSCRIPTION PHASES.	36
FIGURE 11: rDNA TRANSCRIPTION BY RNA POLYMERASE I.	38
FIGURE 12: REPRESENTATION OF RIBOSOME GENESIS.	39
FIGURE 13: CATEGORIES OF UV RAYS AND THEIR ABSORPTION THROUGH THE HUMAN SKIN.	40
FIGURE 14 : DNA DAMAGES REMOVED BY NER.	42
FIGURE 15: NUCLEOTIDE EXCISION REPAIR MECHANISM (NER).	46
FIGURE 16 : CELL CYCLE REGULATION BY CYCLINS AND CDKS.	47
FIGURE 17 : EUKARYOTIC ANIMAL CELL.	48
FIGURE 18 : CHROMOSOMES CENTROMERE AND KINETOCHORES COMPOSITION	51
FIGURE 19: EUKARYOTIC CELL CYCLE.	55
FIGURE 20 : DISEASE RELATED MUTATIONS OF THE TFIID SUBUNITS XPD.	57
FIGURE 21 : 3D STRUCTURE OF XPD/R683W	58
FIGURE 22: 3D STRUCTURE OF XPD/G47R	58
FIGURE 23 : 3D STRUCTURE OF XPD/G602D	59
FIGURE 24 : 3D STRUCTURE OF XPD/K48R	60

List of tables

TABLE 1 : SUBUNIT COMPOSITION AND FUNCTIONAL ROLES OF THE HUMAN TFIIH COMPLEX.	
.....	20
TABLE 2 : EUKARYOTIC RNA POLYMERASES AND FUNCTIONS.....	28
TABLE 3 : EUKARYOTES RNA POLYMERASES AND SUBUNITS.	29
TABLE 4 : PREVALENCE OF XP IN USA, JAPAN AND EUROPE	61
TABLE 5 : COMPARISON OF FEATURES OF XERODERMA PIGMENTOSUM, TRICHOTHIODYSTROPHY AND COCKAYNE SYNDROME.....	65

General introduction

The genetic information that governs human development and physiological maintenance is stored within the genomic sequence of deoxyribonucleic acid (DNA). The integrity of the genome is essential for the proper functioning of cells and the survival of organisms. This stability is largely based on highly conserved DNA repair mechanisms capable of correcting alterations caused by both exogenous and endogenous stresses. Among these mechanisms, Nucleotide Excision repair (NER) plays a fundamental role in eliminating distorting DNA lesions.

The Xeroderma Pigmentosum D protein (XPD), an essential component of the crucial Transcription Factor II H complex (TFIIH), is involved not only in DNA repair but also in transcription and the cellular division. Mutations in XPD, are associated with several rare genetic diseases, including Xeroderma Pigmentosum (XP), Cockayne Syndrome (CS) and Trichothiodystrophy (TTD), each characterized by distinct and often severe clinical manifestations.

This thesis aims to elucidate the impact of mutations affecting XPD on fundamental cellular processes. The first section of the manuscript will present the TFIIH complex, with a particular focus on the subunits XPD. Given the involvement of XPD in gene expression, DNA repair, and cellular division, these key molecular processes will be introduced, highlighting the role of XPD in each of them. Finally, the third section of the manuscript, will explore various XPD mutations and detail the associated pathologies.

By combining biochemical, cellular and genetic approaches, the results section will investigate how these mutations impair DNA repair, alter transcription, and disrupt cell division. A better understanding of XPD's functions and the consequences of its dysfunctions could provide valuable insights into the pathophysiology of related diseases and help pave the way for targeted therapeutic strategies.

Ultimately, exploring the links between XPD mutations, genomic instability, and rare diseases will contribute to deciphering the molecular mechanisms underlying genetic disorders and identifying potential targets for medical interventions.

Section 1: TFIIH and its subunits XPD

1. The TFIIH complex

One of the most pivotal complexes in molecular and cellular processes is the human general Transcription Factor II H (TFIIH) characterized in 1992, by members of my host team (Lu et al. 1992). TFIIH has been the subject of extensive research since then. Studies have ranged from structural analyses of the complex to in vitro and in vivo molecular and biochemical evaluations of its functions in transcription and DNA repair (Egly et Coin 2011; Compe et Egly 2016). Its dual role makes it a critical guardian of genome function and stability.

1.1.Composition

TFIIH is a heterodecameric protein complex divided in two subcomplexes: the Core comprising seven subunits and the CDK Activating Kinase (CAK) composed of three subunits (Compe et Egly 2012; Greber et al. 2019).

Each of the seven subunits of the core contributes to a specific structural or enzymatic function of the complex. The Xeroderma pigmentosum B (XPB), encoded by the gene *ERCC3* is a ATP-dependent helicase (Fan et DuPrez 2015; Chauhan et al. 2021). The subunit p62 (*GTF2H1*) has a strict structural role in the complex (Okuda et al. 2021). The subunits p52 (*GTF2H4*) interacts directly with XPB and regulates its translocase activity (Jawhari et al. 2002; Kappenberger et al. 2020). Contributing to the structural stability of the core complex, p34 (*GTF2H2*) helps to maintain the integrity of TFIIH (Radu et al. 2017).

One of the most important subunit of the complex TFIIH is the Xeroderma pigmentosum D (XPD) encoded by *ERCC2* which functions as a 5' to 3' ATP-dependent helicase (Lehmann 2008; Kuper et al. 2014; Houten et al. 2016). I will describe this crucial multifunction subunit on a specific chapter. Regulating the helicase function of XPD is the subunit p44 (*GTF2H3*) (Coin et al. 1998; J. S. Kim et al. 2015). The last subunits to be discovered is the p8 /Trichothiodystrophy group A (p8/TTD-A) protein encoded by the *GTF2H5* gene. p8/TTD-A is essential for stabilising the whole complex and increasing the efficiency of nucleotide excision repair and regulating as well the ATP activity of XPB (Coin et al. 2006; Giglia-Mari et al. 2006; Gervais et al. 2018).

The CAK is the other subcomplex of TFIIH and is composed of three subunits that contribute to the hole function of the complex (Kaldis 1999; Lolli et Johnson 2005; Coin et al. 2008; Radu et al. 2017). The subunit Cyclin-Dependent Kinase 7 (CDK7) as a kinase function. The Cyclin H regulates the activity of CDK7 and serves as a functional link between TFIIH and cell cycle control

mechanisms (M. Wang et al. 2020). The Ménage A Trois 1 (MAT1) interact with XPD which acts as a bridge connecting the CAK module to the core of TFIIH complex (Busso et al. 2000; Abdulrahman et al. 2013; Rimel et Taatjes 2018). (**Table 1 & Figure 1**)

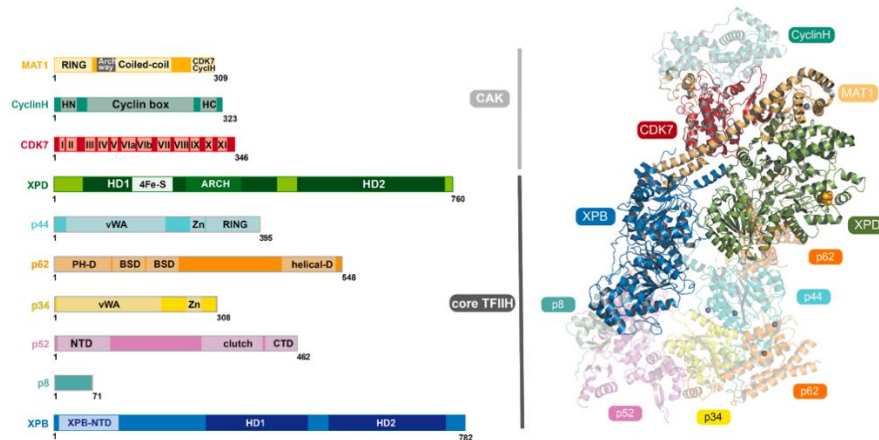


Figure 1 : Subunits of the general transcription factor TFIIH.

TFIIH is constituted of 10 subunits divided into subcomplexes: the Core composed by Xeroderma pigmentosum B (XPB), p62, p52, p34, p33, p8 bridged by Xeroderma pigmentosum D (XPD) to the CDK Associated Kinase (CAK) composed by Cyclin H, Cyclin Dependent Kinase 7 (CDK7) and Menage À Trois 1 (MAT1). The kinase activity of TFIIH is detained by CDK7. XPB is an ATP dependent translocase regulated by the subunit p52 and XPD is ATP dependent 5'3' helicase which activity is regulated by p44. (Kuper et Kisker 2021).

Subcomplex	Subunits	Functions
Core	XPB	ATP dependent 3'5' Translocase
	p52	Regulating positively XPB's ATPase activity
	p34	Structural function
	p62	Structural function
	p44	Regulating positively XPD's helicase activity
	XPD	ATP dependent 5'3' Helicase Bridge the CAK to the Core
	p8	Structural function
CAK	MAT1	-Stabilization and anchor the CAK to the core - Inhibition of XPD's helicase activity
	CDK7	Kinase activity
	Cyclin H	Modulate CDK7 activity

Table 1 : Subunit composition and functional roles of the human TFIIH complex.

The core of TFIIH is composed of XPB, p52, p34, p62, p44 and XPD, with XPB caring an ATP dependent translocase activity and XPD caring a 5'3' ATP dependent helicase activity

1.2. Structure of TFIIH

TFIIH adopts three major structural conformations, each corresponding to a different functional state. From the “Holo” TFIIH can be adopted the “Apo” form of TFIIH adopted during the Transcriptional state and the DNA Repair (NER) state (Yu et al. 2023) (**Figure 2**). The Apo form of TFIIH represents the ligand-free conformation of the complex: untangled to DNA, transcription proteins, or repair substrates. In this inactive state, TFIIH is assembled but not functionally engaged, making it a valuable reference point for understanding how structural changes enable its activation in transcription or DNA repair. Greber et al. resolved the structure of human core-TFIIH using phase plate cryo-electron microscopy, achieving a 3.7 Å resolution (Greber et al. 2019). The structure captures the core complex of TFIIH, comprising XPB, XPD, p62, p52, p44, p34, and TTDA/p8 in its unbound conformation.

The core TFIIH adopts a horseshoe-like overall conformation, with subunits wrapping around a central cavity (Greber et al. 2017). This shape provides a framework that supports dynamic interactions with DNA and other factors during activation. The XPB helicase, located at one end of the horseshoe, is tightly associated with p52 through homologous domains that form a pseudo-symmetric dimer (Kappenberger et al. 2020). This interaction is essential for anchoring XPB in place and possibly stabilizing it in a pre-catalytic (inactive) conformation. Indeed, XPB is not in contact with DNA in this state. Its ATP-binding site is intact but not engaged. This arrangement suggests that XPB requires additional interactions such as with promoter to transition into an active state (Fan et DuPrez 2015). One of the most striking features of the Apo-TFIIH structure is the insertion of p62 into the helicase core of XPD (Barnett et al. 2020). The subunit p62 threads into the DNA-binding groove of XPD, physically blocking substrate access. This configuration autoinhibits XPD in the absence of DNA damage, preventing unnecessary helicase activity (H. Liu et al. 2008). It acts as a safeguard to maintain XPD in an inactive state. Subunits p44 and p34 interact via interlocking zinc-binding domains, stabilizing the core structure (Radu et al. 2017). These domains are structurally conserved and act as a scaffold, connecting the helicases to the rest of the complex. Moreover, p44 influences XPD’s helicase activity enhancing the function (C. Nance et al. 2025). The subunit p8/TTDA is located near XPD and contributes to the stability of the overall complex (Aguilar-Fuentes et al. 2008; Cruz-Becerra et al. 2016).

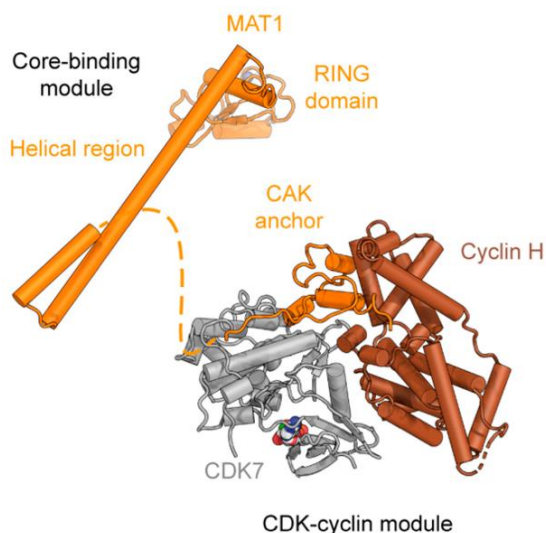


Figure 3 Cryo-EM of the CAK from the apo-TFIIF.

The CAK complex is composed of CDK7 (gray), Cyclin H (dark orange), and MAT1 (light orange). The structure is divided into two main functional regions: the CDK–Cyclin module, which includes the catalytic core CDK7 and its regulatory partner Cyclin H, and the core-binding module of MAT1. Key MAT1 domains are labeled, including the helical region and the RING domain, which are involved in anchoring CAK to TFIIF. The CAK anchor within MAT1 (highlighted in orange) stabilizes interactions between the CDK–Cyclin module and the rest of the complex. This structure reflects the modular and flexible of CAK. Adapted from Greber 2020.

2. Structure and Functional Domain of XPD

2.1. XPD overview

As it has been mentioned above the protein XPD is one of the most pivotal subunits of TFIIF. Presenting the protein generally, the gene *ERCC2*, located in the chromosome 19q13.2 encodes for the protein XPD of 760 Amino Acids (Lehmann 2008). Structurally, XPD belongs to the Superfamily 2 (SF2) helicases and has a distinct four-domain architecture, each critical for its enzymatic activity and protein interactions (Y. Wu et al. 2009; Byrd et Raney 2012). Amongst them, there are, two RecA-like Helicase Domains which (D1 and HD2) (**Figure 4**). 7 helicase motifs (I, Ia, II, III, IV, V and VI) have been identified and participate to the enzymatic function of XPD (Houten et al. 2016). The N-terminal domain contains a conserved iron-sulfur (Fe-S) domain and cluster, which is essential for DNA binding, helicase function, and strand separation during DNA repair (Rudolf et al. 2006; Vashisht et al. 2015). Additionally, XPD possesses a unique Arch domain constituting 25% of the protein size. This domain forms an arch-like structure serving as a platform to interact with MAT1 subunit (Fan et al. 2008; Kralund et al. 2013).

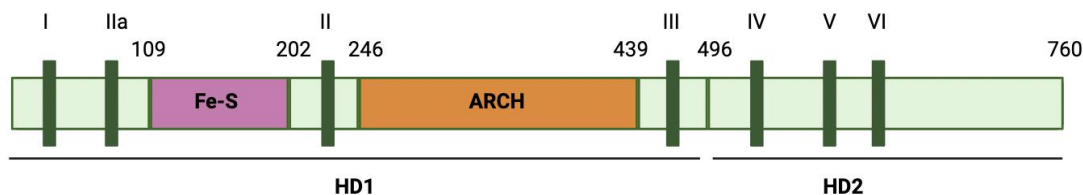


Figure 4 : Structure of XPD/ERCC2.

XPD is a 760 amino acid long protein. It contains two Helicase domain (HD1 and HD2) and 7 helicase motifs represented in green and dark green. The N-terminal region contains the Fe-S domain and cluster (in purple) that is necessary for its DNA binding and enzymatic activity. The Arch domain represented in orange, participates to XPD interaction with the CAK especially with MAT1. The C-terminal region allow its interaction with other TFIIH core protein such as p44 and p62.

2.2. XPD structure

HD1 and HD2 domain's folding are characterized by a central seven-stranded parallel β -sheet flanked by α -helices, forming part of the catalytic core essential for ATP binding and hydrolysis (**Figure 5**) (Liu et al. 2008). The spatial arrangement of these domains creates a central pore-like structure that accommodates single-stranded DNA (ssDNA) during the helicase's translocation process (Kuper, Hove, Maidl, Sauer, et al. 2024). ATP molecule recognizes the Lysine at the position 48 (K48) in the N terminal region. ATP binds in its pocket, promoting its hydrolysis (Ueda et al. 2009). Upon ATP binding, conformational changes in HD1, in coordination with HD2, facilitate the unwinding of DNA strands.

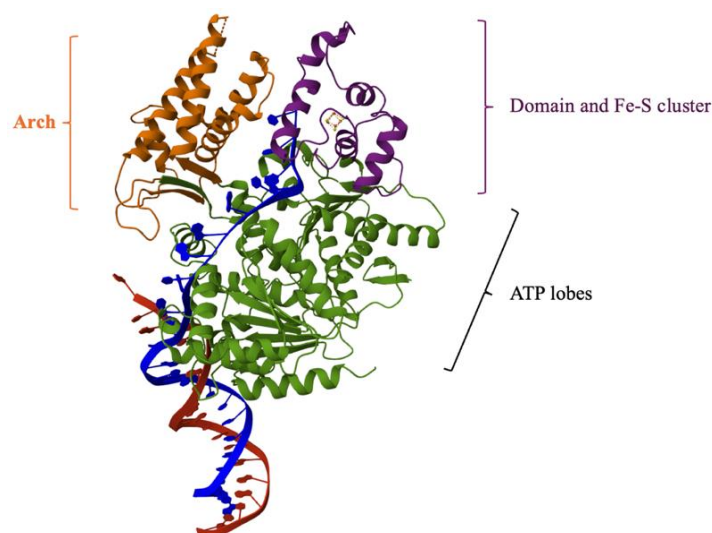


Figure 5: 3D structure of the XPD protein.

The Arch is represented in orange. The Fe-S domain is in purple and the HD1 and HD2 domain forming the ATP lobes recognized by the ATP remains in green PDB (6ROI) (Kokic et al. 2019).

Section 2: XPD's role in major cellular processes

1. Localization, structure and organization of the genome

One of the most intricate features in the study of the living organisms is the storing and the coding of the information required for the development and maintenance of a human organism. These information reside in around 2 meters of genomic DNA protected in the cellular nucleus and organized through multiples levels of compaction (Peterson et Laniel 2004; Piovesan et al. 2019).

Structurally, the DNA exists as a double-stranded helix described by Watson and Crick in 1953, where two antiparallel strands of nucleotides are linked by a sugar-phosphate backbone and held together by specific base-pairing interactions—Adenine (A) pairs with Thymine (T) and Cytosine (C) pairs with Guanine (G) via hydrogen bonds (Watson et Crick 1953). This arrangement ensures the stability and fidelity of genetic information. To achieve higher-order compaction, the double strand is wrapped around an octamer of histone proteins, forming the nucleosome, where 146 base pairs (bp) of DNA are wound around Histone 2 A, (H2A), Histone 2 B (H2B), Histone 3 (H3), and Histone 4 (H4) (Chhetri 2025). Nucleosomes are further coiled into chromatin fibers, which undergoes additional folding and looping to generate highly condensed chromosomes (**Figure 4**) (Misteli 2020).

Beyond structural organization, the accessibility of the genomic information is highly regulated by several mechanisms. Chromatin can exist in two functional states: euchromatin, which is loosely packed and therefore easily accessible for transcription factors, and heterochromatin, which is highly and tightly compacted (Morrison et Thakur 2021). Additionally, chromatin architecture is organized in topologically Associating Domains (TADs), chromatin looping, and nuclear compartmentalization, which contribute to gene regulation and cellular identity (Cramer 2019). Thus, the localization, structure, and organization of genomic DNA in eukaryotic cells reflect an intricate balance between compaction and accessibility, ensuring efficient gene expression, replication, and genome stability while maintaining the necessary structural integrity for cell function and inheritance.

Many processes enable cells to maintain their structure, respond to their environment, and ensure survival. Among them, transcription is a critical phases of gene expression, engaging in the production of proteins necessary for diverse biological functions.

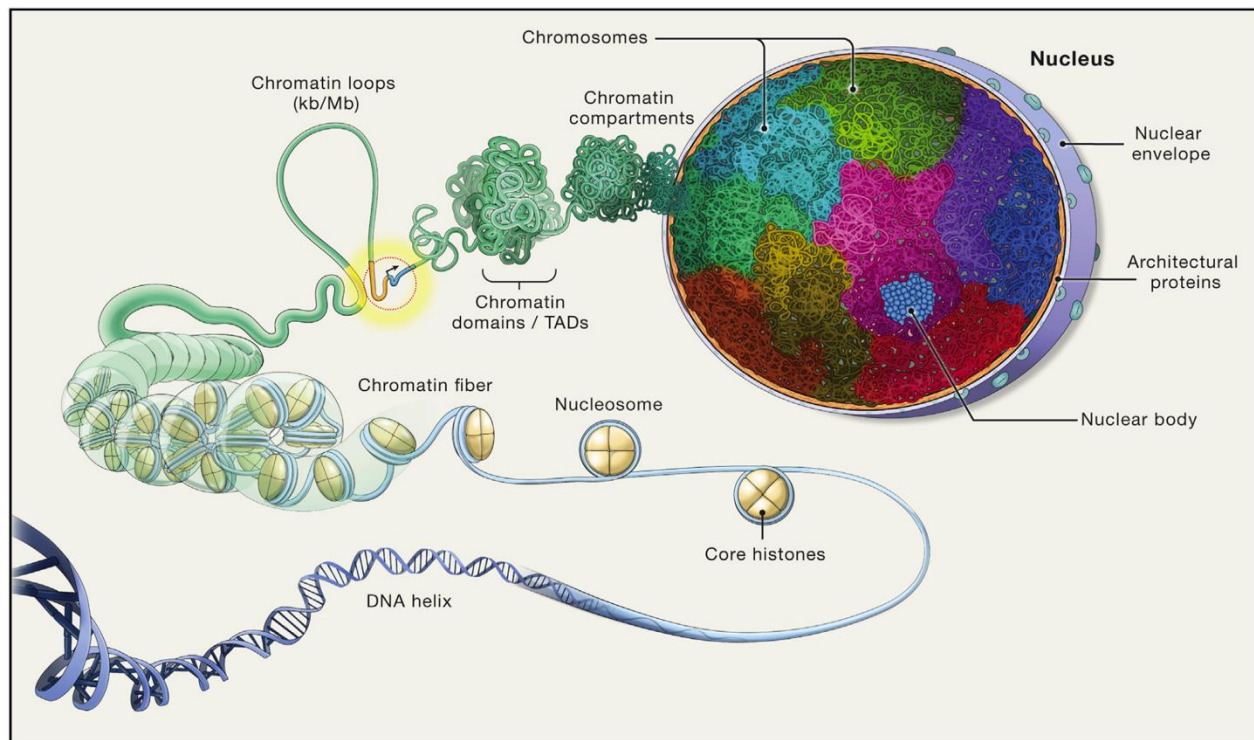


Figure 6: Structure and organization of genomic DNA.

Genome is organized on multiple levels. The double strand DNA organized in a helix is wrapped around an octamer of histones. The DNA fragment tangled around histones represent 146pb and is called nucleosome. Compacted the genome is sectioned into topologically associated domains (TAD) regulating interactions with transcription factors. This organization allows the genomic DNA to be compacted and to fit in a small cellular compartment : the nucleus (Misteli 2020).

2. Transcription mechanism

All the information necessary to develop and maintain a human organism is coded into sequences of nucleotides stored in the genomic DNA. Transcription is the molecular process by which the genomic information is read, decoded and copied into a new molecule of RNA converting DNA into a much more functional format (Spencer et Groudine 1990; Lee et Young 2000; Kornberg 2007; Roeder 2019). 98% of the genome represent the regulatory and repetitive elements and the 2% remaining correspond to the number of genes coding for proteins (Amaral et al. 2023). Taking place in the nucleus for eukaryotes and cytoplasm for prokaryotes, transcription is a complexed mechanism where myriads of proteins respect a precise choreography through the three main steps: Initiation, Elongation and Termination (Schier et Taatjes, s. d.). It's a mechanism finely regulated on several levels to guarantee a proper gene expression.

2.1.RNA polymerase

The enzymes able to read and transcribe RNA from DNA are the RNA polymerases (Barba-Aliaga et al. 2021). Prokaryotes and archaea present a unique enzyme (holoenzyme) when four have been identified in eukaryotes: RNA polymerase I, II, III, IV. Each RNA polymerase transcribes different types of genes and has specific transcription factors, recognition sequences and regulatory elements.

RNA pol I synthesizes the main ribosomal RNA, more specifically: 28S, 5.8S and 18S. RNA pol III transcribes tRNA, 5S rRNA and other small RNAs (**Table 1**) (Goodfellow et Zomerdijsk 2013; Merkl et al. 2020). RNA pol II transcribes messenger RNA (mRNA), a few nuclear RNAs (snRNAs) and micro-RNA (miRNA). RNA pol IV was identified only in plants and plays a role protecting the genome against virus (Borukhov et Nudler 2003; Zhou et Law 2015).

RNA polymerase I, II, and III comprise 14, 12 and 17 subunits respectively (**Table 2**). Focusing on Pol II, the enzyme consists of 10 subunits in the core and a peripheral heterodimer known as the Rpb4/7 (Calvo 2020). The core which includes Rpb1, Rpb2, Rpb3, and Rpb11, which show sequence and structural similarities in RNA pol I, RNA pol III and holoenzyme present in bacteria and archaea (Patrick Cramer 2002; Ryu et Lee 2024). Structural analysis identified intrinsic conformational flexibility within the enzyme. More specifically the CTD region of the polymerase localized in RNA polymerase II subunit Rpb. It contains a heptapeptide motif (Y¹-S²-P³-T⁴-S⁵-P⁶-S⁷) repeated 52 times that plays a pivotal role in transcription and undergoes distinct structural modifications allowing the enzyme to adapt to the various stages of the transcription cycle including initiation, elongation and termination (Cramer et al. 2008; Linhartova et al. 2024).

RNA polymerase	Function	Products
RNA pol I	Transcribes rRNA	28S, 18S and 5.8 S rRNA
RNA pol II	Transcribes mRNA & snRNA	mRNA, snRNA, miRNA
RNA pol III	Transcribes tRNA & 5S rRNA	tRNA, 5SrRNA, U6snRNA

Table 2 : Eukaryotic RNA polymerases and functions

Brief presentation of the different eukaryotic RNA polymerase and their functions. RNA pol I synthesizes the ribosomal RNA 45S later cleaved into 28S, 18S, 5.8 S RNA. RNA pol II synthesizes snRNA and mRNA. This last will be translated into proteins. RNA pol III synthesizes 5S RNA and transport.

RNA polymerases	RNA pol I	RNA pol II	RNA pol III
Ten-subunit core	A190	Rpb1	C160
	A135	Rpb2	C128
	AC40	Rpb3	AC40
	AC19	Rpb11	AC19
	AC12.2	Rpb9	C11
	Rpb5 (ABC27)	Rpb5	Rpb5
	Rpb6 (ABC23)	Rpb6	Rpb6
	Rpb8 (ABC14.5)	Rpb8	Rpb8
	Rpb10 (ABC10 α)	Rpb10	Rpb10
	Rpb12 (ABC10 β)	Rpb12	Rpb12
Rpb4/7 subcomplex	A14	Rpb4	C17
	A43	Rpb7	C25
TFIIF-like subcomplex*	A49	(Tfg1/Rap74)	C37
	A34.5	(Tfg/Rap30)	C53
pol III-specific subcomplex	-	-	C82
	-	-	C34
	-	-	C31
Number of subunits	14	12	17

Table 3 : Eukaryotes RNA polymerases and subunits.

Presentation of the all the subunits of RNA polymerase I, II, and III. The RNA polymerase core is composed of ten subunits with conserved sequences between the different polymerases. A TFIIF-like subcomplex refers to a protein pair or module within a transcription system (outside of Pol II) that performs TFIIF-like roles: aiding polymerase recruitment, promoter binding, and stabilization of the transcription pre-initiation complex (Cramer et al. 2008)

2.2.Promoters

This section will provide a more detailed view of the various factors and mechanisms involved in the transcription of genes by RNA polymerase II. The promoter, a specific DNA region located upstream of the gene, is recognized and bound by the transcriptional machinery during transcription initiation (**Figure 7**) (Core et Adelman 2019).

The core promoter is located ± 50 pb upstream from the Transcription Starts Site (TSS) corresponding to the first nucleotide transcribed and is composed of specific sequences.

The TATA Box (TATA-A/T-A-A/T-A/G) is the canonical core promoter and the first that has been identified. It is present in 15% of the core promoters and positioned 25 to 30 bp upstream the TSS (Ponjavic et al. 2006; Mishal et Luna-Arias 2022)-. This sequence is recognized by the TATA Binding Protein (TBP) and promotes the initiation of transcription (Haberle et Stark 2018). In the core promoter, there is also the TFIIB Recognition Element (BRE) (Brown 2018). There are two BRE sequences, one localized immediately upstream from the TATA box (BREu) at -32 to -37 bp from the TSS and another one downstream of the TATA box (BREd) located a -23 to -17bp. There is the presence as well of the Initiator sequence (Inr) which is found at the TSS (-2 to +4 bp) (Savina et al. 2023). Moreover, the Downstream Promoter Element (DPE) can be also found located at +28 to +33 bp (Sloutskin et al. 2023). The CG box is a regulatory DNA region rich in Guanine and Cytosine, commonly found in eukaryotes and located at -40 to -100 from the TSS. It binds specifics factors promoting the transcription initiation (Mahpour et al. 2018). Together they support precise positioning of RNA pol II (Vo Ngoc et al. 2017).

The TATA box is not present in all promoters (TATA-less promoters) (Ravarani et al. 2016). Indeed, many housekeeping genes often harbor core promoters with disperse TSS and no TATA box, relying therefore on alternative core promoter elements like Inr, DPE sequence and the CG box for RNA pol II recruitment.

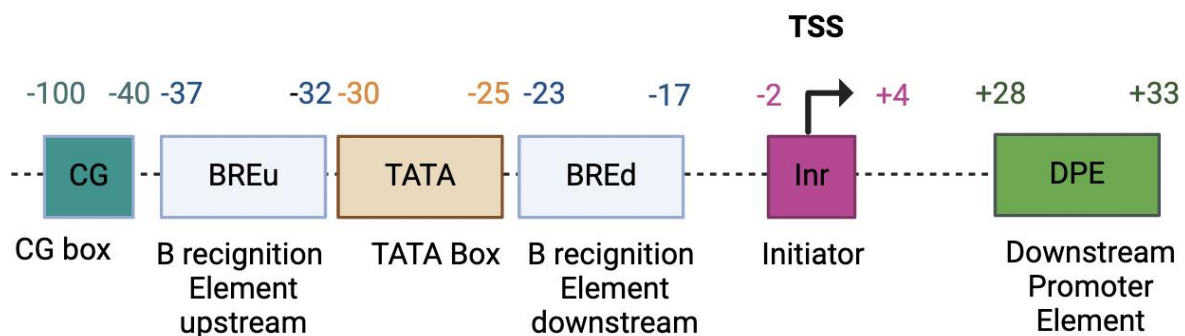


Figure 7 : RNA pol II core promoter composition.

Schematic representation of a core promoter recognized by RNA pol II in eukaryotic cells. Core promoter elements include the TATA box in orange (-25 to -30 upstream from the transcription start site +1), the Initiator (Inr) element overlapping the TSS, the TFIIB recognition elements (BREu and BREd) and the Downstream Promoter Element (DPE), located approximately +28 to +32 downstream of the TSS.

2.3. Enhancer

Enhancers are non-coding DNA sequences that significantly increase the transcription levels of target genes, often acting over long genomic distances (Barshad et al. 2023). Unlike promoters, which are typically located just upstream of the genes they regulate, enhancers can be located kilobases away—either upstream, downstream, within introns, or even on different chromosomes in some cases. They function by serving as binding platforms for Transcription Factors (TF) and Co-Factors (COFs) (**Figure 8**) (Kreibich et Krebs 2022). Once bound, these proteins help recruiting and stabilizing the transcriptional machinery at the promoter region of a gene. Enhancer activity is highly context-specific, depending on cell type, developmental stage, and external signals. Many enhancers are marked by specific histone modifications, such as H3K27ac and H3K4me1, that are open chromatin modifications which help distinguish them from other regulatory elements (Bae et Lesch 2020). Additionally, a single gene can be controlled by multiple enhancers, and a single enhancer can regulate multiple genes, adding layers of complexity to gene regulation (Karnuta et Scacheri 2018).

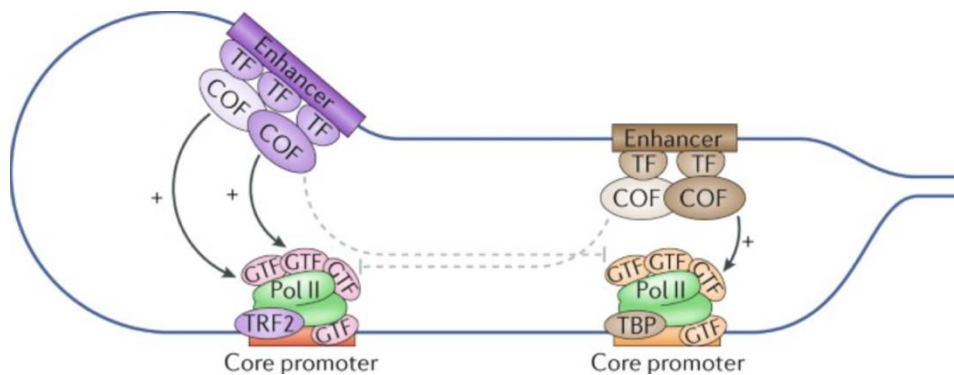


Figure 8: Eukaryotic core enhancers

Different types of core promoters respond differently to distal enhancers, i.e. an enhancer can activate them (solid arrows) or not (dashed arrows). This selectivity or specificity is mediated by different transcription factors (TFs) and cofactors (COFs) that exhibit core-promoter preferences that are likely based on biochemical compatibilities between the cofactors and core-promoter-bound general transcription factors (GTFs). For example, TBP-related factor 2 (TRF2) substitutes for TATA-box binding protein (TBP) at the promoters of many housekeeping genes and is essential for their activation. (Haberle et Stark 2018).

2.4.Silencer

Silencers are regulatory DNA elements that suppress the transcription of specific genes. There are crucial for maintaining gene expression patterns, especially during development and in tissue-specific gene regulation. Indeed, they repress genes expression and participate establishing the cell state during differentiation or in response to environmental signals (H. K. Long et al. 2020). Like enhancers, silencers can function at a distance from the gene and regulate upstream, downstream, or within introns (Segert et al. 2021). They work by binding repressor proteins that interfere with the transcriptional machinery, either by blocking the assembly of transcription factors at the promoter or by recruiting chromatin-modifying enzymes that compact the DNA, making it less accessible for transcription (Pang et Snyder 2020). Silencers can be identified by characteristic histone marks, such as the trimethylation of the Lysin 27 in the histone H3 (H3K27me3) which induces a tighter DNA compaction (Huang et al. 2019).

2.5.Mediator

The Mediator complex is a large, conserved multiprotein coactivator essential for transcriptional regulation by RNA polymerase II (Takahashi et al. 2020). Functioning as molecular bridge, Mediator transmits signals from sequence-specific transcription factors bound at upstream regulatory elements, transcription activating or repressor regions to the core transcriptional machinery assembled at the promoter. It facilitates the recruitment and stabilization of RNA pol II within the promoter (Rengachari et al. 2021). Structurally, the core of Mediator is composed of twenty-six subunits (Med1 to Med 26) organized in three modules: the Head, Middle, Tail. The core interact with the regulatory Kinase containing the Cyclin Dependent Kinases 8 (CDK8) and CDK19 associated with the Cyclin C and a specific Cyclin H (H. Zhang et al. 2021). The Head interacts with the RNA polymerase while the Tail interacts with DNA-bounds activators. (André et al. 2021).

2.6.Cohesin

Cohesin is an annular multiprotein complex that plays a critical role in transcription by stabilizing long-range interactions between enhancers and promoters (Waldman 2020). It facilitates the formation of chromatin loops that allow distal regulatory elements to contact target gene

promoters, thereby supporting efficient recruitment of the transcriptional machinery and fine-tuned gene expression, particularly during development and differentiation.

In addition to its role in gene regulation, cohesin is essential during mitosis, where it maintains sister chromatid cohesion from DNA replication until their separation at anaphase (Choi et al. 2022). This cohesion ensures accurate chromosome segregation and maintains genomic integrity during cell division.

2.7. Transcription steps

2.7.1. Initiation

Initiation is mediated by RNA pol II a variety of General Transcription Factors (GTFs), which are essential for accurate transcription initiation. The first step in transcription initiation begins with the recognition of the core promoter elements, which may include the TATA box, Inr sequence, DPE, GC box, and BRE sequences (Bhuiyan et Timmers 2019). In promoters that contain a TATA box, the TBP, a subunit of the TFIID complex, binds to the TATA sequence located approximately 25-30 base pairs upstream of the transcription start site (TSS) (**Figure 9**) (Andersson et Sandelin 2020). If the promoter lacks a TATA box, alternative elements like the Inr or DPE assist in positioning the transcription both TBP and the BRE sequences, further stabilizing the transcription complex and providing a direct interaction site for Pol II machinery (Smale 1997). Once TFIID is bound, it facilitates the recruitment of TFIIA, which stabilizes the complex and prevents repressors from binding (J. Wang et al. 2020). Next, TFIIB is recruited and interacts with RNA pol II, alongside with the Mediator complex (O'Brien et Ansari 2022). TFIIF binds to RNA pol II and enhances its affinity for the promoter, preventing premature dissociation (Girbig et al. 2022). The final crucial step involves the recruitment of TFIIE and TFIIH, which play critical roles in transcription activation (Compe et al. 2019). TFIIH possesses a helicase activity through its subunit XPB. Unwinding the DNA strands around the transcription start site, XPB creates a transcription bubble that allows Pol II to read the template strand (Chauhan et al. 2021). Interestingly, in the presence of the pre-initiation complex (PIC), p62 inserts into XPD's DNA-binding groove, rendering XPD inactive. This action prevents its helicase activity, allowing XPB to function as the primary translocase during transcription initiation. Although XPD held an inactive state, its structural role ensures the integrity of the PIC necessary for interacting with XPB

and other component of the transcription machinery (Kuper et al. 2014). Additionally, TFIIF contains a kinase, the Cyclin Dependent Kinase 7 (CDK7) that phosphorylates the C-terminal domain of RNA pol II localized in the Rpb1 subunit, specifically at serine 5 and 7 of the heptapeptide repeats (Velychko et al. 2024). This phosphorylation, induce a switch of the RNA pol II conformation promoting the escape of the promoters and beginning of RNA synthesis. This process is tightly regulated by enhancers, silencers, chromatin modifications, and epigenetic factors, ensuring precise gene expression control required for cell differentiation, development, and response to environmental stimuli (Sainsbury et al. 2015).

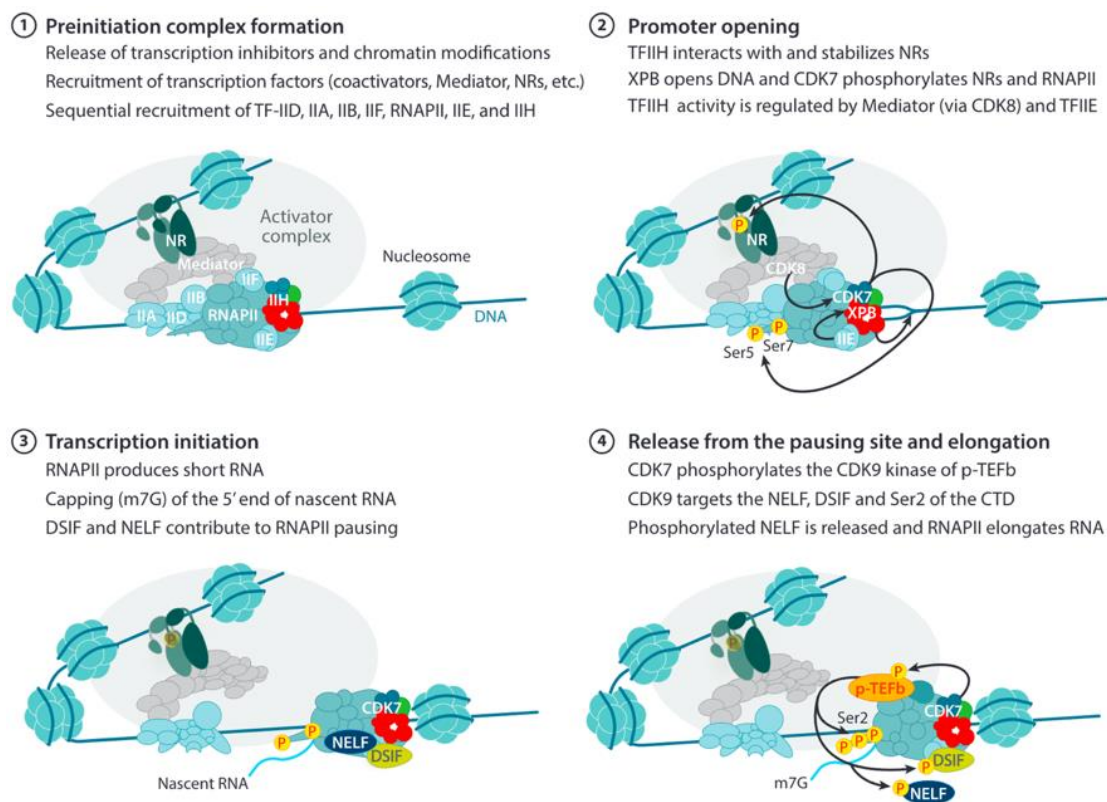


Figure 9 : Pre-Initiation-Complex (PIC).

Step 1: Formation of the PIC at the promoter with the recruitment of the RNA pol II and the general transcription factors TFIIF, a complex composed by ten subunits. One of them, XPB is responsible for the DNA opening. Step2: Phosphorylation of the Serine 5 and 7 in the RNA pol II CTD region by Cdk7 promoting its escaping from the promoter. Step 3: Synthesis and capping of the short the nascent RNA. Pausing of the RNA pol II. Steps 4: Loss of the phosphorylation of S2 and S5. Cdk9 phosphorylate the S2 CTD participating the RNA pol II elongation. **Adapted from Compe & Egly 2016**

2.7.2. Elongation

Before entering into the elongation, DRB Sensitivity Inducing Factor (DSIF) and Negative Elongation Factor (NELF) bind to the pol II and inhibit its activity, forcing Pol II to pause over 20 to 100 nucleotide post TSS (Shao et Zeitlinger 2017). The phosphorylation of DSIF biggest subunits, Spt5 and NELF by the Cyclin dependent kinase 9 (CDK9) belonging to the positive Transcription Elongation Factor b complex (p-TEFb). Additionally, the phosphatase rtr1 dephosphorylates Ser-5 on the CTD, while CDK9 phosphorylates Ser-2 promoting the start of the elongation phase (**Figure 7**) (Y. K. Kim et al. 2002).

During elongation, RNA polymerase II unwinds the DNA double helix, reads the template strand (antisense strand in a 3' to 5' direction), and catalyzes the addition of complementary ribonucleotides (NTPs) to the growing pre-mRNA strand in the 5' to 3' direction (Muniz et al. 2021). As RNA pol II progresses along the DNA, it forms a transcription bubble, where approximately 15-20 base pairs of DNA remain unwound, allowing the enzyme to access the template sequence.

The newly synthesis RNA, is matured through three steps : the capping , the splicing and the poly A tail adding (K.-H. Yeom et al. 2021). This modification is crucial for mRNA stability, nuclear export, and translation initiation. As the nascent RNA emerges from RNA pol II, a 7-methylguanosine (m⁷G) cap is added to the 5' end by the Capping Enzyme Complex (CEC) to protect mRNA form degradation by nucleases (Y. Li et al. 2024). Furthermore, as elongation progresses, splicing factors such as the spliceosome complex are recruited to remove introns and join exons together, ensuring the proper maturation of the mRNA transcript (Bentley 2014).

Additionally, RNA polymerase II-associated proteins such as TFIIS assist in proofreading and rescuing backtracked polymerase, ensuring high-fidelity RNA synthesis (Zatreanu et al. 2019). Once RNA pol II reaches the termination signal, elongation factors dissociate, and the polymerase undergoes conformational changes that prepare it for transcription termination. (Jonkers et Lis 2015).

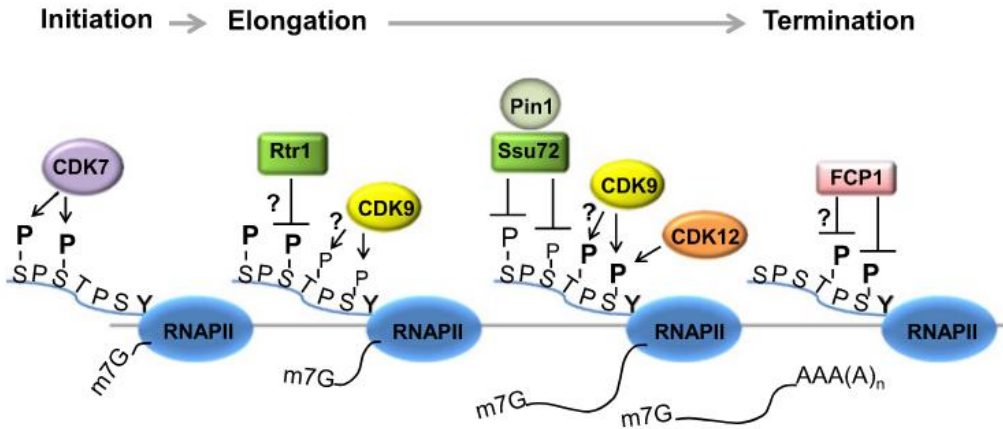


Figure 10: Phosphorylation pattern of the RNA pol II heptapeptide during the transcription phases.

During the initiation, the serine 5 and 7 are phosphorylated by Cdk7 allowing the RNA pol II escape of the promoter. During the pausing, the phosphatase Rtr1 remove the phosphorylation from S5 and S7. Simultaneously Cdk9 phosphorylate S2, promoting transcription elongation (Adapted from Jing-Ping Hsin & James L Manley).

2.7.3. Terminaison

This process is directed by the presence of a polyadenylation signal (AAUAAA), located 10–30 nucleotides upstream of the cleavage site in the 3' Untranslated Region (3' UTR) of the transcript (Sun et al. 2018). (Passmore et Collier 2022).

As soon as RNA pol II transcribes the conserved polyadenylation signal, it initiates recruitment of the cleavage and polyadenylation machinery, notably the Cleavage and Polyadenylation Specificity Factor (CPSF), which directly binds this sequence (So et al. 2019). Simultaneously, the Cleavage Stimulation Factor (CstF) binds downstream to a GU-rich region (Sun et al. 2020). This coordinated assembly activates the CPSF73 endonuclease subunit, which cleaves the nascent pre-mRNA downstream of the AAUAAA signal (Han et al. 2023).

Following cleavage, Poly(A) Polymerase (PAP) adds a poly Adenine tail to the newly formed 3' end of the pre-mRNA (J. Liu et Lu 2024). Meanwhile, RNA pol II continues transcription beyond the cleavage site. However, RNA polymerase II does not immediately dissociate after cleavage; instead, it continues transcribing the downstream non-coding region of the gene, producing a trailing RNA fragment that is rapidly degraded by the 5' to 3' exonuclease Xrn2 (West et al. 2004; Cortazar et al. 2022). Xrn2 binds to the uncapped 5' end of the trailing RNA and degrades it toward the polymerase, ultimately destabilizing RNA pol II participating to it

dissociation from the DNA template. This mechanism ensures that transcription stops efficiently while also preventing unnecessary or aberrant transcriptional readthrough (Brannan et al. 2012).

2.8. Role of TFIIF during RNA polymerase transcription

Although one of the canonical roles of TFIIF occurs during RNA pol II transcription, astonishingly the complex also plays an important role in RNA polymerase I (RNA pol I) transcription. RNA pol I has been describe transcribing ribosomal DNA (rDNA) into a large precursor transcript known as 45S pre-rRNA (Watt et al. 2023). This precursor is subsequently processed into 18S, 5.8S and 28S rRNAs which are essential structural and functional components of the ribosome (**Figure 12**) (Knutson et al. 2020). RNA pol I transcription occurs in the nucleolus and represents one of the most transcriptionally active processes in growing cells.

2.8.1. Initiation

The initiation phase begins with the recognition of the rDNA promoter by specific transcription factors. The Upstream Binding Factor (UBF) binds to upstream enhancer elements of the rDNA promoter (Ray   et al. 2025). Selective Factor 1 (SL1), a complex composed of TBP (TATA-binding protein) and RNA pol I-specific TBP Associated Factors (TAFs), positions RNA pol I correctly on to the promoter (Moss et al. 2023). TIF-IA, a basal RNA pol I transcription factor, regulated by growth signaling pathways such as mTOR and Mitogen Activated Protein Kinase (MAPK) through phosphorylation activates the transcription machinery in response to the cell's physiological state (Mayer et Grummt 2005) (**Figure 11**).

These factors assemble into a Pre-Initiation Complex (PIC) that recruits RNA pol I to the transcription start site. At this stage, RNA pol I begins synthesizing short RNA products known as abortive transcripts (2-10 nucleotides), reflecting instability of the early transcription complex (T.-M. Zhang et al. 2024).

2.8.2. Elongation

To establish productive elongation, RNA pol I overcomes strong contacts with promoter-bound factor such as the TATA binding protein-Transcription factor complex SL1 (TBP-TAF complex SL1) (Tremblay et al. 2021). After the complex SL1 detachment, RNA pol I undergoes

conformational changes that stabilize RNA-DNA interactions in its catalytic cleft and form a stable elongation complex resistant to premature dissociation (Engel et al. 2017). This process is facilitated by RNA pol I-specific subunits such as Polymerase Associated Factor 53 (PAF53), PAF49, which RNA pol I navigate nucleosomal barriers (McNamar et al. 2023). Once promoter escape has occurred, RNA pol I becomes highly processive, synthesizing the complete 45S pre-rRNA.

TFIIF has been discovered contributing directly to RNA pol I transcription elongation (Hoogstraten et al. 2002).

The complex is detected at rDNA promoters and across the gene body, colocalizing with actively transcribing RNA pol I. Unlike for RNA pol II, TFIIF is not required for initiation in RNA pol I (Iben et al. 2002). The complex has been describe promoting efficient elongation likely through the helicase XPB and XPD (Assfalg et al. 2012). Evidence of their participation lies in the consequences in RNA pol I transcription when XPB and XPD are mutated. Indeed, studies revealed, when these subunits are impaired the level of pre-rRNA synthesis decreases contributing to ribosomal stress observed in a specific pathology called Cockayne syndrome. This manuscript will describe more in details this pathology on the third section.

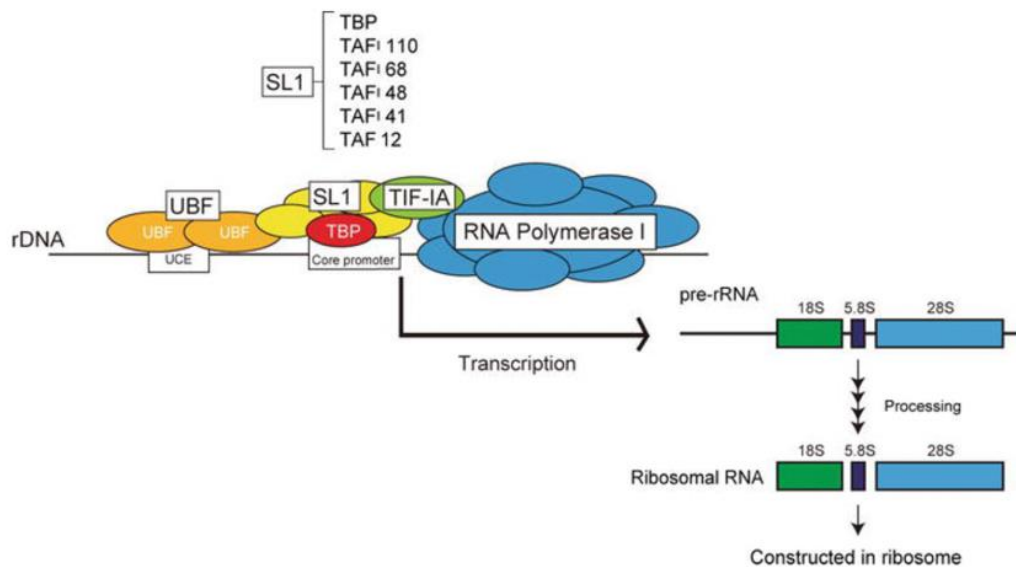


Figure 11: rDNA transcription by RNA polymerase I

Transcription factors UBF, SL1 and TIF-IA recruit RNA polymerase I to the promoter, enabling synthesis of pre-rRNA (45S). This full precursor is then processed into 18S, 5.8S and 28S rRNAs, essential components to the ribosome.

2.8.3. Termination and processing of 45S pre-rRNA

Termination is mediated by Transcription Termination Factor I (TTF-I), which recognizes specific sequences downstream of the rDNA transcription unit and halts RNA pol I activity (Boutin et al. 2019). The released 45S pre-rRNA undergoes stepwise cleavage producing 18S, 5.8S and 28S rRNAs. These rRNAs are subsequently assembled with ribosomal proteins to form the small and large ribosomal subunits of eukaryotic ribosomes.

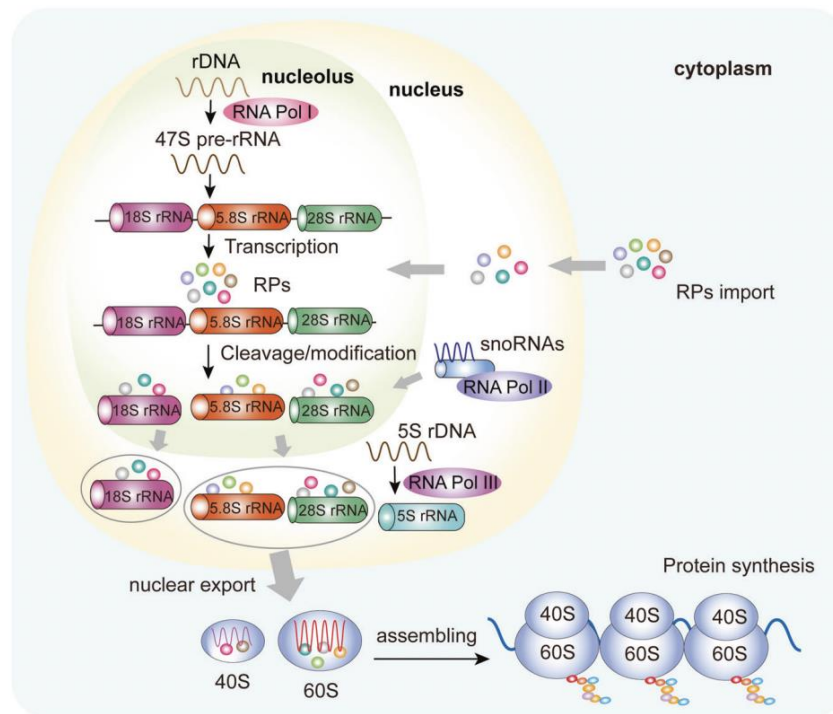


Figure 12: Representation of ribosome genesis.

RNA polymerase I transcribes rDNA into a precursor 45S pre-rRNA containing 18S, 5.8S and 28S rRNA sequences, which are processed in the nucleolus. RNA polymerase III separately transcribes the 5S rRNA, while RNA polymerase II produces mRNAs encoding ribosomal proteins. Mature rRNAs and ribosomal proteins assemble into the 40S and 60S ribosomal subunits, which are then exported to the cytoplasm and combined to form the functional ribosome (Jiao et al. 2023).

3. Nucléotide excision repair

In all cells, DNA is the carrier of genetic information from generation to generation; thus, its integrity must be guaranteed and maintained to ensure the survival of the cell and more largely the entire organism. Nevertheless, DNA throughout our life is constantly jeopardized by exogenous and endogenous factors that can cause damages to its structure. These damages can induce DNA

deformations that must be repaired to prevent the apparition of mutations causing the disruption of cellular physiological processes. Several DNA repair mechanisms exist and are each assigned to specific DNA lesions. This manuscript will focus on the Nucleotide Excision Repair mechanism (NER).

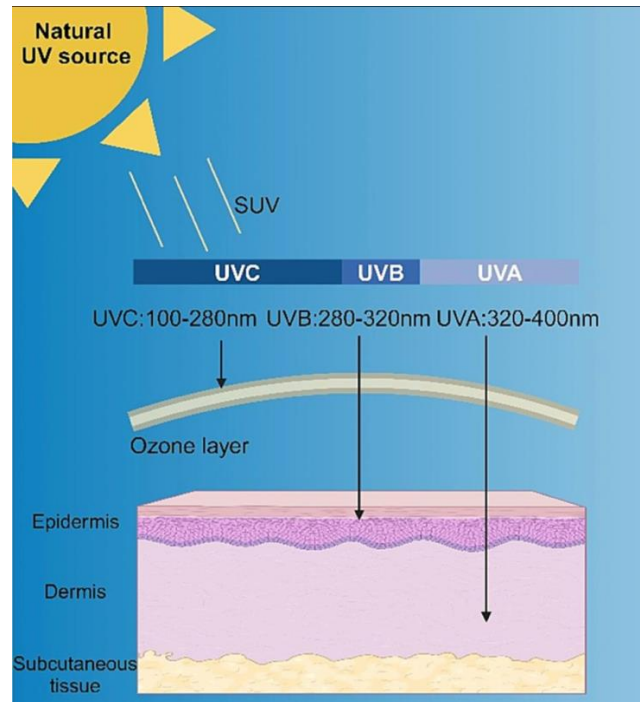


Figure 13: Categories of UV rays and their absorption through the human skin.

The sun's UV rays are divided into three categories: UVA (320-400nm) which can pass through the epidermis to reach the dermis; Most of the UVB (280-320) is absorbed by the ozone layer, though the remaining portion reaches the epidermis. All of the UVC (100-200nm) is absorbed by the ozone layer. (Tang et al. 2024).

3.1.DNA Damage

3.1.1. Cyclobutane pyrimidine dimer and 6-4 Pyrimidine Primidone

A large variety of damages are removed by the NER mechanism: The clinical most relevant NER subtract are *cis-syn*-cyclobutane pyrimidine dimers (CPDs) and the 6-4 pyrimidine primidone photoproducts (6-4PPs) (**Figure 12 A and B**) (Lima-Bessa et al. 2008). There are both formed between adjacent pyrimidines (cytosine or thymine) and are induces by UV lights. The covalent linkage prevents proper hydrogen bonding between the dimerized bases and their complementary bases. The distortion formed, prevent the correct reading and accessibility of the DNA. 6-4PPs inducing more helix distortion (44°) are recognized and therefore repair quicker than the CPDs (30°) (Park et al. 2002; Rastogi et al. 2010).

3.1.2. Bulky DNA adducts

Bulky DNA adducts are also removed by NER (Geacintov et Broyde 2017; J. Kim et al. 2023). These damages are caused by pollutants, benzopyrene adducts contained in cigarette smoke and alkylating agents like cis-diamminedichloroplatinum (II). These chemicals compound bound to DNA blocking normal base pairing (Rechko et al. 2017). Indeed, benzopyrene adducts bind to guanine preventing cytosine from pairing with it. The modified base may be paired incorrectly (guanine mispaired with thymine). If not repaired, after DNA replication, this could lead to a so called transversion ($G \rightarrow T$). Concerning cis-platin, these agents create covalent bonds between complementary bases, preventing the two DNA anti-parallel strands from separating (Dasari et Tchounwou 2014; Yimit et al. 2019). The strands cannot unwind stopping the replication fork to progress. The DNA polymerase would not be able to insert new bases leading to fork collapse (Basu et Krishnamurthy 2010).

3.1.3. 8 oxo guanine

Reactive oxygen species (ROS), caused by oxidative stress, induce the apparition of 8-oxo-guanine (8-oxoG). 8oxoG are an oxidized form of guanine that can pair incorrectly (**Figure 12 C**). The oxidation can mislead the DNA polymerase pairing by mistake the guanine with an adenine instead of a cytosine. This can lead, if not repaired, to a transversion $G \rightarrow T$ (Bruskov 2002).

8oxoG are damages mostly repaired by the Base Excision Repair mechanism (BER) (Rosa et al. 2023). After recognition of the lesion by the 8 Oxo Guanine DNA Glycosylase 1 (OGG1), the enzyme cleaves the N-glycosidic bond, removing the damage base and creating an Apurinic site (AP site) (You et al. 2024). The AP endonuclease 1 (APE1) will be recruited and cleave at the 5' side of the damage, creating a single-strand break with a 3' hydroxyl (OH) group and 5' desoxyribose phosphate group (dRP) (Malfatti et al. 2021). The DNA polymerase β will then remove the dRP group and add the correct nucleotide based on the matrix brand. Finally DNA ligase III connects the newly added base to the sequence (Demin et al. 2021). Recent studies have revealed that NER proteins were involved in the recognition of the damage (Shafirovich et Geacintov 2021). Indeed, the Damage-Specific DNA binding protein 2 (DDB2), implicated in the recognition of the lesion in NER, binds to 8oxoG and recruits OGG1 allowing the activation of the BER mechanism (Kumar et al. 2022).

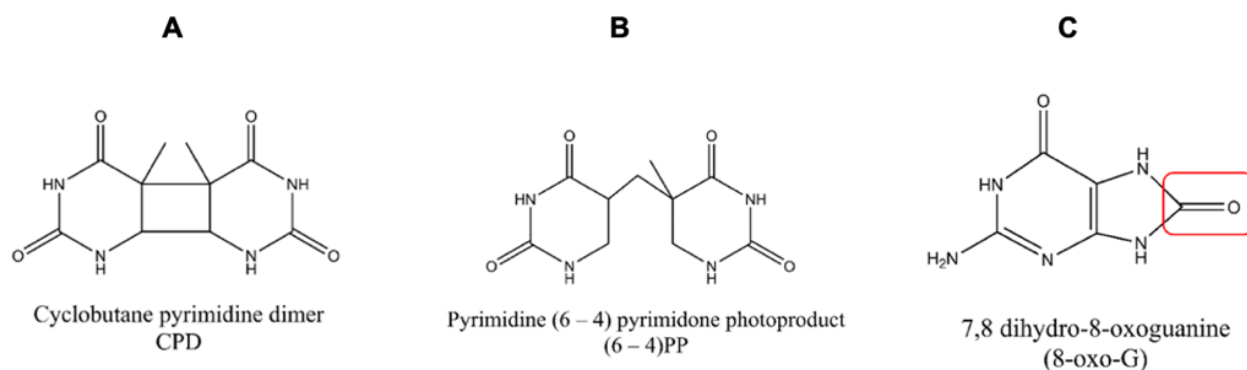


Figure 14 : DNA damages removed by NER.

A.Representation of Cyclo-butane Pyrimidine Dimer (CPD). **B.** Representation of a 6-4 pyrimidine primidone photoproduct (6-4PP). Here we see the C4 of one thymine base liked to the C6 of another thymine base. **C.** Representation of the 7,8 dihydro-8-oxoguanine (8-oxo-G)

3.2. NER mechanism

In eukaryotes, NER is a complex process involving more than 20 proteins. There are two types of NER, i.e., The Global Genome NER (GG-NER) and the Transcription Coupled NER (TC-NER) which differ at the recognition stage (**Figure 7**). GG-NER scans the whole genome for DNA distortions, while TC-NR is tasked for rapid DNA repair on the transcribed strand.

3.2.1. Damage recognition

- GG-NER

In the case of the mammalian GG-NER, lesions are recognized by Xeroderma Pigmentosum factor C (XPC) complexed to RAD23B and Centrin 2 (CETN2) (Kusakabe et al. 2019).

XPC scan the genome for DNA distortion such as UV-induced dimers or bulky chemicals adducts (Cheon et al. 2019). After recognition, XPC binds to the undamaged strand causing the helix to locally separate. Although XPC has a high affinity for 6-4PP inducing a larger DNA deformation the protein shows a lower affinity for CPDs. CPDs are the most abundant photolesions and cause a minimal distortion in DNA compared to 6-4PP. The incurvation of 33° is first detected by UV Damage DNA Binding protein (UV DDB), a heteromeric protein composed by DDB1 and DDB2 complexed with Xeroderma Pigmentosum E (XPE). DDB2 will enhance the distortion, helping the recognition of the lesion by XPC and inducing the activation of NER (Kusakabe et al. 2019).

Moreover, the DDB1 is a connector protein for ubiquitin ligase (Meng et al. 2022). The ubiquitin ligase is activated upon DDB2 binding and ubiquitinates DDB2 and XPC. The ubiquitination of DDB2 promotes its degradation by the proteasome after extraction from NER complexes. In parallel, the ubiquitination of XPC, increases its binding with the DNA damage. XPC taking over the damage promotes the recruitment of TFIIH, participating to DDB2 dissociation (Ribeiro-Silva et al. 2020).

- **TC-NER**

The complex XPC-CENT2-RAD23 is not required in TC-NER. In this sub-pathway, the stalling of RNA pol II during elongation at DNA lesion acts as a primary sensor for DNA damage (Nieto Moreno et al. 2023). When RNA pol II encounters a DNA lesion in the template strand, it can stall instead of proceeding with transcription (Kokic et al. 2024). This stalling is often described as RNA pol II "backtracking" where it retreats from the original transcriptional position on the DNA. One of the key factors that facilitate the resolution of RNA pol II backtracking is the Transcription elongation Factor IIS (TFIIS) (Gregersen et Svejstrup 2018). TFIIS aids in the cleavage of the backtracked RNA, allowing RNA pol II to resume transcriptional elongation. By inducing RNA cleavage, TFIIS acts as an anti-backtracking factor that helps reactivate transcription following such stall.

The arrested RNA pol II recruits the Cockayne Syndrome complementation group B (CSB) at the damages region (Llerena Schiffmacher et al. 2023). CSB is an ATP-dependent chromatin remodeler that belong to the SWItch/Sucrose Non-Fermentable (SWI/SNF) family strongly binds the upstream stalled RNA pol II to push it past the obstacles. After recognizing the lesion, CSB induce the recruitment of Cockayne Syndrome A (CSA) (Llerena Schiffmacher et al. 2024). CSA interacts with Cullin-4, (CUL4), RING-Box protein 1(RBX1), DDB1 and the E3 ubiquitin ligase forming the CRL4^{CSA} Complex. This interaction enhance the recruitment of UV-Stimulated Scaffolding protein A (UVSSA) and the Elongation Factor 1 (ELOF1) (Van Sluis et al. 2024; Van Der Weegen et al. 2021). CSA complex and CSB collaborate to facilitate the ubiquitination of the lysine 1268 of the RNA pol II to promote its eviction or degradation (Nakazawa et al. 2020). TFIIH can then be recruited at the damaged lesion. The recruitment of TFIIH is promoted by the Serine/Threonine Kinase 19 (STK19) which is recruited on stalled RNA pol II by CSA and enhances the ubiquitination of UVSSA (J. Li et al. 2024).

3.2.2. DNA opening and XPD role in NER

TFIIH recruitment coordinates with the removing of DDB2 and is subsequent to the recruitment of Xeroderma Pigmentosum A (XPA) (Ribeiro-Silva et al. 2020). The interaction of subunits p62 and XPB with XPC facilitates the recruitment of the complex to the damage (Barnett et al. 2020, 44). Interestingly, cryo-EM data conducted in yeast recently revealed that coordination between XPB and XPC is essential for initiating DNA unwinding (Van Eeuwen et al. 2021). XPB helps to generate torsional stress and preunwinds the DNA, while XPC acts as an anchor to position the DNA appropriately for repair, ensuring that the unwinding process is both effective and efficient. Moreover, the removal of the CAK from TFIIH promoted by the arrival of XPA activates the helicase functions of its core, facilitating the unwinding of DNA around the lesion (Coin et al. 2008; Peissert et al. 2020).

One of the most critical events during NER, is the DNA opening. Following XPB initiation, the proper DNA unwinding at the lesion is ensured by the 5' to 3' ATP dependent helicase XPD creating a 25 to 30 nt bubble around the damage region allowing the proper access to the damage for the repair proteins (Kuper, Hove, Maidl, Neitz, et al. 2024). The p44 subunit of TFIIH interacts with XPD and by doing so enhances its ATPase activity, which is crucial for DNA unwinding (Coin et al. 2007; Mao et Mills 2024). Moreover, recent studies have revealed that adding to the helicase activity of XPD, the XPD-p44 heterodimer verify the presence of NER damages (Fu et al. 2022). This damage verification function is performed by sliding a single-stranded DNA (ssDNA) through the central tunnel of the XPD protein, which is formed by an iron-sulfur cluster and an arch domain. Once, they recognize a damage, both proteins form a covalent adducts with the DNA damage, suggesting that p44 may additionally facilitate the verification process by actively interacting with the damaged substrates (Petruseva et al. 2021).

Following, XPA binds to the 5' end of the damaged strand and plays a crucial role in bridging the formation of a pre-incision complex. The Replication protein A (RPA), a single-stranded DNA-binding protein, stabilizes the unwound DNA and coats the undamaged strand to protect and prevent reannealing or unwanted modifications (Topolska-Woś et al. 2020). If the damage is verified, TFIIH facilitates the recruitment of the downstream nucleases XPG and XPF-ERCC1, which create strand incisions flanking the lesion.

3.2.3. Damage excision and DNA resynthesis

The protein XPA, plays a crucial role in guiding the exonucleases XPF-ERCC1 and XPG onto their respective cleavage sites. XPF-ERCC1 and XPG make incisions at the 5' and 3' sides of the lesion, respectively. A comprehensive genome-wide analysis of human GG-NER and TC-NER demonstrated that ERCC1-XPF incises the DNA approximately 20 ± 5 nucleotides upstream of the lesion, while XPG cleaves 6 ± 3 nucleotides downstream (Faridounnia et al. 2018). This coordinated enzymatic activity results in the excision of a single-stranded DNA fragment degraded by 3'5' exonuclease Three prime Repair Exonuclease 1 (TREX1) (S. H. Kim et al. 2022). Recent studies discovered the involvement of Helicase-Like-Transcription Factor (HLTF) in the eviction of the DNA damage (Van Toorn et al. 2022). Once recruited, HLTF uses its ATP-dependent translocase motor to promote the dissociation of the incision complex, which contains repair factors like TFIIH, XPG, and ERCC1-XPF, as well as the incised oligonucleotide. This active eviction process is essential for transitioning from the incision step to repair synthesis, allowing for the efficient loading of downstream factors such as the DNA polymerase. Following the eviction of the damaged fragment, DNA polymerases are recruited (Lehmann 2011; Van Der Weegen et al. 2021).

There are three DNA polymerases involved in the resynthesis of the damaged strand: δ , ϵ , κ (Ashton et al. 2023). The processivity factor Proliferating Cell Nuclear Antigen (PCNA) allows the DNA polymerase to bind the lagging strand together with Replication factor Complex (RFC1 - RFC) (Schrecker et al. 2022). On the other hand, an ubiquitinated PCNA and X-ray repair cross complementing 1(XRCC1) recruits the DNA polymerase κ (Ogi et al. 2010). The advanced strand is repair by DNA polymerase ϵ paired with the alternative clamp loader Chromosome Transmission Fidelity factor 18 (CTF18) and RFC (Stokes et al. 2020). DNA synthesis and ligation is then needed to connect the new fragment with the genomic DNA. Ligases and DNA polymerases are selected regarding the cell cycle stage. The couple, Pol δ and ligase III α oversees the synthesis and the ligation during the interphase of the cell cycle (Hamdan et De Biasio 2023). On the other hand, Pol ϵ collaborated with ligase I during the DNA synthesis phase (S) preparing the entrance in mitosis (Bhandari et al. 2023).

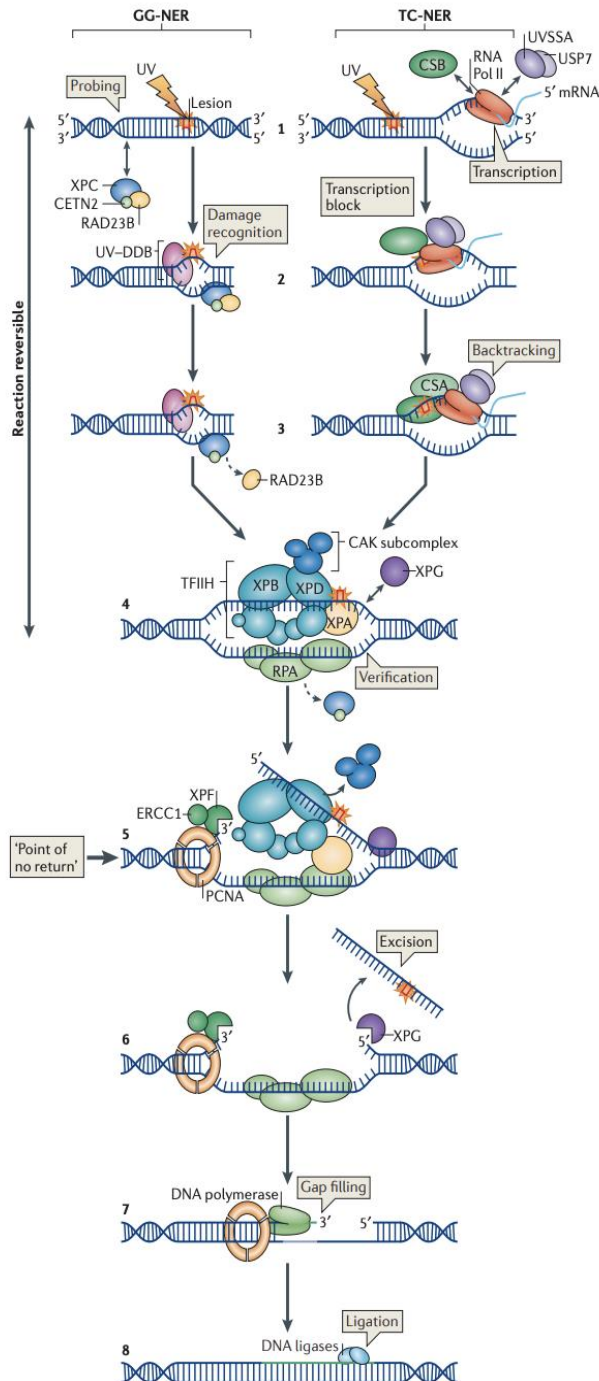


Figure 15: Nucleotide excision repair mechanism (NER).

UV induce DNA damages such as 6-4PP and CPD. During GG NER (left), the complex XPC-CEN2-HR23B (GG-NER), helped by the complex UV-DDB detects the damage. During the TC-NER (right) RNA pol II acts as a primary sensor and recognize de lesion while in elongation of the lesion. CSB, SSA and USP7 interacts with RNA pol II. CSB recruits CSA at the damaged region. Following the RNA pol II backtracks leaving the lesion open for NER factors. After recognition, TFIIF is recruited in both GG-NER and TC-NER. The CAK dissociated from the core of TFIIF allowing the helicase XPD to open the DNA a 25 to 30nt bubble around the lesion forming. Upon the DNA opening, XPD, XPB and XPA verifies the existence of lesions. RPA is recruited and coat the undamaged strand preventing the helix from reannealing. XPA recruits endonucleases XPF/ERCC1 and XPG which cleave respectively at 5' and 3' surrounding the lesion removing a 22-30nucleotide long strand. PCNA, which is rapidly positioned after the 5' incision by XPF-ERCC1, recruits DNA Pol δ, DNA Pol κ or DNA Pol ε for gap-filling. Gap filling starts right after the 5' incision is made. The NER reaction is completed through sealing the newly synthesis strand to the genome by DNA ligase 1 or DNA ligase 3 (Marteijn et al. 2014).

4. Cell cycle and Checkpoints

The cell cycle is a fascinating and complex process involving numerous regulatory proteins conducting one mother cell through a sequence of events towards the production of two daughter cells (Russell 1998 ; Maiato 2021). It is divided in two main events: The interphase which consist in three stages: the Gap1 stage (G1), the DNA Synthesis stage (S) and the Gap 2 (G2). The second part is Mitosis (M) during which the cell goes through five different phases: Prophase, Prometaphase, Metaphase, Anaphase and Telophase (Russell 1998). The transition throughout is coordinated by Cyclins and Cyclin-Dependent Kinases (CDKs), whose tight regulation levels ensure a precise and controlled advancement of the all process (Pellarin et al. 2025).

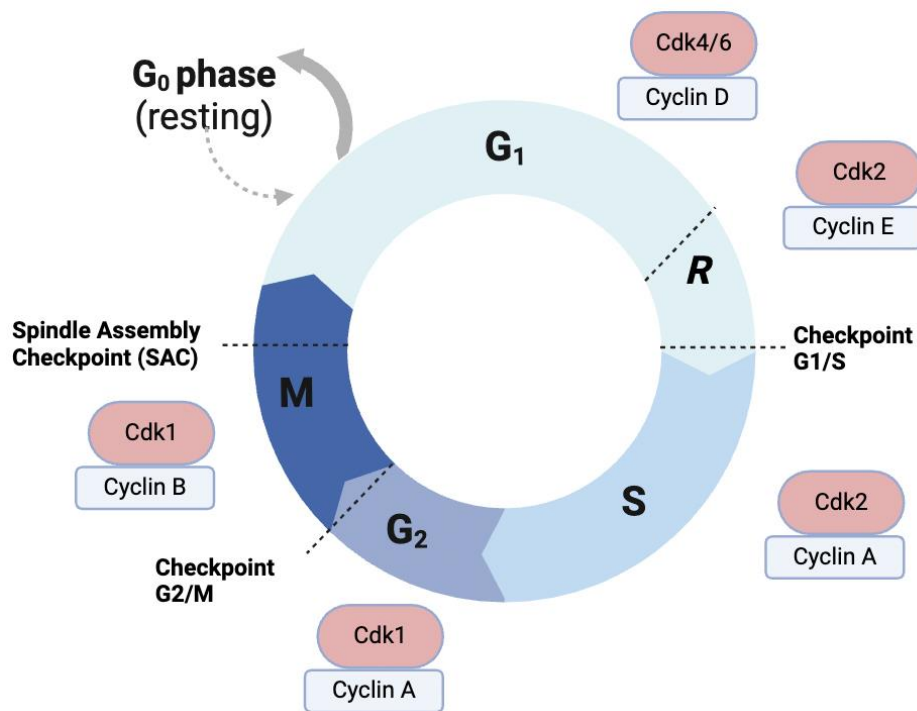


Figure 16 : Cell Cycle regulation by Cyclins and CDKs

The cell cycle is divided in two parts. The first part consist of is the interphase composed by: G₁, S and G₂ stages. The second part is Mitosis (M) where the cell undergoes division. During G₁: the cell grows and prepares for DNA replication. The Cyclin D/CDK4/6 complex begins to phosphorylate several proteins activating DNA replication genes. In late G₁, the cell encounters a Restriction checkpoint (R) determining whether the conditions are optimal to progress towards the S phase. If it's the case the Cyclin E/CDK2 fully phosphorylates Rb, ensuring the transition to S phase, where DNA is replicated. In G₂, the cell continues to grow, scans for DNA lesions that could have happened after replication and prepares for mitosis. The G₂/M checkpoint act as gatekeeper, if the cell cycle halt and repair the lesion. Once is ready, the G₂/M checkpoint is validated. The Cyclin A/CDK1 activates Cdc25, which triggers Cyclin B/CDK1 to initiate Mitosis.

4.1. Interphase

An eukaryotic cell is characterized by the presence of the nucleus containing the compacted genomic DNA enclosed in a plasma membrane (Chadha et al. 2024). The zone between the nucleus and the membrane, is the cytoplasm where organelles are localized. Amongst organelles, can be found: the mitochondria producing the ATP through cellular respiration, the Endoplasmic Reticulum (ER) involved in proteins synthesis and the Golgi Apparatus, implicated in the transport of proteins and lipids (Gomes et Shorter 2019).

Structurally a network of protein filaments forms the cytoskeleton where microtubules, microfilaments and intermediate filaments intertwine providing support and facilitating movement within the cell (Goodson et Jonasson 2018). Another central cellular organelle is the centrosome. Composed of two structures called centrioles it is a microtubule-organizing center where the microtubules meet and reorganize to participate in the cell division (**Figure 15**) (Vasquez-Limeta et Loncarek 2021).

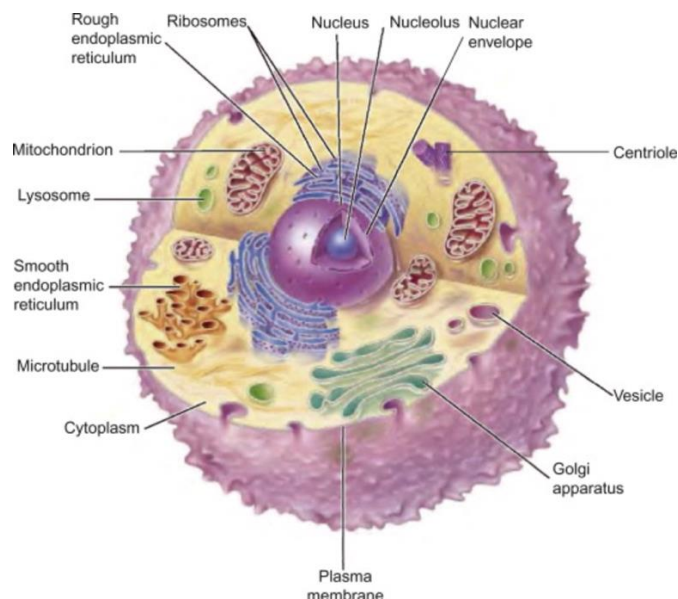


Figure 17 : Eukaryotic Animal Cell.
(J. Wu et al. 2013)

4.1.1. Gap 1 (G1)

The interphase begins with the Gap 1 stage (G1). During this phase, the cell increases in size, synthesizes proteins, and produces organelles needed for DNA replication. Alongside, the

environment is evaluated, checking the amounts of nutrients, growth factors as well as space separating the cells indicating whether the conditions are favorable for division (Z. Wang 2022).

At the late G1 stage, the cell undergoes a Restriction checkpoint (R) or “the point of no return”. It often referred as a “decision” window to determine the pursuit of the cell division leading to the S phase or entering a resting state called G0 (Marescal et Cheeseman 2020; Pennycook et Barr 2020). During this stage, the Cyclin D level rises and the protein binds to CDK4 and CDK6 forming the two major complexes in G1 (Pawlonka et al. 2021). Both complexes induce a partial phosphorylation of the Retinoblastoma protein (Rb) bound to the inactive transcription factor E2 (E2F) (Chung et al. 2019; S. Kim et al. 2022). Once phosphorylated, E2F free activates the transcription of the genes required for DNA synthesis such as POLA1 encoding for DNA polymerase α and PCNA (Pennycook et Barr 2020; Rubin et al. 2020).

The cell also evaluates if the external environment is optimal by checking the presence of growth factors stimulating the cell cycle progression (Z. Wang 2021). The density of cells all around is also considered. Indeed, too many cells nearby could trigger a contact inhibition and halt the cell division (Schnyder et al. 2020). A high level of nutrient such as glucose, oxygen amino acids is required to promote the cell division. (Yanagida et al. 2011). Most importantly, the DNA integrity is verified through the Ataxia Telangiectasia Mutated (ATM) and the ATM and Rad3-related (ATR) pathway before replication. If errors and/or breaks were to be found, the cycle will halt while repairs are carried out (De Marco Zompit et Stucki 2021). Once a cell passes the R checkpoint, it will evolve towards the G1/S checkpoint. Cyclin E/CDK2 complex initiates DNA replication by completing the phosphorylation of the Rb proteins. E2F free activates the genes required for initiating the DNA synthesis preparing to the cell to enter into the S phase (Fagundes et Teixeira 2021).

4.1.2. DNA synthesis (S)

Once the R checkpoint and the G1/S checkpoints are through, the cell enters in the Synthesis phase (S). The primary event of the S phase is the complete replication of the cell's DNA. Each chromosome is duplicated to produce two sister chromatids, ensuring an evenly split set of chromosome repartition between the two daughter cells (Limas et Cook 2019).

The level of the Cyclin A rises and the Cyclin A/cdk2 complex drives the early S phase (Mailand et Diffley 2005). This complex phosphorylates specific proteins such as the DNA

polymerase α , δ , the PCNA and the Cell Division Control Protein 6 (Cdc6) promoting DNA synthesis. This last protein is a key component of the pre-replication complex (pre-RC) (House et al. 2025). Cdc6 helps to recruit the Minichromosome maintenance helicase (MCM helicase) on the DNA which is essential for unwinding the double helix (Wei et Zhao 2016). Once the replication is completed, the cell enters in G2 phase (Eykelboom et al. 2013).

4.1.3. Gap 2 (G2)

Once the cell has finished replicating its DNA, it enters G2. The goal of this phase is to check for any DNA damage that may have occurred during replication and to prepare the cell for the G2/M checkpoint, which allows the cell to enter mitosis (M) (Yam et al. 2022).

During early G2, the Cyclin A/cdk1 complex is dominant (Ng et al. 2023). When the cell has completed its DNA replication, this complex phosphorylates the MCM helicase and Cdc6, inhibiting their activities and preventing replication from repeating (Amasino et al. 2023). Meanwhile, the ATR/ATM pathway is activated to check for DNA damage (Blackford et Jackson 2017). During late G2, Cyclin B levels gradually increase and bind to cdk1, forming Cyclin/cdk1, also called Maturation Promoting Factor (MPF) (Gavet et Pines 2010). This inhibition is removed by the phosphatase Cell division cycle 25 (Cdc25) allowing the cell to enter Mitosis (Crncec et Hochegger 2019).

4.2. Mitosis

4.2.1. Prophase

Prophase is the first stage of mitosis, during this phase, the chromatin fibers condense into visible chromosomes, each consisting of two sister chromatids joined at a central point called the centromere (Gibcus et al. 2018). During prophase, Condensin I and Cohesion coil the chromatin fibers more tightly, compacting the DNA (**Figure 16 A and Figure 18**) (Wood, Severson, et Meyer 2010; John K. Eykelboom et al. 2024). As the chromosomes condense, the Nuclear Envelope begins to Breakdown (NEB) (Hashimoto et Tanaka 2021). Meanwhile, the mitotic spindle, composed of microtubules, starts to polymerase from the duplicated centrosomes that have migrated, under the action of a crucial the kinesin Eg5, to the opposite poles of the cell (Diaz et al. 2019).

4.2.2. Prometaphase

In prometaphase, the nuclear envelope collapses, allowing microtubules to bind to the duplicated chromosomes (Ferreira et Maiato 2021). Kinetochores, composed of the Ndc80 complex and CENP-A/CENP-C, are localized at the centromere and anchor chromosomes to the mitotic spindle, forming a stable interface (**Figure 16 B and C**). Two other types of microtubules exist to form the mitotic spindle positioning the chromosomes: Interpolar microtubules, originating from opposite centrosomes, overlap in the center of the cell, thus contributing to the separation of chromosomes and maintaining the stability of the mitotic spindle. Astral microtubules anchor the spindle poles to the cell membrane (A. F. Long et al. 2019).

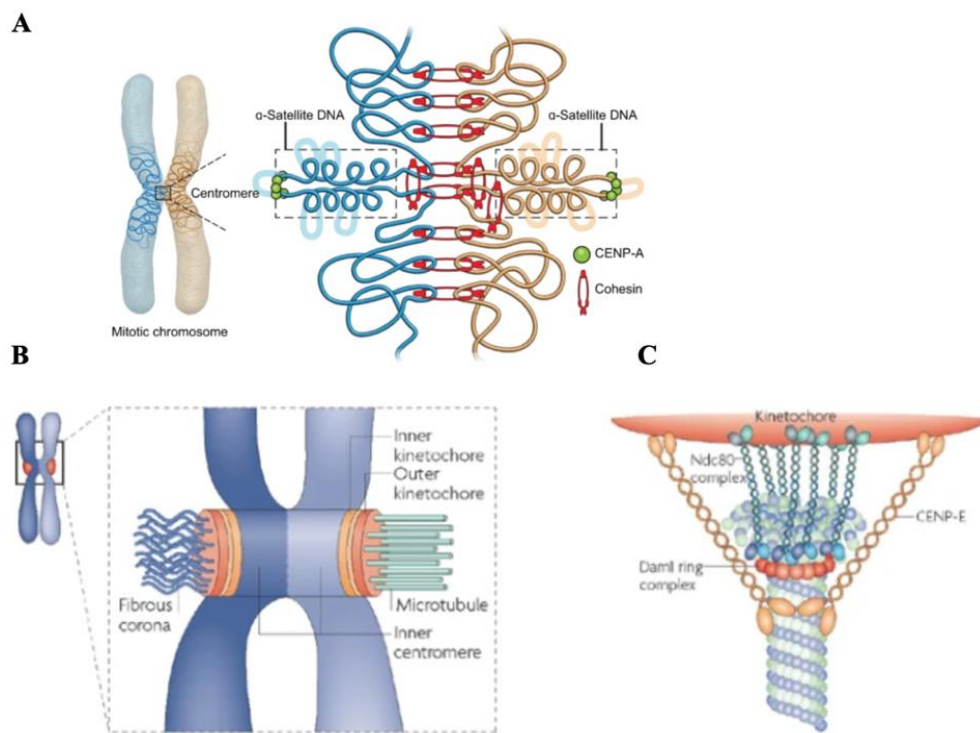


Figure 18 : Chromosomes centromere and kinetochores composition

A.Chromosome centromeres. Cohesin promotes DNA coil to compact the genome. The CENP-A interaction directly with the chromatid and participate in the forming the binding to the microtubules. **B.**The left chromatid is unattached and at the right chromatid can be found the inner and outer kinetochores connecting the chromatid to the microtubules. **C.** Amongst proteins binding the chromatid to the microtubule can be found the Ndc80 complex, CENP-E. Adapted from Cheeseman and Desai 2008

Astonishingly in drosophila, it has been shown that XPD plays a critical role during prometaphase in addition to its known function in DNA repair (E. Yeom et al. 2015). Indeed, it has been found that XPD, through its interaction with the protein Galla-1 and Crumb (Crb), forming

together, the Crb-Galla-XPB (CGX) complex, is essential for proper spindle assembly and chromosome behavior during this critical mitotic stage. Moreover, studies conducted in 2020 have revealed that, surprisingly XPB interacts with Klp61F, an Eg5 homologue motor protein, to regulate spindle dynamics (Hwang et al. 2020).

In human cells, during prometaphase XPB has been identified complexed with the protein MMS19 and the Galla-1, MSS19-Interacting Protein of 18 kDa (MIP18) (also known as FAM96B), ADP/ATP translocase 2 (ANT2) and the Cytosolic Iron-Sulfur Assembly Component 1(CIAO1) forming altogether the MMXD complex (Ito et al. 2010).

Recent studies conducted in the team have revealed that XPB interacts with the kinesin Eg5 which is involved in spindle formation and chromosomes segregation (Compe et al. 2022). The beginning of this critical partnership begins during the prometaphase and is observed throughout the final mitotic phase. Overall, these XPB complexes participate to mitotic spindle assembly. Mutations and/or lack of members of these complexes induce mitotic defect.

4.2.3. Metaphase

Metaphase is a critical stage of mitosis, marked by the precise alignment of chromosomes along the metaphase plate, a plane equidistant between the cell's two poles. This alignment ensures that each daughter cell will receive an identical set of chromosomes during cell division (**Figure 18**) (Oriola et al. 2018). During metaphase, several key proteins work together to ensure that chromosomes are properly aligned and attached to the mitotic spindle before separation.

During metaphase, several motor and structural proteins work together to organize and stabilize the mitotic spindle. The kinesin Eg5 pushes the spindle poles apart by generating sliding forces between antiparallel microtubules to promote spindle bipolarity (Mann et Wadsworth 2019; She et al. 2020). In contrast, HSET (kinesin-14) generates inward pulling forces to maintain pole cohesion and balance Eg5's activity (X. Liu et al. 2024). Cytoplasmic dynein which is anchored at the cell cortex, pull the spindle poles towards the cell's periphery to ensure that the spindle is positioned correctly within the cell (Raaijmakers et Medema 2014). At the chromosome level, CENP-E and the Ndc80 complex help to align chromosomes at the metaphase plate and maintain tension at the kinetochores (Ustinov et al. 2020).

4.2.4. Anaphase

From metaphase to anaphase, the cell must go through the Spindle Assembly Checkpoint (SAC) that ensure the proper attachment of chromosome to the microtubules guarantying a good segregation and distribution of genetic material (M. Wang et al. 2024). the SAC monitors attachment and tension through proteins like mitotic spindle Assembly checkpoint protein (Mad1-2), BUB1 Mitotic Checkpoint Serine/Threonine Kinase (Bub1), Bub3, BubR1, and Monopolar spindle1 (Mps1), delaying progression if errors are detected (Pachis et Kops 2018; T. Kim et Gartner 2021; Silva et Bousbaa 2022; Elowe et Bolanos-Garcia 2022; Ju et al. 2021). If any kinetochore is unattached, the Checkpoint is activated, recruiting a Mitotic Checkpoint Complex (MCC) to the kinetochores (Villarroya-Beltri et Malumbres 2022). The MCC inhibits the Anaphase-Promoting Complex/Cyclosome (APC/C), preventing the transition from metaphase to anaphase (Hu et al. 2022). Moreover, Aurora B kinase, corrects faulty attachments by sensing tension at kinetochores (Titova et al. 2023). Together, these proteins coordinate a highly regulated process that ensures accurate chromosome segregation and prevents genomic instability. The SAC delays mitosis until all kinetochores are attached, ensuring correct chromosome alignment (Sinha et al. 2019). If unattached kinetochores persist, the cell may either undergo apoptosis or experience 'slippage', exiting mitosis with unresolved chromosome segregation.

Anaphase is a critical stage in cell division characterized by the coordinated separation of sister chromatids (**Figure 18**) (Vukušić et Tolić 2021). Central to this process are cohesins, which initially hold sister chromatids together at their centromeres. During anaphase, these cohesins are cleaved by Separase, enabling the chromatids to separate (Brooker et Berkowitz 2014; Garcia-Luis et al. 2022). The Anaphase-Promoting Complex/Cyclosome (APC/C), specifically its activator the Cell Division Cycle protein 20 (CDC20), plays a crucial role by promoting the degradation of Cyclins, which ultimately triggers the transition from metaphase to anaphase (Kapanidou et al. 2017; Tsang et Cheeseman 2023). Eg5 and dynein participate in the chromatid separation. Once the chromatids are freed, dynein and kinesin, track them along the spindle microtubules toward opposite poles of the cell.

4.2.5. Telophase and cytokinesis

Telophase is the final stage of mitosis, marking the conclusion of nuclear division and the restoration of the interphase state within the daughter cells (Summers 2020; Z. Wang 2022). During telophase, the separated sister chromatids, now individual chromosomes, begin to de-condense back into their more relaxed chromatin form as the nuclear envelope reassembles around each set of chromosomes, creating two distinct nuclei within the cell (Antonin et Neumann 2016). The Cdk1 activity decreases triggering the de-condensation (Jones et al. 2018). The reformation of the nuclear envelope is facilitated by the recruitment of nuclear laminin filaments that organize and encapsulate the genetic material (Sapra et al. 2020). Laminin filaments, play a crucial role in supporting the reassembly of the nuclear envelope. They undergo phosphorylation entering into mitosis by Cdk1, and during telophase for nucleus reformation, they are dephosphorylated, by Protein Phosphatase 1 (PP1) and Protein Phosphatase 2 (PP2), allowing them to reassemble into a network that supports the nuclear envelope (Mehta et al. 2022). Concurrently, the contractile ring composed of actin filaments, myosin II, formin and Anillin (ANLN), begins to form at the cell's equatorial plane in preparation for cytokinesis representing the final separation of the cytoplasmic contents into two daughter cells (Schwayer et al. 2016). The completion of telophase signals the end of mitosis, as the cell cycle heads towards cytokinesis and the eventual return to interphase, setting the stage for cell growth and preparation for the next round of division. The final stage which is responsible for physically dividing the cell is called cytokinesis. As the furrow deepens, the cytoplasm is pinched into a narrow bridge, within which a dense structure called the midbody forms. The midbody serves as a signaling and structural hub, recruiting key proteins like Aurora B kinase, Centrosomal protein 55 (CEP55), and Endosomal Sorting Complex Required for Transport-III protein (ESCRT-III) components to coordinate the final separation (Ota et al. 2023; Tandon et Banerjee 2020; Richard et al. 2024). The last step, known as abscission, is carried out by the ESCRT machinery, which cuts the membrane at the midbody, fully dividing the two cells. Throughout the mitotic phases, XPD progresses along the mitotic spindle. The team studies revealed that during the cytokinesis, XPD is localized at the midbodies. Interestingly, it is not the only NER protein located in the midbodies. Indeed, recent analysis enlightened that Cockayne Syndrom A (CSA) and Cockayne Syndrom B (CSB) facilitate ubiquitin-dependent degradation, triggering abscission (Paccosi et al. 2020).

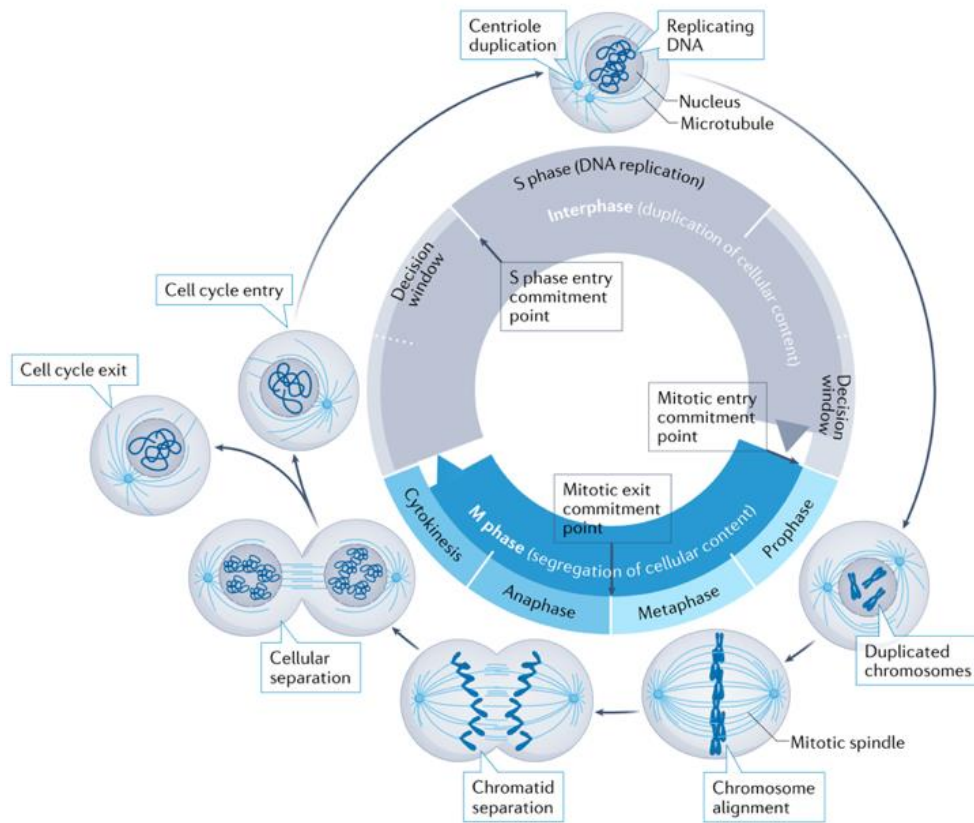


Figure 19: Eukaryotic Cell cycle.

The Mitosis stage happens after the G2/M checkpoint. From there, the cell undergoes different phases: the prophase (Chromosome condensations), the metaphase (Chromosome alignment), the anaphase (the chromosomes segregates) and cytokinesis (the daughter cells newly formed separates). During these phases, there is a crucial checkpoint accruing between the metaphase and the anaphase: the Spindle Assembly Checkpoint (SAC). The SAC is a protein complex verifying the proper positioning and alignment of chromosomes at the spindle and right attachment to the kinetochores. Once the SAC is passed, the cell can continue in anaphase. (Adapted from Matthews, Bertoli and de Bruin, 2022)

Section 3: XPD mutations inducing various pathologies

Mutations found within the gene ERCC2 coding for the protein XPD are responsible for the development of rare autonomic genetic disorders: Xeroderma pigmentosum (XP), Xeroderma Pigmentosum associated to the Cockayne syndrome (XP/CS) and the trichohiodystrophy (TDD). In this part, the manuscript will present the R683W, G47R, G602D and K48R mutations of XPD.

1. XPD mutations

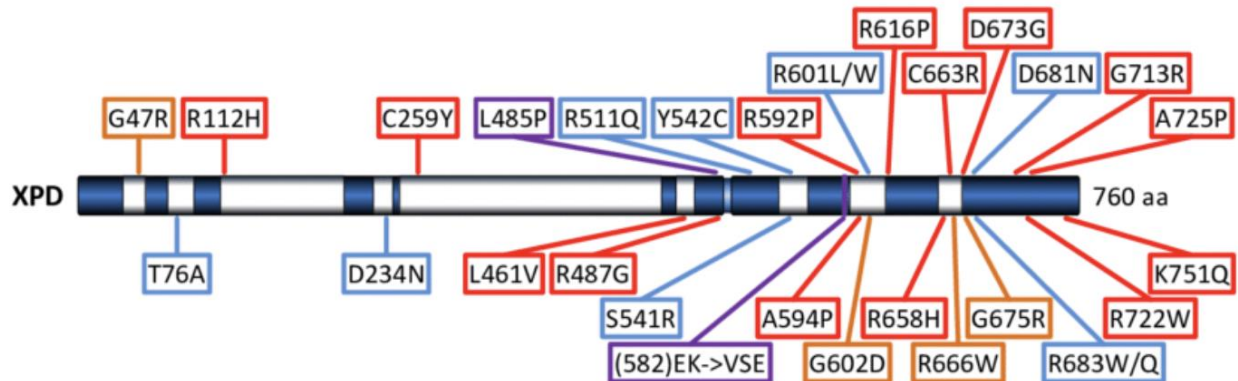


Figure 20 : Disease related mutations of the TFIIH subunits XPD.

The red boxes represent the Xeroderma Pigmentosum (XP) mutations. The blue boxes are for the Trichothiodystrophy (TDD) and the orange boxes represent the Xeroderma Pigmentosum /Cockayne Syndrome mutations XP/CS (Dehm et Tindall 2007).

1.1. XPD/R683W

The XPD R683W mutation is the most frequent mutation identified in patients with Xeroderma Pigmentosum group D (XP-D). It corresponds to a C-to-T substitution at the first base of exon 22 in the *XPD* gene translated into the modification of a conserved arginine (R) residue located near the C-terminal region of the helicase domain in a tryptophane (W) (**Figure 20 and Figure 21**) (Boyle et al. 2008; Emmert et al. 2009; Takaoka et al. 2021). This missense mutation destabilizes the interaction between XPD and other TFIIH subunits, particularly p44, which is essential for helicase activation. Substitution with tryptophan introduces a bulky, hydrophobic side chain that likely disrupts local structural integrity and weakens XPD's association with the TFIIH core (Yan et al. 2019). Functionally, the R683W mutation impairs DNA repair capacity, leading to

hypersensitivity to UV-induced damage. Interestingly, cells carrying this mutation also exhibit defects in chromosome alignment and segregation during mitosis (Compe et al. 2022).

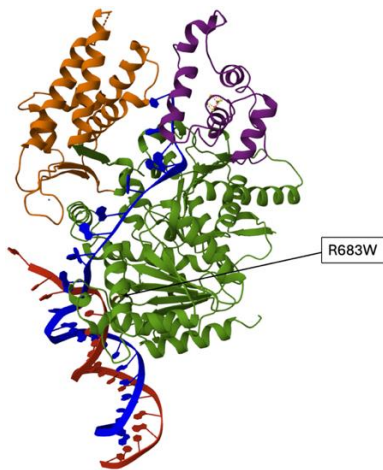


Figure 21 : 3D structure of XPD/R683W

The Arch domain is colored in orange, in purple the Fe-S domain, in green the HD1 and HD2 domains, while the DNA double helix is represented in blue and red. The R683W mutation site is located in the Helicase Domain (HD2). (*PDB: 6RO4*).

1.2. XPD/G47R

The XPD G47R mutation, found in patients with Xeroderma Pigmentosum–Cockayne Syndrome (XP/CS), affects a conserved glycine residue within the ATP-binding pocket of the helicase domain (**Figure 22**) (Fujimoto et al. 2005). Structurally, this substitution introduces a bulky, charged arginine that distorts the local conformation of the ATP-binding site, disrupting XPD's ATPase activity and, consequently, its helicase function (Horibata et al. 2015). This impairs the unwinding of DNA during nucleotide excision repair (NER), reducing the cell's ability to respond to UV-induced DNA damage.

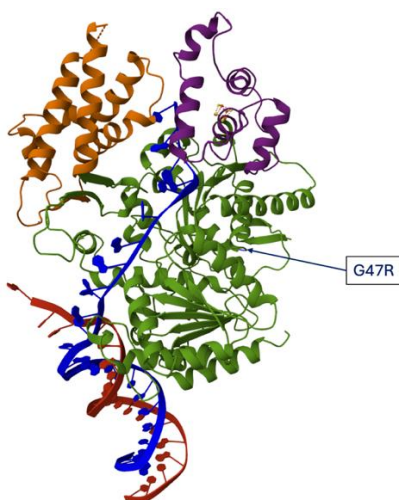


Figure 22: 3D structure of XPD/G47R

The G47R mutation, located is located in the Helicase Domain 1 (HD1) (*PDB: 6RO4*).

1.3. XPD/G602D

The XPD G602D mutation, associated with Xeroderma Pigmentosum–Cockayne Syndrome (XP/CS), affects a conserved glycine within one of the helicase domains critical for DNA unwinding (**Figure 23**) (Dubaele et al. 2003; Godon et al. 2012). Structurally, replacing glycine with aspartic acid introduces a negatively charged residue that disrupts the spatial arrangement of the helicase core, leading to a loss of enzymatic activity (Fan et al. 2008). This mutation abolishes XPD's helicase function, severely impairing nucleotide excision repair (NER) and compromising the cellular response to UV-induced DNA damage (Vélez-Cruz et al. 2013).



Figure 23 : 3D structure of XPD/G602D

The G602D mutation is located in the Helicase Domains (HD2) introducing a negative charge residue leading to the loss of the enzymatic activity (*PDB: 6RO4*).

1.4. XPD/K48R

The Lysine 48 is a conserved residue within the ATP-binding site of the helicase domain, essential for stabilizing ATP during catalysis (Winkler et al. 2000; Lehmann 2001). Substituting the lysine with arginine (**Figure 24**), despite their chemical similarity, disrupts proper ATP coordination, resulting in a loss of ATPase and helicase activity (Panchal et al. 2020). Structurally, the bulk and charge distribution of arginine alters the local conformation of the active site, impairing XPD's ability to unwind DNA.

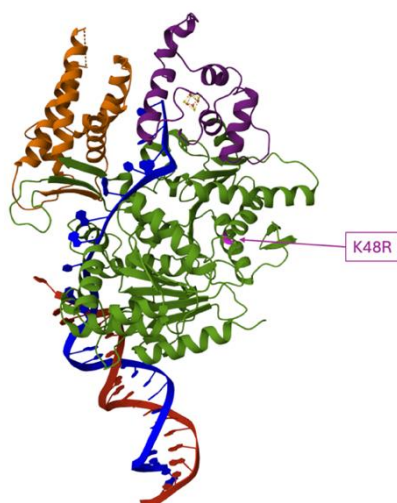


Figure 24 : 3D structure of XPD/K48R

The K48R mutation in XPD is located in the Helicase Domain A (HD1).

2. Pathologies associated with XPD's mutations

2.1. Xeroderma Pigmentosum (XP)

Originally described in 1874 by Dr MORIZ KOHN KAPOSÍ, Xeroderma pigmentosum (XP) is a rare genetic disorder characterized by patients presenting various phenotypes such as an extreme sensitivity to UV rays, premature skin aging, and a significantly heightened risk of developing skin cancer (Leung et al. 2022). One of the most prominent clinical manifestations is marked photosensitivity, in which affected individuals exhibit exaggerated cutaneous responses to minimal UV exposure (Abeti et al. 2019). This results in severe sunburns and erythema after even brief periods outdoors. The photosensitivity stems from a failure to resolve DNA photoproducts, such as Cyclobutane Pyrimidine Dimers (CPDs) and 6-4 photoproducts, due to mutations in key NER genes (Koch et al. 2016). Cutaneous involvement is progressive and severe. Patients commonly develop xerosis, i.e. an extreme dry skin, epidermal atrophy, and lentiginous hyperpigmentation in sun-exposed areas (Brambullo et al. 2022). Notably, there is a significantly increased incidence of Non-Melanoma Skin Cancers (NMSCs), including Basal Cell Carcinoma (BCC) and Squamous Cell Carcinoma (SCC), with onset often occurring in the first decade of life (Zheng et al. 2023). Melanoma may also develop, with a median onset in the second to third decade. These malignancies are attributed to cumulative, unrepaired UV-induced mutations in cutaneous cells. Ocular involvement is also observed in XP patients. Manifestations include photophobia, conjunctival xerosis, all of which result from chronic UV-induced ocular surface damage and oxidative stress (Lim et al. 2017).

2.1.1. Causes

XP is an autosomal recessive pathology caused by mutation found in genes coding for proteins involved in NER mechanisms. There are seven different types of XP: XPA (*XPA*), XPB (*ERCC3*), XPC (*XPC*), XPD (*ERCC2*), XPE (*ERCC4*), XPG (*ERCC5*), XPF (*ERCC4*) (Yurchenko et al. 2023). Mutations affect the proper function or/and structure of the protein impairing the DNA damage repair. Mutations found in the gene coding for Polymerase H (*POL H*) involved in DNA replication has also been described inducing XP-V (Guo et al. 2013).

2.1.2. Epidemiology

XP is estimated at between 1 and 3/1,000,000 births in Europe and the United State of America (Nikolaev et al. 2022). Concerning the prevalence of XP, it varies with the countries. In Japan, the prevalence is significantly higher, with the disease affecting approximately one in 22,000 individuals (Nishigori et al. 2019). It should be noted that almost 1% of the Japanese population carry one of the many pathogenic variants in the XP-A gene, which explains the frequency and founder effect of the disease in this country (Hirai et al. 2006). The worldwide prevalence of the different forms of XP varies according to geographical area. Although XP-C is the most common form worldwide (43%), the prevalent form of XP varies from region to region. In France, XP-C is in the majority, followed by XP-A, XP-D and XP-B (**Table 4**) (HAS 2021).

XP Type	Genes	United States	Japan	Europe
XP-E	<i>DDB2</i>	3%	3%	—
XP-D	<i>ERCC2</i>	28%	5%	16%
XP-B	<i>ERCC3</i>	1%	0%	2%
XP-F	<i>ERCC4</i>	0%	7%	3%
XP-G	<i>ERCC5</i>	3%	1%	9%
XP-V	<i>POLH</i>	7%	25%	13%
XP-A	<i>XPA</i>	9%	55%	20%
XP-C	<i>XPC</i>	43%	3%	31%

Table 4 : Prevalence of XP in USA, Japan and Europe

Adapted from the HAS rapport published in 2021

2.1.3. Treatment

As it is an incurable disease, treatments for XP patients relay on preventive measures such as photoprotection or surgical removal. To prevent cancerous cells to proliferate, different treatments can be used.

The 5-fluorouracil (5-FU) is used primarily for the treatment of early skin lesions and skin cancers (Chen et al. 2018). As a chemotherapeutic agent, 5-FU is effective in targeting and treating cancerous cells and can be administered topically as a cream or lotion for superficial lesions. 5-FU functions as an antimetabolite that disrupts DNA synthesis, thereby inhibiting the growth of rapidly dividing cancerous cells, which is crucial in managing skin cancers in XP patients (Lansiaux 2011; Chon et al. 2017). Its topical application allows for targeted treatment of affected areas, effectively reducing the risk of cancer progression.

The Imiquimod is used to treat superficial skin cancers and precancerous lesions, such as actinic keratosis and superficial basal cell carcinoma (Hossain et al. 2021). The molecule acts as an immune response modifier, stimulating the local immune system to enhance the body's ability to fight off abnormal cells. It is typically applied as a topical cream directly to the affected areas, promoting the destruction of cancerous and precancerous cells while sparing healthy tissue (Yuan et al. 2018).

Interferons alpha are a group of proteins that enhance the immune system's ability to fight infections and tumors (Dirar et al. 2020). They can inhibit the proliferation of cancer cells, promote apoptosis, and enhance the activity of immune cells. In XP patients, interferon therapy can be administered either topically or systemically, depending on the extent and type of lesions being treated.

2.2. Cockayne syndrome (CS) and XP/CS

Describe for the first time in 1936 by the British physician Dr Edward Alfred Cockayne. Cockayne syndrome (CS) is an autosomal recessive rare genetic disorder characterized by growth retardation, neurological disorders, motor impairment and diminution of sight and hearing. Patients faces appear prematurely aged and cachexia (Laugel, s. d.).

There are three types of CS:

- Type I: The “classical form” Starting at one-year old, the patient begins by presenting growth retardation, neurological disorders then a diminution of the sight and hearing (M. A. Nance et Berry 1992).
- Type II: The most severe form of the disease. It manifests at birth with more severe neurological disorders and eyes abnormalities (Natale et Raquer 2017).
- Type III: This type is a milder form (Benkhaira et al. 2021).

CS can be associate with XP (XP/CS) with patients presenting in addition to the previous symptoms a high skin and eye sensibility to UVs predisposition to develop skin cancers.

2.2.1. Causes:

There are two groups of CS corresponding to the two affected proteins CSA encoded by *ERCC8* and CSB encoded by *ERCC6* (Okur et al. 2020). Given their involvement in TC-NER, mutation within CSA and CSB impaired the TC-NER mechanism and the restauration of transcription after UVs exposition.

Associated with XP the gene affected are *ERCC3* coding for XPB (XP-B/CS), *ERCC2* coding for XPD (XP-D/CS) and *ERCC5* coding for XPG 5XP-G/CS).

2.2.2. Epidemiology

Cockayne syndrome is rare disorders with an estimate incidence of 2,7 per 1,000,000 births in West Europe (Pascucci et al. 2018). No racial or sexual predilection has been declared for CS. To date, 30 cases of CS-A and 78 CS-B have been identified.

2.2.3. Treatments

The management and treatment of Cockayne syndrome (CS) focuses on alleviating symptoms and providing supportive care, as there is no cure for the disorder.

Physical therapy is essential for preventing contractures and improving mobility, while occupational therapy helps enhance fine motor skills and daily living activities such as feeding and grooming (Karikkineth et al. 2017). Occasionally, medications can be prescribed to manage

symptoms like tremors and spasticity, ensuring that patients receive the necessary support to function effectively.

2.3. Trichothiodystrophy

Trichothiodystrophy (TTD) is a rare genetic disorder primarily characterized by brittle, fragile hair with low sulfur content (Garon et al. 2023). It may also be associated with developmental delays, dry and scaly skin (ichthyosis), short stature, photosensitivity, and abnormalities in the nails and teeth. Symptoms vary from person to person, and some may have more severe forms of the condition, including frequent infections or signs of premature aging (Stefanini et al. 2010).

2.3.1. Causes

TTD is caused by mutations in proteins involved in DNA repair and gene transcription, particularly XPD (*ERCC2*), XPB (*ERCC3*), p8/TTD-A (*GTF2H5*) (Tavasoli et al. 2025).

2.3.2. Epidemiology

Trichothiodystrophy is extremely rare, with an estimated prevalence of fewer than 1 in 1,000,000 people worldwide (Compe et Egly 2007). Fewer than 100 cases have been reported in medical literature. Due to its varied symptoms and similarities with other conditions, some cases may go undiagnosed or be misdiagnosed.

2.3.3. Treatments

There is currently no cure for TTD. Treatment focuses on managing symptoms and improving quality of life. This may include gentle hair care, moisturizers for dry skin, physical and speech therapy, and educational support for developmental challenges. For those with photosensitivity, strict sun protection is essential (Lambert et al. 2010). A multidisciplinary medical team is often required to provide individualized care based on each patient's needs. Recent studies conducted in patients have revealed the impressive effect of dupilumab on atopic dermatitis in TTD patients (Gruber et al. 2021). In patients with trichothiodystrophy (TTD) who also suffer from atopic dermatitis, dupilumab may be considered as a treatment option to manage inflammatory skin symptoms.

<u>Symptoms/Manifestations</u>	<u>TDD</u>	<u>XP</u>	<u>XP/CS</u>
Skin			
Photosensitivity	yes	yes	yes
Lentiginous pigmentation	no	yes	yes
Predisposition to skin cancer	no	yes	yes
Eyes			
Photophobia	yes	no	yes
Cancer (anterior eye/lids)	yes/no	yes	not reported
Congenital cataract	no	no	no
Pigmentary retinal degeneration	no	no	yes
Somatic			
Short stature	yes	no	yes
Immature sexual development	yes/no	no	yes
Neurological disorders			
Progressive sensorineural deafness	no	no	yes
Developmental delay	yes	no	yes
Progressive neurological degeneration	unreported	no	yes
Primary neuronal degeneration	no	no	no
Dysmyelination of brain	yes	no	yes
Cerebral atrophy	no/yes	no	yes
Cerebellar atrophy	no	no	yes
Calcification (basal ganglia)	no/yes	no	yes
Diseases mechanism			
Molecular defects	XPB, XPD, p8	XPA-XPG XPV	XPB, XPD, XPG

Table 5 : Comparison of features of Xeroderma pigmentosum, Trichothiodystrophy and Cockayne syndrome.

This table provides a comparison of the main clinical features observed in three rare DNA repair disorders: Trichothiodystrophy (TTD), Xeroderma Pigmentosum (XP), and the combined form XP/CS (Xeroderma Pigmentosum / Cockayne Syndrome). Each row of the table highlights a specific symptom or

clinical characteristic, indicating its presence, frequency, or severity across the three conditions. Adapted Kramer & DiGiovanna & Tamura 2024

XPB is a key component of the TFIIH complex, which plays critical roles in nucleotide excision repair, transcription initiation, and cell cycle regulation. Alterations in its function are associated with a spectrum of rare genetic disorders, including xeroderma pigmentosum, trichothiodystrophy, and combined XP/Cockayne syndrome. These syndromes are characterized by varying degrees of photosensitivity, cancer predisposition, developmental delay, and neurodegeneration - reflecting the complexity of the cellular pathways involved.

Understanding how dysfunction of a single protein such as XPB can lead to such diverse clinical outcomes remains a key challenge. This project aimed to elucidate the molecular mechanisms by which XPB contributes to genome maintenance and cell regulation, and how its disruption may drive disease development in XP, TTD and XP/CS.

To address this, the experimental work was structured around two projects. The first explores XPB interaction with the mitotic kinesin Eg5 in fibroblast of XP patients carrying the R683W mutations.

The second study focuses on three XPB variants - G47R, G602D (identified in XP/CS patients) and K48R (an artificial mutation). Using cell-based assays, we evaluated how these variants affect DNA repair efficiency, transcriptional dynamics, and cell cycle progression. The results provide mechanistic insight into how disruptions in XPB function translate into the overlapping but distinct features of these syndromes.

Together, these results provide new perspectives on the cellular consequences of XPB dysfunction and help explain the clinical variability observed in related disorders

Results

Article 1: Phosphorylation of XPD drives its mitotic role independently of its DNA repair and transcription functions – Science Advances

Presentation and personal contributions

Xeroderma pigmentosum group D (XPD) is a protein with 5'-3' ATP-dependent helicase activity. It is a subunit of the general transcription factor TFIIH and plays a role in nucleotide excision repair (NER) by facilitating DNA opening at UV-induced lesions. During transcription, XPD ensures the integrity of TFIIH and anchors the complex near the promoter of protein-coding genes. Mutations in XPD lead to UV hypersensitivity and the development of several pathologies, such as xeroderma pigmentosum (XP), which increases the risk of skin cancer. Independently of TFIIH, XPD can also interact with other factors. Recent studies have shown the presence of XPD in the mitotic process, where it interacts with the kinesin Eg5, a key protein in chromosome segregation during anaphase. However, the role of XPD in mitosis remains poorly defined. A better understanding of the function of XPD and the effects of its various mutations is crucial for deciphering the phenotypic diversity associated with XPD mutations and the mechanisms underlying skin cancer development.

The objective of my first project was to determine the consequences of XPD mutations in the mitotic process and to assess the role of its enzymatic activity in this mechanism.

First, I participated in a project investigating the presence of XPD during mitosis and its interaction with the kinesin Eg5, a motor protein involved in mitotic spindle organization. This work led me to study fibroblasts from XP patients carrying the XPD/R683W mutation, which exhibit defects in chromosome alignment and segregation. When these XPD/R683W cells overexpress a wild-type XPD protein (XPD/WT), these defects are corrected.

We then sought to determine the impact of XPD phosphorylation during mitosis. Cells overexpressing a non-phosphorylatable form of XPD exhibited aberrant chromosome segregation, whereas cells overexpressing a constitutively phosphorylatable form did not. This suggests that phosphorylation of threonine at position 425 is necessary for proper chromosome segregation.

Given the role of XPD in DNA repair and transcription mechanisms, I also investigated the impact of this phosphorylation in these two processes. Using overexpression approaches with phosphorylatable or non-phosphorylatable XPD forms in XPD/R683W-mutated cells, our findings

suggest that the phosphorylation status of XPD does not influence either cell survival after UV irradiation or transcription activation.

This first project allowed me to develop plethora ways to study cell division. Indeed, I learned several methods of cell synchronization using nocodazole, Taxol and thymidine. I sharpened my eye into differentiating a defective mitosis from a normal mitotic phase. Going further, I develop helpful skills in using adapted microscopes (confocal, Zeiss) to better detect the mitotic phases and all around.

MOLECULAR BIOLOGY

Phosphorylation of XPD drives its mitotic role independently of its DNA repair and transcription functions

Emmanuel Compe^{1*}, Evanthia Pangou², Nicolas Le May¹, Clémence Elly¹, Cathy Braun¹, Ji-Hyun Hwang³, Frédéric Coin¹, Izabela Sumara², Kwang-Wook Choi³, Jean-Marc Egly^{1,4}

The helicase XPD is known as a key subunit of the DNA repair/transcription factor TFIIH. However, here, we report that XPD, independently of other TFIIH subunits, can localize with the motor kinesin Eg5 to mitotic spindles and the midbodies of human cells. The XPD/Eg5 partnership is promoted upon phosphorylation of Eg5/T926 by the kinase CDK1, and conversely, it is reduced once Eg5/S1033 is phosphorylated by NEK6, a mitotic kinase that also targets XPD at T425. The phosphorylation of XPD does not affect its DNA repair and transcription functions, but it is required for Eg5 localization, checkpoint activation, and chromosome segregation in mitosis. In XPD-mutated cells derived from a patient with xeroderma pigmentosum, the phosphomimetic form XPD/T425D or even the nonphosphorylatable form Eg5/S1033A specifically restores mitotic chromosome segregation errors. These results thus highlight the phospho-dependent mitotic function of XPD and reveal how mitotic defects might contribute to XPD-related disorders.

INTRODUCTION

The human xeroderma pigmentosum group D gene *XPD* (also named *ERCC2*) encodes an adenosine triphosphate (ATP)-dependent 5'-3' helicase of 760 amino acids (1). This protein is known to be one of the 10 subunits of the TFIIH (Transcription Factor II H) complex, which is involved in nucleotide excision repair (NER) pathway and in transcription mediated by the RNA polymerase II (RNAPII) (2). In NER, besides its contribution to reveal ultraviolet (UV)-induced DNA damage, the helicase activity of XPD opens the double-stranded DNA to further allow the removal of the damaged oligonucleotide by XPG and XPF (Xeroderma Pigmentosum G and F) endonucleases (1, 3). In transcription, while its helicase activity is dispensable, XPD has a structural function by bridging the cyclin-dependent kinase (CDK)-activating kinase (CAK) subcomplex [containing the cyclin H, MAT (Ménage à trois 1), and the kinase CDK7] to the core of TFIIH (XPB, p62, p52, p44, p34, and p8/TTDA) through an interaction with MAT1 and p44, respectively.

In addition, XPD can be found within TFIIH-independent complexes. In particular, XPD can be associated to the CAK without the presence of the core-TFIIH (4–6). This XPD/CAK association inhibits CAK activity (7), which is required during cell cycle by phosphorylating CDKs (including CDK1, CDK2, CDK4, and CDK6). In *Drosophila*, the Xpd inhibitory action on CAK activity seems to be circumvented by the association of Xpd to Mms19 (8). XPD and MMS19 were found in human cells associated with the adenine nucleotide translocase ANT2 and the cytosolic iron-sulfur protein

assembly (CIA) machinery factors CIAO1 and macrophage inflammatory protein 18 in a complex named MMS19-MIP18-XPD (MMXD), which contributes to proper chromosome segregation in mitosis (9). Together, these observations suggest that XPD might play cellular functions independently of its presence within TFIIH. However, it remains unclear how XPD itself contributes to cell division and which molecular mechanisms drive the switch, allowing XPD to participate to these distinct cellular processes.

Mutations in the *XPD* gene result in different human autosomal recessive disorders (online Mendelian Inheritance in Man number: 126340), such as XP and trichothiodystrophy (TTD). Patients with XP-D develop severe phenotypes including neurological abnormalities and numerous skin defects ranging from excessive freckling to multiple skin cancers (10). These patients can sometimes develop XP combined with Cockayne syndrome, which associates XP phenotypes with severe dwarfism, mental retardation, and skeletal abnormalities (11). The principal hallmark of TTD is dry sparse hairs and brittle nails, but these patients can also develop other symptoms including ichthyosis, intellectual disability, reduced stature, and hypogonadism (12, 13). Numerous studies were undertaken to determine the molecular and phenotypic consequences of XPD mutations. Although, until now, diseases resulting from XPD mutations are considered to be essentially related to DNA repair disorders (14), the various XPD functions suggest that defects in other cellular processes may contribute the pathophysiological process.

Here, we show that during mitosis, XPD localizes differently to other TFIIH subunits and that it interacts with Eg5, a motor kinesin protein required for establishing bipolar spindle (15, 16). This XPD/Eg5 partnership is promoted upon phosphorylation of Eg5/T926 by the major mitotic kinase CDK1, and conversely, it is reduced once Eg5/S1033 is phosphorylated by NEK6 (never in mitosis gene A-related kinase 6). In addition to Eg5, we show that NEK6 phosphorylates XPD at its threonine-425 (T425) residue, which promotes the association of XPD with the CAK module of TFIIH, revealing a fine-tuned regulatory process that conditions the partnerships of XPD and in extenso its role in mitosis. Notably, XP-D patient cells bearing mutations

Copyright © 2022
The Authors, some
rights reserved;
exclusive licensee
American Association
for the Advancement
of Science. No claim to
original U.S. Government
Works. Distributed
under a Creative
Commons Attribution
License 4.0 (CC BY).

Downloaded from https://www.science.org on February 19, 2025

¹Institut de Génétique et de Biologie Moléculaire et Cellulaire (IGBMC), Expression et Réparation du Génome, Equipe labellisée Ligue contre le Cancer, CNRS/INSERM/Université de Strasbourg, BP 163, Illkirch Cedex, C. U., 67404 Strasbourg, France.

²Institut de Génétique et de Biologie Moléculaire et Cellulaire (IGBMC), Cycle Cellulaire et Signalisation de l'Ubiquitine, CNRS/INSERM/Université de Strasbourg, BP 163, Illkirch Cedex, C. U., 67404, Strasbourg, France. ³Department of Biological Sciences, Korea Advanced Institute of Science and Technology, Daejeon, Korea. ⁴College of Medicine, National Taiwan Institute, Taipei 10051, Taiwan.

*Corresponding author. Email: compe@igbmc.fr

affecting the interaction between XPD and Eg5 display defective mitotic progression including chromosome segregation errors, which partially result from deficient spindle assembly checkpoint (SAC) activation. These mitotic defects are rescued upon overexpression of the phosphomimetic form XPD/T425D and of the nonphosphorylatable form Eg5/S1033A. Together, these results highlight a TFIH-independent mitotic function for XPD that is disrupted when XPD is mutated, suggesting that in addition to DNA repair and transcription defects, mitotic deficiencies contribute to XP-D phenotypes.

RESULTS

XPD colocalizes and interacts with Eg5 during mitosis

To gain first insights into the role of XPD during mitosis, we first analyzed its localization throughout the cell cycle. Confocal microscopy analysis of XPD/wild-type (WT) (HeLa) cells (Fig. 1A) showed that while XPD was mostly nuclear during interphase (images A.1 to A.2; as a factor involved in transcription and DNA repair) (2), its localization was dynamically changing during mitotic progression. XPD was essentially nuclear in prophase (images A.5 to A.6), but during prometaphase (images A.9 to A.10) and metaphase (images A.13 to A.14), XPD was excluded from the chromosomes with a substantial fraction being enriched at the mitotic spindle. While its localization persisted at the mitotic spindle, XPD also localized at the midzone in anaphase (images A.17 to A.18). XPD enriched at the midbody in telophase (images A.21 to A.22) contrary to its partner p44 (the regulatory subunit of the XPD helicase within TFIH) and the CAK module (which phosphorylates CDKs, as well as RNAPII and nuclear receptors; fig. S1A, images A.1 to A.4, and A.5 to A.8) (2). Similarly, MMS19 (a partner of XPD within the mitotic MMXD complex having partial localization at the mitotic spindle in metaphase; fig. S1B) (9) did not localize at the midbody (fig. S1A, images A.9 to A.12), highlighting the fact that XPD might be found in mitosis independently from the CAK, TFIH, and MMXD. However, we were surprised to find that XPD partially colocalized with the key mitotic motor kinesin Eg5 at microtubules in prometaphase (Fig. 1A, images A.9 to A.12), metaphase (images A.13 to A.16), and anaphase (images A.17 to A.20) and at the midbody in telophase (images A.21 to A.28). This colocalization of XPD and Eg5 during mitosis prompted us to investigate possible partnership between them. Immunoprecipitation assays from whole-cell extracts of XPD/WT cells synchronized in mitosis revealed that endogenous XPD interacted with Eg5 (Fig. 1B, lane 4); note that a truncated form of human recombinant XPD (XPD 444-760) coimmunoprecipitated with Eg5 (fig. S1C, lane 5), suggesting that at least the C-terminal part of XPD might interact with Eg5. In addition, we observed that deoxyribonuclease 1 treatment of whole-cell extracts from XPD/WT cells in mitosis did not affect the XPD/Eg5 partnership (Fig. 1C, lane 3), and the presence of single-stranded DNA, which is known to tightly bind XPD (17, 18), did not influence the binding of recombinant XPD with Eg5 (fig. S1D, lane 5).

Phosphorylation of Eg5 regulates its partnership with XPD

To further understand how XPD and Eg5 interact, we generated a truncated form of Eg5 (1-897), in which its C-terminal part has been deleted. Immunoprecipitation assays showed that the Eg5 1-897 truncated form no longer interacted with recombinant XPD (Fig. 2A, lanes 6 to 10), suggesting that the C-terminal part of Eg5 (amino acids 898 to 1056) is essential for the XPD/Eg5 partnership. Knowing

that the C-terminal part of Eg5 is subjected to phosphorylations (15), we wondered whether Eg5 might also be phosphorylated by CDK7 (as a subunit of the CAK module, which can be associated to XPD in the absence of core-TFIH) (4-6). In vitro kinase assays showed that CAK was unable to phosphorylate Eg5/WT (Fig. 2B, lane 6). On the contrary, Eg5/WT was phosphorylated by the CDK1 [associated to cyclin B1 (CCNB1)] (lane 7), a posttranslational modification observed during mitosis (19, 20). Accordingly, Eg5/T926A, in which the threonine residue T926 has been mutated into alanine, was not targeted by CDK1 (lane 8). We next observed that the presence of XPD did not modify the ability of CDK1 to phosphorylate Eg5 at T926 (compare lanes 7 and 9). We also investigated whether phosphorylation of Eg5 at T926 might affect its partnership with XPD. Notably, Eg5/T926D, in which the threonine-to-aspartate substitution mimics a constitutive phosphorylation (21), enhanced its binding with XPD relative to Eg5/WT (Fig. 2C, lanes 5 and 6).

Since Eg5 is also targeted by the kinase NEK6 at the serine residue S1033 (a phosphorylation required for proper mitotic spindle formation) (22), coimmunoprecipitation assays were performed with purified XPD and different recombinant Eg5 proteins. We first observed that the nonphosphorylatable form Eg5/S1033A had a moderately increased capacity to interact with XPD/WT relative to Eg5/WT and the phosphomimetic form Eg5/S1033E (Fig. 2D, compare lanes 5 to 7). The simultaneous presence of the phospho-mimetic S1033E and T926D mutations (resulting in Eg5/T926D-S1033E), circumvented the stimulatory effect of the T926D substitution (Fig. 2E, lanes 7 and 9), suggesting that the phosphorylation status of Eg5 regulates its partnership with XPD.

Mutations found in patients with XP-D alter XPD/Eg5 partnership

We next wondered whether mutations found in patients with XP-D might disturb XPD/Eg5 partnership. The mutations XPD/R112H, XPD/R683W, and XPD/R722W were selected for their location in either the N-terminal (/R112H) or the C-terminal (/R683W and /R722W) part of XPD, their loss-of-function evolutionary effect (which is mixed for /R112H and /R722W and severe for /R683W) (23), and their association with either TTD (XPD/R112H and /R722W) or the cancer-prone disease XP (XPD/R683W). Purified mutant XPD proteins were first incubated with immunoprecipitated Eg5 (Fig. 3A). After washing at either 300 or 500 mM salt concentration, XPD/R722W (lanes 7 and 14) and XPD/R683W (lanes 20 to 21) interacted much less with Eg5 when compared to that obtained with XPD/WT (lanes 5, 12, 18, and 19). The partnership of Eg5 with XPD/R112H was similar to that observed with XPD/WT (compare lanes 5, 6, 12, and 13), suggesting that mutations located in the C-terminal part of XPD are detrimental for its interaction with Eg5. Since phosphorylation at T926 of Eg5 promoted its interaction with XPD/WT (Fig. 2C), we next investigated whether this phosphorylation modulated the ability of Eg5 to interact with XPD/R683W. However, contrary to Eg5/WT, Eg5/T926D did not modify its interaction with XPD/R683W (Fig. 3B, compare lanes 2 and 4).

Knowing that TFIH subunits (especially CDK7 and XPB) can be posttranslationally modified (24, 25), we examined whether any phosphorylation of XPD might modulate its interaction with Eg5. We primarily analyzed whether XPD might be phosphorylated by kinases targeting Eg5, namely, CDK1/CCNB1 and NEK6. In vitro kinase assays revealed that XPD was not phosphorylated by CDK1 (associated to CCNB1; Fig. 3C, lane 5) and CDK7 (within CAK,

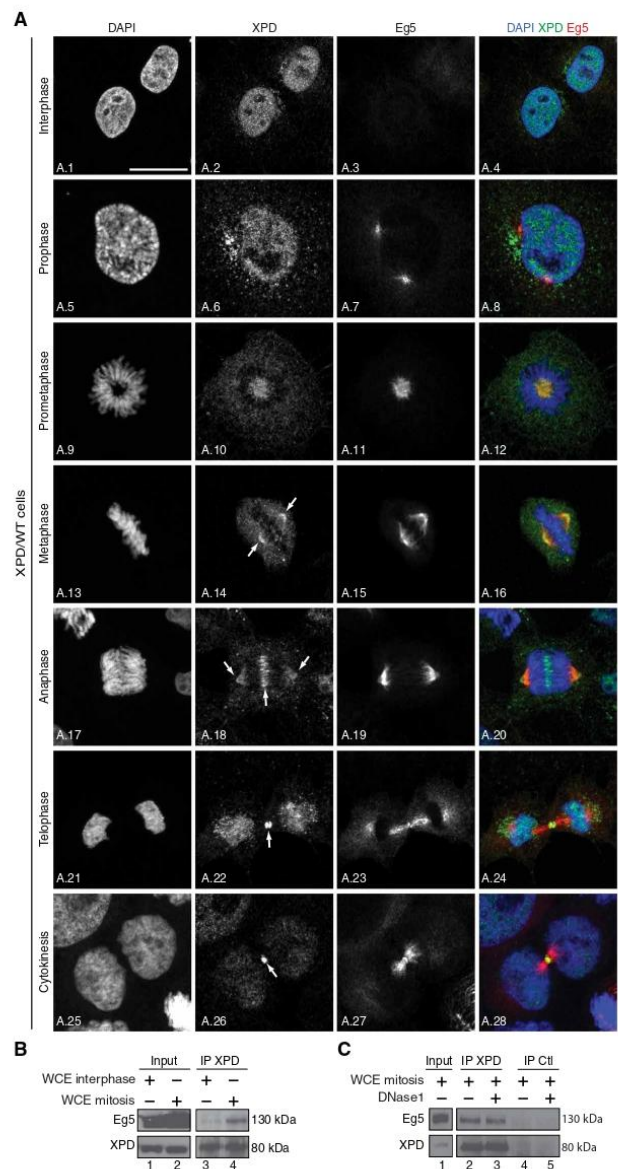


Fig. 1. XPD colocalizes and interacts with Eg5. (A) Immunofluorescence analysis of XPD and Eg5 during interphase and different mitotic phases. Human XPD/WT cells were synchronized by double thymidine block and release, collected 9 hours after release, and analyzed by confocal microscopy at interphase, prophase, prometaphase, metaphase, anaphase, and telophase/cytokinesis. The arrows point to the localization of XPD at the mitotic spindle, the midzone, and at the midbody. Scale bar, 5 μ m. (B) Whole-cell extracts (WCEs) were isolated from XPD/WT cells in interphase and mitosis (cells were treated 16 hours with nocodazole and collected 90 min after nocodazole release). After immunoprecipitation with anti-XPD (IP XPD), the coimmunoprecipitated proteins were resolved by SDS-polyacrylamide gel electrophoresis (SDS-PAGE) and blotted with anti-XPD and anti-Eg5. The results are representative of two independent experiments. (C) Whole-cell extracts were isolated from XPD/WT cells in mitosis [as indicated (B)], treated (when indicated, +) with deoxyribonuclease 1 (DNase1) (5 μ g), and incubated (16 hours, 4°C) with anti-XPD (IP XPD) or irrelevant immunoglobulin G (IgG; IP Ctl) bound to magnetic beads. After washes, the coimmunoprecipitated proteins were resolved by SDS-PAGE and blotted with anti-XPD and Eg5. The results are representative of two independent experiments.

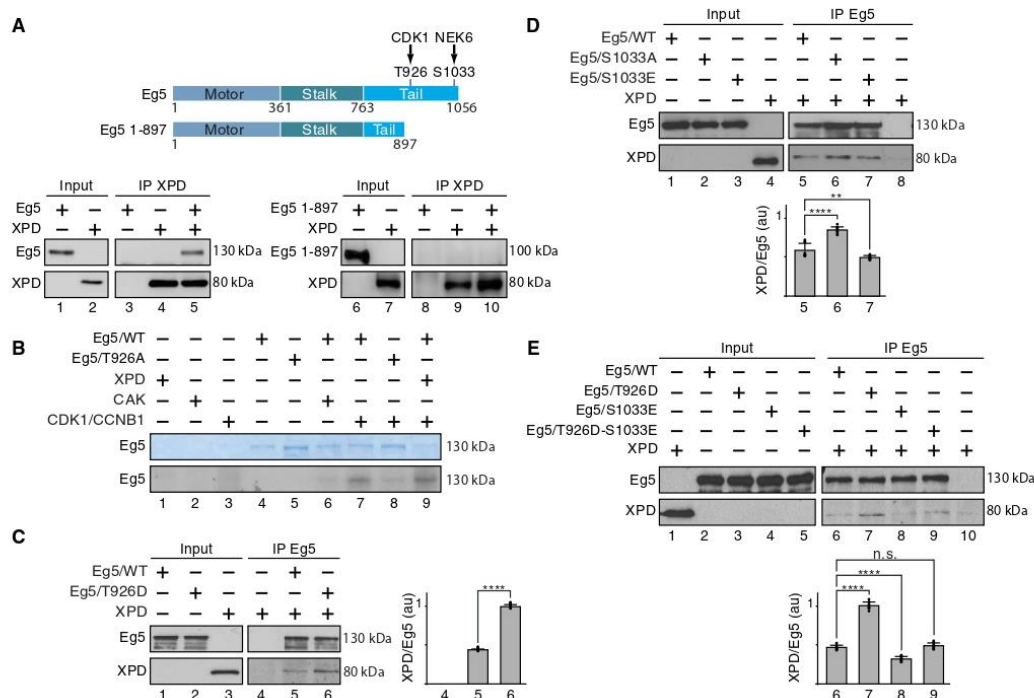


Fig. 2. Phosphorylation modulates the partnership of Eg5 with XPD. (A) Schematic representation of the entire 1056-amino acid Eg5 protein (with the Motor, Stalk, and Tail domains) and the truncated form Eg5/1-897; the residues T926 and S1033 (which are phosphorylated by CDK1 and NEK6, respectively) are also indicated. Immunoprecipitated XPD (IP XPD) was incubated with either entire Eg5 or Eg5/1-897, and after washes, the coimmunoprecipitated proteins were resolved by SDS-PAGE and blotted with anti-XPD and anti-Eg5. (B) Purified Eg5/WT and Eg5/T926A were incubated (as indicated, +) with recombinant XPD, CAK (CDK7/cyclin H/MAT1), and CDK1/CCNB1 in the presence of [γ -³²P]ATP (0.14 μ M). Coomassie blue-stained gel (top) and the corresponding autoradiography (bottom) are shown. (C to E) When indicated (+), immunoprecipitated Eg5/WT, Eg5/T926D, Eg5/S1033A, Eg5/S1033E, or Eg5/T926D-S1033E was incubated with purified XPD/WT. After washes, the coimmunoprecipitated proteins were resolved by SDS-PAGE and blotted with anti-Eg5 and anti-XPD. The immunoprecipitated signals (IP) for XPD and Eg5 were quantified ($n = 3$, means \pm SD), and the ratio XPD/Eg5 were plotted in arbitrary units (au). ** $P < 0.01$ and **** $P < 0.0001$, Student's t test; n.s., not significant.

lane 7). However, NEK6 turned out to phosphorylate XPD (lane 3). Direct interaction was observed between recombinant XPD and NEK6 (Fig. 3D, lane 3), and confocal immunofluorescence microscopy analysis showed colocalization of XPD and NEK6 at the mitotic spindle and spindle poles in the early mitotic stages of prometaphase and metaphase (fig. S2A, images A.1 to A.4 and A.5 to A.8). Further experiments showed that contrary to the N- (XPD 1-245, lane 7) and the C-terminal (XPD 444-760, lane 9) part of XPD, the ARCH domain of XPD was notably phosphorylated by NEK6 (Fig. 3E, lane 8). Liquid chromatography coupled to tandem mass spectrometry (LC-MS/MS) next identified the threonine residue T425 as a potential target for NEK6. As a control, we observed a reduction for the phosphorylation by NEK6 of recombinant XPD 245-443 carrying the T425A mutation (Fig. 3F, lanes 3 and 5), although residual phosphorylation was still occurring because of the targeting of a residue not identified by LC-MS/MS or nonspecific phosphorylation following the substitution of the main phosphorylatable residue T425.

Since the phosphorylation status of Eg5 conditioned its partnership with XPD (Fig. 2, C to E), we then studied what might be the

consequences of XPD phosphorylation on its interaction with Eg5. Coimmunoprecipitation assays showed that recombinant XPD/WT, XPD/T425A, and XPD/T425D interacted similarly with purified Eg5 (Fig. 3G), suggesting that the phosphorylation of XPD at T425 did not influence its interaction with Eg5. However, coimmunoprecipitation assays using whole-cell extracts isolated from HeLa (XPD/WT) cells overexpressing either Flag-tagged XPD/WT, XPD/T425A, or XPD/T425D revealed a stronger interaction of the CAK with XPD/T425D relative to that with XPD/WT and XPD/T425A (Fig. 3H, lanes 6 to 8). The interaction with other factors known to bind the ARCH domain (amino acids 245 to 443) of XPD, such as MMS19 (26) and the XPG NER endonuclease (27, 28), was not modified by the XPD phosphorylation at T425 (fig. S2, B and C, respectively). Furthermore, the interaction of core-TFIIH with XPD/WT was not changed in the presence of either XPD/T425A or T425D (fig. S2D).

Mitosis is perturbed in XP-D patient cells

We then analyzed whether XPD phosphorylation might be altered in XP-D patient cells. Antibodies against phospho-threonine were

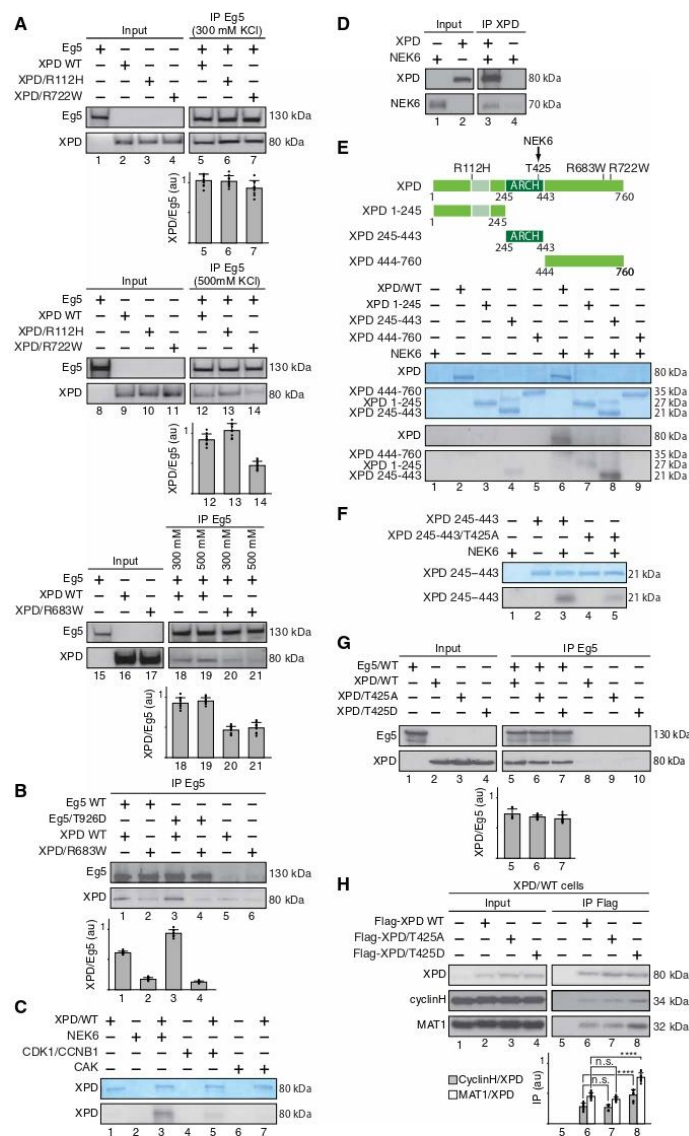


Fig. 3. Phosphorylation of Eg5 regulates its partnership with XPD. (A) Coimmunoprecipitation at either 300 or 500 mM salt concentration of Eg5 (IP Eg5) with either XPD/WT, XPD/R112H, XPD/R722W, or XPD/R683W. The ratio XPD/Eg5 were plotted in au ($n = 3$, means \pm SD). (B) Immunoprecipitated Eg5/WT and Eg5/T926D were incubated with either XPD/WT or XPD/R683W. The graph shows the ratio XPD/Eg5 ($n = 3$, means \pm SD) in au. (C) Purified XPD was incubated with either recombinant NEK6, CDK1/CCNB1, or CAK (CDK7, cyclin H, and MAT1) in the presence of [γ - 32 P]ATP (0.14 μ M). Coomassie blue-stained gel containing XPD (top) and the corresponding autoradiography (bottom) are shown. (D) Flag-XPD (IP XPD) was immunoprecipitated and incubated with tagged glutathione S-transferase (GST)-NEK6. As control, anti-Flag magnetic beads were incubated with GST-NEK6 alone. (E) Entire XPD and its truncated forms 1-245, 245-443, and 444-760 were incubated with NEK6 in the presence of [γ - 32 P]ATP (0.14 μ M). Coomassie blue-stained gels and the corresponding autoradiographies are shown. (F) The ARCH domain (XPD 245-443) and its mutated form (XPD 245-443/T425A) were incubated with NEK6 in the presence of [γ - 32 P]ATP (0.14 μ M). Coomassie blue-stained gel and the corresponding autoradiography are shown. (G) Coimmunoprecipitation of Eg5 (IP Eg5) with either XPD/WT, XPD/T425A, or XPD/T425D. The graph shows the ratio XPD/Eg5 ($n = 3$, means \pm SD) in au. (H) Coimmunoprecipitation assays with whole-cell extracts isolated from XPD/WT cells overexpressing either Flag-XPD/WT, Flag-XPD/T425A, or Flag-XPD/T425D. The graph shows the ratio cyclin H/XPD (gray bars) and MAT1/XPD (open bars; $n = 3$, means \pm SD) in au. **** $P < 0.0001$, Student's t test.

used to immunoprecipitate phosphorylated proteins from whole-cell extracts of XPD/WT (HeLa) and XPD/R683W (HD2) cells (29, 30), at interphase and mitosis. Western blot analysis revealed a higher XPD phosphorylation rate in XPD/WT cells during mitosis than during interphase (Fig. 4A, compare lanes 2 and 8; see also quantification, right). Notably, the XPD phosphorylation was reduced both during interphase and mitosis in XPD/R683W cells when compared to that observed in XPD/WT cells (compare lanes 2 and 5, as well as lanes 8 and 11). Furthermore, XPD phosphorylation weakly increased between interphase and mitosis in XPD/R683W cells (compare lane 5 to lane 11).

These observations prompted us to determine the fate of XPD and Eg5 along the cell cycle. Western blot analysis of cells synchronously progressing through mitosis revealed that the level of XPD (as well as of the XPB and cyclin H subunits of TFIH) did not change along the mitotic time course and was nearly similar in XPD/WT and XPD/R683W cells (Fig. 4B, lanes 1 to 5 and 6 to 10, respectively). No differences were observed between XPD/R683W and XPD/WT cells for the accumulation of Eg5 or several established mitotic markers such as Polo-like kinase 1 (which triggers G₂-M transition and establishes bipolar spindle) (31), AURORA B (which controls condensation of the chromosomes and their attachment to the mitotic spindle) (32), and H3-pS10 (the mitotic marker phospho-histone H3 serine-10). Immunofluorescence microscopy analysis of XPD/R683W cells (fig. S3A) revealed that the localization of mutated XPD during mitosis did not notably differ from what had been previously observed in XPD/WT cells (Fig. 1A), with a fraction of XPD that still colocalized with Eg5 at the mitotic spindle (fig. S3A, images A.10 to A.12, A.14 to A.16, and A.18 to A.20) and at the midbody (images A.22 to A.24).

Notably and contrary to XPD/WT cells, XPD/R683W cells displayed a large variety of severe mitotic defects, including misaligned chromosomes at metaphase and lagging chromosomes and chromatin bridges at anaphase (Fig. 4C, images C.3 and C.4). The total number of XPD/R683W cells with abnormal mitotic phenotype was significantly increased (79% versus 23%) relative to XPD/WT cells (Fig. 4D, open box and black box, respectively). Although protein overexpression can be harmful to the cells and have limiting effects (33), we observed that overexpression of tagged XPD/WT-green fluorescent protein [GFP; as verified by Western blots, Fig. 4D (right); by immunofluorescence, Fig. 4C (images C.9 and C.10)] rescued the chromosome segregation errors in XPD/R683W-mutated cells (images C.7 and C.8; Fig. 4D, gray box); note that the presence of the GFP tag did not interfere with the ability of XPD to interact with Eg5, as verified by coimmunoprecipitation assays (fig. S3B). Furthermore, we noticed that the distribution of mitotic stages (Fig. 4E) was markedly different in XPD/R683W cells (open boxes) when compared to XPD/WT cells (black boxes): reduction of the population of XPD/R683W cells in prometaphase (14% versus 34%) and metaphase (22% versus 41%) and increase in anaphase (41% versus 19%) and telophase (23% versus 6%). Overexpression of tagged XPD/WT-GFP restored the distribution of mitotic stages in XPD/R683W cells (gray boxes), highlighting the deleterious effects of the XPD/R683W mutation in mitosis.

Phosphorylation of XPD is required for proper mitosis

We next determined whether XPD phosphorylation regulates Eg5 localization and mitotic spindle assembly. Synchronized XPD/WT and XPD/R683W cells were subjected to immunofluorescence

microscopy with antibodies targeting Eg5 and α -tubulin, which marks the formation and maintenance of the mitotic spindle as a readout for Eg5 activity (15). When compared to XPD/WT (Fig. 5A, images A.1 to A.5), the XPD/R683W cells (images A.6 to A.10) displayed various defective spindle phenotypes, such as bundled microtubules and unfocused spindle poles [image A.9; quantification, Fig. 5D (bar 2)], which were accompanied by a reduced Eg5 localization at the mitotic spindle (Fig. 5A, image A.8; Fig. 5C, plot 2). Defective Eg5 localization on microtubules and the associated mitotic spindle phenotypes were rescued upon XPD/WT overexpression [Fig. 5A (images A.11 to A.15); Fig. 5B (lane 2); Fig. 5, C and D (plot 3 and bar 3)]. Notably, Eg5 localization and consequent mitotic spindle defective phenotypes were restored in XPD/R683W cells upon overexpression of the phosphomimetic form XPD/T425D [Fig. 5A (images A.21 to A.25); Fig. 5B (lane 4); Fig. 5, C and D (plot 5 and bar 5)] but not of the nonphosphorylatable XPD/T425A [Fig. 5A (image A.16 to A.20); Fig. 5B (lane 3); Fig. 5, C and D (plot 4 and bar 4)]. Furthermore, while the XPD/R683W cells exhibited a higher rate of chromosome segregation errors than XPD/WT cells (Fig. 5E, bars 1 and 2), overexpression of either XPD/WT or XPD/T425D reduced these mitotic phenotypes (bars 3 and 5); cytokinesis failure detected in XPD/R683W cells was also reduced upon overexpression of either XPD/WT or XPD/T425D (fig. S4A, compare images A.6 to A.10 with images A.11 to A.15 and A.21 to A.25). No rescue was observed upon overexpression of XPD/T425A [Fig. 5E (bar 4) and fig. S4A (images A.16 to 20)]. Together, these results strongly suggest that the XPD phosphorylation drives the proper localization of Eg5, the correct assembly of the mitotic spindle, and, in extension, the faithful chromosome segregation.

To further dissect the mitotic role of XPD, XPD/WT and XPD/R683W cells were synchronized in prometaphase with nocodazole (16 hours, 100 ng/ml), washed out, and then collected at different time points. Western blot analysis revealed that the level of XPD and cyclin H did not change along the time course and was similar in XPD/WT and XPD/R683W cells (Fig. 6A). Eg5 accumulated at $t = 0$ in XPD/WT (Fig. 6A, lane 2) and XPD/R683W (lane 7) cells to then decrease at the end of the time course (lanes 3 to 5 and 8 to 10). The phosphorylation of Eg5 at T926 by CDK1 followed the premature degradation of CCNB1 in XPD/R683W cells (compare lanes 4 and 5 and 9 and 10). In sharp contrast to XPD/WT cells, the prometaphase-arrested XPD/R683W cells slightly progressed through mitosis 45 and 90 min after nocodazole release (Fig. 6B, compare bars 3 and 4 and 8 and 9), to finally reach interphase at 180 min, while a large majority of XPD/WT cells were still undergoing mitosis (compare bars 5 and 10), suggesting that XPD/R683W cells might exit mitosis prematurely.

We then checked whether the SAC, a process known to control the proper segregation of chromosomes during mitosis (34), might be defective in XPD/R683W cells. XPD/WT and XPD/R683W cells were treated with Taxol, which stabilizes microtubules and blocks metaphase to anaphase transition due to SAC activation. Such treatment induced prolonged mitotic arrest in XPD/WT cells (Fig. 6C, box 1), while in contrast, a significant number of XPD/R683W cells exited Taxol-induced mitotic arrest (box 4), displaying chromosome segregation errors (fig. S5A). The localization of the key SAC component BubR1 (budding uninhibited by benzimidazoles related 1) (35) to kinetochores [labeled with serum from patients with CREST (calcinosis, Raynaud phenomenon, esophageal dysmotility, sclerodactyly, telangiectasia) scleroderma] was significantly reduced in XPD/R683W cells (Fig. 6D, plot 2; Fig. 6E, images E.3 and

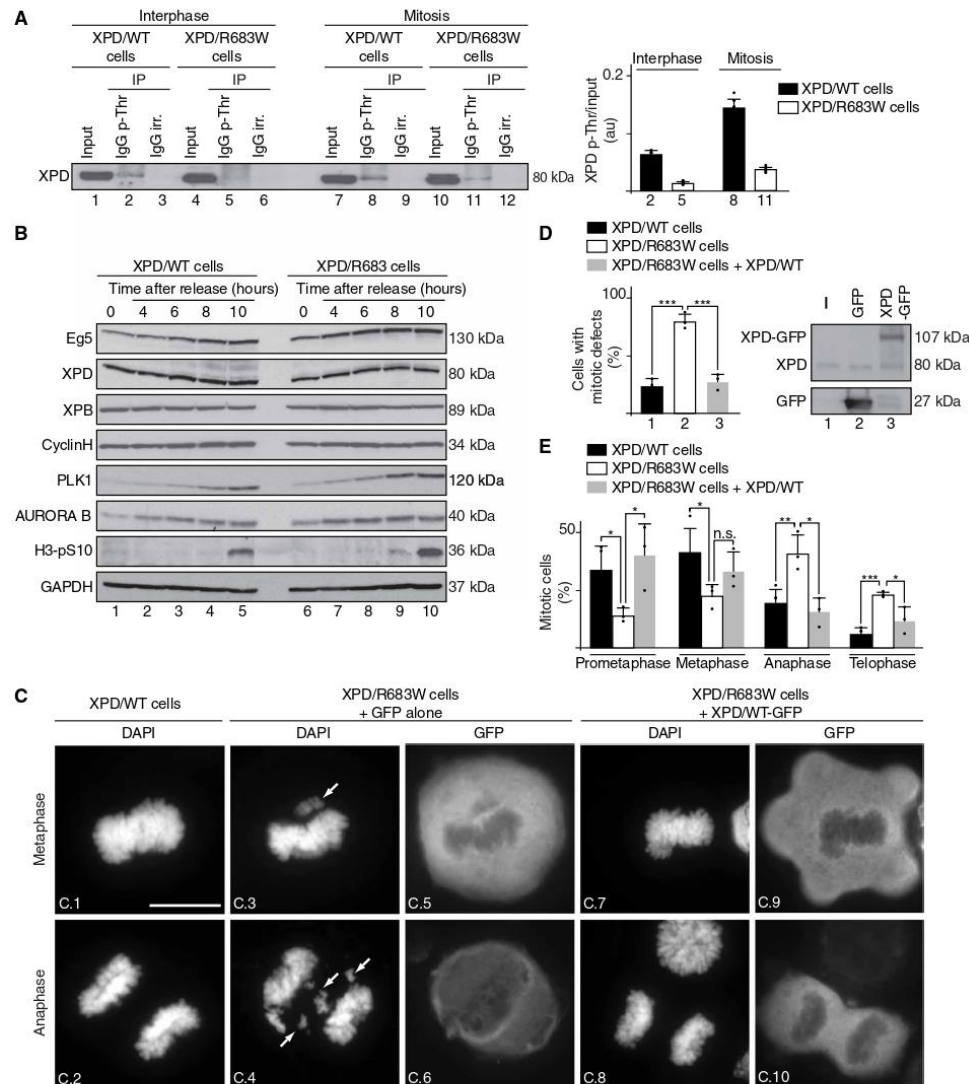


Fig. 4. Mitosis is disrupted in XP-D patient cells. (A) Whole-cell extracts were isolated from XPD/WT and XPD/R683W cells in interphase and mitosis (upon nocodazole treatment and release for 90 min). Immunoprecipitations were performed with either irrelevant IgG (IgG irr.) or anti-phospho-threonine IgG (IgG p-Thr). The graph shows the ratio phosphorylated XPD (XPD p-Thr)/input in normal and XPD-mutated cells ($n = 3$, means \pm SD) in au. (B) Western blot analysis ($n = 3$) of XPD/WT- and XPD/R683W-mutated cells synchronized with double thymidine block, released and collected at 0, 4, 6, 8, and 10 hours. glyceraldehyde-3-phosphate dehydrogenase (GAPDH) was used as loading control. (C and D) XPD/WT cells and XPD/R683W cells overexpressing the tag GFP alone or GFP-XPD/WT were analyzed in mitosis (upon nocodazole treatment and release for 90 min). The arrows point to chromosome segregation errors at metaphase and anaphase. Scale bar, 5 μ m. (D) Percentage of mitotic cells displaying either a normal or a defective mitotic phenotype (at least 130 cells per experiment and per condition were counted). $n = 3$, means \pm SD; *** $P < 0.001$, Student's t test). Western Blots show overexpressed Tag GFP and XPD/WT-GFP. (E) XPD/WT cells (black bars) and XPD/R683W cells overexpressing either tag GFP alone (open bars) or GFP-XPD/WT (gray bars) were analyzed in mitosis (upon nocodazole treatment and release for 90 min). The data are shown as percent mitotic cells in each mitotic stage compared to the total cell number counted ($n = 3$, means \pm SD; at least 130 cells per experiment and per condition were counted; * $P < 0.05$, ** $P < 0.01$, and *** $P < 0.001$, Student's t test).

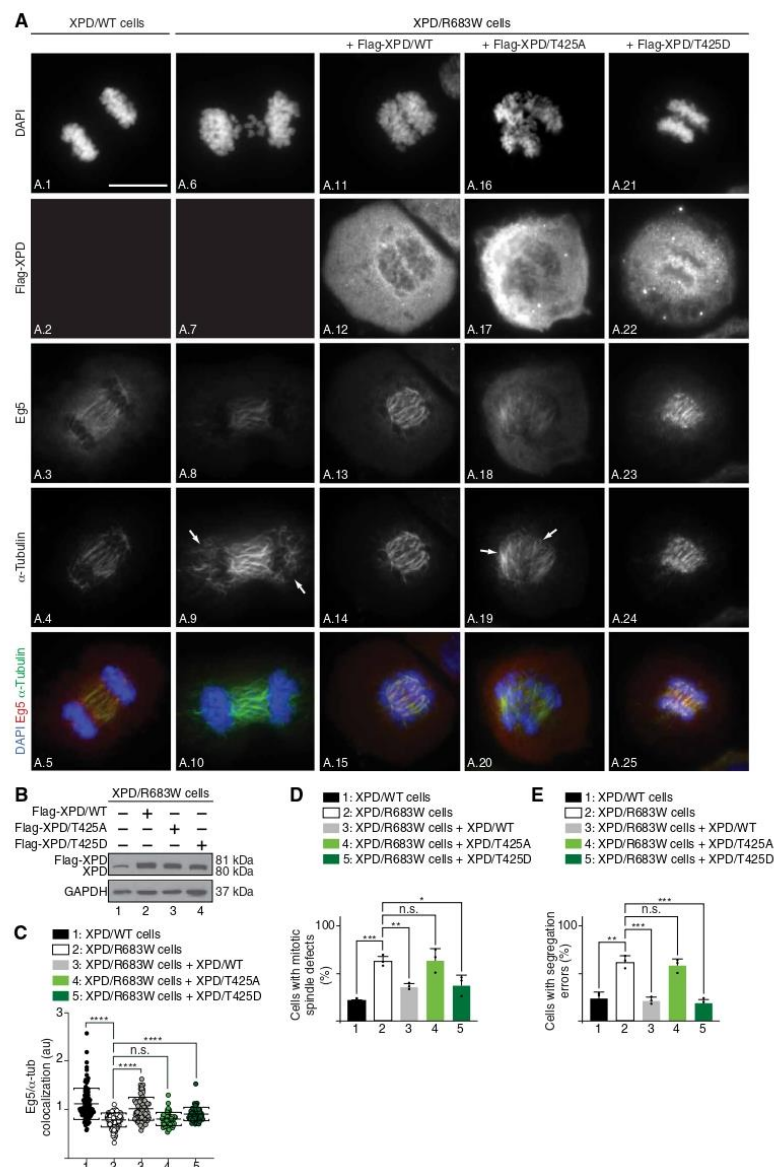


Fig. 5. Phosphorylation of XPD is critical for mitosis. (A) Immunofluorescence of XPD/WT and XPD/R683W cells in anaphase overexpressing either Flag-XPD/WT, Flag-XPD/T425A, or Flag-XPD/T425D. Cells were synchronized in mitosis for 16 hours with nocodazole (100 ng/ml) and collected 90 min after nocodazole release. Immunofluorescence analyses were performed with antibodies targeting the Flag-Tag, Eg5, and α -tubulin. Chromosomes were stained with DAPI. The arrows point to mitotic spindle defects. Scale bar, 5 μ m. (B) Overexpression of Flag-XPD/WT (lane 2), Flag-XPD/T425A (lane 3), and Flag-XPD/T425D (lane 4) in XPD/R683W cells were analyzed by Western blots. The level of endogenous XPD can be visualized in nontransfected XPD/R683W cells (lane 1). (C) Relative presence of Eg5 on the mitotic spindle [$n = 3$, means \pm SD; two-tailed Student's t test for sample 1 versus 2 and ordinary one-way analysis of variance (ANOVA) test for sample 2 versus 3, sample 2 versus 4, or sample 2 versus 5; **** $P < 0.0001$]. (D and E) Percentage of cells displaying mitotic spindle defects (D) and with segregation errors (E) ($n = 3$, means \pm SD; at least 300 cells per experiment and per condition were counted; * $P < 0.05$, ** $P < 0.01$, and *** $P < 0.001$, Student's t test).

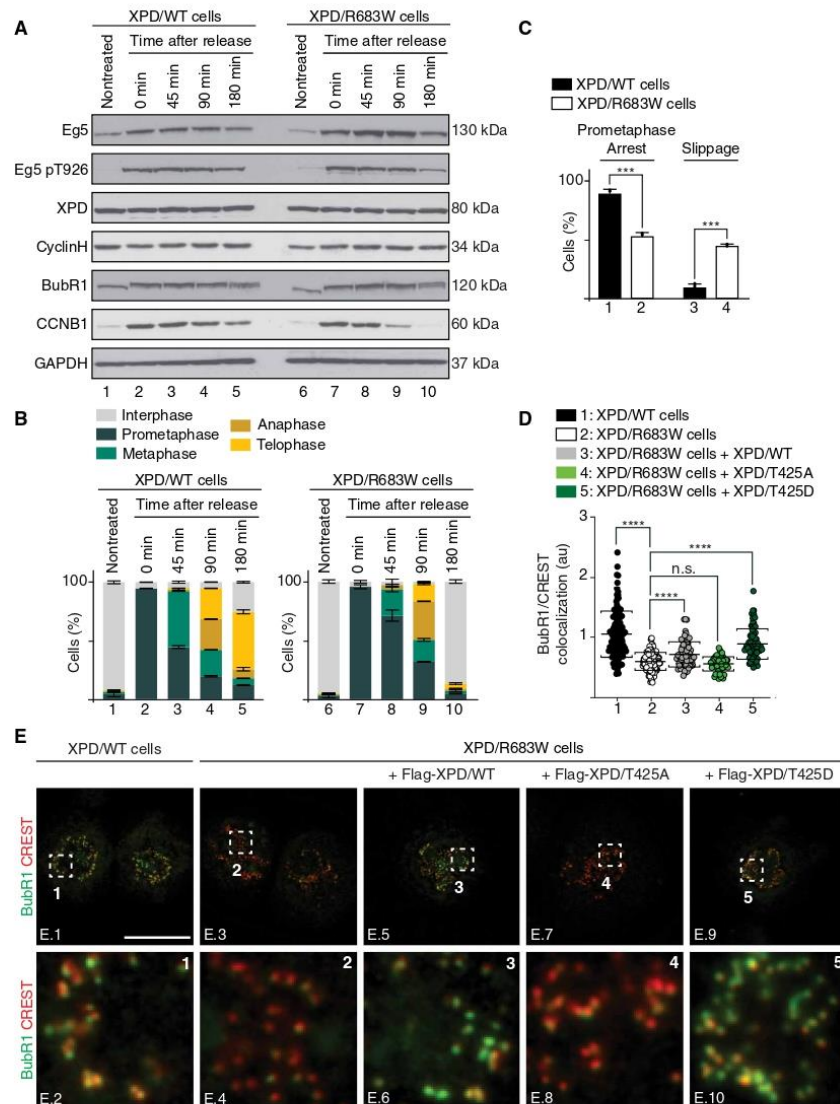


Fig. 6. Mitotic slippage in XPD-mutated patient cells. (A and B) XPD/WT and XPD/R683W cells were synchronized with nocodazole, released, and harvested at indicated time points. (A) Whole-cell lysates were isolated and used for immunoblot analyses. GAPDH was used as loading control. (B) Fixed cells were mounted and stained with DAPI. The percentage of XPD/WT and XPD/R683W cells in different mitotic phases was quantified at the indicated time points after nocodazole release ($n=2$, means \pm SD; at least 200 to 250 cells were analyzed per condition and per experiment). (C) WT (black bars) and XPD/R683W (open bars) cells were treated with Taxol (16 hours, 1 μ M). The percentage of cells arrested in prolonged prometaphase or exited mitosis was quantified ($n=3$, means \pm SD; at least 300 cells per experiment and per condition were counted; *** $P < 0.001$, Student's t test). (D and E) WT and XPD/R683W cells overexpressing the Flag-Tag alone or fused to either XPD/WT, XPD/T425A, or XPD/T425D were synchronized in prometaphase with Taxol (16 hours, 1 μ M). (E) Immunostaining of BubR1 and kinetochores (stained with CREST). Regions of interest are shown in the corresponding numbered panels. Scale bar, 5 μ m. Unmerged images for Flag-XPD, BubR1, and CREST are provided in fig. S5B. (D) The relative intensity levels of BubR1 on individual kinetochores were quantified by using the Fiji software ($n=3$, means \pm SD; two-tailed Student's t test for sample 1 versus 2 and ordinary one-way ANOVA test for sample 2 versus 3, sample 2 versus 4, or sample 2 versus 5; **** $P < 0.0001$).

E.4; fig. S5B, images B.9 to B.16). Notably, the total BubR1 protein levels remained unchanged between XPD/WT and XPD/R683W cells (Fig. 6A). The BubR1 localization to kinetochores was restored upon overexpression of either XPD/WT or XPD/T425D (Fig. 6D, plots 3 and 5; Fig. 6E, images E.6 and E.10; fig. S5B, images B.17 to B.24 and B.33 to B.40) but not of XPD/T425A (Fig. 6D, plot 4; Fig. 6E, image E.8; fig. S5B, images B.25 to B.32), suggesting that XPD

phosphorylation is critical to maintain a functional mitotic checkpoint and to ensure correct chromosome segregation.

Eg5/S1033A circumvents mitotic defects in XP-D cells

We also investigated whether the phosphorylation of Eg5 might, in turn, affect the mitotic phenotypes observed in XP-D cells. Unexpectedly, the overexpression of the nonphosphorylatable form Eg5/S1033A

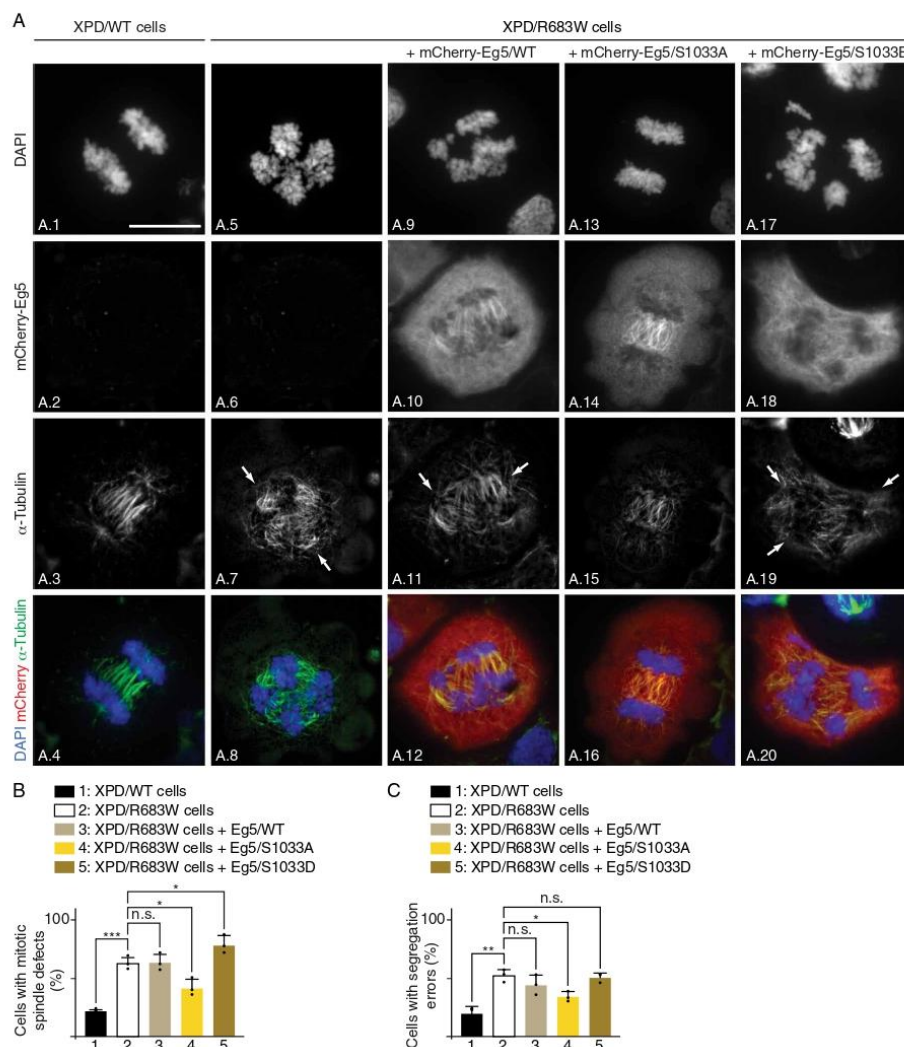


Fig. 7. Eg5/S1033A restores mitotic defects in XPD-mutated patient cells. (A) Immunofluorescence of XPD/WT and XPD/R683W cells overexpressing either tagged mCherry-Eg5/WT, mCherry-Eg5/S1033A, or mCherry-Eg5/S1033E in anaphase. Cells were synchronized in mitosis for 16 hours with nocodazole (100 ng/ml) and collected 90 min after nocodazole release. Immunofluorescence analyses were performed with antibodies targeting the mCherry Tag and the mitotic spindle marker α -tubulin. Chromosomes were stained with DAPI. Arrows point to DNA bridges. Scale bar, 5 μ m. (B and C) Percentage of cells displaying mitotic spindle defects (B) and segregation errors (C) ($n = 3$, means \pm SD; at least 300 cells per experiment and per condition were counted; * $P < 0.05$, ** $P < 0.01$, and *** $P < 0.001$, Student's t test).

in XPD/R683W cells significantly rescued the mitotic spindle and chromosome segregation defects observed at anaphase [visualized by the α -tubulin marker and 4',6-diamidino-2-phenylindole (DAPI) staining, respectively; Fig. 7A (compare image A.7 with A.15 and A.5 with A.13); quantification, Fig. 7, B and C (bars 2 and 4)] and at telophase (fig. S6A, images A.5 to A.8 and A.13 to A.16). On the contrary, overexpression of either Eg5/WT (which might therefore still be in vivo phosphorylated) or Eg5/S1033E did not modify the mitotic phenotypes resulting from XPD/R683W [Fig. 7A (images A.9 to A.12 and A.17 to A.20); Fig. 7, B and C (bars 3 and 5)]. Likewise, aberrant chromosome segregation and defective spindle formation observed at telophase were still present in XPD/R683W cells upon overexpression of either Eg5/WT or Eg5/S1033E (fig. S6A, images A.9 to A.12 and A.17 to A.20). Note that the tagged mCherry-Eg5/WT, /S1033A, and /S1033E proteins that were expressed at the same level, associated similarly to the endogenous Eg5 protein (fig. S6B). Furthermore, although having a lower capacity than XPD/WT to bind Eg5 (fig. S6C, compare bars 6 to 8 and 10 to 12), we observed that XPD/R683W exhibited a stronger interaction with Eg5/S1033A than with Eg5/S1033E (bars 11 and 12). Together, our data suggest that mitotic defects resulting from mutation of XPD can be restored by the nonphosphorylatable form S1033A of its partner Eg5.

Phosphorylation of XPD is specifically required for its mitotic function

We next were wondering whether the phosphorylation of XPD and Eg5, as well as their partnership, might affect the helicase activity of XPD, which is absolutely required during DNA repair (2). In the presence of the regulatory p44 subunit of TFIIH (which promotes the helicase activity of XPD) (36), XPD/T425A and XPD/T425D recombinant proteins exhibited the same helicase activity as XPD/WT [as observed in an in vitro assay by the displacement of the 5' ³²P-labeled 25-nucleotide (nt) single-stranded DNA annealed to the 52-nt single-strand DNA; Fig. 8A], suggesting that phosphorylation of XPD does not affect DNA repair activity. We also observed that addition of Eg5 modified neither the helicase activity of XPD (Fig. 8B) nor the removal of damaged oligonucleotides when added in an in vitro NER assay (containing cis-platinated DNA as a substrate, XPC, XPA, RPA, XPF/ERCC1, and XPG, as well as XPD, core-IIH, and CAK; fig. S7A). Knowing that patients with XPD mutations develop photosensitivity (10), we evaluated the cell viability upon UV irradiation. When compared to XPD/WT cells, XPD/R683W-mutated cells exhibited a lower survival rate, which was circumvented upon overexpression of either XPD/T425A, XPD/T425D, or XPD/WT (Fig. 8C). However, no restoration was detected upon overexpression of either XPD/R683W, XPD/R683W-T425A, or XPD/R683W-T425D (fig. S7B) and of Eg5/WT, Eg5/S1033A, and Eg5/S1033E (Fig. 8D). Together, the above data suggest that neither the phosphorylation of XPD nor that of Eg5 can rescue the deleterious effect of the XPD/R683W mutation in DNA repair.

We also analyzed whether the phosphorylation of XPD and its association with Eg5 might affect RNA synthesis. In vitro transcription assay [containing the adenovirus major late promoter (AdMLP) template, RNAPII, TFIIA, -IIB, -D(TBP), -E, -F, core-IIH, and CAK] showed that addition of either XPD/T425A or XPD/T425D promoted RNA synthesis with the same efficiency as XPD/WT (Fig. 8E). Furthermore, in vitro transcription was not altered by the addition of Eg5 (Fig. 8F). We also investigated the impact of XPD and Eg5 phosphorylation on the transactivation process by using the all-trans-retinoic acid (t-RA)-inducible *RAR β 2* gene as a model (37).

Overexpression of XPD/T425A and XPD/T425D restored similarly to XPD/WT the *RAR β 2* gene expression in XPD/R683W cells (Fig. 8G), restoration that did not occur upon overexpression of XPD/R683W, XPD/R683W-T425A, and XPD/R683W-T425D (fig. S7C). The overexpression of either Eg5/S1033A, Eg5/S1033E, or Eg5/WT was unable to rescue the *RAR β 2* expression deficiency observed in XPD/R683W cells (Fig. 8H), which was in accordance with the fact that Eg5 neither targeted nor influenced the formation of the transcription preinitiation complex (PIC; fig. S7D). Together, our results demonstrate that DNA repair and transcription are not dependent on the phosphorylation of both XPD and Eg5, which seems to be specifically required for mitosis.

DISCUSSION

The present study aims to dissect the role of XPD in mitosis, beside its key functions in transcription and DNA repair as part of TFIIH. By establishing a phospho-dependent partnership with the motor kinase protein Eg5, XPD critically regulates mitotic progression in a TFIIH-independent manner. XPD mutations lead to chromosome segregation errors, which might contribute to the development of clinical features observed in XP-D patients.

In human cells, the protein XPD can be found either associated to the CAK module, within TFIIH, or as a part of MMXD (7, 9). XPD, independently of TFIIH and MMXD subunits (fig. S1, A and B), interacts and colocalizes with the motor kinesin Eg5, especially to mitotic spindle and midbodies (Fig. 1, A and B) (16). These observations raise questions on a potential mechanism regulating the ability of XPD to be either internalized within complex such as TFIIH or bound to other factors including Eg5. This switch mechanism might imply coordinated and sequential posttranslational modifications.

In this regard, we found that the mitotic kinase NEK6 (38) localizes with XPD in early phases of mitosis (fig. S2A) and phosphorylates the ARCH domain of XPD, at position T425 (Fig. 3E). This phosphorylation affects the ability of XPD to interact with the CAK module of TFIIH (Fig. 3H) but not with either Eg5 (Fig. 3G) or other factors such as MMS19, XPG, and the core-TFIIH (fig. S2, B to D) (26–28). Contrary to NEK6, neither CDK8 (a subunit of the transcription complex Mediator) (24, 39), CDK7 (the kinase of the CAK module targeting transcription factors and mitotic CDKs) (2), nor CDK1 (a key mitotic kinase targeted by CDK7) (40) is able to phosphorylate XPD (Fig. 3C). Notably, we demonstrate that the phosphorylation of XPD at position T425 is critical for its mitotic functions (Figs. 5, A to E, and 6, D and E) without affecting its role in both DNA repair (Fig. 8, A and C) and transcription (Fig. 8, E and G). Besides the phosphorylation of XPD and given the obvious implication of XPD and Eg5 in mitosis, we subsequently observed that the phosphorylation of Eg5 is critical by modulating the Eg5/XPD partnership. While the Eg5/XPD interaction is promoted by the phosphorylation of Eg5 at T926 (Fig. 2C), it decreases when Eg5 is simultaneously phosphorylated at S1033 (Fig. 2E).

A better understanding of the phospho-dependent XPD/Eg5 partnership also came from studies of XPD-mutated forms. XPD mutations found in most patients with XP-D alter the ability of XPD to interact with Eg5 (Fig. 3A), which consequently disrupt the localization of Eg5 on microtubules, as observed in XPD/R683W-deficient cells (Fig. 5, A and C). This Eg5 mislocalization can be rescued by the expression of XPD/WT only if it is phosphorylatable at position T425 (Fig. 5). In addition, the overexpression of the

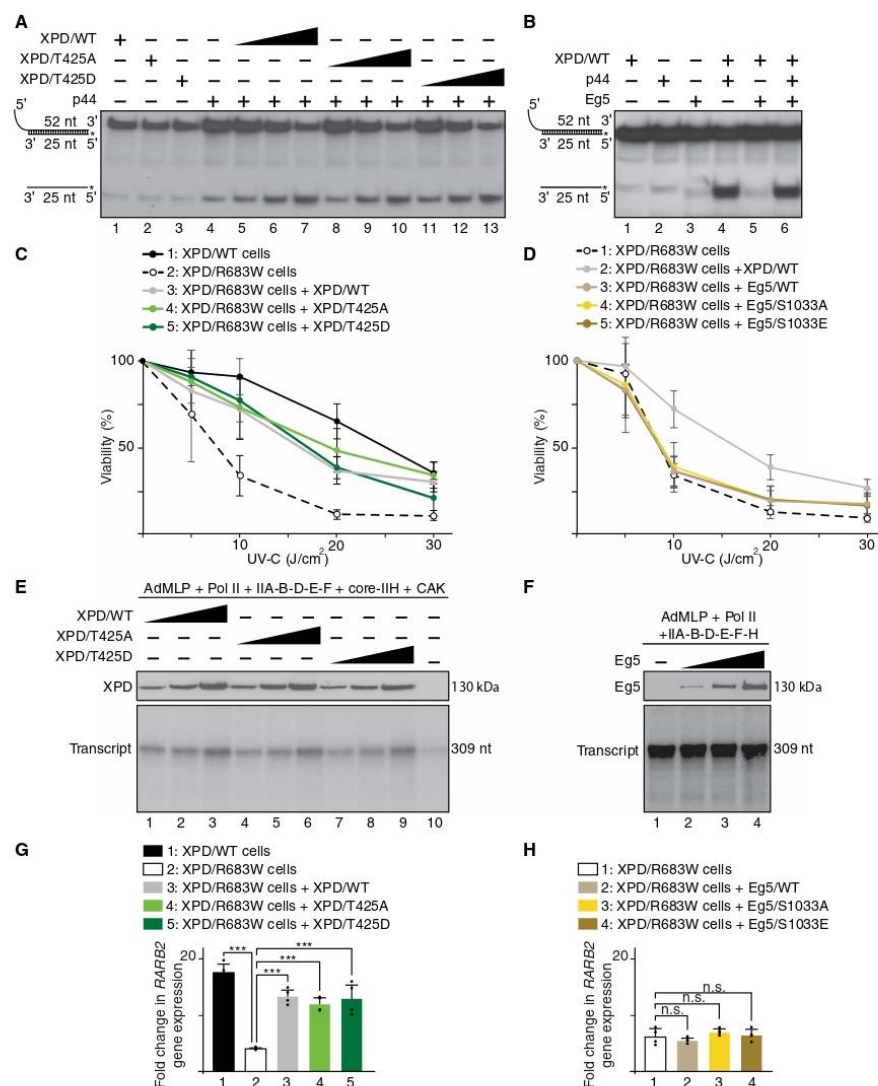


Fig. 8. DNA repair and transcription do not require XPD phosphorylation. (A and B) Helicase assays in the presence (+) of p44 and Eg5 and increasing amounts of XPD/WT, XPD/T425A, and XPD/T425D. Single- and double-stranded DNA are indicated. (C) XPD/WT and XPD/R683W cells overexpressing XPD/WT, XPD/T425A, or XPD/T425D were treated with increasing doses of UV-C, and cell survival was determined 48 hours later. Data were normalized to unexposed cells (means ± SD of two experiments in triplicates). Significant statistical difference (Student's *t* test): between XPD/WT and XPD/R683W cells at 5 J/cm² (*P* < 0.001) and at 10, 20, and 30 J/cm² (*P* < 0.0001); between XPD/R683W and XPD/R683W + XPD/WT or XPD/R683W + XPD/T425A cells at 10, 20, and 30 J/cm² (*P* < 0.0001); and between XPD/R683W and XPD/R683W + XPD/T425D cells at 5 (*P* < 0.01), 10, and 20 J/cm² (*P* < 0.0001) and at 30 J/cm² (*P* < 0.001). (D) XPD/R683W cells overexpressing XPD/WT, Eg5/WT, Eg5/S1033A, or Eg5/S1033E were treated as indicated (C) (means ± SD of two experiments in triplicates). Significant statistical difference (Student's *t* test) between XPD/R683W + XPD/WT cells and XPD/R683W + XPD/R683W + Eg5/WT, XPD/R683W + Eg5/S1033A, or XPD/R683W + Eg5/S1033E at 10, 20 (*P* < 0.0001), and 30 J/cm² (*P* < 0.0001). (E) In vitro transcription assay with AdMLP template, RNAPII, TFIIA, TFIIB, TFIID(TBP), TFIIE, TFIIH core-IIH, CAK and increasing amounts of XPD/WT, XPD/T425A, or XPD/T425D. (F) Transcription assay with AdMLP template, RNAPII, TFIIA, TFIIB, TFIID(TBP), TFIIE, TFIIH core-IIH, CAK and increasing amounts of XPD/WT, XPD/T425A, or XPD/T425D. (G) *RARβ2* gene expression (normalized to the GAPDH RNA amount) after 8 hours of t-RA treatment in XPD/WT and XPD/R683W cells overexpressing XPD/WT, XPD/T425A, or XPD/T425D. The *RARβ2* mRNA expression is presented as *n*-fold induction relative to nontreated cells (means ± SD of two experiments in triplicates; ****P* < 0.001, Student's *t* test). (H) *RARβ2* gene expression in XPD/R683W cells overexpressing either Eg5/WT, Eg5/S1033A, or Eg5/S1033E (means ± SD of two experiments in triplicates; n.s., not significant).

nonphosphorylatable form Eg5/S1033A (which prevents XPD/Eg5 dissociation; fig. S6C) can circumvent mitotic failures (Fig. 7, A to C) but not DNA repair deficiencies (Fig. 8D) observed in XPD/R683W-mutated cells. These results suggest that the mitotic defects observed in XPD-mutated cells would not be related to defective DNA repair. Moreover, it even seems that functional mitosis might not require the DNA-dependent helicase activity of XPD (which is strongly reduced by the XPD/R683W mutation) (41). Although the mitotic function of XPD may not require its DNA-dependent helicase activity and its ability to bind DNA (illustrated by its chromosome exclusion in mitosis; Fig. 1A), it would be of interest to determine whether mitosis might be affected in cells bearing mutations (such as XPD/G47R) located within the ATP-binding site of XPD. Note that none of the transcription/DNA repair functions of XPD as a component of TFIIH are affected by Eg5 and this, whatever its phosphorylated status (Fig. 8, B, D, F, and H, and fig. S7, A and D). By highlighting the central role played by NEK6, our results suggest that phosphorylation process conditions the TFIIH-independent role of XPD in mitosis by acting as a switch mechanism to fine-tune its partnerships. Note that XPD is not the only component of TFIIH having mitotic functions. In particular, the CAK subcomplex (via CDK7) is known to phosphorylate and activate CDK1, which promotes entry into mitosis (42). Furthermore, TFIIH subunits (in particular, p52 and XPB) might be implicated in condensing and maintaining chromosome structure during mitosis in vertebrates (43) and *Drosophila* (44, 45).

In addition, to underline the phospho-dependent mitotic function of XPD apart from its DNA repair/transcription functions, the present study provides insights into the understanding of the clinical features observed in patients with XP-D. In particular, by affecting the Eg5 localization and the microtubule organization (Fig. 5, A to E), the XPD/R683W mutation has deleterious consequences for mitosis, resulting in misaligned chromosomes, lagging chromosomes, and chromatin bridges (Fig. 4, C and D), which likely lead to cytokinesis defects (fig. S4A) (46). The chromosome segregation errors arise, in part, from defective SAC (or mitotic checkpoint) since the XPD-mutated cells bypass mitotic arrest by the microtubule poison Taxol (Fig. 6C) and prematurely exit mitosis (Fig. 6B), a process termed mitotic slippage (47) that is clearly illustrated by the premature degradation of CCNB1 (Fig. 6A). In addition to the genomic instabilities resulting from NER defect, the mitotic slippage evidenced here might contribute to the development of clinical features, especially the high risk of cancers commonly observed in patients with XP-D (10, 48). In addition and knowing that processes other than mitosis require Eg5, such as growth and morphology of postmitotic neurons (49–51), defective action of Eg5 might contribute to neurological abnormalities of patients with XP-D. Since the clinical heterogeneity observed between patients with XP-D (52) might result from the combinatory effects of XPD-mutated forms (53), the effect of different mutated XPD on DNA repair, transcription, and mitosis process should be examined in suitable cellular models. Phenotypic recovery by Eg5 might be helpful to compensate the deleterious mitotic effects resulting from XPD mutations.

MATERIALS AND METHODS

Cell counting

Cells (at least 100 per condition and per experiment) were analyzed in a blinded manner for their chromosomal and mitotic spindle

phenotypes. Normal and defective (chromosome misalignments, lagging chromosomes, anaphase/telophase bridges, and polylobed/abnormal nuclei) chromosomal phenotypes were assessed by DAPI staining. Normal and defective bipolar mitotic spindle formations were assessed by α -tubulin staining.

Cell synchronization

Cells were synchronized in different stages of cell cycle by double thymidine block and release protocol. Briefly, 2 mM thymidine was added twice for 16 hours with an 8-hour interval in fresh medium between the thymidine treatments. After the second thymidine block was complete, cells were released in thymidine-free media and collected at the indicated time points. In addition, cells were synchronized in prometaphase using nocodazole (16 hours, 100 ng/ml) or Taxol (16 hours, 1 μ M).

Cell viability assays

Cells (50,000 cells per well in six-well petri dishes) were exposed to various doses of UV-C (predominantly 254 nm; Philips TUV lamp). After 48 hours, the cells were stained with 0.2% Crystal Violet (Sigma-Aldrich). After washing and drying, the stain was solubilized with 1% SDS and the optical density (595 nm) was measured.

Helicase assays

The helicase assay probe (27) was incubated as indicated (+) with XPD (WT, T425A, or T425D), p44, and Eg5, in the presence of ATP. Single- and double-stranded DNA were separated by electrophoresis and analyzed by autoradiography.

Immunofluorescence microscopy

Once collected, the cells were centrifuged (on Thermo Scientific Shandon Cytospin 4 Cytocentrifuge, 5 min at 1000 rpm) and fixed [4% paraformaldehyde (PFA), 10 min]. After permeabilization (0.5% NP-40 for 5 min), the cells were washed [phosphate-buffered saline (PBS)–0.01% Triton], blocked (3% bovine serum albumin, 1 hour), and subsequently incubated with primary antibodies (see Key Resources Table) in blocking buffer. After washing (PBS–0.01% Triton), the corresponding secondary antibodies were added. Glass coverslips were then added on cells already mounted with either Mowiol (Calbiochem) or ProLong Gold Antifade agent (Invitrogen) containing DAPI. Images were taken with a $\times 63$ objective using Zeiss epifluorescence microscope and/or confocal microscopy (Nikon spinning disk). Image analysis was performed using ImageJ software.

Immunoprecipitation assays

Depending on the coimmunoprecipitation assays, WT and mutated forms of Eg5 and XPD were coincubated together with specific antibodies (as indicated) bound to protein G magnetic beads (Dynabeads, Invitrogen). After extensive washings, Western blots were performed using antibodies raised against the proteins of interest.

Kinase assays

Highly purified proteins were incubated 30 min at 30°C with either recombinant CAK, CDK1/CCNB1, or NEK6 in the presence of [γ - 32 P]ATP (0.14 μ M).

LC-MS/MS analysis

Purified XPD-ARCH domain has been subjected to double digestion with trypsin and chymotrypsin. Samples were analyzed using an Ultimate 3000 nano-RSLC (Thermo Scientific) coupled in line

with an LTQ-Orbitrap Elite mass spectrometer via a nanoelectrospray ionization source (Thermo Scientific). Peptides were identified by database searching using SequestHT (Thermo Fisher Scientific) with Proteome Discoverer 2.4 software (PD2.4, Thermo Fisher Scientific) on *Homo sapiens* database (Swiss-Prot; reviewed and released 6 April 2020; 20,286 entries). Precursor and fragment mass tolerances were set at 7 parts per million and 0.02 Da, respectively, and up to two missed cleavages were allowed. Oxidation (M) and phosphorylation (S/T/Y, +79.966) were set as variable modification.

NER assays

Dual-incision assays were carried out in the presence of ATP (2 mM), plasmid (Pt-GTG) with single cisplatin adduct, purified XPC/hHR23B, core-TFIIH, CAK, XPD, XPA, RPA, XPG, XPF/ERCC1, and Eg5 (when indicated).

PIC formation assays

Biotinylated AdMLP bound to streptavidin magnetic beads was incubated with RNAPII, TFIIA, TBP, TFIIB, TFIIF, TFIIIE, core-IIH, CAK, XPD, and Eg5. After several washing, the bound fractions were resolved by SDS-polyacrylamide gel electrophoresis followed by immunoblotting (54).

Plasmid transfections

Transient transfections of cDNAs encoding either mCherry alone, mCherry-Eg5/WT, mCherry-Eg5/S1033A, mCherry-Eg5/S1033E, GFP alone, XPD/WT-GFP, Flag-XPD/WT, Flag-XPD/T425A, or Flag-XPD/T425D were performed using X-tremeGENE9 (Roche) according to the manufacturer's instructions.

Purifications of recombinant proteins

The different forms of Flag-Eg5 (/WT, /1-897, /T926A, /T926D, /S1033A, /S1033E, and /T926D-S1033E) were produced in *Escherichia coli*. To purify Flag-MMS19, XPG, core-TFIIH (containing XPB, p62, p52, p44, p34, and p8), Flag-CAK (Flag-CDK7, cyclin H, and MAT1), and the different forms of Flag-XPD (/WT, /T425A, /T425D, /R112H, /R683W, /R722W, /1-245, /245-443, /245-443, 245-443/T425A, and /444-760), Sf21 insect cells were infected with the corresponding baculoviruses. The whole-cell extracts were then incubated with agarose beads bound to either anti-XPG (to immunoprecipitate XPG), anti-p44 (to immunoprecipitate core-TFIIH), or anti-M2-Flag (to immunoprecipitate Eg5, MMS19, CAK, and XPD) antibody. The recombinant proteins were then eluted with the corresponding epitope peptide.

Reagents and resources

The reagents and resources (antibodies, chemical, cell lines, oligonucleotides, recombinant DNA, primers, software, and materials) used to accomplish this work are available in Key Resources Table (Supplementary Materials).

Retrotranscription and real-time quantitative polymerase chain reaction

Total RNAs (2 µg) were reverse-transcribed by using Moloney murine leukemia virus RT and random hexanucleotides. FastStart DNA Master SYBR Green kit and the LightCycler apparatus (Roche Diagnostics) have been used to accomplish the real-time quantitative polymerase chain reaction. Primers are available in Key Resources Table (Supplementary Materials).

Strength of the SAC response

Cells were treated with Taxol (16 hours, 1 µM) to induce prometaphase arrest. Cells were next collected by cytospin, fixed (4% PFA, 10 min), and washed three times with PBS. Fixed cells were mounted and stained with Mowiol containing DAPI (see Key Resource Table). The strength of the SAC response was monitored by counting the number of cells arrested in prometaphase versus the number of cells that displayed anaphase-like phenotypes based on their DNA morphology.

Transcription assays

After preincubation of the AdMLP template with RNAPII, TFIIA, TBP, TFIIB, TFIIF, TFIIIE, TFIIH, and Eg5, RNA synthesis was initiated by the addition of nucleoside triphosphate (200 µM), including radiolabeled cytidine triphosphate (0.15 µM) (55). The transcription activity was assessed after 20 min of incubation.

SUPPLEMENTARY MATERIALS

Supplementary material for this article is available at <https://science.org/doi/10.1126/sciadv.abp9457>

[View/request a protocol for this paper from Bio-protocol.](#)

REFERENCES AND NOTES

1. P. Sung, V. Bailey, C. Weber, L. H. Thompson, L. Prakash, S. Prakash, Human xeroderma pigmentosum group D gene encodes a DNA helicase. *Nature* **365**, 852–855 (1993).
2. E. Compe, J. M. Egly, Nucleotide excision repair and transcriptional regulation: TFIIH and beyond. *Annu. Rev. Biochem.* **85**, 265–290 (2016).
3. K. Sugawara, J. Akagi, R. Nishi, S. Iwai, F. Hanaoka, Two-step recognition of DNA damage for mammalian nucleotide excision repair: Directional binding of the XPC complex and DNA strand scanning. *Mol. Cell* **36**, 642–653 (2009).
4. J. T. Reardon, H. Ge, E. Gibbs, A. Sancar, J. Hurwitz, Z. Q. Pan, Isolation and characterization of two human transcription factor IIH (TFIIH)-related complexes: ERCC2/CAK and TFIIH. *Proc. Natl. Acad. Sci. U.S.A.* **93**, 6482–6487 (1996).
5. R. Drapkin, G. LeRoy, H. Cho, S. Akoulitchev, D. Reinberg, Human cyclin-dependent kinase-activating kinase exists in three distinct complexes. *Proc. Natl. Acad. Sci. U.S.A.* **93**, 6488–6493 (1996).
6. M. Rossignol, I. Kolb-Cheynel, J. M. Egly, Substrate specificity of the cdk-activating kinase (CAK) is altered upon association with TFIIH. *EMBO J.* **16**, 1628–1637 (1997).
7. J. Chen, S. Laroche, L. Li, B. Suter, Xpd/Ercc2 regulates CAK activity and mitotic progression. *Nature* **424**, 228–232 (2003).
8. R. N. Nag, S. Niggl, S. Sousa-Guimaraes, P. Vazquez-Pianzola, B. Suter, Mms19 is a mitotic gene that permits Cdk7 to be fully active as a Cdk-activating kinase. *Development* **145**, dev156802 (2018).
9. S. Ito, L. J. Tan, D. Andoh, T. Narita, M. Seki, Y. Hirano, K. Narita, I. Kuraoka, Y. Hiraoka, K. Tanaka, MMXD, a TFIIH-independent XPD-MMS19 protein complex involved in chromosome segregation. *Mol. Cell* **39**, 632–640 (2010).
10. J. J. DiGiovanna, K. H. Kraemer, Shining a light on xeroderma pigmentosum. *J. Invest. Dermatol.* **132**, 785–796 (2012).
11. A. R. Lehmann, The xeroderma pigmentosum group D (XPD) gene: One gene, two functions, three diseases. *Genes Dev.* **15**, 15–23 (2001).
12. P. H. Itin, A. Sarasin, M. R. Pittelkow, Trichothiodystrophy: Update on the sulfur-deficient brittle hair syndromes. *J. Am. Acad. Dermatol.* **44**, 891–920; quiz 921–894 (2001).
13. S. Faghri, D. Tamura, K. H. Kraemer, J. J. DiGiovanna, Trichothiodystrophy: A systematic review of 112 published cases characterises a wide spectrum of clinical manifestations. *J. Med. Genet.* **45**, 609–621 (2008).
14. J. E. Cleaver, E. T. Lam, I. Revet, Disorders of nucleotide excision repair: The genetic and molecular basis of heterogeneity. *Nat. Rev. Genet.* **10**, 756–768 (2009).
15. B. J. Mann, P. Wadsworth, Kinesin-5 regulation and function in mitosis. *Trends Cell Biol.* **29**, 66–79 (2019).
16. J.-H. Hwang, L. T. Vuong, K.-W. Choi, Crumbs, Galla and Xpd are required for kinesin-5 regulation in mitosis and organ growth in *Drosophila*. *J. Cell Sci.* **133**, jcs246801 (2020).
17. R. A. Pugh, M. Honda, H. Leesley, A. Thomas, Y. Lin, M. J. Nilges, I. K. O. Cann, M. Spies, The iron-containing domain is essential in Rad3 helicases for coupling of ATP hydrolysis to DNA translocation and for targeting the helicase to the single-stranded DNA-double-stranded DNA junction. *J. Biol. Chem.* **283**, 1732–1743 (2008).
18. C. N. Buechner, K. Heil, G. Michels, T. Carell, C. Kisker, I. Tessmer, Strand-specific recognition of DNA damages by XPD provides insights into nucleotide excision repair substrate versatility. *J. Biol. Chem.* **289**, 3613–3624 (2014).

19. A. Blangy, H. A. Lane, P. d'Hérin, M. Harper, M. Kress, E. A. Nigg, Phosphorylation by p34cdc2 regulates spindle association of human Eg5, a kinesin-related motor essential for bipolar spindle formation in vivo. *Cell* **83**, 1159–1169 (1995).
20. K. E. Sawin, T. J. Mitchison, Mutations in the kinesin-like protein Eg5 disrupting localization to the mitotic spindle. *Proc. Natl. Acad. Sci. U.S.A.* **92**, 4289–4293 (1995).
21. J. He, Z. Zhang, M. Ouyang, F. Yang, H. Hao, K. L. Lamb, J. Yang, Y. Yin, W. H. Shen, PTEN regulates Eg5 to control spindle architecture and chromosome congression during mitosis. *Nat. Commun.* **7**, 12355 (2016).
22. J. Rapley, M. Nicolás, A. Groen, L. Regué, M. T. Bertran, C. Caelles, J. Avruch, J. Roig, The NIMA-family kinase Nek6 phosphorylates the kinesin Eg5 at a novel site necessary for mitotic spindle formation. *J. Cell Sci.* **121**, 3912–3921 (2008).
23. S. E. Tsutakawa, A. Bacolla, P. Katsonis, A. Bralić, S. M. Hamdan, O. Lichtarge, J. A. Tainer, C. L. Tsai, Decoding cancer variants of unknown significance for helicase-nuclease-RPA complexes orchestrating DNA repair during transcription and replication. *Front. Mol. Biosci.* **8**, 791792 (2021).
24. S. Akoulitchev, D. Reinberg, The molecular mechanism of mitotic inhibition of TFIID is mediated by phosphorylation of CDK7. *Genes Dev.* **12**, 3541–3550 (1998).
25. F. Coint, J. Aurio, A. Tapias, P. Clivio, W. Vermeulen, J. M. Egly, Phosphorylation of XPB helicase regulates TFIID nucleotide excision repair activity. *EMBO J.* **23**, 4835–4846 (2004).
26. A. A. Vashisht, C. C. Yu, T. Sharma, K. Ro, J. A. Wohlschlegel, The Association of the Xeroderma Pigmentosum Group D DNA Helicase (XPD) with transcription factor IIF is regulated by the cytosolic iron-sulfur cluster assembly pathway. *J. Biol. Chem.* **290**, 14218–14225 (2015).
27. W. Abdulrahman, J. Iltis, L. Radu, C. Braun, A. Maglott-Roth, C. Giraudon, J. M. Egly, A. Poterszman, ARCH domain of XPD, an anchoring platform for CAK that conditions TFIID DNA repair and transcription activities. *Proc. Natl. Acad. Sci. U.S.A.* **110**, E633–E642 (2013).
28. S. Peissert, F. Sauer, D. B. Grabarczyk, C. Braun, G. Sander, A. Poterszman, J. M. Egly, J. Kuper, C. Kisker, In TFIID the Arch domain of XPD is mechanistically essential for transcription and DNA repair. *Nat. Commun.* **11**, 1667 (2020).
29. A. Keriell, A. Stary, A. Sarasin, C. Rochette-Egly, J. M. Egly, XPD mutations prevent TFIID-dependent transactivation by nuclear receptors and phosphorylation of RARα. *Cell* **109**, 125–135 (2002).
30. R. T. Johnson, S. Squires, G. C. Elliott, G. L. Koch, A. J. Rainbow, Xeroderma pigmentosum D-HeLa hybrids with low and high ultraviolet sensitivity associated with normal and diminished DNA repair ability, respectively. *J. Cell Sci.* **76**, 115–133 (1985).
31. S. Schmucker, I. Sumara, Molecular dynamics of PLK1 during mitosis. *Mol. Cell. Oncol.* **1**, e954507 (2014).
32. V. Krenn, A. Musacchio, The Aurora B kinase in chromosome Bi-orientation and spindle checkpoint signaling. *Trends Mol. Med.* **21**, 364–372 (2015).
33. B. Bolognesi, B. Lehner, Reaching the limit. *eLife* **7**, e39804 (2018).
34. A. Musacchio, The molecular biology of spindle assembly checkpoint signaling dynamics. *Curr. Biol.* **25**, R1002–R1018 (2015).
35. M. Kapanidou, S. Lee, V. M. Bolanos-Garcia, BubR1 kinase: Protection against aneuploidy and premature aging. *Trends Mol. Med.* **21**, 364–372 (2015).
36. F. Coint, J. C. Marinoni, C. Rodolfo, S. Fribourg, A. M. Pedrini, J. M. Egly, Mutations in the XPD helicase gene result in XP and TTD phenotypes, preventing interaction between XPD and the p44 subunit of TFIID. *Nat. Genet.* **20**, 184–188 (1998).
37. N. Le May, D. Mota-Fernandes, R. Velez-Cruz, I. Iltis, D. Biard, J. M. Egly, NER factors are recruited to active promoters and facilitate chromatin modification for transcription in the absence of exogenous genotoxic attack. *Mol. Cell* **38**, 54–66 (2010).
38. J. K. Rimel, Z. C. Poss, B. Erickson, Z. L. Maas, C. C. Ebmeier, J. L. Johnson, T. M. Decker, T. M. Yaron, M. J. Bradley, K. B. Hamman, S. Hu, G. Malojcic, J. J. Marneau, P. W. White, M. Brault, L. Tao, P. DeRoy, C. Clavette, S. Nayak, L. J. Damon, I. H. Kalthauer, H. Bunch, L. C. Cantley, M. Geyer, J. Iwasa, R. D. Dowell, D. L. Bentley, W. M. Old, D. J. Taatjes, Selective inhibition of CDK7 reveals high-confidence targets and new models for TFIID function in transcription. *Genes Dev.* **34**, 1452–1473 (2020).
39. J. Soutourina, Transcription regulation by the Mediator complex. *Nat. Rev. Mol. Cell Biol.* **19**, 262–274 (2018).
40. A. Heim, B. Rymarczyk, T. U. Mayer, Regulation of cell division. *Adv. Exp. Med. Biol.* **953**, 83–116 (2017).
41. S. Dubaele, L. P. de Santis, R. J. Bienstock, A. Keriell, M. Stefanini, B. van Houten, J. M. Egly, Basal transcription defect discriminates between xeroderma pigmentosum and trichothiodystrophy in XPD patients. *Mol. Cell* **11**, 1635–1646 (2003).
42. S. Laroche, K. A. Merrick, M. E. Terret, L. Wohlbold, N. M. Barboza, C. Zhang, K. M. Shokat, P. V. Jallepalli, R. P. Fisher, Requirements for Cdk7 in the assembly of Cdk1/cyclin B and activation of Cdk2 revealed by chemical genetics in human cells. *Mol. Cell* **25**, 839–850 (2007).
43. J. Haase, R. Chen, W. M. Parker, M. K. Bonner, L. M. Jenkins, A. E. Kelly, The TFIID complex is required to establish and maintain mitotic chromosome structure. *eLife* **11**, e75475 (2022).
44. M. Fregoso, J. P. Lainé, J. Aguilar-Fuentes, V. Mocquet, E. Reynaud, F. Coint, J. M. Egly, M. Zurita, DNA repair and transcriptional deficiencies caused by mutations in the Drosophila p52 subunit of TFIID generate developmental defects and chromosome fragility. *Mol. Cell. Biol.* **27**, 3640–3650 (2007).
45. G. Cruz-Becerra, S. Valerio-Cabrera, M. Juarez, A. Bucio-Mendez, M. Zurita, TFIID localization is highly dynamic during zygotic genome activation in Drosophila, and its depletion causes catastrophic mitosis. *J. Cell Sci.* **131**, jcs211631 (2018).
46. M. Mendoza, Y. Barral, Co-ordination of cytokinesis with chromosome segregation. *Biochem. Soc. Trans.* **36**, 387–390 (2008).
47. D. Sinha, P. H. G. Duijff, K. K. Khanna, Mitotic slippage: An old tale with a new twist. *Cell Cycle* **18**, 7–15 (2019).
48. R. Dahiya, Q. Hu, P. Ly, Mechanistic origins of diverse genome rearrangements in cancer. *Semin. Cell Dev. Biol.* **123**, 100–109 (2021).
49. L. Ferhat, C. Cook, M. Chauviere, M. Harper, M. Kress, G. E. Lyons, P. W. Baas, Expression of the mitotic motor protein Eg5 in postmitotic neurons: Implications for neuronal development. *J. Neurosci.* **18**, 7822–7835 (1998).
50. K. A. Myers, P. W. Baas, Kinesin-5 regulates the growth of the axon by acting as a brake on its microtubule array. *J. Cell Biol.* **178**, 1081–1091 (2007).
51. P. W. Baas, K. A. Myers, Forces generated by kinesin-5 are a major regulator of microtubule transport and the growth properties of the axon. *J. Neurochem.* **102**, 168–168 (2007).
52. H. Fassihi, M. Sethi, H. Fawcett, J. Wing, N. Chandler, S. Mohammed, E. Craythorne, A. M. Morley, R. Lim, S. Turner, T. Henshaw, I. Garwood, P. Giunti, T. Hedderley, A. Abiona, H. Naik, G. Harrop, D. McGibbon, N. G. Jaspers, E. Botta, T. Nardo, M. Stefanini, A. R. Young, R. P. Sarkany, A. R. Lehmann, Deep phenotyping of 89 xeroderma pigmentosum patients reveals unexpected heterogeneity dependent on the precise molecular defect. *Proc. Natl. Acad. Sci. U.S.A.* **113**, E1236–E1245 (2016).
53. T. Ueda, E. Compe, P. Gatz, K. H. Kraemer, J. M. Egly, Both XPD alleles contribute to the phenotype of compound heterozygote xeroderma pigmentosum patients. *J. Exp. Med.* **206**, 3031–3046 (2009).
54. E. Compe, C. M. Genes, C. Braun, F. Coint, J. M. Egly, TFIIE orchestrates the recruitment of the TFIID kinase module at promoter before release during transcription. *Nat. Commun.* **10**, 2084 (2019).
55. M. Gerard, L. Fischer, V. Moncollin, J. M. Chipoulet, P. Chambon, J. M. Egly, Purification and interaction properties of the human RNA polymerase B(II) general transcription factor BTF2. *J. Biol. Chem.* **266**, 20940–20945 (1991).

Acknowledgments: We thank O. Baspinar, L.-C. Chia, M. Cigrang, and A. Zachary for contributions; N. Troffer-Charlier and I. Kolb-Cheynel for the production of recombinant baculoviruses; B. Morlet and L. Negroni for the mass spectrometry analyses; and D. Orioli, A. Poterszman, and Y. Trotter for fruitful discussions. We also thank the IGBMC cell culture facility. **Funding:** This study was supported by NRF-2014K1A1A2042982 through the National Research Foundation of Korea (funded by the Ministry of Education, Science and Technology, Republic of Korea), ANR TFIID-2021, the Ligue contre le cancer (Equipe Labélisée 2019–2021, 2022–2024), and grants ANR 2022 MITORARE and ANR-10-LABX-0030-INRT (a French State fund managed by the Agence Nationale de la Recherche under the frame program Investissements d'Avenir ANR-10-IDEX-0002-02). E.P. was a recipient of a postdoctoral fellowship from Fondation pour la Recherche Médicale (FRM) and ANR-10-LABX-0030-INRT. C.E. is supported by a PhD fellowship from the "Région Réunion." **Author contributions:** E.C., E.P., N.L.M., J.-H.H., K.-W.C., and J.-M.E. conceived and/or designed the experiments. E.C., E.P., N.L.M., C.B., and C.E. carried out the experiments. E.C., E.P., N.L.M., and J.-M.E. analyzed the data. E.C., F.C., I.S., and K.-W.C. provided expertise, reagents, materials, and/or analysis tools. E.C. and J.-M.E. wrote the paper. **Competing interests:** The authors declare that they have no competing interests. **Data and materials availability:** All data needed to evaluate the conclusions in the paper are present in the manuscript, the Supplementary Materials, and the Source Data file.

Submitted 8 March 2022

Accepted 28 June 2022

Published 17 August 2022

10.1126/sciadv.abp9457

Article 2: Mutations in XPD differently affect transcription, nucleotide excision repair and mitosis.

Introduction

Transcription Factor IIH (TFIIH) is a large protein complex containing ten subunits, which can be resolved into two subcomplexes: the core-TFIIH (including the helicase XPD, the translocase XPB, p62, p53, p44, p34 and p8) and the CAK subcomplex (including MAT1, Cyclin H and the kinase CDK7). Whereas TFIIH has been initially defined as a general transcription factor related to RNA polymerase II (RNAPII), it has been shown that TFIIH is also involved in the Nucleotide Excision Repair (NER) pathway, a DNA repair process implicated in the removal of bulky DNA lesions generated from UV rays ¹. Among the ten subunits of TFIIH, the Xeroderma Pigmentosum group D gene (*XPB*, also called *ERCC2*) encodes an ATP-dependent 5'-3' helicase of 760 amino acids {Sung, 1993 #2129}. During NER, the helicase activity of XPD contributes first to reveal the presence of the backbone distortion originated by a DNA lesion resulting from UV light, and then to open the DNA around the lesion before dual incision². In the course of transcription initiation, while its helicase activity is dispensable, XPD has a structural function by maintaining the interaction between the CAK subcomplex and core-TFIIH^{3,4}.

Intriguingly, the XPD protein is not limited to its presence in TFIIH, as it has been detected in different TFIIH-independent complexes where it plays additional functions. XPD has been found in association with the CAK sub-complex independently of the presence of other TFIIH subunits. {Reardon, 1996 #439}. The binding of XPD to the CAK downregulates the activity of the kinase module, which is involved in mitotic progression by sequentially phosphorylating -via CDK7- key mitotic CDKs such as CDK1, CDK2, CDK4, and CDK6 ⁵. The XPD/CAK partnership is possibly prevented by other factors, such as Mms19 (a part of a complex allowing the correct Fe-S cluster assembly on XPD) as observed in *Drosophila* ^{6,7}. Xpd has also been discovered in early *Drosophila* embryos associated with Crumbs (Crb) and Galla (ortholog of mammalian MIP18) in a CGX complex, which is required for proper chromosome segregation during nuclear division ⁸. In human cells, XPD has been observed partnering with MMS19 and MIP18 in a complex named MMXD (*MMS19-MIP18-XPD*), which possibly contributes to chromosome segregation in mitosis ⁹. Finally, XPD has been very recently identified in mitotic human cells as a partner of Eg5, a motor kinesin protein required for the establishment of a functional bipolar mitotic spindle ¹⁰.

The key role played by XPD is illustrated by the fact that mutations in the *XPB/ERCC2* gene result in different human autosomal recessive disorders, including trichothiodystrophy (TTD) and xeroderma pigmentosum (XP), which is sometimes associated to Cockayne Syndrome (XPCS).

Dry, sparse hair and brittle nails characterize TTD, but several other manifestations occur in TTD, including mental retardation, ichthyotic skin, reduced stature, and hypogonadism ^{11,12}. While the principal hallmark of XP is photosensitivity and numerous skin abnormalities (ranging from excessive freckling to skin cancer predisposition), XP patients can also develop progressive neurological degeneration¹³. When XP is combined with Cockayne Syndrome (XPCS), patients develop in addition to XP phenotypes severe dwarfism, mental retardation as well as skeletal and dental abnormalities ¹⁴.

Having observed that XPD mutations affect NER ^{3,4}, the XPD-associated diseases were historically considered as DNA repair disorders ^{15,16}. However, the diversity of XPD functions as well as the heterogeneity of the phenotypes observed in XP-D patients suggest that cellular processes other than DNA repair might be affected. Previous studies already revealed that transcription might be disrupted in fibroblasts isolated from patients ^{17,18,19}. Furthermore, recent observations suggested that XPD mutations related to XP might affect mitosis ^{9,10}.

To date, no systematic study has been undertaken to compare the consequences of diverse XPD mutations on various cellular processes. This was made difficult by the fact that the used cellular models are required to transcribe actively, to repair DNA efficiently and to divide regularly. However, the cells commonly isolated from patients (either fibroblasts or lymphoblasts) and carrying distinct XPD mutations divide little and have low transcriptional activity, making it difficult to simultaneously study NER, transcription and mitosis. Furthermore, comparing patient cells to each other is challenging due to the significant genomic heterogeneity among them. In addition, the fact that most of the patients are compound heterozygotes adds to the difficulties of understanding the consequences of each XPD mutation ²⁰. Therefore, new cell lines with the same genetic background but carrying different XPD mutations have been generated by using the CRISPR/Cas9 genome editing method. Several mutations have been selected on the basis of their position and their impact on protein activity. Among the selected mutations, limited homozygous cells have been generated while others are still in progress. In particular, we were able to generate homozygous cells with endogenous GFP-tagged XPD protein bearing the XPD/G47R substitution, a mutation mostly found in compound heterozygous XP and XPCS patients ^{21,22,23}. Of note, only one homozygous patient with this variant has been reported to develop cerebro-oculo-facio-skeletal syndrome (COFS) ²⁴. Located in the Walker A motif for ATP binding, the XPD/G47R mutation disrupts ATP hydrolysis, which in consequence alters the helicase activity of XPD and thus NER

⁴. It is worthwhile to notice that biochemical analyses also suggested that XPD/G47R mutation might not alter transcription initiation ⁴. In addition, we also generated homozygous cells with endogenous GFP-tagged XPD bearing the synthetic XPD/K48R substitution, a mutation also located in the Walker A motif for ATP binding ²⁵. Whereas the XPD/K48R mutation is not found in patients, different biochemical studies showed that this mutation abrogates the ATPase and consequently the helicase activity of XPD, without affecting the structure of the protein and the viability in *Saccharomyces cerevisiae* ^{26,27}. *Further experiments also showed that during transcription initiation, TFIIH containing XPD/K48R supports promoter escape but less actively than the wild-type form* ^{28, 29} We also successfully generated homozygous cells with endogenous GFP-tagged XPD bearing the XPD/G602D substitution, which is found in compound heterozygous XP and XPCS patients ^{30, 31, 32}. This mutation targets a mobile region of helicase motif V that is implicated in both ATP and ssDNA binding ³³. As a consequence, this mutation strongly affects the helicase activity of XPD and NER ^{4,33}. On the contrary, basal transcription seems not to be affected by XPD/G602D ⁴.

Taking advantage of these new cellular models, we initiated a systematic study to compare the consequences of the mutations XPD/G47R, /K48R and /G602D on NER, mitosis and transcription. Our results show that these processes are differently disrupted according to the nature of the XPD mutation, which might contribute to explain the phenotypic diversity associated with each of these mutations.

Results

Homozygous human osteosarcoma U-2OS knock-in (KI) cell line was initially generated by CRISPR/Cas9-mediated genome editing to express an endogenous fluorescent GFP-tagged version of XPD (see Methods). Similar genome editing strategy was employed to insert XPD mutations, especially the recessive mutation c.139G>C [p.Gly47Arg] (in exon 3 and found in XP and XPCS patients) ²¹⁻²⁴, the synthetic mutation c.142A>C;143A>G; 144G>C [p.Lys48Arg] (located in exon 3 that abrogates ATPase activity and could therefore be considered as a control) ^{26,27} and c.1805G>A;1806C>T [p.Gly602Asp] (in exon 19 and found in XP and XPCS patients) ³⁰⁻³² (Figure 1A).

After sequencing analysis to select homozygous clones with the corresponding expected gene editing (Figure 1B), Western Blots showed that the level of GFP-tagged XPD/G47R (Figure 1C,

lanes 3-4), /K48R (lane 5-6) and /G602D (lane 7-8) proteins was slightly reduced when compared to that observed for XPD-GFP/WT; no reduction was observed for other TFIIH subunits (i.e. XPB, p52, MAT1). Immunofluorescence analysis next revealed that most of the GFP signal was located within the nucleus (Figure 1D), suggesting that the C-terminally tagged XPD-GFP/WT (image D.2), /G47R (image D.4), /K48R (image D.6) and /G602D (image D.8) proteins are correctly exported into the nucleus {Santagati, 2001 #171}. In addition, the different GFP-tagged proteins (Figure 1E) coimmunoprecipitated with other subunits of TFIIH (e.g. XPB and Cyclin H), suggesting that the tagged XPD proteins were properly internalized within the TFIIH complex.

Fluorescence Recovery After Photobleaching (FRAP) experiments were next performed to evaluate the dynamic mobility of the different GFP-tagged XPD proteins (Figure 1F). Knowing that incomplete fluorescence recovery indicates immobilization of the fluorescently-tagged XPD protein to the chromatin {Vermeulen, 2011 #7540}, we observed that the immobile fraction of either XPD/G47R ($13.8 \pm 5.0\%$), /K48R ($14.5 \pm 3.9\%$) and /G602D ($13.3 \pm 5.5\%$) was similar to that observed for the WT form ($13.1 \pm 4.1\%$), suggesting that the different mutations do not affect the mobility of XPD in basal conditions.

XPD mutations similarly alter DNA repair.

Since XPD is intimately implicated in NER ¹, further experiments were next undertaken to study in more details the properties of the mutated XPD-GFP proteins after irradiation. Using live-cell imaging after femtosecond laser micro-irradiation (see Methods), we first analyzed the dynamic properties of the GFP-tagged XPD proteins by measuring their real-time accumulation at local DNA damages (LDD) {Schmalz, 2023 #9879}. Three-photon-mediated photoproducts generation promoted the rapid relocation to the irradiated area of the XPD-GFP/WT (Figure 2A, the calculated area under curve -AUC- was 220.7 ± 3.3). On the contrary, a lower accumulation at LDD was observed for XPD-GFP/K47R (AUC of 158.3 ± 3.4) XPD-GFP/K48R (AUC of 139 ± 4.0) and /G602D (AUC of 118 ± 3.5).

Cells were next subjected to local UV-C irradiation and the localization of XPD-GFP was analysed by immunofluorescence (Figure 2B). We first observed that enhanced fluorescence signal of XPD-GFP/WT emerged in spots of damage (visualized by using antibodies recognizing cyclobutane pyrimidine dimers -CPDs- lesions) within 30 min following local UV-C irradiation (Figure 2B, image B.6). On the contrary, a very low signal was observed at local damages for the

different XPD mutated proteins (image B.15, B-24 and B.33 for XPD/G47R, /K48R and /G602D, respectively). In addition, while the fluorescent signals of XPD-GFP/WT was reduced two hours post-UV-C irradiation (image B.9), a slight signal for XPD/G47R (image B.18), /K48R (image B.27) and /G602D (image B.36) persisted at local damages.

Immunofluorescence-based quantification of CPDs was next performed in the nucleus of XPD mutated cells at different times post UV-C irradiation (Figure 2C) ³⁴. While repair of CPD lesions progressively occurred in XPD-GFP/WT cells, our results showed that the different XPD mutated cells failed to correctly repair CPDs even after 48 hours post UV-C irradiation (Figure 2C). In parallel, immunofluorescence analyses also revealed that XPD mutated cells had a lower ability to repair pyrimidine-pyrimidone (6-4) photoproducts (6-4PPs) (Figure 2D). Finally, we observed that XPD mutant cell lines exhibited reduced viability upon UV-C irradiation compared to WT cells (Figure 2E). This highlights the deleterious effect of the different XPD mutations on the ability of mutant cells to properly repair UV-induced DNA damage.

Figure 1

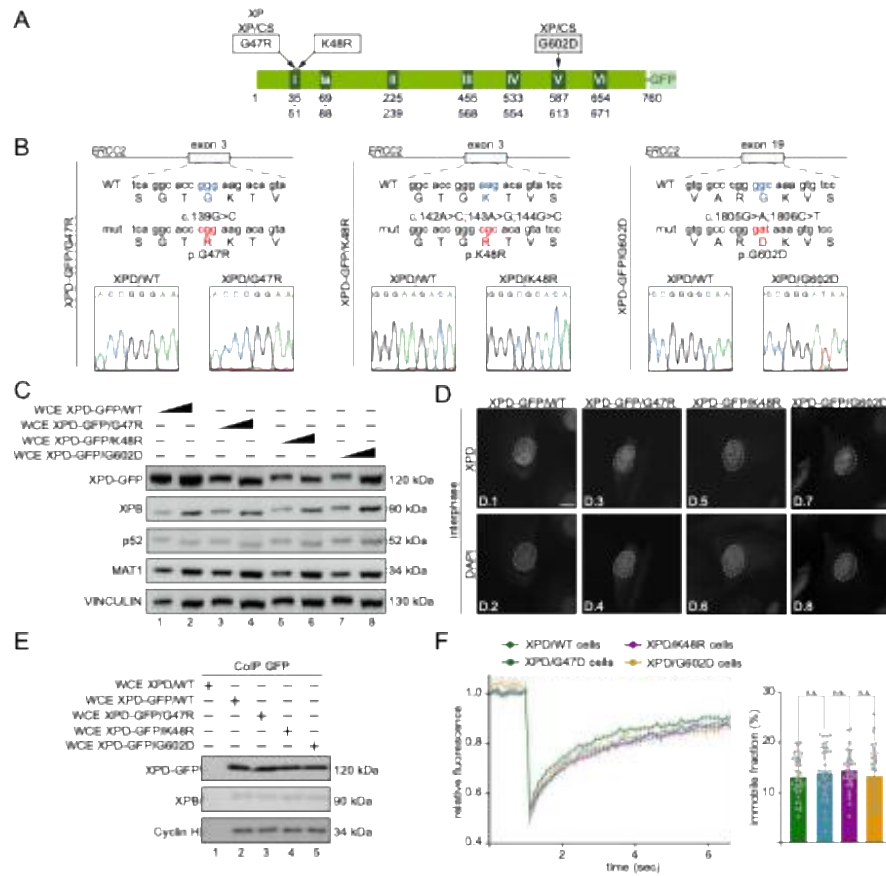


Figure 1 – characterization of new XPD mutated cell models

(A) Diagram of the human GFP-tagged 760-aa XPD protein with the 7 (I–VI) helicase motifs. Amino acid changes resulting from either artificial (XPD/K48R) or mutations found in XP and XP/CS patients (XPD/G47R and /G602D) are depicted. The GFP tag located at the C terminal part of XPD is indicated.

(B) Schematic representation of the *ERCC2* gene encoding XPD and localization of the mutations (c.139G>C [p.Gly47Arg]) and (c.142A>C;143A>G; 144G>C [p.Lys48Arg]) in exon 3 as well as of the mutation (c.1805G>A;1806C>T [p.Gly602Asp]) in exon 19 generated with CRISPR/Cas9 methodology. Sequencing analysis confirmed full allelic targeting of the *ERCC2* locus in U-2 OS clones designed as either XPD/G47R, /K48R or /G602D; non-mutated cells (XPD/WT) have been used as control.

(C) Western blot analyses of XPD in whole-cell extracts (WCE) isolated from U-2OS cells expressing endogenous GFP tagged XPD/WT, /G47R, /K48R and /G602D cells. Vinculin was used as loading control. The results are representative of two independent experiments.

(D) Immunolocalization of XPD in the nucleus during interphase. Fixed cells were also stained with DAPI to visualize DNA by fluorescence microscopy. Scale bar, 10µm.

(E) CoImmunoprecipitation (CoIP) assays were performed from whole cell extracts with Ab-GFP cross-linked on magnetic beads, resolved by SDS-PAGE, and blotted with antibodies against XPD, XPB and cyclin H. The results are representative of two independent experiments.

(F) FRAP analysis of XPD-GFP mobility in XPD/WT, /G47R, /K48R and G602D U-2 OS cells (n=19 for each cell line). XPD-GFP fluorescence was background-corrected and normalized to average pre-bleach values, which were set at 1. The graph shows the calculated immobile fractions for each condition. n.s., not statistically significant (Student's *t* test).

Figure 2

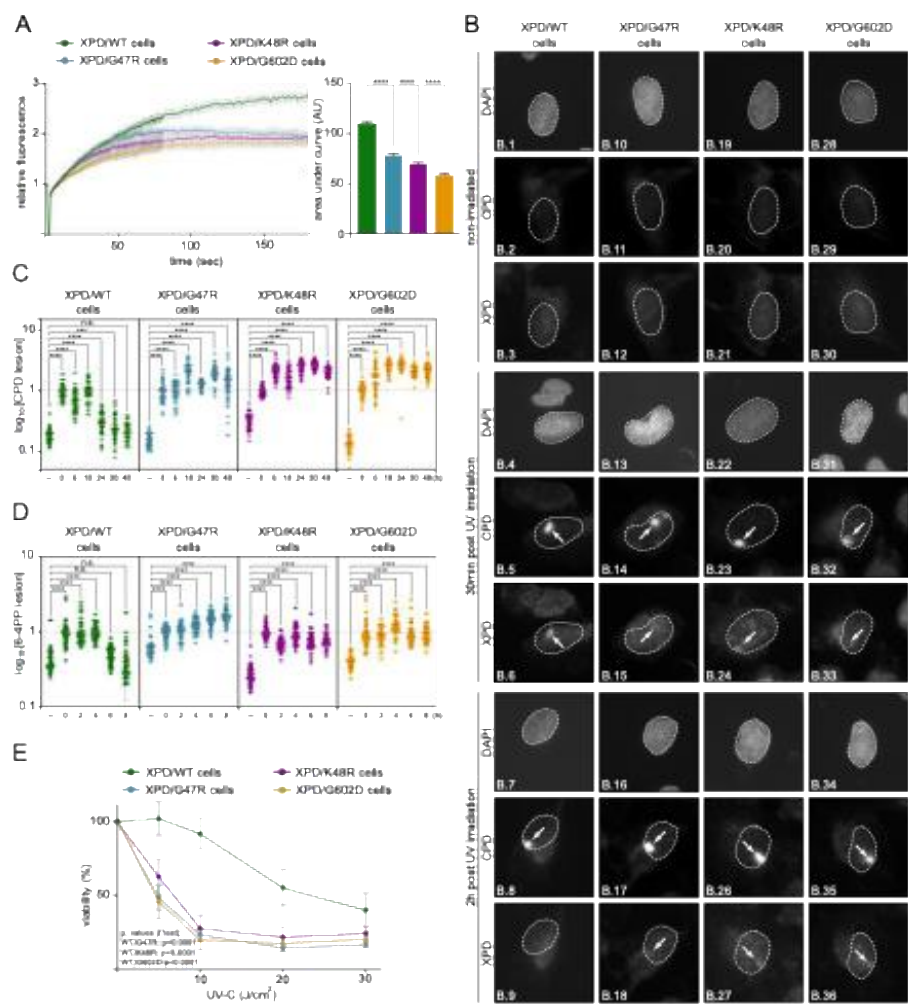


Figure 2

(A) Relative accumulation at local DNA damage (LDD) of endogenously expressed GFP-tagged XPD/WT, /G47R, K48R and /G602D during the first 180 seconds post laser irradiation. GFP fluorescence intensity at the LDD was measured over time using live-cell confocal imaging and normalized to the pre-damage intensity (set to 1). The curves represent the average relative intensity of 20 cells (mean \pm SEM). The graph shows the Area Under the Curve (AUC), which was measured between 1 and the shelf on the curve. **** $P < 0.0001$, Student test.

(B) Representative images of XPD/WT (pictures A1-9), /G47R (pictures A10-18), /K48R (pictures A19-27) and /G602D (pictures A28-36) cells before and 30 minutes and 2h after local UV-C irradiation (15 J/m²). CPD and GFP were localized by using specific antibodies. Scale bar: 10 μ m

(C-D) XPD-GFP/WT (green), /G47R (blue), /K48R (violet) and /G602D (orange) cells were labeled with anti-6-4PP (C) or anti-CPD (D) antibodies and signals were quantified using Fiji at the different times (in hours, h) indicated in the panels. Graph represents the number of lesions remaining in the genome at different time points normalized to the measure performed immediately after UV irradiation (as a value of 1; logarithmic scale). The means (red bars \pm s.d.) for each time point were obtained from 50 cells (*** $P < 0.001$, **** $P < 0.0001$, Student *t* test; n.s., not significant). Source data are provided as a Source Data file.

(E) Viability of XPD/WT (green), /G47R (blue), /K48R (violet) and /G602D (orange) cells was determined 48 hours after irradiation with different UV-C doses. Data were normalized to unexposed cells (means \pm SD of three independent experiments performed in triplicates; significant statistical difference $P < 0.0001$, Student's *t* test, between XPD/WT and the different mutated lineages).

XPD mutations differently alter chromosome segregation.

Knowing that XPD participates in chromosome segregation during mitosis^{9,10}, we next analysed the consequences of XPD mutations in this process. Confocal microscopy analysis was first performed to detail the dynamic changes of XPD localization during mitotic progression (Figure 3A)¹⁰. While XPD-GFP/WT was mostly located within the nucleus in interphase (Figure 1D) and in prophase (Figure 3A, pictures A.1-2), it was excluded from the chromosomes and randomly diffused around them with an enrichment at the mitotic spindle during metaphase (pictures A.3-4). XPD-GFP/WT localization was next enriched at the midzone during anaphase (pictures A.5-6), which was followed by its enrichment at the midbody in telophase (pictures A.7-8). Strikingly, the localization during mitosis of mutated XPD-GFP/G47R (pictures A.9-16), /K48R (pictures A.17-24) and /G602D (pictures A.25-32) did not notably differ from what had been visualized in XPD-GFP/WT cells. However, and contrary to that observed in XPD-GFP/WT, /G47R and K48R cells, XPD-GFP/G602D cells displayed mitotic defects, especially misaligned chromosomes at anaphase (picture A.30). The total number of XPD-GFP/G602D cells with abnormal mitotic phenotypes was indeed slightly but significantly increased ($15 \pm 2\%$) relative to XPD/WT cells ($95 \pm 2\%$) (Figure 3B).

To further determine whether the chromosome segregation errors observed in XPD-GFP/G602D might result from mitotic premature exit, as previously observed in XPD/R683W mutated cells¹⁰, cells were synchronized in prometaphase with nocodazole (16 hours, 100 ng/ml), washed out, and collected at different time points. Western blot analysis first showed that the level of mitotic markers, such as Polo-like kinase 1 (Plk1), a protein kinase essential to control mitotic division³⁵ and CCNB1 (G2/mitotic-specific cyclin-B1, a key regulatory protein associated to CDK1 that is essential to chromosome condensation and spindle pole assembly checkpoint)³⁶ promptly increased at t0 to then progressively decreased post-release in a similar way in WT and the different XPD-mutant cell lines (Figure 3C). In parallel, the level of the motor kinesin Eg5 (a mitotic partner of XPD required for establishing the bipolar spindle)^{10,37,38} similarly accumulated in the different XPD cell lines at t0 and slightly decreased during the time course. In addition, we observed that the prometaphase-arrested XPD/WT, /G47R, /K48R and /G602D cells similarly progressed through mitosis 30, 60 and 90 min after nocodazole release (Figure 3D), suggesting that the XPD-GFP/G47R, /K48R and /G602D do not exit mitosis prematurely, contrary to other XPD mutated cells such as XPD/R683W cells¹⁰.

We then checked whether the Spindle Assembly Checkpoint (SAC) occurs correctly in the XPD-GFP/G602D mutated cells, knowing that SAC controls the proper segregation of chromosomes during mitosis³⁹. Cells were treated with Taxol, a chemical compound that stabilizes microtubules and consequently blocks metaphase to anaphase transition by actively maintaining the SAC process (Figure 3E). This treatment induced a prolonged and similar mitotic arrest in XPD-GFP/WT, /G47R, /K48R and /G602D cells, revealing no premature exit from the mitotic arrest. All together, these results show that chromosome segregation is defective in cells carrying the XPD/G602D mutation, as previously suggested in patient fibroblasts⁹. However, this defective chromosome segregation does not result from SAC alteration, contrary to what was observed in XPD/R683W cells¹⁰ suggesting that mitosis might be differently altered depending on the nature of the selected XPD mutation.

Figure 3

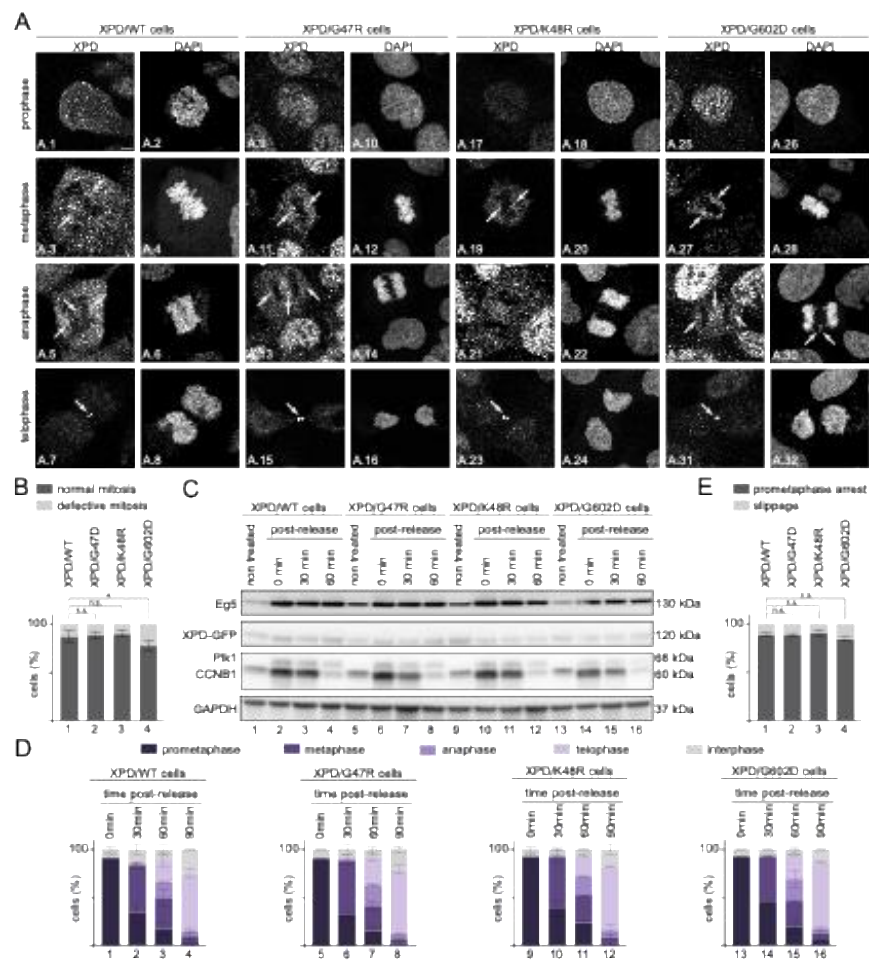


Figure 3

(A) Immunofluorescence analysis of XPD during different mitotic phases. GFP-tagged XPD/WT, /G47R, /K48R and /G602D cells were synchronized by double thymidine block and collected 9 hours after release, and analyzed by confocal microscopy at prophase, metaphase, anaphase, and telophase. The marked localizations of XPD at the mitotic spindle, the midzone, and at the midbody are indicated by arrows. Images were acquired with the same microscopy system and constant parameters. Scale bar, 5 μ m.

(B) Percentage of GFP-tagged XPD/WT, /G47R, /K48R and /G602D cells displaying either a normal or a defective mitotic phenotype ($n=3$, means \pm SD; at least 200 at 500 cells for each cell line were analyzed; $*P < 0.05$, Student's t test; n.s., not statistically significant).

(C) Western blot analysis of Eg5, XPD-GFP, Plk1, CCNB1 in XPD/WT, /G47R, /K48R and /G602D-mutated cells that were either non-treated or synchronized with nocodazole, released and collected at 0, 30 and 60 minutes. GAPDH was used as loading control.

(D) GFP-tagged XPD/WT, /G47R, /K48R and /G602D cells were synchronized with nocodazole, released, harvested 0, 30, 60 and 90 minutes after release, mounted and stained with DAPI. The percentage (%) of cells in different mitotic phases was quantified at the indicated time points after nocodazole release ($n= 2$, means \pm SD; at least 700 to 1100 cells were analyzed per cell line and per experiment).

(E) Percentage of GFP-tagged XPD/WT, /G47R, /K48R and /G602D cells arrested in prolonged prometaphase or exited mitosis upon Taxol treatment (16 hours, 1 μ M) ($n = 3$, means \pm SEM; at least 200 at 250 cells for each lineage were counted; n.s., not statistically significant, *, $P<0.05$, Student's t test).

XPB mutations disrupt transcription of protein coding genes.

To investigate the transcriptional impact of XPB mutations, we first analysed the ability of the XPB mutated cells to incorporate alkyne-modified uridine analog *5-ethynyl uridine* (EU) into newly transcribed RNAs (Figure 4A). While the EU labelling was similar in XPB-GFP/WT and /G47R, a lower incorporation was observed in XPB/K48R and /G602D when compared to that found in XPB/WT cells, suggesting defective RNA synthesis in these XPB mutated cells.

In order to further investigate the transcriptional effects of XPB mutations, we conducted gene expression profiling by RNA-sequencing (RNA-seq) analysis. Compared to XPB-GFP/WT cells, we observed significantly dysregulated genes in all 3 mutant cell types (Figure 4B). Unexpectedly however, the number of dysregulated genes strongly varied between them. Indeed, while the number of dysregulated genes was relatively low in XPB-GFP/G47R cells (Figure 4C, left volcano plot), a much higher number of dysregulated genes was observed in XPB-GFP/K48R and /G602D cells. Compared to what was observed in XPB-GFP/WT cells, 26, 346 and 258 genes were over-expressed in XPB-GFP/G47R, /K48R and /G602D cells, respectively (Figure 4C). Strikingly, whereas only 67 genes showed a significantly lower expression in XPB-GFP/G47R cells, 464 and 972 genes were under-expressed in XPB-GFP/K48R and /G602D cells, respectively (Figure 4C).

Giving the surprisingly strong impact on gene expression of XPB mutations, especially in XPB/K48R and XPB/G602D cells, we undertook a comparative analysis of the dysregulated genes and observed significant overlaps (Figure 4D). In particular, over two thirds of genes under-expressed in XPB-GFP/G47R and /K48R cells were also under-expressed in XPB-GFP/G602D cells (left Venn diagram). Hypergeometric distribution and representation factor tests strongly suggested that these overlaps were not due to coincidence but rather pointed at a common mechanism behind these major transcriptional effects. These observations prompted us to further analyse the nature of the dysregulated genes and to identify the biological and molecular processes that might be impacted in the XPB mutated cells. However, Gene Ontology (GO) analysis of dysregulated genes shared by at least two mutants showed only very slight enrichments of different biological processes (Figure 4E). The relatively high false discovery rate (FDR) values suggested that the gene function was not the determinant of dysregulation by XPB mutations. Interestingly, and contrary to what was observed for the genes commonly over-expressed in the different XPB mutated cells, we observed that commonly under-expressed genes were significantly enriched in longer genes (Figure 4F), suggesting that transcriptional elongation might be affected.

Previous works unveiled that TFIIH mutations might affect the transactivation mediated by nuclear receptors, a class of DNA-binding transcription factors responsible for sensing hormones and their metabolites and regulating specific target genes⁴⁰. In particular, it has been observed that upon retinoic acid (RA) treatment, the expression of Retinoic Acid Receptors (RAR) target genes such as *RARB2* expression was affected in XPD mutated cells^{17,19}. Rather than focusing only on *RARB2* gene expression, high throughput RNA sequencing analysis was performed to determine the global impact of XPD mutations on the expression of RAR-target genes. After RA treatment (6h, 1 μ M), we observed that the number of repressed and induced genes differed between the various cell lines (Figure 5A and 5B). We observed an induction (Adj. p-val < 0.05 and FC > 2) of roughly 300-400 genes in all four cell types (Figure 5A and 5B). Notably however, many of the 383 upregulated genes in XPD-GFP/WT cells were found to be less induced (and in a few cases not induced at all) in the XPD mutant cells (Figure 5D). This was especially clear in the XPD-GFP/K48R and /G602D cells, where roughly 60 out of the 383 upregulated genes by RA in XPD-GFP/WT cells displayed a lesser induction (Figure 5D). Interestingly, we also observed that 172 genes were commonly induced in the different cell lines after RA treatment (Figure 5C). However, whereas the level of upregulation of these 172 common RA-target genes was similar in XPD-GFP/WT and /G47R, a weaker induction of many of these genes was observed in the XPD-GFP/K48R and /G602D cells (Figure 5E). This observation prompted us to compare, among the 172 common upregulated RA-target genes, the ones with weaker induction post RA treatment (\log_2 (FC) < -0.5 as threshold) in XPD-mutated cells versus XPD-GFP/WT cells (Figure 5F-G). There was significant overlap in the weaker induced genes between the different XPD mutant cells (Figure 5F). Strikingly, an enrichment of genes encoding long mRNA was observed among the less induced genes (Figure 5G). Collectively, these data showcase the systematic gene expression defects related to XPD mutations (especially XPD/K48R and G602D) and point towards a potential transcriptional elongation deficiency.

Figure 4

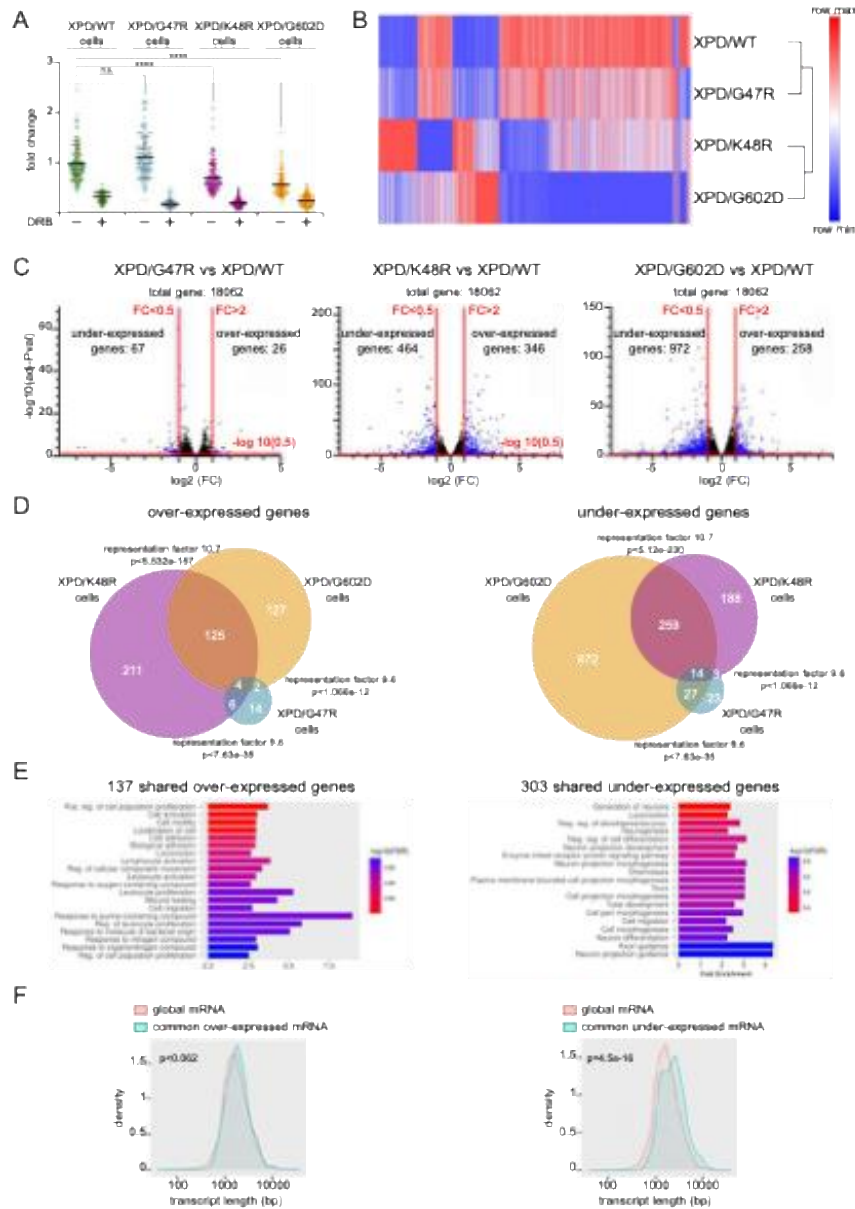


Figure 4

(A) To follow transcription mediated by RNAPII, RNAs were labelled by 5EU incorporation. Transcription block of RNAPII was simultaneously achieved by treatment with actinomycin D. As control, cells were treated with 5,6-dichloro-1-beta-D-ribofuranosylbenzimidazole (DRB) for 24 hours to block transcription by RNAPII (****, $P < 0.0001$, Student's t test).

(B) Heatmap depicting all significantly dysregulated genes in the XPD-mutated cell lines compared to XPD-GFP/WT cells, determined by RNA-Seq. Dysregulated genes were defined as $\log_2(\text{Fold change, FC}) > 1$ or < -1 and adjusted P-value < 0.05 . Values represented as $\log_2(\text{FC})$ with relative color schemes.

(C) Volcano plots showing the number of either under- or over-expressed genes in the XPD-mutated cells when compared to XPD-GFP/WT cells.

(D) Venn diagram comparing significantly over-expressed (left panel) or under-expressed (right panel) coding genes in XPD-mutant cell lines. Representation factor and hypergeometric p-values are represented.

(E) Gene Ontology (GO) analysis of the over- (left panel) or lower- (right panel) expressed genes shared by at least two XPD-mutant cell lines, as identified in (D). The histogram shows the top dysregulated biological processes according to the FDR and fold enrichment.

(F) Transcript length analysis of over- (left panel) and under- (right panel) expressed genes shared by at least 2 mutants compared with all other genes in the genome. P-value is indicated.

Figure 5

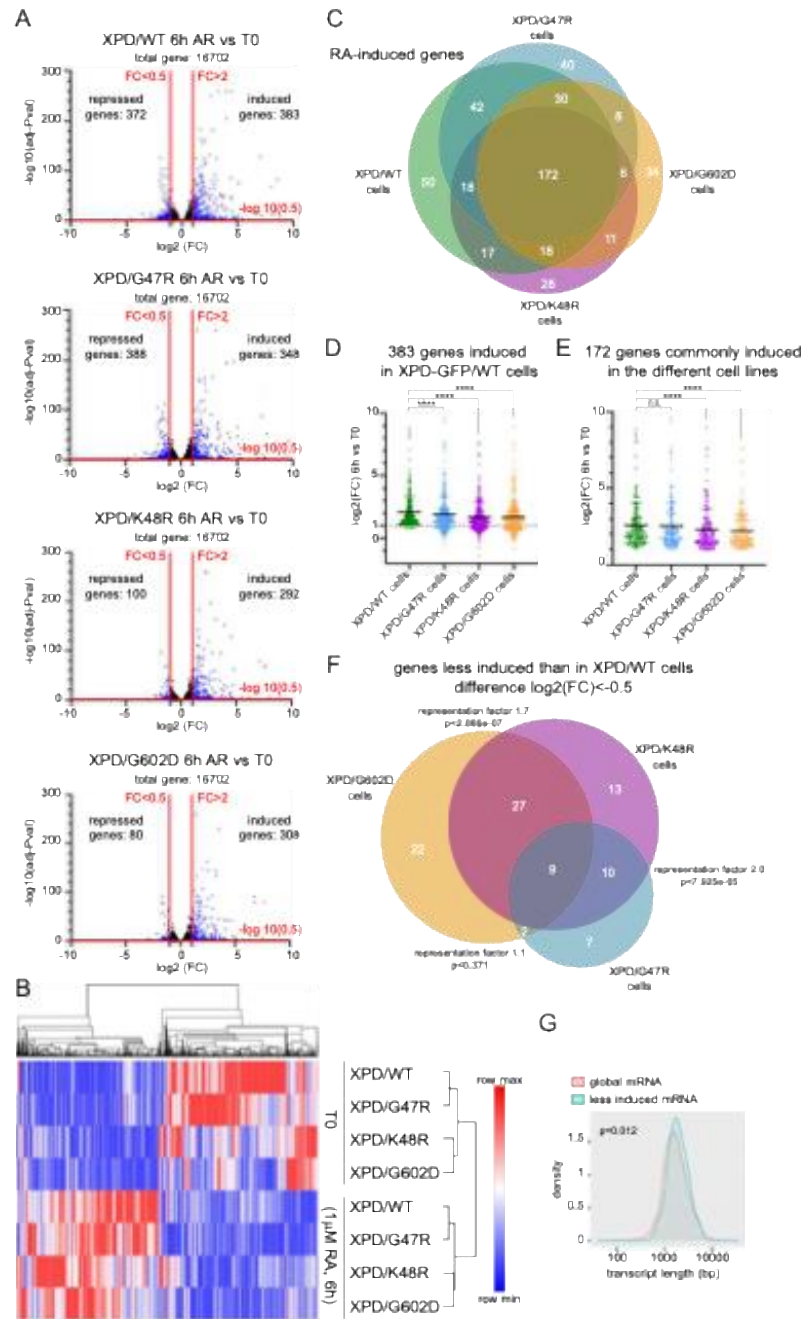


Figure 5

(A) Volcano plots determined by RNA-Seq showing the level of genes expression upon RA treatment (6h, 1 μ M) in the different cells. Dysregulated genes were defined as $\log_2(\text{Fold change FC}) > 1$ or < -1 and adjusted P-value < 0.05 .

(B) Heatmap depicting all significantly dysregulated genes after RA treatment in the different cell lines. Values represented as $\log_2(\text{FC})$ with relative color schemes.

(C) Venn diagram comparing significantly upregulated genes by RA treatment in indicated cells.

(D) Scatter plot depicting relative expression levels of the 383 genes upregulated by RA treatment in the different XPD-GFP cell lines. Error bars indicate mean values + SD. Two-way ANOVA test was used to determine the p-values (vs. XPD-GFP/WT; **** $P < 0.0001$).

(E) Scatter plot depicting relative expression levels in the indicated cell lines of the 172 genes commonly upregulated after RA treatment, as identified in (C). Error bars indicate mean values + SD. Two-way ANOVA test was used to determine the p-values (vs. XPD-GFP/WT; **** $P < 0.0001$).

(F) Venn diagram comparing genes with weaker induction post RA treatment in either XPD-mutated cells than in XPD-GFP/WT cells (Difference in $\log_2(\text{FC}) < -0.5$). Representation factor and hypergeometric p-values are represented.

(G) Transcript length analysis of genes with weaker induction after RA treatment in either XPD-mutant cell line than in XPD-GFP/WT cells. P-value is indicated.

Discussion

The present study aims to dissect in a cellular context the impact of XPD mutations in DNA repair, mitosis and transcription. While the studied mutations similarly affect NER, they differently disrupt mitosis and transcription, highlighting the fact that the heterogeneity of the clinical features associated to XPD mutations can result from heterogenous alterations in different cellular processes.

Mutations in the TFIIH complex, especially in its subunits p8/TTDA, XPB and XPD, are related to different autosomal recessive disorders, including XP, XPCS and TTD ¹. While only few mutations have been identified in p8/TTDA (mutations that are only related to TTD) and XPB (mutations related to either XP, XPCS or TTD), more than 70 distinct protein alterations (associated to either XP, XPCS or TTD) have been identified in ERCC2/XPD ³². The vast majority of the mutations found within XPD are clustered in the C-terminal third of the protein and no specific disease-related domains can be highlighted, as adjacent mutations can result in distinct phenotypes. In addition, most of the XP-D patients are compound heterozygotes with a combination of different alterations on both ERCC2/XPD alleles. In this context, it is relatively difficult to apprehend the impact of each mutation and putative biallelic effects might be difficult to distinguish from the influence of the genetic background. Consequently, a large program has been initiated (in collaboration with the TACGENE platform of the French National Museum of Natural History) to produce new cellular tools with the same cellular background (U-2OS) by using CRISPR/Cas9-mediated gene editing strategy. To date, different XPD mutated cell lines are already available. This is particularly the case for the cellular models presented here that harbour either the point mutation XPD/G47R, /K48R or /G602D (Figure 1A). It is worth noting that other mutations were initially selected on the basis of their position and effect on XPD activity. This was particularly the case of the point mutation XPD/R683W, which is found in homozygous and compound heterozygous XP patients ^{20,41}. Extensively studied at a biochemical level, the XPD/R683W mutation is known to destabilize the partnership between XPD and its catalytic p44 subunit, which disrupts the integrity of TFIIH and affects the enzymatic activity of XPD ^{4,17}. While we successfully generated cells bearing either the G47R, K48R or G602D point mutations on both XPD/ERCC2 alleles, it has been however unrealizable to generate homozygous cells with the XPD/R683W mutation. Of note, our genome editing strategy has been controlled several times and we obtained many clones harboring the R683W substitution on one allele and the wild-type form

on the second *ERCC2/XPD* allele. Although poorly understood, the lack of viability of XPD/R683W homozygous clones could be linked to the nature of the cells used (i.e. osteosarcoma U-2OS cells). Other experiments are currently being developed using retinal pigment epithelial hRPE-1 cells, which is a non-cancerous cell-type that can be an alternative to the U-2OS cancer cell line for CRISPR/Cas9 genome editing strategy.

During the characterization of the different XPD mutated cell lines, a slight reduction of the amount of the XPD/G47R, /K48R and /G602D mutated proteins has been observed (Figure 1C). This reduction was not accompanied by a lower amount of other TFIIH subunits, and the integrity of the TFIIH complex was preserved (Figure 1E). Interestingly, a slight reduction of the amount of TFIIH subunits was previously observed in fibroblasts isolated from compound heterozygous patients bearing either the XPD/G47R or /G602D mutation {Botta, 2002 #104}. However, the reduction of TFIIH subunits in XPD/G47R and /G602D fibroblasts was much less pronounced to that observed in cells bearing XPD mutations related to TTD {Botta, 2002 #104}. Here, we cannot exclude that the slight reduction of XPD-GFP/G47R, /K48R and /G602D might contribute to the lower accumulation of the fluorescent signal at local DNA damages just after laser micro irradiation (Figure 2A). The slight reduction cannot however explain the inability of XPD mutated cells to fully repair UV-induced lesions several hours after irradiation (Figures 2C-D), which might be due to defects in NER activity. Previous observations showed that the XPD/G47R mutation affects the ATPase activity of XPD, which in turn disrupts its helicase activity and consequently DNA opening around the lesion ⁴. Similarly, ATP hydrolysis is abrogated by the XPD/K48R mutation, which in turn affects the repair of UV lesions ²⁵ (Figures 2C-D). For its part, the XPD/G602D mutation directly disrupts the helicase activity of XPD and thus NER ⁴. It is therefore not surprising to find that NER is deeply affected in the different cell lines (Figures 2C-D). What is more interesting is that our results suggest that XPD/G47R, /K48R and /G602D equally affect NER, leading to the same level of viability of the different XPD mutated cells after increasing UV-C doses (Figure 2E). While our results clearly illustrate the fact that NER is deeply disrupted in the different cell lines, it would nevertheless be interesting to carry out other experiments to better characterize NER defects in these cellular models. FRAP approaches will allow us to assess the level of immobilization of the different XPD mutated forms after UV-C irradiation. Our immunofluorescence assays 2h post local UV-C irradiation (which need to be repeated to better visualize the accumulation of XPD at CDP lesions), suggested that XPD-GFP/G47R, /K48R and

/G602D persisted at local DNA damages (Figure 2B, pictures B.18, B.27 and B.36, respectively). FRAP analyses will thus allow us to measure the immobilization of the XPD-GFP mutated forms at different times post UV-C irradiation. Interestingly, it has been recently suggested that prolonged binding of TFIIH to DNA damage might correlate with disease severity ⁴². It would be therefore interesting to determine how the different XPD mutated forms persist at local DNA lesions.

Contrary to NER, mitosis seems to be differently affected by XPD mutations. Indeed, while no clear mitotic abnormalities have been observed in XPD-GFP/G47R and /K48R cells, we measured a higher number of abnormal mitotic phenotypes (including lagging and misaligned chromosomes) in XPD-GFP/G602D cells (Figure 3B). Of note, abnormal mitotic spindle formation has been previously observed in compound heterozygous fibroblasts bearing the XPD/G602D mutation as well as in XPD/R683W mutated cells ^{9,10}. Interestingly, it has been shown that defective mitotic progression in XPD/R683W mutated cells might partially result from deficient activation of the spindle assembly checkpoint (SAC) ¹⁰, a mechanism that contributes to coordinate mitotic progression by controlling the state of chromosome attachment to the mitotic spindle ³⁹. However, we did not observe similar SAC alterations in XPD/G602D mutated cells (Figure 3E), suggesting that the SAC might be differently affected according to the nature of the XPD mutation. Previous observations also showed that mitotic progression is affected in XPD/R683W mutated cells ¹⁰. However, the XPD/G47R, /K48R and /G602D cells did not show mitotic premature exit (Figures 3C-D). Taking together, the results already obtained suggest that mitosis might be differently affected according to the nature of the XPD mutation. Although we cannot exclude that mitotic alterations observed in XPD/G602D cells might be the consequences of defects in other cellular mechanisms, further investigations should be performed to better determine the impact the XPD/G602D substitution in mitosis. It would be relevant to analyse whether the XPD/G602D mutation disrupts the ability of XPD to interact with Eg5, a motor kinesin protein strongly implicated in the bipolar mitotic spindle formation ³⁷. Indeed, previous results showed that XPD can interact with Eg5 and mutations located in the C-terminal part of XPD (such as XPD/R683W) are known to affect their partnership ^{10,38}. Defective XPD/Eg5 interaction can lead to Eg5 mislocalization on microtubules, which disrupts the mitotic spindle structure and chromosome segregation. Consequently, it would be of interest to perform coimmunoprecipitation and pulldown assays to analyse the partnership between Eg5 and XPD/G602D. In parallel, immunofluorescence

analyses will allow us to examine Eg5 localization as well as the mitotic spindle formation in XPD/G602D mutated cells.

In addition to their effects on NER and mitosis, our results revealed that XPD mutations differently affect transcription. Previous works showed that XPD mutations can impact transcription of specific genes by disrupting TFIIH integrity (such as XPD/R683W and /R722W)^{18,19}. The different mutations studied here are known to particularly affect the activity of XPD, *which is not required in transcription, at least during initiation*^{4,25}. To better understand the molecular impact of these XPD mutations in transcription, further investigations should be undertaken. We first would like to confirm the dysregulation of specific genes by performing quantitative RT-PCR. In parallel, western blots analyses will allow us to determine the consequences at a protein level of the dysregulation of specific genes. While gene function does not appear to be a prerequisite for the dysregulation caused by XPD mutations (Figure 4E), it seems that the expression of genes encoding long RNAs is particularly affected by XPD mutations (Figures 4F and 5G). Therefore, it would be also interesting to study the recruitment of transcription factors to DNA. Chromatin Immunoprecipitation coupled to sequencing (ChIP-seq) should be undertaken to identify genome-wide DNA binding sites for distinct transcription factors, including RNAPII (by targeting its RPB1 subunit) and TFIIH (notably XPD-GFP). It would also be possible to analyse epigenetic marks such as the acetylation of the lysine residue at N-terminal position 27 of the histone H3 protein (H3K4me3), which is commonly found at proximal and distal regions of transcription start sites (TSS) and widely considered as an active transcription mark. This work would be performed in basal conditions as well as post RA treatment. ChIP-seq will be complementary to our RNA-seq analysis, since comparative analysis will allow us to determine whether defective gene expression in XPD mutated cells is related to defective recruitment of the transcription machinery along genes bodies. In parallel, the fact that *RNA synthesis (Figure 4A) and expression of genes encoding long RNAs are defective in XPD mutated cells (Figures 4F and 5G) prompt us to perform nascent RNA-seq analyses, which will allow us to measure genome-wide changes in nascent RNA production*⁴³. *Different time points would allow us to evaluate the efficiency of RNA synthesis by RNAPII, which will permit to determine whether defective elongation might occur in XPD mutated cells.*

Taking together, our results suggest that NER, mitosis and transcription might be differently altered depending on the nature of the XPD mutation. This contributes to the phenotypic variability observed in patients bearing these different mutations. As detailed in the discussion, further experiments should be undertaken to improve the quality of this work. We expect to submit a final version of the manuscript soon.

This work highlights the relevance of our strategy based on the development of new cellular models that permit to study and compare the impact of different mutations in various cellular processes. This is of prime interest knowing that XPD seems to be implicated in other cellular mechanisms than NER, mitosis and transcription. Indeed, it has been recently showed that, under oxidative stress, an enhanced recruitment of XPD occurred into mitochondrial compartment ⁴⁴. Such relocation of XPD into mitochondria seems to protect mitochondrial genome stability by facilitating an efficient repair of oxidative DNA damage. Accordingly, our cellular models would allow us to determine what could be the impact of different XPD mutations on mitochondrial genome stability. In addition, recent results revealed that TFIIH prevents telomere replication problems by interacting with TRF1, a protein of the shelterin complex that protects chromosome ends ⁴⁵. However, the molecular functions of TFIIH and the consequences of XPD mutations during telomere replication still remain largely elusive. Our cellular models might help us to better apprehend the roles played by TFIIH in telomere replication and to determine whether XPD mutations might affect this process. Finally, the results obtained from the cellular models already generated prompts us to develop new cell lines bearing other mutations in XPD as well as in XPB and p8/TTDA. It would be also interesting to generate compound heterozygotes cell lines bearing distinct mutations that will allow us to clearly and finely determine the synergic impact of mutations in different cellular processes.

Materials and Methods

Generation and culture of cell lines. U-2OS osteosarcoma cells endogenously expressing GFP tagged XPD were previously generated and cultured in DMEM with 1g/L glucose supplemented with 10% FCS and 40 µg/mL gentamicin at 37°C in a 5% CO₂ atmosphere. To perform gene editing, 2.10⁶ cells were transfected by electroporation with DNA donor (containing the edit of interest), Cas9 and guide RNA (gRNA). The cells were then sorted by FACS 3 days post-transfection to generate single-cell clones. Digital PCR has been first performed to screen cells bearing expected substitution and Sanger sequencing was next performed to confirm clones carrying the expected gene editing.

Cell counting. The different cell lines were analyzed in a blinded-manner for their chromosomal and mitotic spindle phenotypes. Normal and defective chromosomal phenotypes were assessed by DAPI staining.

Cell synchronization. Double thymidine block and release (DTBR) protocol was used to synchronize cells, as previously described ¹⁰. Cells have also been synchronized in prometaphase using Nocodazole (16h, 100ng/ml) or Taxol (16h, 1µM).

Cell viability. Cells (250 000 cells per well in 6-well petri dishes) were exposed to different doses (5, 10, 20 and 30 J/cm²) of UV-C (Philips TUV lamp, 254nm) and maintained 48h in normal condition of culture. After staining with Crystal Violet (0.2%, Sigma), washings and drying, the stain was solubilized with 1% SDS to measure optical density (595nm).

Fluorescence recovery after photobleaching (FRAP). FRAP experiments were conducted with a Leica TCS SP8 microscope and immersion objective under the same excitation conditions described above. An image size of 256 × 25 and a zoom factor of 3 were used to achieve a frequency of 10 images per second. Ten pre-bleach images and 50 post-bleach images were acquired. Photobleaching was performed at 100% power using the 488 nm Argon laser for 160 ms in a circular region of 3 µm within the nucleus. The mobility of GFP-tagged proteins was analyzed by quantifying the recovery of the signal in the bleached region using custom FiJi macros. The

immobile fraction was determined from normalized measurements as the inverse of the fluorescence plateau. The mean values between 5 and 7 seconds (final UV average) were calculated, and the immobile fraction was determined using the following formula: $F_{\text{imm}} = 1 - (\text{final UV average})$.

Western blot and co-immunoprecipitation assays. Western Blot analyses were undertaken from whole cell extracts in RIPA buffer. Co-immunoprecipitations assays were performed using GFP-trap magnetic beads (ChromoTek). After several washes, bound proteins were resolved by SDS-PAGE and detected with antibodies targeting the proteins of interest.

Laser-induction of local damage and live-cell confocal microscopy. Confocal TCS Leica SP8 upright microscope (Leica Microsystems) with a Ti:Sapphire laser option (Chameleon Vision II, Coherent) was used for fluorescence time lapse recording as well as for induction of DNA damage through three-photon irradiation. Cells were maintained at 37°C during imaging and data were collected using a Leica HCX IRAPO L 25x, 0.95 NA water immersion objective. Time lapse recording was performed using the FRAP wizard of the LASX confocal microscope control software. DNA damages by laser microirradiation were induced by three-photon absorption using the Ti:Sapphire laser set at 800nm, power set to 55% transmission intensity, 72% EOM gain, corresponding to 260mW measured at the back focal plane of the objective. Two or three pixels thick rectangular ROIs were scanned through the nucleus with 2 iterations. At least one cell was preserved from three-photon irradiation and was used for photobleaching quantification.

Immunofluorescence-based DNA lesion quantification. Cells were irradiated with UV-C (15 J/m²) and maintained in normal condition of culture for different recovery time intervals. Prior to labeling, DNA was denatured (2 M HCl) and blocked in 10% Fetal Calf Serum. Cyclobutane pyrimidine dimers (CPD) and 6–4 photoproducts (6–4PP) were then immunolabelled using anti-CPD and anti-6-4PP antibodies, respectively. Following image acquisition, signal intensity was quantified by ImageJ software to determine the percentage of CPD and 6–4PP removal (100% represents the % of lesions measured just after UV irradiation).

Reagents and Resources. The reagents and resources (antibodies, chemical, cell lines, oligonucleotides, recombinant DNA, software and materials) used to accomplish this work are available in the Key Resources Table.

EU incorporation. 5-ethynyl uridine (EU) labelling (1h, 1uM) of newly formed RNA in 1.10^5 cells was performed using the Click-iT RNA Alexa Fluor 596 imaging kit (Invitrogen). Transcription block of RNAPI was simultaneously achieved by treatment with actinomycin D (50ng/ml). As control, cells were treated in parallel with 5,6-dichloro-1-beta-D-ribofuranosylbenzimidazole (DRB) for 24 hours to block transcription by RNAPII. Microscopic images were taken with a Leica DM 4000 B equipped with a CoolSnap FX monochrome camera and the intensity of the EU signal was quantified using Fiji software.

Bulk RNA-Seq and analysis. Library preparation was performed at the GenomEast platform at the Institute of Genetics and Molecular and Cellular Biology using TruSeq Stranded Total RNA Reference Guide PN 1000000040499. Total RNA-Seq libraries were generated from 700ng of total RNA using TruSeq Stranded Total RNA Library Prep Gold kit and TruSeq RNA Single Indexes kit A and B (Illumina, San Diego, USA), according to manufacturer's instructions. Briefly, cytoplasmic and mitochondrial ribosomal RNA (rRNA) was removed using biotinylated, target-specific oligos combined with Ribo-Zero rRNA removal beads. Following purification, the depleted RNA was fragmented into small pieces using divalent cations at 94°C for 8min. Cleaved RNA fragments were then copied into first strand cDNA using reverse transcriptase and random primers followed by second strand cDNA synthesis using DNA Polymerase I and RNase H. Strand specificity was achieved by replacing dTTP with dUTP during second strand synthesis. The double stranded cDNA fragments were blunted using T4 DNA polymerase, Klenow DNA polymerase and T4 PNK. A single 'A' nucleotide was added to the 3' ends of the blunt DNA fragments using a Klenow fragment (3' to 5'exo minus) enzyme. The cDNA fragments were ligated to double stranded adapters using T4 DNA Ligase. The ligated products were enriched by PCR amplification. Surplus PCR primers were further removed by purification using AMPureXPbeads (Beckman-Coulter) and the final cDNA libraries were checked for quality and quantified using capillary electrophoresis. Libraries were sequenced on an Illumina HiSeq 4000 sequencer as single read 50 base reads. Image analysis and base calling were performed using RTA version 2.7.7 and bcl2fastq

version 2.20.0.422. Reads were preprocessed to remove adapter and low-quality sequences (Phred quality score below 20). After this preprocessing, reads shorter than 40 bases were discarded for further analysis. These preprocessing steps were performed using cutadapt version 1.10. Reads were mapped to rRNA sequences using bowtie version 2.2.8 and reads mapping to rRNA sequences were removed for further analysis. Reads were mapped onto the hg38 assembly of Homo sapiens genome using STAR version 2.5.3a. Gene expression quantification was performed from uniquely aligned reads using htseq-count version 0.6.1p1, with annotations from Ensembl version 75 and “union” mode. Only non-ambiguously assigned reads have been retained for further analyses. Read counts have been normalized across samples with the median-of-ratios method proposed by Anders and Huber to make these counts comparable between samples. Comparisons of interest were performed using the Wald test for differential expression and implemented in the Bioconductor package DESeq2 version 1.16.1. Genes with high Cook’s distance were filtered out and independent filtering based on the mean of normalized counts was performed. P-values were adjusted for multiple testing using the Benjamini and Hochberg method. Volcano plots were generated using the Prism10 statistical software (GraphPad). Heatmaps were generated using Morpheus software ([https:// software.broadinstitute.org/morpheus](https://software.broadinstitute.org/morpheus)). Venn diagrams were generated using DeepVenn ⁽⁴³⁾ and representation factors and hypergeometric P-values were determined using Graeber lab software (<https://systems.crump.ucla.edu/hypergeometric/>). Gene Ontology and Transcript Length was performed using ShinyGO (<https://bioinformatics.sdstate.edu/go/>).

Conclusion/Perspectives

The work presented in this manuscript has advanced our understanding of the molecular and cellular consequences of mutations in the XPD protein, a key 5'-3' helicase subunit of the TFIIH complex. XPD plays essential roles in NER, transcription, and, more recently, has been implicated in processes related to cell division.

While diseases associated with XPD mutations such as Xeroderma Pigmentosum, the combined Xeroderma Pigmentosum /Cockayne Syndrome, and Trichothiodystrophy) have long been attributed solely to defects in DNA repair, our findings demonstrate that the functional impact of XPD mutations extends well beyond that single pathway.

1. DNA Repair: Findings and Future Directions

Our results show that all XPD mutations examined G47R, K48R, and G602D similarly impair NER. Live-cell imaging following femtosecond laser micro-irradiation revealed a significantly reduced recruitment of mutant XPD-GFP proteins to sites of DNA damage, compared to wild-type. This observation was supported by immunofluorescence analysis, which showed low or delayed accumulation of mutant XPD at CPD lesions and persistent presence at damage sites even two hours post-irradiation. Importantly, these recruitment defects were associated with inefficient repair of both CPDs and 6-4PPs, as well as reduced cell viability following UV-C exposure. While the integrity of the TFIIH complex appeared preserved, the impaired recruitment and defective enzymatic activity of mutant XPD proteins—particularly their compromised helicase or ATPase functions—likely underlie the NER deficiencies. Interestingly, all three mutations produced a comparable level of NER disruption, suggesting that the nature of the defect may lie in a common mechanistic bottleneck within the repair pathway.

To further clarify the dynamics of this defect, future work will involve FRAP-based analyses to evaluate the immobilization and residence time of the mutated proteins at DNA lesions. This may help determine whether prolonged or defective binding of TFIIH correlates with impaired repair kinetics and potentially with disease severity. Additional quantitative imaging and biochemical studies will also be necessary to better understand the interaction of mutant XPD with other NER factors and to refine the molecular map of how specific mutations disrupt the repair process.

2. Mitosis: Findings and Future Directions

Our findings demonstrate that mutations in XPD differentially affect mitotic processes, particularly chromosome segregation. Confocal microscopy revealed that the dynamic localization of XPD-GFP during mitosis was preserved across all variants studied—including G47R, K48R, and G602D showing enrichment at the mitotic spindle during metaphase, at the midzone in anaphase, and at the midbody during telophase, comparable to wild-type XPD. However, a significant increase in mitotic abnormalities, such as misaligned chromosomes, was specifically observed in XPD/G602D cells. In contrast, no such defects were detected in G47R or K48R mutant cells. To investigate whether these segregation errors were associated with premature mitotic exit, as previously described in XPD/R683W mutant cells, synchronized progression assays were performed following nocodazole treatment and release. Western blot and microscopy analyses indicated that all XPD-mutated cell lines progressed through mitosis with kinetics comparable to wild-type, and no premature exit was observed. Furthermore, Spindle Assembly Checkpoint integrity was confirmed by sustained mitotic arrest following Taxol treatment in all tested lines, indicating that SAC function remains intact in XPD/G602D cells.

These results suggest that the mitotic defects associated with the G602D mutation arise independently of SAC disruption or global mitotic timing alterations. A plausible hypothesis is that this mutation impairs specific molecular interactions required for proper spindle function. In light of previous reports indicating that XPD interacts with the mitotic motor protein Eg5 an essential component of bipolar spindle assembly and it is conceivable that the G602D substitution compromises this interaction. Accordingly, future work will involve co-immunoprecipitation and pulldown assays to evaluate the physical association between XPD/G602D and Eg5. In parallel, immunofluorescence-based localization studies of Eg5 will be conducted to assess potential mislocalization and structural abnormalities in the mitotic spindle. These investigations will provide further insight into how distinct mutations in XPD contribute to mitotic errors and chromosomal instability, thereby offering a more nuanced understanding of the molecular basis underlying the phenotypic diversity associated with XPD-related syndromes.

3. Transcription: Findings and Future Directions

Collectively, our findings indicate that XPD mutations exert differential but significant effects on transcriptional regulation, particularly in the context of protein-coding genes. Incorporation assays using 5-ethynyl uridine (EU) revealed a marked reduction in nascent RNA synthesis in cells expressing the XPD/K48R and XPD/G602D variants, in contrast to XPD/G47R cells, which displayed RNA synthesis levels comparable to wild-type. Transcriptome-wide RNA sequencing further substantiated these observations, uncovering widespread gene expression alterations in XPD-mutated cells. Notably, the extent of transcriptional dysregulation varied across mutations, with XPD/G47R associated with minimal changes, whereas XPD/K48R and XPD/G602D exhibited a substantial number of both up- and downregulated genes. Comparative analyses revealed significant overlap among dysregulated gene sets, suggesting the existence of a shared molecular mechanism underlying the observed expression changes. Interestingly, gene ontology analysis failed to identify coherent functional enrichment, while transcript length emerged as a critical parameter, with long genes being disproportionately downregulated. These results strongly implicate a potential deficiency in transcription elongation as a consequence of impaired XPD function. Further evidence in support of this hypothesis was obtained under conditions of transcriptional induction. Following retinoic acid (RA) stimulation, XPD/K48R and XPD/G602D cells exhibited a blunted induction of RA-responsive genes relative to wild-type and XPD/G47R cells. A subset of RA target genes, particularly those with longer transcripts, displayed significantly reduced activation, reinforcing the notion that XPD mutations compromise transcriptional elongation rather than initiation. Taken together, these data suggest that XPD plays a supportive role in facilitating efficient transcription elongation, particularly in the context of complex gene architectures or transcriptionally demanding conditions.

To explore these mechanistic insights in greater depth, a multi-tiered experimental strategy will be employed. qRT-PCR and western blot analyses will be performed to validate RNA-seq results and assess changes at the protein level. Chromatin immunoprecipitation followed by high-throughput sequencing will be conducted to map genome-wide occupancy of key transcriptional components, including RNA polymerase II, TFIIF subunits (e.g., XPD-GFP), and active chromatin marks such as H3K4me3. These analyses will be performed both under basal conditions and following RA stimulation, thereby enabling the identification of potential defects in recruitment or retention of the transcriptional machinery. In parallel, nascent RNA sequencing will be utilized to directly

assess RNA polymerase II elongation dynamics across gene bodies. By integrating these complementary approaches, we aim to delineate the specific contribution of XPD's enzymatic activity to transcriptional fidelity and to determine the extent to which elongation defects may underlie the pathological manifestations associated with XPD mutations.

Altogether, this study provides novel insights into the several cellular functions of XPD and emphasizes the functional heterogeneity associated with different disease-linked mutations. By demonstrating that mutations in the same gene can differentially affect distinct cellular pathways, this work contributes to a better understanding of the molecular basis of the phenotypic variability observed in TFIIH-related syndromes, including xeroderma pigmentosum (XP), trichothiodystrophy (TTD), and Cockayne syndrome (CS).


Annexes

Pan-inhibition of super-enhancer-driven oncogenic transcription by next-generation synthetic ecteinascidins yields potent anti-cancer activity

Received: 25 April 2024

Accepted: 19 December 2024

Published online: 08 January 2025

 Check for updates

Max Cigrang^{1,2,3,4,10}, Julian Obid^{1,2,3,4,10}, Maguelone Nogaret^{1,2,3,4}, Léane Seno^{1,2,3,4}, Tao Ye^{1,2,3,4}, Guillaume Davidson^{1,2,3,4}, Philippe Catez^{1,2,3,4}, Pietro Berico^{1,2,3,4,5,6}, Clara Capelli^{1,2,3,4}, Clara Marechal^{1,2,3,4}, Amélie Zachayus^{1,2,3,4}, Clémence Elly^{1,2,3,4}, Marie Jose Guillen Navarro⁷, Marta Martinez Diez⁷, Gema Santamaria Nunez⁷, Tsai-Kun Li^{8,9}, Emmanuel Compe^{1,2,3,4}, Pablo Avilés⁷, Irwin Davidson^{1,2,3,4}, Jean-Marc Egly^{1,2,3,4,9}, Carmen Cuevas⁷ & Frédéric Coin^{1,2,3,4}✉

The plasticity of cancer cells facilitates their ability to adopt heterogeneous differentiation states, posing a significant challenge to therapeutic interventions. Specific gene expression programs, driven in part by super-enhancers (SEs), underlie cancer cell states. Here we successfully inhibit SE-driven transcription in phenotypically distinct metastatic melanoma cells using next-generation synthetic ecteinascidins. Through functional genomic methodologies, we demonstrate that these compounds inhibit the expression of genes encoding lineage-specific or ubiquitous transcription factors/coactivators by selectively targeting the CpG-rich sequences within their promoters and/or enhancers. This prevents the formation of transcription factor/coactivator condensates necessary for SE-dependent gene expression. Consequently, these compounds exhibit cytotoxic activity across distinct subpopulations of metastatic melanoma cells and inhibit tumor proliferation, including those resistant to current therapies. These findings extend to other cancers, like small cell lung cancer, recently approved for ecteinascidin-based treatment. Overall, our study provides preclinical proof that pan-inhibition of SE-dependent genes with synthetic ecteinascidins is a promising therapeutic approach for tumors with heterogeneous transcriptional landscapes.

In recent years, the concept of ‘transcriptional addiction’ has emerged as a hallmark of cancer cells. Indeed, dysregulated gene expression programs and their associated transcriptional regulatory machinery play crucial roles in sustaining cancer cell phenotypes, thereby rendering them susceptible to transcriptional inhibitors^{1–3}. One of the primary mechanisms contributing to gene expression dysregulation in

cancer cells involves the aberrant acquisition of large clusters of enhancers known as “super-enhancers” (SEs), which drive and maintain the robust expression of oncogenes. SEs are characterized by the aggregated histone modifications H3K27ac and H3K4me1, over longer genomic distances compared to typical enhancers^{6,7}. Moreover, SE-dependent oncogene transcription requires the activity of ubiquitous

A full list of affiliations appears at the end of the paper. ✉e-mail: fredr@igbmc.fr

transcription factors (e.g., the Cyclin Dependent Kinase 7 (CDK7) of TFIIH) and transcriptional coactivators (e.g., Bromodomain-containing protein 4 (BRD4)), and is maintained by core autoregulatory feedback loops involving master transcription factors and the Mediator complex⁸. Recent evidence has demonstrated that SEs form phase-separated biomolecular condensates, concentrating the transcription apparatus in nuclear puncta to drive the high expression of their regulated oncogenes⁹. Targeting these oncogenic SEs and their spatial organization has emerged as a potential therapeutic strategy¹⁰. Therefore, several compounds aiming to disrupt factors involved in oncogenic SE-driven gene expression, including CDK7 and BRD4 inhibitors, have entered clinical trials^{11,12}. However, they have had limited success due to poor pharmacokinetics and short half-lives^{13–16}.

Cutaneous melanoma is often cited as a prime example of transcriptional addiction due to its frequent dysregulation of specific transcription factors and signaling pathways that drive its aggressive behavior and resistance to treatment^{17–20}. Despite significant advances in developing inhibitors targeting the mutated MAPK signaling pathway (BRAFi and MEKi), along with the introduction of immune checkpoint inhibitors targeting programmed cell death protein 1 (PD-1) and cytotoxic T-lymphocyte-associated antigen 4 (CTLA-4), this cancer remains the most lethal form of skin cancer. Indeed, more than 50% of metastatic melanoma patients either do not initially respond or eventually acquire resistance to these therapies^{21–23}. Melanoma cells evade conventional therapeutic strategies by transitioning between melanocytic/differentiated states, governed by SE-dependent genes essential for cell proliferation, such as the *lineage-specific master transcription factors* *Micropthalmia-associated transcription factor* (MITF) and the *SRY-box transcription factor 10* (SOX10), and mesenchymal-like/undifferentiated states, governed by key regulator genes such as the *AXL Receptor Tyrosine Kinase* (AXL) and the *Activator Protein (AP-1)/TEAD* genes implicated in targeted therapy/immunotherapy resistance and invasion^{18,24–30}. This phenotypic adaptation/switch, facilitated by dynamic transcriptional and epigenetic reprogramming mechanisms in response to microenvironmental cues, complicates treatment outcomes^{19,31} and underscores the need for therapeutics that can uniformly target divergent transcription programs governing different tumor cell states³².

Ecteinascidins, a group of natural compounds derived from marine organisms, particularly tunicates, have garnered significant attention due to their anticancer properties³³. Synthetic ecteinascidins refer to compounds that are chemically synthesized to mimic the structure and biological activity of natural ecteinascidins. These synthetic compounds are designed to retain the anticancer properties of natural ecteinascidins while potentially offering advantages such as improved potency, selectivity, and pharmacokinetic properties. A notable member of this class is lurbinectedin, derived from the natural compound trabectedin. Lurbinectedin acts as a DNA binder and transcriptional inhibitor^{34,35}. It is the first molecule approved by the FDA for the treatment of relapsed small-cell lung cancer (SCLC) in the last decade, showcasing the considerable potential of synthetic ecteinascidins as anticancer compounds³⁶.

In this work, in an effort to potentially enhance the benefits of these DNA binders, we develop next-generation synthetic ecteinascidins and test these compounds on melanoma cells due to their well-established transcriptional addiction and propensity for treatment resistance. Our study demonstrates potent anti-proliferative and apoptotic effects of these next-generation DNA binders on differentiated and undifferentiated *BRAF*, *NRAS*, and triple-wild type mutated melanoma cells in various in vitro 2-D and 3-D models and in cell-derived xenograft (CDX) mouse models. We further observe that these compounds potently inhibit a set of genes encoding ubiquitous transcription factors/coactivators through binding to the CpG islands located in their promoters and/or enhancers. These factors are highly enriched at cell-specific SEs, regulating the expression of cancer-

promoting genes. Consequently, synthetic ecteinascidins disorganize the phase-separated condensates of transcription factors/coactivators, inducing a pan-inactivation of SEs in melanoma cells irrespective of their cell state and driver mutations. This mechanism of action is not observed with BRAFi, MEKi, or DNA-damaging agents such as dacarbazine. Intriguingly, we demonstrate that this uncovered mechanism is also operative in clinically relevant scenarios, such as the treatment of SCLC cells with lurbinectedin, thereby explaining the clinical efficiency of this compound.

Results

Lurbinectedin shows notable efficacy against distinct melanoma cell types

To ascertain the cytotoxic effects of the first-in-class synthetic ecteinascidin lurbinectedin (Fig. 1a) on melanoma cells, we first conducted a dose-response analysis across ten metastatic melanoma cell cultures representing the two primary phenotypes and encompassing the most prevalent driver mutations. We evaluated primary differentiated melanocytic-type cultures derived from patient biopsies, including MM011 (NRAS^{Q61K}), MM074 (BRAF^{V600E}), MM117 (Triple-wt), alongside commonly used metastatic melanoma cell lines 501mel (BRAF^{V600E}), IGR37 (BRAF^{V600E}) and SkMel-28 (BRAF^{V600E}) (Table 1). These cells demonstrated moderate to high expression levels of the lineage-specific master transcription factors MITF and SOX10, while showing low to undetectable expression levels of the pro-metastatic factors EGFR and AXL^{14,18,37} (Fig. 1b). Additionally, we examined primary undifferentiated metastatic mesenchymal-like melanoma cell cultures derived from patient biopsies, including MM029 (BRAF^{V600K}), MM047 (NRAS^{Q61R}) and MM099 (BRAF^{V600E}), along with the undifferentiated metastatic mesenchymal-like melanoma cell line IGR39 (BRAF^{V600E}). These cells exhibited low to undetectable levels of MITF and SOX10, but elevated expression levels of EGFR and/or AXL¹⁴.

We observed varying sensitivities of these metastatic melanoma cells to clinically utilized targeted therapy agents, such as the BRAF inhibitors (BRAFi) vemurafenib and dabrafenib, as well as the MEK inhibitor (MEKi) trametinib (Fig. 1c–e and Table 1). Differentiated BRAF^{V600E} melanoma cells were the most responsive to these compounds, whereas undifferentiated cells displayed high resistance. In stark contrast, all melanoma cells showed high sensitivity to lurbinectedin, with IC50 values in the low nanomolar range, from 0.44 to 2.07 nM (Fig. 1f and Table 1). Furthermore, we generated vemurafenib-resistant cells 501mel^{Vemur} and MM074^{Vemur} by exposing initially sensitive cells to increasing drug concentrations in vitro (Fig. 1c and Table 1)¹⁴. These cells acquired a hyperpigmentation phenotype and exhibited cross-resistance to dabrafenib (in the case of MM074^{Vemur}) and trametinib (Fig. 1d, e and Table 1), yet remained highly sensitive to lurbinectedin (Fig. 1f and Table 1).

Collectively, these findings underscore the heightened sensitivity of melanoma cells to lurbinectedin, regardless of cellular phenotypes or driver mutations.

Next-generation ecteinascidins show high cytotoxic effects on melanoma cells

In our pursuit of enhancing the anti-cancer efficacy of synthetic ecteinascidins, we synthesized and assessed next-generation compounds. These molecules, named ecubectedin and PM54, exhibit distinct chemical structures in the non-DNA-binding moieties³⁸. Ecubectedin features a substituted spiro-β-carboline, while PM54 contains a spiro-benzofuropyridine (Fig. 2a, b). Spiro compounds often exhibit enhanced biological activities due to their rigid and three-dimensional structures, which can lead to improved interactions with biological targets. The introduction of a spiro-benzofuropyridine in PM54 is particularly relevant because this moiety was not previously identified in natural ecteinascidins. These unique three-dimensional shapes can contribute to increased selectivity for specific biological

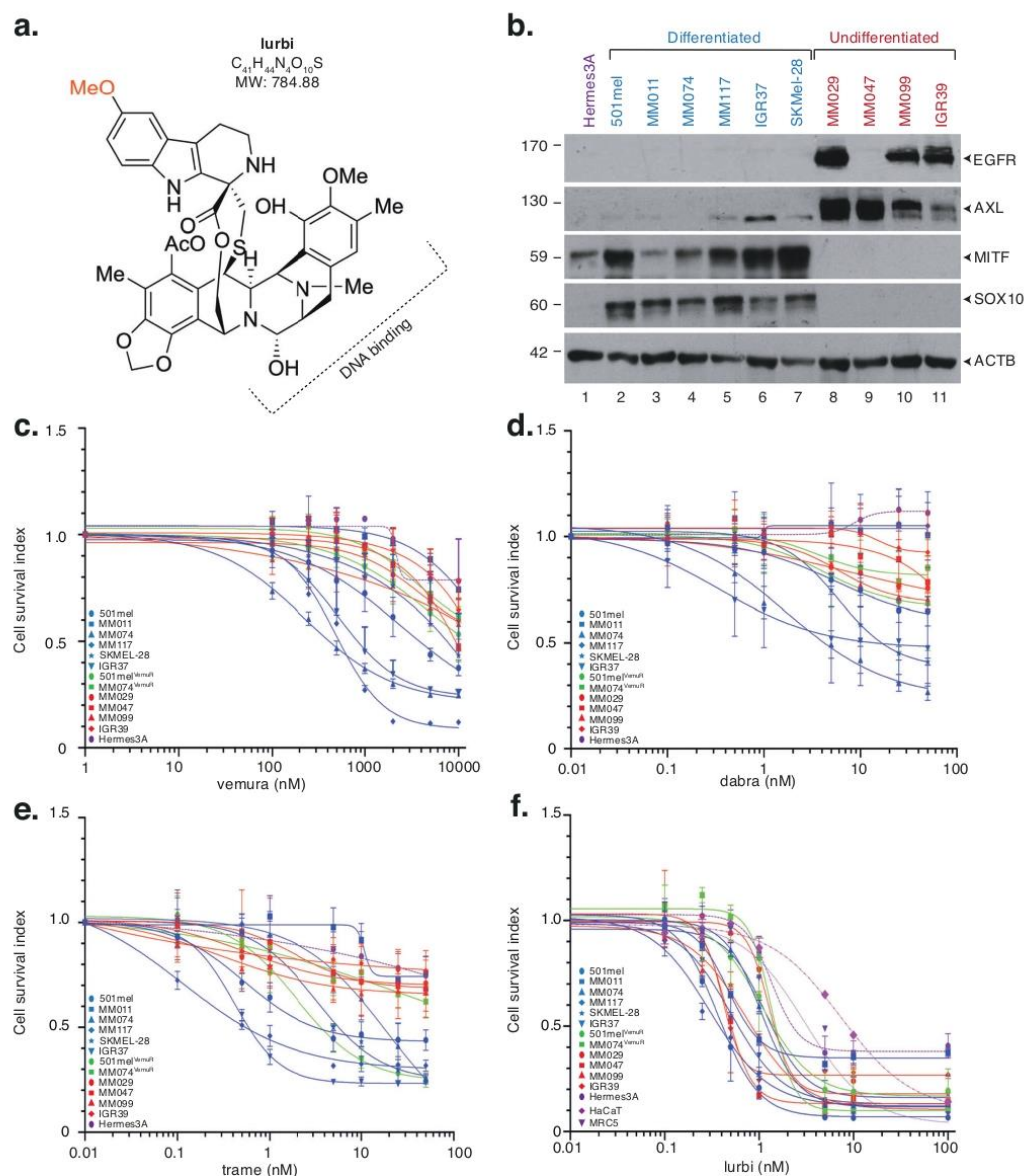


Fig. 1 | Metastatic melanoma cells show high sensitivity to lurbinectedin. **a** Chemical structure of lurbinectedin, the first-in-class synthetic ecteinascidin containing tetrahydroisoquinoline subunits. The moiety of the molecule interacting with DNA is indicated. Molecular Weight (MW) is indicated. **b** Protein lysates from either the immortalized Hermes3A melanocytes, differentiated melanoma cells 501mel, MM011, MM074, MM117, IGR37 and SKMel-28 or undifferentiated melanoma cells MM029, MM047, MM099 and IGR39 were immuno-blotted for proteins as indicated. Molecular mass of the proteins is indicated (kDa). Source data are provided as a Source Data file. This experiment was repeated independently three times with similar results. **c–f** Indicated melanoma cells were treated

with increasing concentrations of vemurafenib **c**, dabrafenib **d**, trametinib **e**, or lurbinectedin **f** for 72 h. Mean growth is shown relative to vehicle (DMSO)-treated cells. Error bars indicate mean values \pm Standard Deviation (SD) for three biological triplicates. Differentiated (MITF-High, proliferative) melanoma cells are shown in blue, while undifferentiated (MITF-low, invasive) melanoma cells are shown in red. Hyperpigmented melanoma cells with acquired resistance to vemurafenib are shown in green. Immortalized Hermes3A melanocytes, skin keratinocyte HaCaT and embryonic fibroblastic MRC5 cells are shown in violet. Source data are provided as a Source Data file.

Table 1 | Melanoma cell sensitivity against MAPKi and synthetic ecteinascidins

Cells	G	S/T	P	G	veru	dabra	tram	lurb	ecub	PM54	B-lurb	B-PM54
HaCat	M	WT	Kera	WT	nd	nd	nd	3.2 nM	5.2 nM	10.3 nM	nd	nd
MRC5	M	WT	Fibro	WT	nd	nd	nd	7.5 nM	2.9 nM	12.5 nM	nd	nd
Hermes3A	M	WT	Mel	WT	>10 μM	>50 nM	>50 nM	2.7 nM	2.9 nM	4.9 nM	nd	nd
501mel	F	MNS/NS	Diff	BRAF ^{V600E}	2.4 μM	>50 nM	3.0 nM	0.4 nM	1.2 nM	1.7 nM	1.4 nM	5.0 nM
MM011	F	LNM/SSM	Diff	NRAS ^{G12S}	>10 μM	>50 nM	>50 nM	0.5 nM	1.0 nM	1.4 nM	nd	nd
MM074	F	LNM/SSM	Diff	BRAF ^{V600E}	225 nM	4.7 nM	0.5 nM	1.1 nM	1.1 nM	3.8 nM	nd	nd
MM117	NS	NS/NS	Diff	Triple-WT	490 nM	>50 nM	10.2 nM	0.3 nM	0.7 nM	1.2 nM	nd	nd
SKMEL-28	M	ALN/NS	Diff	BRAF ^{V600E}	>10 μM	1.0 nM	5.1 nM	1.2 nM	1.3 nM	1.7 nM	nd	nd
GR37	M	GLN/NS	Diff	BRAF ^{V600E}	520 nM	25.3 nM	0.5 nM	0.5 nM	1.0 nM	1.5 nM	nd	nd
501mel ^{veru}	F	MNS/NS	Pigmented	BRAF ^{V600E}	>10 μM	>50 nM	>50 nM	1.1 nM	1.0 nM	2.1 nM	nd	nd
MM074 ^{veru}	F	LNM/SSM	Pigmented	BRAF ^{V600E}	>10 μM	>50 nM	4.6 nM	1.3 nM	1.6 nM	3.1 nM	nd	nd
MM029	F	LNM/SSM	Undiff	BRAF ^{V600E}	>10 μM	>50 nM	>50 nM	1.3 nM	1.4 nM	4.7 nM	1.4 nM	6.0 nM
MM047	M	NS/NS	Undiff	NRAS ^{G12S}	>10 μM	>50 nM	>50 nM	0.4 nM	0.9 nM	1.4 nM	nd	nd
MM099	M	LT/NS	Undiff	BRAF ^{V600E}	>10 μM	>50 nM	>50 nM	0.7 nM	1.4 nM	1.8 nM	nd	nd
GR39	M	LT/SSM	Undiff	BRAF ^{V600E}	>10 μM	>50 nM	>50 nM	0.4 nM	0.8 nM	0.8 nM	nd	nd
MM074 + INFY	F	LNM/SSM	Pseudo-Inter	BRAF ^{V600E}	8 μM	ns	ns	0.9 nM	1.0 nM	1.0 nM	nd	nd

IC50 of vemurafenib (veru), dabrafenib (dabra), trametinib (tram), lurbicetin (lurb), ecubictin (ecub) and PM54 against various melanoma cells. The gender (G) of the patient, site and tumor type (S/T), phenotype (P) and genotype (G) of these cells are indicated. Hermes3A are transformed melanocytes. WT= Wild-type; NS= Not Specified; MNS= Metastatic; Not Specified; LNM= Lymph Node Metastasis; SSM= Superficial Spreading Melanoma; ALN= Axillary Lymph Node; LT= Left Thigh; GLN= Groin Lymph Node; nd= Not Determined. IC50 of Bio-lurb (B-lurb) and Bio-PM54 (B-PM54) are also indicated.

targets, reducing off-target effects and warranting further investigation. We observed that all melanoma cells displayed high sensitivity to these next-generation synthetic ecteinascidins, with IC50 values in the low nanomolar range, spanning from 0.7 to 5 nM (Fig. 2c, d and Table 1). Notably, the non-cancerous Hermes3A immortalized melanocytes, the skin keratinocyte HaCat cells, and the embryonic fibroblastic MRC5 cells were consistently 3- to 7-times less sensitive to synthetic ecteinascidins compared to melanoma cells.

These findings demonstrate that the next-generation synthetic ecteinascidins exhibit high cytotoxic effects on a range of melanoma cells containing distinct driver mutations and cellular phenotypes.

Synthetic ecteinascidins induce melanoma cell apoptotic death

We next compared the efficacy of synthetic ecteinascidins on cell proliferation and survival. Clonogenic assays demonstrated a significant impact of these molecules on all tested metastatic melanoma cell cultures or cell lines (Fig. 3a), accompanied by a significant inhibition of melanoma cell proliferation (Fig. 3b). Concurrently, there was a notable blockade of cell cycle progression in the G2/M phase (Fig. 3c) and induction of apoptosis (Fig. 3d). The compounds also significantly inhibited the invasion capacities of undifferentiated metastatic melanoma cell cultures (Fig. 3e). Lurbicetin is known to trigger a DNA damage response characterized by the activation of γH2AX due to drug-induced DNA breaks³¹. Using immunofluorescence, we observed γH2AX accumulation in differentiated 501mel or undifferentiated MM029 cells upon treatment with the three synthetic ecteinascidins (Supplementary Fig. 1a–d), which was confirmed by immunoblotting (Supplementary Fig. 1e). In parallel, phosphorylation of the protein kinase ataxia telangiectasia mutated (ATM), the master damage response protein, was observed in these cells (Supplementary Fig. 1e). Of note, MAPKi did not induce activation of γH2AX in sensitive 501mel cells.

We further employed 3-D melanosphere culture assays to assess the response of melanospheres derived from the melanocytic-like MM074 cells to BRAFi and MEKi. In sharp contrast to the response observed in 2-D cultures, BRAFi and MEKi failed to reduce cell viability in the 3-D cultures, even at doses equivalent to 5x of the IC50 concentrations determined in 2-D (Supplementary Fig. 2a). Conversely, synthetic ecteinascidins demonstrated significant cytotoxic effects on MM074 melanospheres (Supplementary Fig. 2b), inducing apoptosis at nanomolar concentrations (Supplementary Fig. 2c). These findings elucidate the pro-apoptotic impacts of synthetic ecteinascidins on both differentiated and undifferentiated melanoma cells cultured in 2- or 3-D settings.

Synthetic ecteinascidins exhibit robust anti-tumor activities

The above data prompted us to examine the impact of synthetic ecteinascidins on melanoma cell-derived xenograft (CDX) mouse models. We first monitored the tumor volumes following intravenous (IV) administration of synthetic ecteinascidins once per week for three consecutive weeks at a concentration of 1.2 mg/kg. Treatments commenced (d.0) when the tumors reached 150 mm³ in athymic nude female mice aged 4 to 6 weeks (*n*=10/group) and finished fourteen days later (d.14). We tested CDXs obtained from two highly proliferative melanoma cell lines widely used for drug screening (LOX-IMVI^{BRAF-V600E} and WM-266-4^{BRAF-V600E})³⁹. For both CDXs, we observed significant tumor growth regression upon treatment with synthetic ecteinascidins, starting d.5 (Fig. 4a, b). The tumor growth delay was persistent even after d.14 when treatment was withdrawn, and lasted until d.25, emphasizing a period of latency of 10 days following the end of the treatment. Simultaneously, a marked augmentation in overall survival was observed, predominantly evident during the latency phase (Fig. 4c, d).

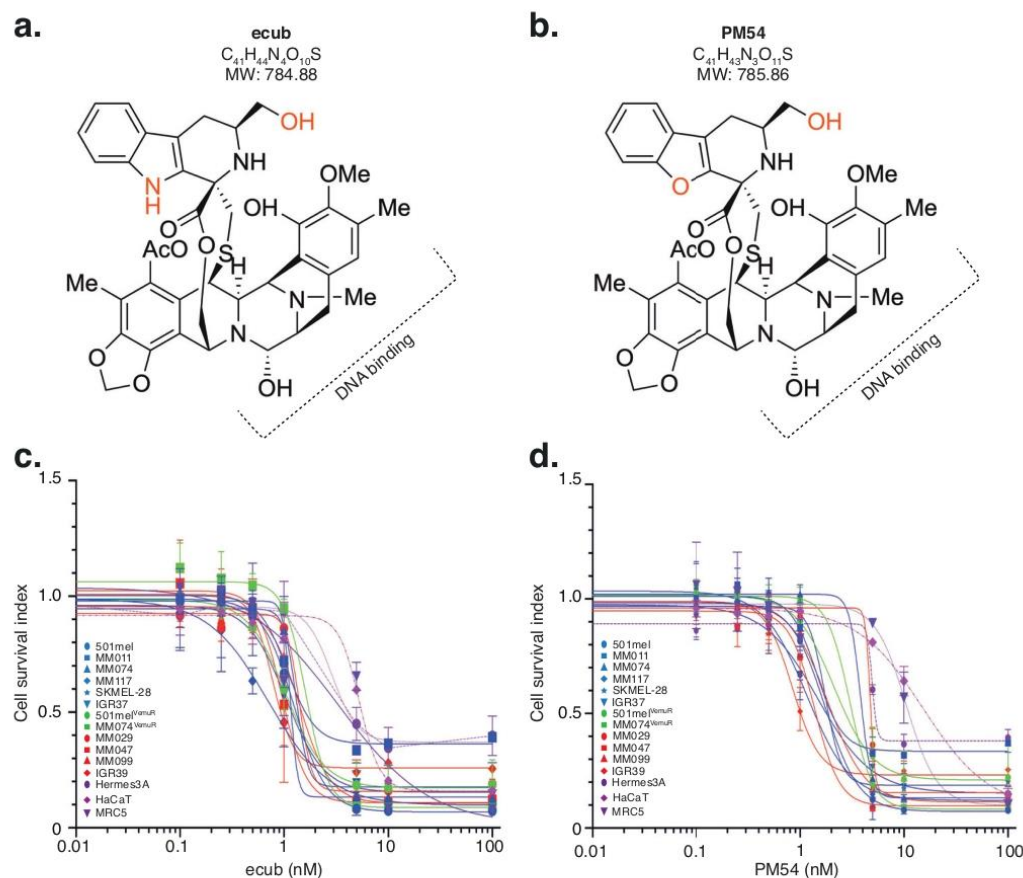


Fig. 2 | Metastatic melanoma cells show high sensitivity to next-generation synthetic ecteinascidins. **a, b** Chemical structure of ecubectedin **a** and PM54 **b**, two next-generation synthetic ecteinascidins analogs of lurbinectedin. The modifications are highlighted in red. The moiety of the molecule interacting with DNA is indicated. Molecular Weight (MW) is indicated. **c, d** Indicated melanoma cells were treated with increasing concentrations of ecubectedin **c** or PM54 **d**, for 72 h. Mean growth is shown relative to vehicle (DMSO)-treated cells. Error bars

indicate mean values \pm Standard Deviation (SD) for three biological triplicates. Differentiated (MITF-high, proliferative) melanoma cells are shown in blue, while undifferentiated (MITF-low, invasive) melanoma cells are shown in red. Hyperpigmented melanoma cells with acquired resistance to vemurafenib are shown in green. Immortalized Hermes3A melanocytes, skin keratinocyte HaCaT and embryonic fibroblastic MRC5 cells are shown in violet. Source data are provided as a Source Data file.

We next analyzed the effect of the drugs on MAPKi-resistant cells using the 501mel and 501mel^{Vemur} cells. Once the tumors reached a size of 150 mm³ in female NSG mice, a single IV dose of either ecubectedin or PM54 at a concentration of 1.2 mg/kg was administered to the animals ($n = 8$ /group). Twenty-four hours after this single IV dose, we assessed the mitotic or apoptotic indexes on tumor sections using immunostaining of phospho-histone H3 (pHH3) or caspase-3 cleavage, respectively⁴⁰. We observed a significantly decreased mitotic index and increased apoptosis upon treatment with synthetic ecteinascidins, for CDXs derived from both 501mel and 501mel^{Vemur} (Supplementary Fig. 3a–d). Consequently, we observed that treatments with synthetic ecteinascidins significantly impacted the tumor growth of CDXs derived from 501mel and 501mel^{Vemur} melanoma cells (Figs. 4e and 2f) and increased the overall survival of the mice (Fig. 4g, h). Altogether, these studies suggest that synthetic ecteinascidins are highly active at inhibiting the growth and inducing apoptosis in melanoma tumors in vivo, even in those presenting resistance to clinically relevant treatments.

Synthetic ecteinascidins affect the expression of cancer-promoting genes

Given the proposed impact of lurbinectedin on transcription³⁵, we conducted gene expression profiling (RNA-Seq) in 2-D cultures of differentiated and undifferentiated melanoma cells. Following the treatment with synthetic ecteinascidins, major transcriptional effects were observed, with a large number of genes being downregulated for both cell types, and a lesser number of genes being upregulated (Supplementary Fig. 4a–c and Supplementary Data 1). However, significant differences in the types of genes being affected in either differentiated or undifferentiated cells were observed. Among the downregulated genes, we noted the presence of several cancer-promoting genes such as *MITF*, *Paired Box 3* (*PAX3*) or *SOX10* specifically in differentiated melanoma cells or *AXL*, *Epidermal Growth Factor Receptor* (*EGFR*), *SRY-Box Transcription Factor 9* (*SOX9*), *FOS Like 2* (*FOSL2*) and *TEAD4* specifically in undifferentiated cells. These data were confirmed in 2-D models by RT-qPCR and/or immunoblotting (Supplementary

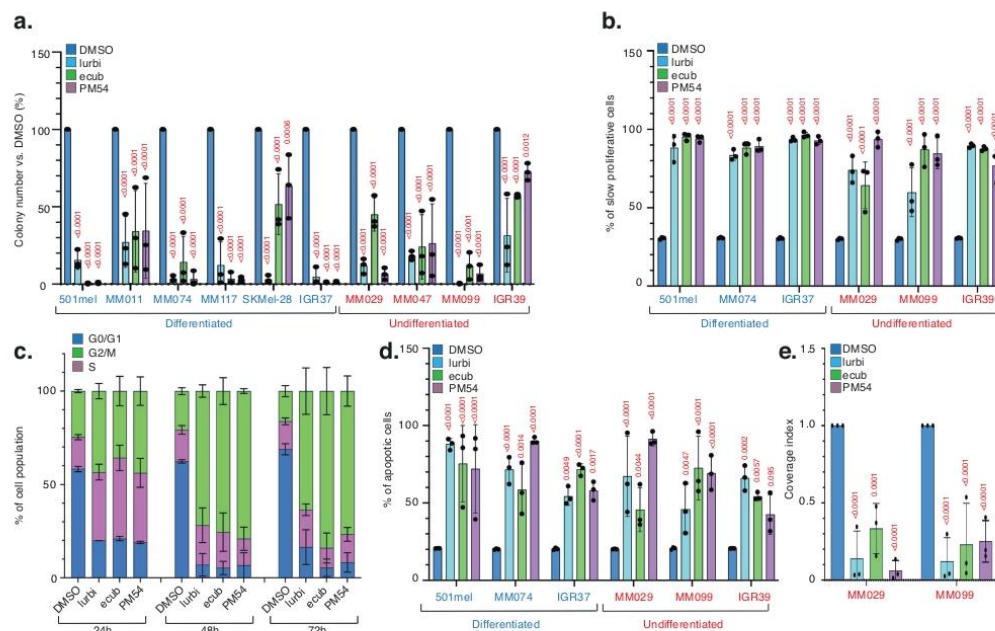


Fig. 3 | Synthetic ecteinascidins induce cell cycle arrest and apoptosis.

a Metastatic melanoma cells were treated with either vehicle (DMSO), lurbicetin, ecubectin or PM54 (1xIC50 concentration, 48 h) and allowed to grow for additional 10 days in the absence of drugs. Results are shown as the mean colony numbers \pm SD for three biological triplicates. Ordinary one-way ANOVA using Dunnett's multiple comparisons test was used to determine the p -values (vs. DMSO). Source data are provided as a Source Data file. **b** Metastatic melanoma cells were incubated with CellTrace and subsequently treated with either vehicle (DMSO), lurbicetin, ecubectin or PM54 (1xIC50 concentration, 72 h). Quantifications of populations with high CellTrace signal in DMSO or drug-treated cells are shown as mean values \pm SD for three biological triplicates. Proliferative cells show low CellTrace signal while non proliferative cells show high CellTrace signal. Ordinary one-way ANOVA using Dunnett's multiple comparisons test was used to determine the p -values (vs. DMSO). Source data are provided as a Source Data file. **c** 501mel cells were treated with either vehicle (DMSO), lurbicetin, ecubectin

or PM54 (1xIC50 concentration, 72 h). Cell cycle was studied by propidium iodide staining and flow cytometry, and results are shown as mean values \pm SD for three biological triplicates. Source data are provided as a Source Data file. **d** Metastatic melanoma cells were treated with either vehicle (DMSO), lurbicetin, ecubectin or PM54 (1xIC50 concentration, 72 h). Apoptosis was studied by flow cytometry using annexin V-APC staining. Results are shown as mean values \pm SD for three biological triplicates. Ordinary one-way ANOVA using Dunnett's multiple comparisons test was used to determine the p -values (vs. DMSO). Source data are provided as a Source Data file. **e** MM029 and MM099 metastatic melanoma cells were treated with either vehicle (DMSO), lurbicetin, ecubectin or PM54 (1xIC50 concentration, 48 h). Invasion was determined using Boyden chamber assays. Results are shown as mean values of coverage index \pm SD for three biological triplicates. Ordinary one-way ANOVA using Dunnett's multiple comparisons test was used to determine the p -values (vs. DMSO). Source data are provided as a Source Data file.

Fig. 5a–d) and in 3-D models by RT-qPCR (Supplementary Fig. 5e,f). Collectively, our findings underscore the significant and partially cell-type-specific inhibition of expression of cancer-promoting genes in metastatic melanoma cells upon treatment with synthetic ecteinascidins.

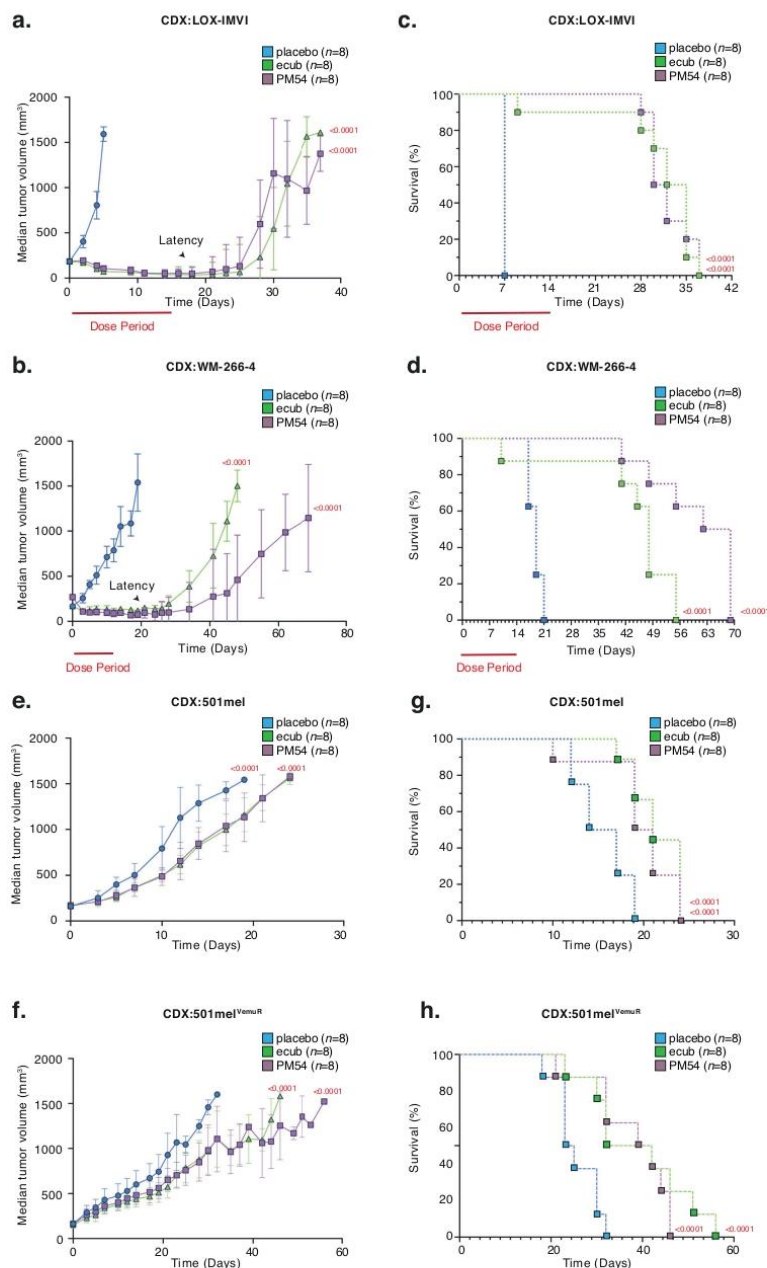
We next undertook a comparative analysis of gene expression profiles in response to treatment with synthetic ecteinascidins. Notably, the three molecules commonly down-regulated 1365 and 1104 genes in differentiated and undifferentiated cells, respectively (Supplementary Fig. 6a). It is worth mentioning that among these genes, 757 displayed consistent down-regulation (and only 110 displayed up-regulation) across both differentiated and undifferentiated cells in response to all the three compounds (Supplementary Fig. 6b,c,d and Supplementary Data 2). Gene ontology (GO) analysis revealed that a substantial proportion of these 757 genes were intricately involved in transcriptional processes (Supplementary Fig. 6e and Supplementary Data 2 and 8).

We subsequently compared each next-generation synthetic ecteinascidin with lurbicetin. We observed that ecubectin exhibited strikingly similar effects, with no genes exhibiting statistically significant differential expression upon a comparative analysis in

either differentiated or undifferentiated cells (Supplementary Fig. 7a,b). In stark contrast, PM54 distinctly induced specific transcriptional effects compared to lurbicetin, revealing a more focused alteration in gene expression, as a smaller subset of genes exhibited deregulation in both differentiated and undifferentiated melanoma cells, (Supplementary Fig. 7a,c). This distinction was further substantiated by GO analysis, which elucidated that PM54 exerts weaker effects on genes involved in diverse cellular processes such as interferon response or oxidative phosphorylation but exerts a more direct influence on genes involved in transcriptional regulation (Supplementary Fig. 7d and Supplementary Data 2 and 8). Globally, our analysis demonstrates that PM54 distinguishes itself by exerting the least influence on the transcriptional program of melanoma cells, while presenting virtually the same cytotoxic effects, emphasizing a unique and potentially advantageous pharmacological profile.

Synthetic ecteinascidins suppress the expression of SE-dependent genes

To decipher the molecular mechanism underlying the cytotoxicity of synthetic ecteinascidins, we conducted an extensive analysis of RNA-Seq datasets derived from three distinct cancer cell types treated with



lurbinectedin. These cells were derived from metastatic melanoma (501mel), metastatic non-SCLC (A549) (GSE179074³⁵) and metastatic SCLC (DMS53) (GSE179074³⁵), the latter being a cancer type for which lurbinectedin has recently gained clinical approval. This analysis revealed that a common set of 642 genes underwent significant down-regulation upon drug exposure (Fig. 5a and Supplementary Data 3). GO analysis revealed once again a strong enrichment of genes involved in

transcriptional regulation (Supplementary Fig. 8a and Supplementary Data 2 and 8), with notable downregulated genes including ubiquitous transcription factors/coactivators (such as *CDK7*, *CDK12*, *CDK13*, *E1A-associated cellular p300 (EP300)*, *CREB-binding protein (CBP)*) and genes coding for Mediator complex subunits (such as *CDK8* and *MED13*). These results were confirmed in differentiated and undifferentiated melanoma cells by immunoblotting (Fig. 5b). Notably, in vivo

Fig. 4 | Potent in vivo effects of synthetic ecteinascidins. **a, b** Indicated CDX models ($n = 10$ at the beginning of the experiment) from LOX-IMVI **a** or WM-266-4 **b** melanoma cells were treated with placebo, ecubectedin or PM54 at 1.2 mg/kg once a week for 3 consecutive weeks (on days 0, 7 and 14) and tumor volumes were measured. Results are shown as mean values \pm SD for “ n ” mice. The red bar indicates the dose period. The latency phase is indicated by an arrow. Logrank (Mantel–Cox) test was used to determine the p -values. Source data are provided as a Source Data file. **c, d** Indicated CDX models ($n = 10$ at the beginning of the experiment) from LOX-IMVI **c** or WM-266-4 **d** melanoma cells were treated weekly with Placebo, ecubectedin or PM54 at 1.2 mg/kg and survival was assessed. Results are shown as mean values \pm SD for “ n ” mice. The red bar indicates the dose period. The latency phase is indicated by an arrow. Logrank (Mantel–Cox) test was used

to determine the p -values. Source data are provided as a Source Data file.

e, f Indicated CDX models ($n = 8$ at the beginning of the experiment) from 501mel **e** or 501mel^{luciferase} **f** melanoma cells were treated once with Placebo, ecubectedin or PM54 at 1.2 mg/kg and tumor volumes were measured. Results are shown as mean values \pm SD for “ n ” mice. Logrank (Mantel–Cox) test was used to determine the p -values. Source data are provided as a Source Data file. **g, h** Indicated CDX models ($n = 8$ at the beginning of the experiment) from 501mel **g** or 501mel^{luciferase} **h** melanoma cells were treated once with Placebo, ecubectedin or PM54 at 1.2 mg/kg and survival was assessed. Results are shown as mean values \pm SD for “ n ” mice. Logrank (Mantel–Cox) test was used to determine the p -values. Source data are provided as a Source Data file.

experiments utilizing melanoma CDXs also demonstrated a rapid down-regulation of these genes, together with lineage-specific master transcription factors such as *MITF*, *SOX10* or *PAX3* following short-term treatments with synthetic ecteinascidins (Fig. 5c).

Ubiquitous transcription factors/coactivators and the mediator complex are pivotal in driving oncogenic expression in cancer cells by activating genes dependent on SEs. Therefore, in an effort to identify SEs in our melanoma cell models, we performed Cut&Tag assays targeting H3K27ac and BRD4 in differentiated and undifferentiated cells (501mel and MM029, respectively). Using the Rank Ordering of Super-Enhancers (ROSE) algorithm and cross-referencing the list of SEs identified from the Cut&Tag on H3K27ac and that on BRD4, we identified 533 and 347 bona fide SEs in differentiated and undifferentiated metastatic melanoma cells, respectively (Supplementary Fig. 8b,c and Supplementary Data 4). Subsequently, we identified by ROSE 1,255 and 951 genes putatively regulated by these bona fide SEs, in differentiated and undifferentiated melanoma cells, respectively (Supplementary Fig. 8d and Supplementary Data 4). Although 261 SE-dependent genes were shared between differentiated and undifferentiated cells, most SE-dependent genes seemed to be cell-state-specific. We next crossed these data with the list of down-regulated genes in both differentiated and undifferentiated metastatic melanoma cells following treatments with synthetic ecteinascidins and observed a significant enrichment of SE-dependent genes among those down-regulated genes (Fig. 5d). This was also observed in vivo, where SE-dependent oncogenes such as *MITF*, *SOX10*, *SAMMSON* or *MYC* were strongly downregulated upon treatment with synthetic ecteinascidins (Fig. 5c).

Synthetic ecteinascidins target transcriptionally active, CpG-rich genomic regions

We next sought to map the genome-wide binding sites of synthetic ecteinascidins in melanoma cells. Using bioactive biotinylated versions of lurbectedin and PM54 (Bio-lurbi and Bio-PM54) (Table 1), we conducted an in situ mapping of our compounds to genomic DNA using Chem-map⁴¹. We performed three biological replicates per compound, using both differentiated or undifferentiated melanoma cells (501mel and MM029, respectively), observing a high reproducibility with Spearman correlations exceeding 0.7 (Supplementary Fig. 9a). Our analysis revealed approximately 30,000 drug-binding sites in differentiated and 15,000 in undifferentiated cells (Fig. 6a and Supplementary Data 5). Notably, approximately 75 % of the identified drug-binding sites were found to be located in gene regions, with promoter (~25–34 %) and intronic (~32–35%) binding frequencies being consistent for both Bio-lurbi and Bio-PM54, in both cell types (Fig. 6b and Supplementary Fig. 9b). Overall, we observed a highly significant correlation between drug-bound gene promoters and genes down-regulated by the drugs (Fig. 6c and Supplementary Fig. 9c). Genome-wide, peaks of synthetic ecteinascidins predominantly co-localized with the transcriptionally active H3K27ac chromatin mark, RNAPII, BRD4 and positive ATAC-seq signals, and not with the repressive H3K27me3 chromatin mark (GSE205463⁴²) (Fig. 6d and Supplementary Fig. 9d). Indeed, between 80 and 90 % of

the synthetic ecteinascidins binding sites in 501mel and MM029 cells exhibited substantial overlaps with ATAC-seq signals (Fig. 6e and Supplementary Fig. 9e–g). Furthermore, our genome-wide analysis indicated that over 35% of synthetic ecteinascidins binding sites in 501mel cells and over 45 % in MM029 cells exhibited substantial overlaps with CpG islands (Fig. 6f and Supplementary Fig. 9h). Most of the CpG islands bound by the drugs were located in open chromatin regions, positive for ATAC-seq signal (Fig. 6g and Supplementary Fig. 9i). These data underscore the preferential binding of synthetic ecteinascidins to transcriptionally active genomic sites such as promoter regions, and suggest that they target the CpG islands located within these sites.

Synthetic ecteinascidins exhibit distinct patterns of chromatin binding associated with cell phenotypes

We subsequently integrated the chem-map data and observed a robust overlap (~80%) between the promoter regions bound by Bio-lurbi and those bound by Bio-PM54 in a given cell type (Fig. 7a, left panel). Notably, among the promoters bound by synthetic ecteinascidins, a significant fraction demonstrated concurrent binding by the two drugs in both cell types (Fig. 7a, right panel). This included promoters that regulate the expression of ubiquitous transcription factors/coactivators or Mediator subunits (Supplementary Data 6). In these promoters, such as those regulating expression of *EP300* or *CDK7*, a pronounced overlap was observed between the binding sites of synthetic ecteinascidins and CpG islands, H3K27ac, RNAPII and ATAC-seq signal (Fig. 7b).

Apart from the commonality in drug-bound promoters depicted above, each melanoma cell type also exhibited a subset of distinct and unique binding sites associated with its specific cellular phenotype. We observed a strong overlap between cell-state-exclusive binding sites and cell-state-specific H3K27ac sites at the corresponding genomic loci, once again suggesting a connection between drug binding and open chromatin (Fig. 7c and Supplementary Fig. 10a–d). In these specific binding sites, we identified sets of promoters which indeed demonstrated exclusive activity in either differentiated or undifferentiated cells. For instance, synthetic ecteinascidins bound to the promoter of the lineage-specific master transcription factor *MITF* gene only in differentiated cells, where it is highly expressed (Fig. 7d). Conversely, the promoter regulating the *Baculoviral IAP repeat-containing protein 3* gene (*BIRC3*), an inhibitor of apoptosis expressed only in undifferentiated melanoma cells, was occupied by synthetic ecteinascidins in undifferentiated but not in differentiated cells (Fig. 7e).

When examining the deposition of synthetic ecteinascidins along the *MITF* gene, drug-binding to its SE was also observed (Fig. 7d). In agreement, almost all (~95 %) of the bona fide SEs identified by ROSE in differentiated and undifferentiated cells were directly bound by the compounds (Fig. 7f). To gain a global understanding of the interplay between synthetic ecteinascidins and enhancer activity, we used the Active-By-Contact (ABC) model⁴³ to integrate our ATAC-seq, Cut&Tag, and RNAseq data with publicly available HiC data obtained in

differentiated melanoma cells (GSE105491⁴⁴). We generated a genome-wide annotation of all active cis-candidate regulatory regions (cCRE) directly implicated in activating gene expression in 501mel cells

(Supplementary Fig. 11a). Based on differential gene expression data, this model thus allowed the prediction of interactions between active enhancers and genes that were either positively or negatively

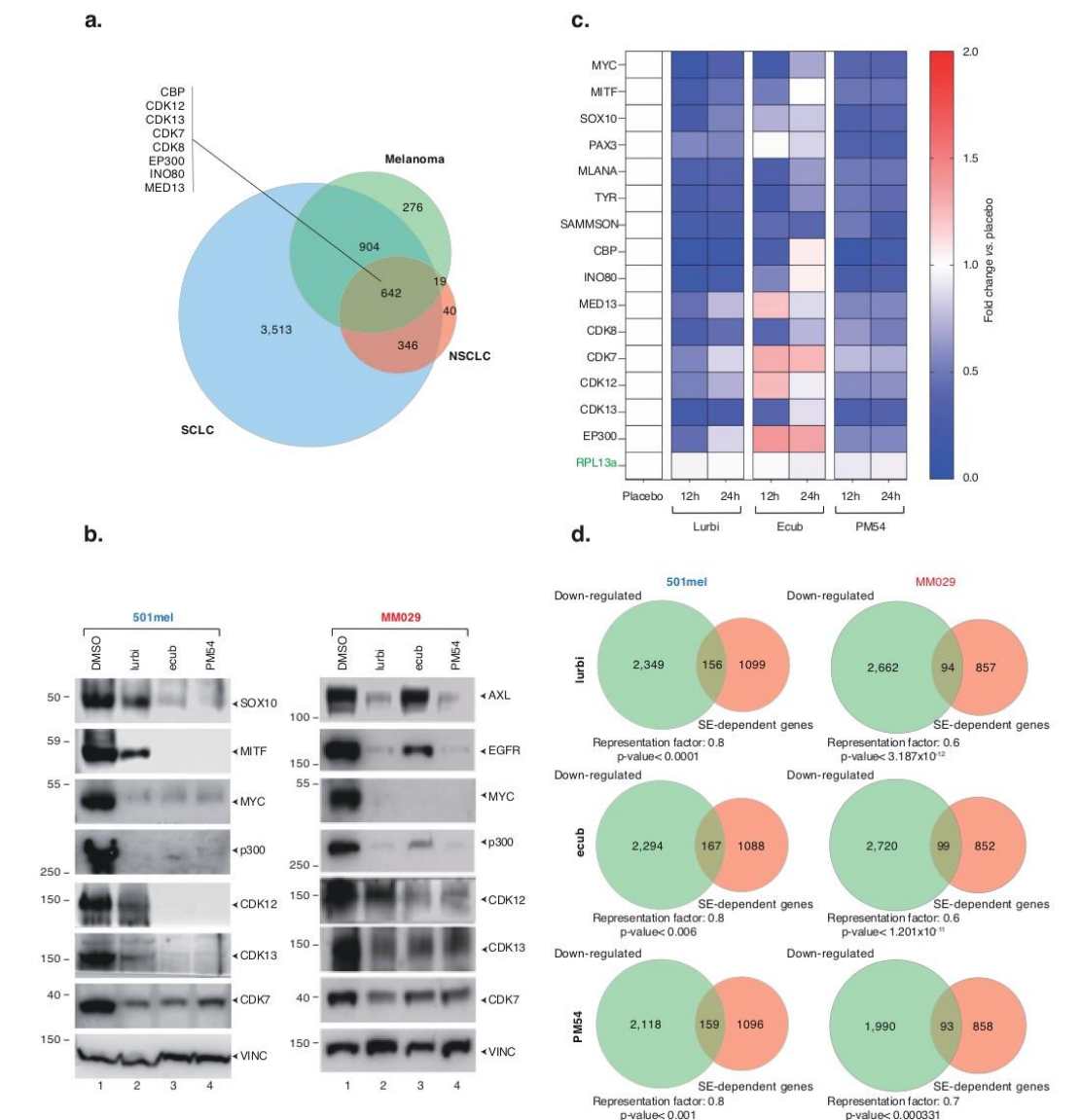
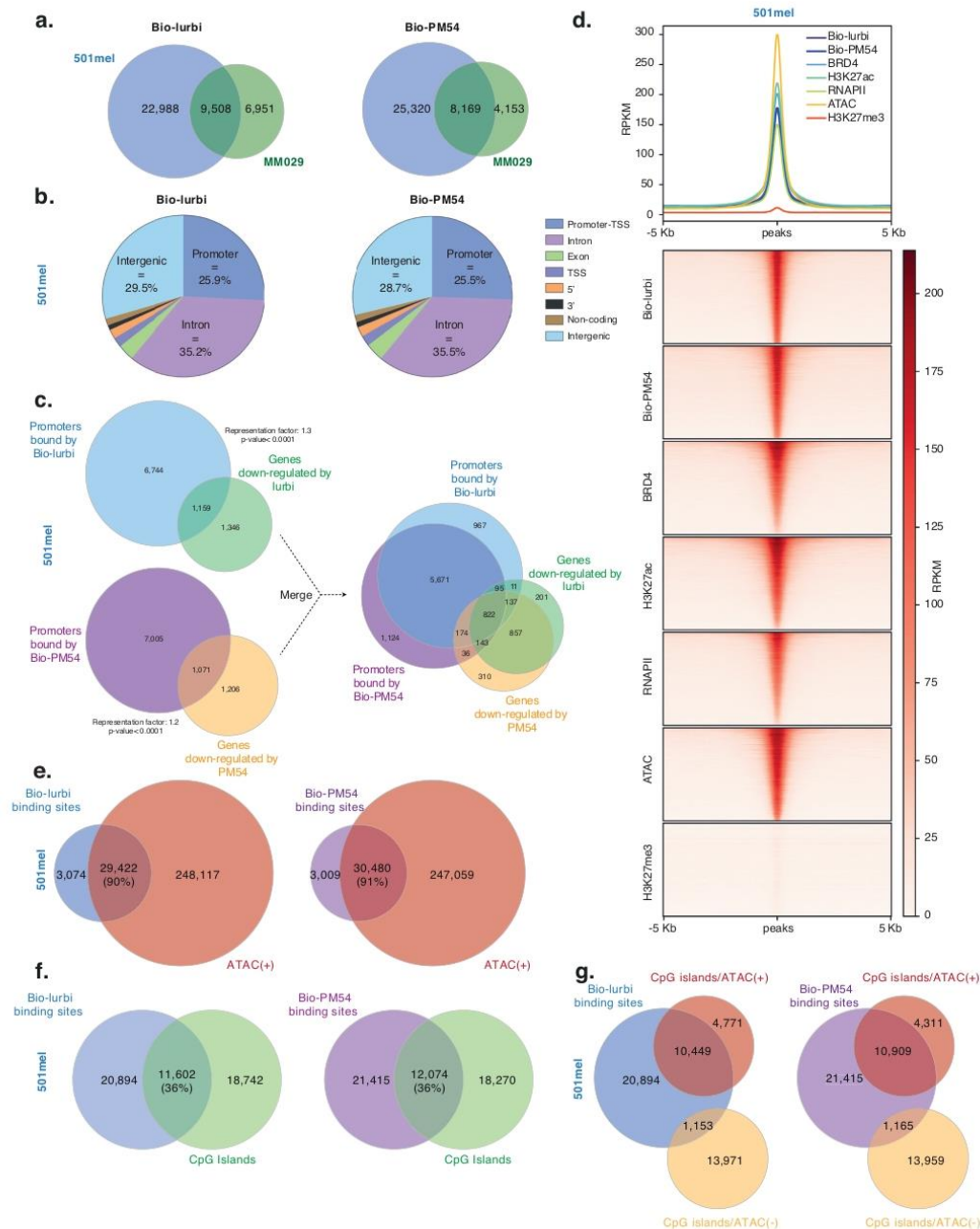


Fig. 5 | Synthetic ecteinascidins inhibit the expression of SE-dependent genes. **a** Venn diagram showing the overlap of genes down-regulated in melanoma (GSE256100), SCLC (GSE179074) and NSCLC (GSE179074), following treatment with lurbinatecin. **b** Differentiated 501mel (left) or undifferentiated MM029 (right) melanoma cells were treated with synthetic ecteinascidins as indicated (5x10⁻⁵ concentration, 24 h) and protein lysates were immuno-blotted for proteins as indicated. Molecular mass of the proteins is indicated (kDa). Source data are provided as a Source Data file. This experiment was repeated independently three times with similar results. **c** CDKs from 501mel cells ($n=3$) were treated with a single dose of

lurbinatecin, ecubectin or PMS4 at 1.2 mg/kg and tumors were collected 12 or 24 h later. Heatmap shows average placebo-normalized expression of the indicated genes obtained by qRT-PCR analysis. RPL13a is a housekeeping gene. **d** Venn diagram showing the overlap of genes down-regulated by synthetic ecteinascidins, as indicated, in 501mel (left) or MM029 cells (right) (10x10⁻⁵ concentration, 8 h) ($n=3$) and SE-dependent genes identified in these cells using H3K27ac- and BRD4-profiling by Cut&Tag and the ROSE algorithm⁴⁵. Representation factor and hypergeometric p -value are indicated and were determined using Graeber lab software. Hypergeometric distribution test was used to determine the p -values.



impacted by treatment with synthetic ecteinascidins. Notably, 4436 enhancers were inferred to be in contact with the promoters of genes down-regulated by treatment with synthetic ecteinascidins, such as the SE controlling *SOX10* expression (Supplementary Fig. 11b), while only 736 enhancers were inferred to be in contact with promoters of genes up-regulated by the same treatments (Supplementary Data 6). Enhancers controlling the expression of down-regulated genes tended

to be characterized by a higher ABC-score (higher enhancer activity) and contacted more genes than enhancers controlling expression of up-regulated genes (Supplementary Fig. 11c). In conclusion, the ABC model indicates that genes under the dependence of strong enhancers, such as SEs, might be particularly vulnerable to synthetic ecteinascidins, and that active enhancer-promoter interactions might be weakened by drug binding.

Fig. 6 | Synthetic ecteinascidins bind to CpG-rich sequences located in open chromatin regions. **a** Venn diagram of drug-binding sites (Bio-lurbi in the left and Bio-PM54 in the right) in 501mel vs. MM029 cells ($n = 3$). **b** Pie chart showing the distribution of annotated peaks (in percentages) for Bio-lurbi (top) and Bio-PM54 (bottom) all over the genome (hg19) in 501mel cells ($n = 3$). **c** Left panel: Venn diagram ($n = 3$) between promoters bound by Bio-lurbi or Bio-PM54 and genes down-regulated by lurbicetidin or PM54 in 501mel cells. Right panel: the two Venn diagrams ($n = 3$) were merged. Representation factor and hypergeometric p -value are indicated and were determined using Graeber lab software. Hypergeometric distribution test was used to determine the p -values. **d** Upper panel: Metaplot distribution ($n = 3$) of Bio-lurbi, Bio-PM54, BRD4, RNAPII, H3K27ac, H3K27me3 enrichment and ATAC-Seq signals in a ± 5 kb window around the occupied DNA binding sites of Bio-lurbi in differentiated 501mel cells. Lower panel: Heatmap

profiles representing the read density clusterings obtained with seqMINER for the DNA-occupied sites of Bio-lurbi in differentiated 501mel cells relative to Bio-PM54, BRD4, RNAPII, H3K27ac, H3K27me3 enrichments and ATAC-Seq signals. Peak order is determined by Bio-lurbi and identical for all clusterings. **e** Venn diagram ($n = 3$) between Bio-lurbi (left) or Bio-PM54 (right) binding sites and positive ATAC-Seq peaks (indicative of chromatin open regions) in differentiated 501mel cells. **f** Venn diagram ($n = 3$) between Bio-lurbi (left) or Bio-PM54 (right) binding sites and human CpG islands in differentiated 501mel cells. **g** Venn diagram ($n = 3$) between Bio-lurbi (left) and Bio-PM54 (right) binding sites in differentiated 501mel cells and human CpG islands. Human CpG islands are divided into those found in open chromatin regions (CpG islands/ATAC(+)) and those found in closed chromatin regions (CpG islands/ATAC(-)).

Collectively, these findings suggest that synthetic ecteinascidins impact SE-mediated oncogenic transcription by binding to and inhibiting the activity of the promoters of ubiquitous transcription factors/coactivators enriched at SEs, and potentially by directly targeting the enhancer/SEs driving oncogenic expression.

Synthetic ecteinascidins disrupt coactivator condensation at SEs

It was demonstrated that SE-enriched transcriptional coactivators such as BRD4 or the MED1 subunit of the Mediator complex form discrete nuclear puncta at SEs *ex vivo* to ensure robust expression of SE-dependent genes⁹. Based on the above data, we hypothesized that synthetic ecteinascidins could disrupt these condensates. Immunofluorescence revealed nuclear puncta for BRD4 that co-localized with the SE-specific histone mark H3K27ac in differentiated or undifferentiated melanoma cells (Supplementary Fig. 12a). Synthetic ecteinascidins disrupted BRD4 and MED1 puncta in both types of cells, similar to what was observed with 1,6-hexanediol, widely used to disorganize liquid-like condensates⁹ (Fig. 8a, b and Supplementary Fig. 12b). In contrast, treatment with dacarbazine, an alkylating compound that causes DNA damage and that is clinically used in the treatment of melanoma, did not affect BRD4 and MED1 puncta (Fig. 8a, b and Supplementary Fig. 12b). Treatment with the MEK1 trametinib even resulted in a significant increase in BRD4 and MED1 puncta, likely due to the reprogramming of enhancer/SE formation observed in melanoma cells following MEK1 treatment, leading to hyperdifferentiation⁴⁵. In agreement with these observations, trametinib and dacarbazine did not decrease the expression of SE-dependent genes such as *MITF* and *SOX10* in differentiated cells (MEK1 even increased their expression) or *AXL* and *EGFR* in undifferentiated cells (Supplementary Fig. 12c,d). ChIP-qPCR was used to further reveal that together with the inhibition of expression observed above, the level of H3K27ac and BRD4 was significantly reduced at the SEs regulating the expression of *MITF*, *SOX10*, *EGFR* or *AXL*, upon short-term treatment with synthetic ecteinascidins (Fig. 8c, d and Supplementary Fig. 12e,f). Note also that the level of H3K27ac was unaffected at the promoter of the 60S Ribosomal Protein L13a (RPL13a) housekeeping gene in these conditions (Supplementary Fig. 12g,h). Collectively, these results indicate that synthetic ecteinascidins disrupt the integrity of transcriptional condensates, consequently leading to the inactivation of SEs. They also highlight the specific mechanism of action of these drugs compared to current clinical treatments.

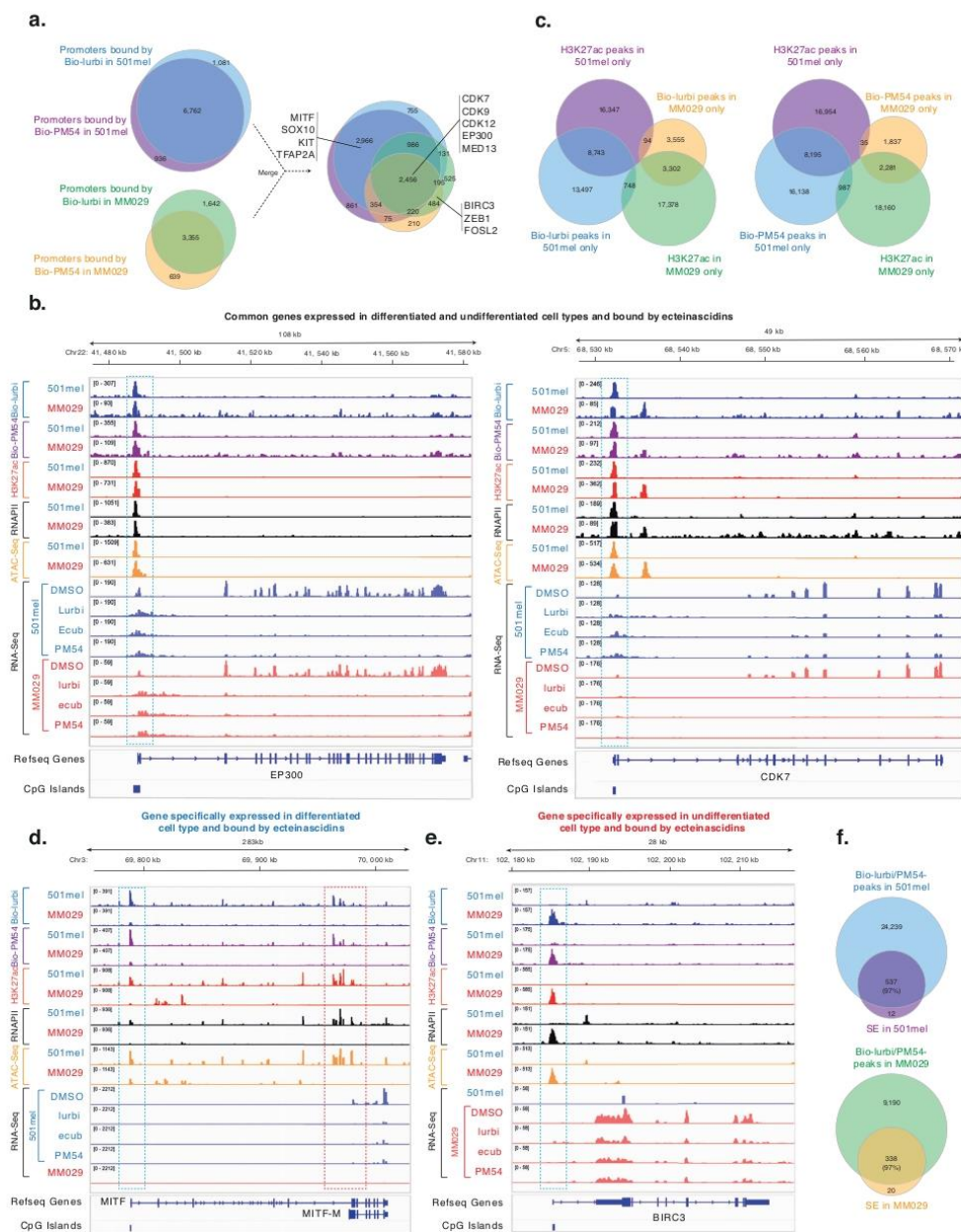
Synthetic ecteinascidins induce waves of transcriptional inhibition in melanoma and SCLC cells

The data above imply a model in which the inhibition of ubiquitous transcription factors/coactivators induces the inhibition of SE-dependent oncogenes. To test this model, we conducted kinetic analyses, revealing that transcription factors/coactivators were down-regulated before SE-dependent genes in melanoma cells (Fig. 9a, b and Supplementary Fig. 13a,b). We explored whether a similar mechanism

could occur in SCLC following treatment with synthetic ecteinascidins. We observed that transcription factors/coactivators were down-regulated very early in SCLC DMS53 cells upon treatments with synthetic ecteinascidins, followed by the inhibition of SCLC-specific SE-dependent genes such as *Achaete-scute homolog 1 (ASCL1)*, *B-Cell Leukemia/Lymphoma 2 (BCL2)*, *MYC*, *Neurogenic Differentiation Factor 1 (NEUROD1)* or *TEAD1* genes (Fig. 9c). In agreement, a significant enrichment of SE-dependent genes was observed among those down-regulated upon treatment with synthetic ecteinascidins in these cells (Supplementary Fig. 13c). While the ChIP-qPCR data in Fig. 8 cannot be generalized to all dysregulated genes in melanoma, we extended this analysis to SCLC using published data (GSE179074⁴⁵). We re-analyzed these data by focusing on three groups of genes with H3K27ac peaks at their TSS: those commonly down-regulated in melanoma, SCLC, and NCLC (348 genes); SCLC-specific SE-dependent genes (424 genes); and genes that were commonly unaffected (1434 genes) (Supplementary Data 7). ChIP-seq for H3K27ac, performed before and after treatment with lurbicetidin (GSE195663³⁵), revealed a loss of this active transcriptional mark at the promoters of commonly down-regulated genes (e.g., *CDK3*) and SCLC-specific super-enhancer-dependent genes (e.g., *MYC*) (Fig. 9d, e). Notably, H3K27ac was significantly less affected at the promoters of genes whose expression was unaffected by lurbicetidin, such as the housekeeping gene *RPL13a*. Overall, these data suggest that synthetic ecteinascidins induce an initial inactivation of promoters regulating the expression of transcription factors and coactivators, which triggers a secondary inactivation of the promoters of SE-dependent oncogenes.

Discussion

Metastatic melanoma cells exhibit significantly higher mutational burdens compared to other cancer types, potentially leading to proportional dysregulation of gene expression patterns. Furthermore, the well-documented cell-state plasticity of melanoma cells underscores their robust reliance on tightly regulated oncogenic gene expression programs. This cancer type, therefore, serves as an ideal model for investigating the clinical relevance and therapeutic potential of targeting oncogenic transcriptional addiction. Comparative analyses were conducted to evaluate the impact of three synthetic ecteinascidins relative to clinically utilized MAPKi agents. Notably, metastatic undifferentiated melanoma cells displaying inherent resistance to MAPKi/immunotherapy, as well as *in vitro* engineered hyperpigmented cells with acquired MAPKi resistance⁴⁴, exhibited comparable sensitivity to the three synthetic ecteinascidins at low nanomolar concentrations. Single-cell sequencing has unveiled additional cell states within melanoma tumors, such as interferon-active melanoma cells that emerge during the minimal residual disease phase, post-treatment with MAPKi^{19,30}. The significance of these cells in the context of resistance to treatment has been significantly underestimated. In an attempt to mimic these cell subpopulations *in vitro*, we have generated pseudo-interferon-active melanoma cells by treatment with interferon- γ . Intriguingly, these pseudo-interferon-active melanoma



cells exhibited sustained sensitivity to synthetic ecteinascidins while acquiring resistance to MAPKi (Supplementary Fig. 14 and Table 1). In vivo, we observed significant decreases in mitotic indexes and increases in cell death and overall survival in four different melanoma CDX models, including MAPKi-resistant CDXs. Our data demonstrate that synthetic ecteinascidins exhibit high cytotoxic impact both in vitro and in vivo on the most common melanoma cell phenotypes, as

well as on drug-tolerant cell populations emerging during the minimal residual disease phase.

Our results elucidate the mechanisms of action of synthetic ecteinascidins, highlighting their common features and revealing some notable differential molecular effects. Low nanomolar doses of synthetic ecteinascidins consistently reduced the proliferation and invasive capacities of metastatic melanoma cells while inducing

Fig. 7 | Synthetic ecteinascidins exhibit distinct patterns of chromatin binding associated with cell phenotypes. **a** Left panel: Venn diagrams ($n = 3$) between promoters bound by Bio-lurbi and Bio-PM54 in 501mel (top) and MM029 (bottom) cells. Right panel: the two Venn diagrams were merged. **b** Gene tracks of Bio-lurbi, Bio-PM54, RNAPII, H3K27ac occupancy, ATAC-seq and RNA-Seq signals at CDK7 (left) or EP300 (right) loci in 501mel or MM029 cells. RNA-Seq signals show that these genes are expressed in both 501mel and MM029 melanoma cells. In blue, drug binding at promoters is highlighted. Localization of CpG islands is shown. **c** Left panel: Venn diagrams ($n = 3$) comparing genomic bindings sites uniquely bound by Bio-lurbi in either 501mel or MM029 cells with H3K27ac peaks found exclusively in either 501mel or MM029 cells. Right panel: Venn diagrams comparing genomic bindings sites uniquely bound by Bio-PM54 in either 501mel or MM029 cells with H3K27ac peaks found exclusively in either 501mel or MM029 cells. We considered different peaks as overlapping if there was at least 1 bp of overlap. **d** Gene tracks of Bio-lurbi, Bio-PM54, RNAPII, H3K27ac occupancy, ATAC-seq and

RNA-Seq signals at the MITF locus in 501mel or MM029 cells. RNA-Seq signals show that this gene is only expressed in differentiated 501mel cells. The red square indicates the SE regulating the expression of MITF. In blue, drug binding at the promoter is highlighted. In red, drug binding at the SE is highlighted. Localization of CpG islands is shown. Note that MITF-M isoform is expressed in melanoma. **e** Gene tracks of Bio-lurbi, Bio-PM54, RNAPII, H3K27ac occupancy, ATAC-Seq and RNA-Seq signals at the BIRC3 locus in 501mel or MM029 cells. RNA-Seq signals show that this gene is only expressed in undifferentiated MM029 melanoma cells. In blue, drug binding at the promoter is highlighted. Localization of CpG islands is shown. **f** Upper panel: Venn diagrams ($n = 3$) comparing all genomic bindings sites commonly bound by Bio-lurbi and Bio-PM54 and bona fide super-enhancers identified in 501mel cells. Lower panel: Venn diagrams comparing all genomic bindings sites commonly bound by Bio-lurbi and Bio-PM54 and bona fide super-enhancers identified in MM029 cells.

apoptosis and blocking the cell cycle in the G2/M phase. Drug treatments also led to the significant disruption of oncogene expression. Importantly, the transcriptional effects of the compounds appeared to exhibit a high degree of specificity for distinctly overexpressed oncogenes depending on the melanoma cell state. For instance, while the expression of housekeeping genes was unaffected in 2- or 3-D conditions by short-term drug treatments, lineage-specific drivers of proliferation such as MITF, SOX10 or PAX3 were strongly inhibited specifically in differentiated cells. In undifferentiated cells, different genes were affected, such as the key regulators AXL or EGFR, the anti-apoptotic protein BIRC3 or the cell-type master transcription factors FOSL2 and TEAD4. These observations arguably reveal the most interesting feature of these next-generation compounds: synthetic ecteinascidins appear to specifically inhibit the distinct oncogenic transcription programs on which a given cancer cell subpopulation depends. Thus, this unique mechanism of action differentiates synthetic ecteinascidins from conventional chemotherapeutic DNA-binding/DNA-modifiers, such as platinum derivatives or dacarbazine, which induce DNA damage uniformly across the genome. Moreover, the efficacy of synthetic ecteinascidins does not depend on the phenotypic nature of the melanoma cell, a feature that differentiates these drugs from conventional MAPKi therapies and immunotherapies²⁰.

Mechanistically, our results highlight a multifaceted mechanism of action by which synthetic ecteinascidins impede oncogenic transcription. Synthetic ecteinascidins bind to promoter/enhancer regions of genes encoding ubiquitous transcription factors/coactivators, usually strongly enriched at SEs, leading to their rapid inhibition. This effect is likely potentiated by the fact that promoters/enhancers of genes encoding lineage-specific master transcription factors such as MITF or SOX10 are also heavily bound by synthetic ecteinascidins in melanoma cells. These master regulators are known to bind SEs to form autoregulatory loops that constitute the core transcriptional regulatory circuitries of cancer cells. The disruption of these oncogenic expression loops, coupled with the strong binding of synthetic ecteinascidins to SEs themselves, albeit with uncertain biological consequences, potentially ensures the robust inhibition of SE-driven oncogenic transcription. Importantly, these observations extend beyond melanoma cells, as SE-driven transcription was also inhibited in SCLC cells exposed to synthetic ecteinascidins, establishing these molecules as potential universal pan-disruptors of SEs. Overall, the inhibition of SE-driven oncogenic transcription has a potent cytostatic/cytotoxic impact on cancer cells, as demonstrated *in vivo* by the inhibition of cell proliferation and induction of apoptosis. In a second line of attack, synthetic ecteinascidins induce DNA breaks that persist over time and that synergize with transcription inhibition to trigger cell death.

Delving deeper into the transcriptional effects elicited by the three compounds, we observed that while the gene expression changes elicited by lurbinectedin and ecubectedin greatly overlapped, the

transcriptional effects of PM54 significantly diverged. Notably, PM54 treatments deregulated fewer genes than lurbinectedin or ecubectedin while eliciting the same cytostatic and cytotoxic effects, potentially representing a clinical benefit. Although the exact mechanism explaining this difference is yet to be determined, it may be related to the fact that the moiety modified in PM54 vs. lurbinectedin is located in the area of the molecule described as interacting with DNA binding proteins/transcription factors⁴⁶. Such a differential interaction between the drug and transcription factors might result in fewer systemic gene expression disruptions and, thus, fewer unwanted secondary effects, while still potentially targeting oncogenic SE-dependent gene expression, leading to cancer cell death. Consequently, Phase I clinical trials for PM54 in advanced solid tumors, including melanoma, were initiated (ClinicalTrials.gov Identifier: NCT05841563, EudraCT Number 2022-002031-65).

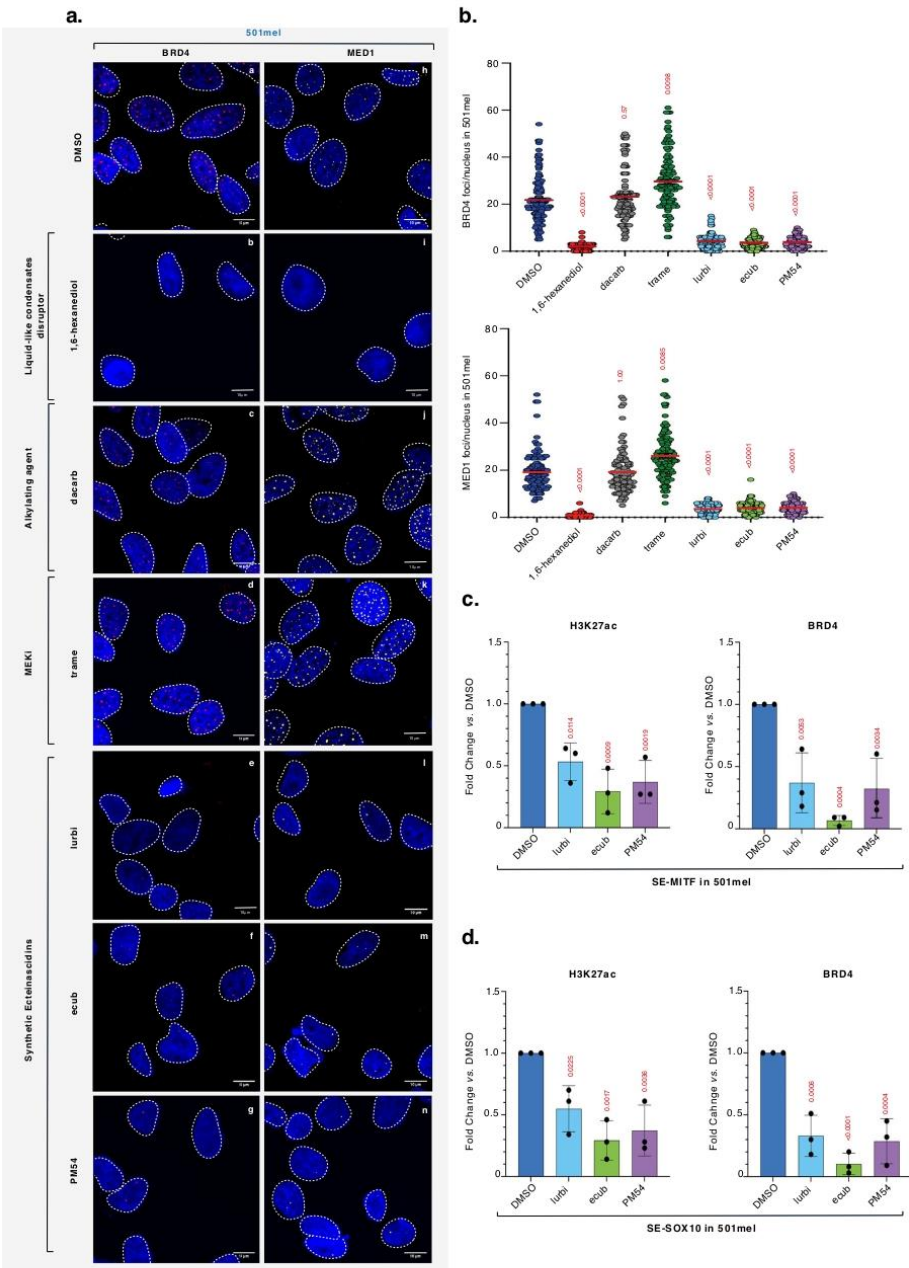
Collectively, our data provide a comprehensive overview of the cellular and molecular effects of a potential therapeutic approach to melanoma and other transcriptionally-addicted cancers based on SE-dependent oncogenic inhibition. The current study further illuminates the intricacies of gene expression dependencies of different melanoma cell subpopulations and their molecular responses to transcriptional disruptions. This preclinical work might justify the clinical testing of synthetic ecteinascidins as a second-line melanoma treatment following MAPKi/immunotherapy relapse, but it also highlights the potential benefits of further exploring the effects of additional structural analogs. Finally, recent observations demonstrated that synthetic ecteinascidins, such as lurbinectedin, synergize with immune checkpoint blockade and stimulates proliferation of CD4⁺ and CD8⁺ T cells. These immune-modulatory functions make synthetic ecteinascidins a potential platform for immunotherapy combination in melanoma^{47,48}.

Methods

All animal experimental procedures were reviewed and approved by an Internal Ethical Committee and by "O.H. Universidad Miguel Hernández de Elche" and "O.H. Hospital General Universitario Gregorio Marañón", and, finally, authorized by "Comunidad Autónoma de Madrid, CAM" (regional Institutional Animal Care and Use Committee), reference PROEX 042/16 and PROEX 285.7/23. All experimental procedures were performed in accordance with national and international laws and policies: Spanish directive RD 53/2013 and EU Directive 2010/63/EU. Animals were euthanized through the administration of an overdose of a general anesthetic when their tumors reached ca. 1500 mm³ and/or severe necrosis was seen. Treatments which produced >20 % lethality and/or 20 % net body weight loss were considered toxic and stopped.

Cell culture and treatment

When registered, cells used in this work are identified by a research resource identification number (RRID number (<https://rrid.site>)). Cell



line identity, when applicable, was confirmed annually through STR profiling provided by ATCC's cell authentication service. Hermes3A, RRID:CVCL_VS10; DMS53, RRID:CVCL_1177; 501mel, RRID:CVCL_4633; SKMEL-28, RRID:CVCL_0526; IGR37, RRID:CVCL_2075; IGR39, RRID:CVCL_2076; WM266-4, RRID:CVCL_2765; LOX-IMVI, RRID:CVCL_1381; A549, RRID:CVCL_0023; HaCaT, RRID:CVCL_0038; MRC5, RRID:CVCL_0440. All cells were obtained from ATCC or

collaborators, as indicated in Supplementary Data 8. Cells were grown at 37 °C in 5% CO₂ (10 % for Hermes 3A) and were regularly checked for mycoplasma contamination by the PluriCell East Platform (<https://www.igbmc.fr/en/platforms-and-services/services/pluricell-east>). MM patient-derived short-term melanoma cultures (MM011, MM074, MM117, MM029, MM047, MM099) are derived from patient biopsies and were grown in HAM-F10 (Gibco, Invitrogen) supplemented with 10

Fig. 8 | Synthetic ecteinascidins disrupt transcription factor/coactivator condensates at SEs. **a** Representative confocal microscopy images ($n = 3$) of 501mel melanoma cells treated with either DMSO, the condensate disruptor 1,6-hexanediol (3% vol, 20 min), the MEK1 trametinib (15 nM, 10 h), the DNA damaging agent dacarbazine (50 μ M, 10 h) or the synthetic ecteinascidins (5xIC50, 10 h). Cells were immunostained with anti-BRD4 (red) or anti-MED1 (white) antibodies. Images of the cells were obtained with the same microscopy system and constant acquisition parameters for a given staining. Source data are provided as a Source Data file. Scale bar: 10 μ m. **b** The numbers of MED1 and BRD4 foci per nucleus observed in 501mel

cells following treatment with the drugs described above are shown \pm SD for three biological triplicates. Red bars indicate mean integrated density. One-way ANOVA with post-hoc Tukey adjustment comparisons were used to determine the p -values (vs. DMSO). **c**, **d** ChIP-qPCR monitoring the fold change of H3K27ac mark or BRD4 protein at the SEs regulating MITF (left) or SOX10 (right) in mock- or synthetic ecteinascidin-treated (5xIC50, 10 h) differentiated 501mel cells. Error bars indicate mean values \pm SD for three biological triplicates. One-way ANOVA with post-hoc Tukey adjustment comparisons were used to determine the p -values (vs. DMSO). Source data are provided as a Source Data file.

% Fetal Calf Serum (FCS), 25 mM HEPES, 5.2 mM GLUTAMAX and penicillin-streptomycin. Melanoma cell lines 501mel and SKmel28 were grown in RPMI w/o HEPES (Gibco, Invitrogen) supplemented with 10 % FCS and gentamycin. Vemurafenib-resistant cells (501mel^{IVemur} and MM074^{IVemur}) were additionally supplemented with 1.5 mM of vemurafenib. Melanoma IGR cell lines (IGR37 and IGR39) were grown in RPMI w/o HEPES (Gibco, Invitrogen) supplemented with 15 % FCS and gentamycin. Immortalized melanocytes Hermes-3A were grown in RPMI w/o HEPES supplemented with 10 % FCS, penicillin-streptomycin, 200 nM TPA (Sigma Aldrich), 200 p.m. Cholera Toxin (Sigma Aldrich), 10 ng/mL hSCF (Life Technologies), 10 nM EDN-1 (Sigma Aldrich) and 2 mM Glutamine (Invitrogen). HaCaT and MRC5 were grown in DMEM (1g/L glucose) +10% FCS + Gentamycin 40 mg/mL. SCLC cell line DMS53 was grown in Waymouth's MB medium (Gibco, Invitrogen), supplemented with 10% FCS and gentamycin. 501mel, SKmel28, IGR and DMS53 cells were purchased from ATCC, MM and Hermes-3A cells were obtained from collaborators. Vemurafenib (PLX4032), trametinib (GSK1120212), dabrafenib (GSK2118436) and dacarbazine (S1221) were purchased from Selleckchem. 1,6-Hexanediol was obtained from Sigma Aldrich (88571). Lurbinectedin (PM1183), ecubectedin (PM14), and PMS4 were obtained from PharmaMar S.A. Recombinant Human IFN- γ was obtained from Peprotech (300-02).

Different in vitro drug incubation periods were chosen depending on the nature of the experiments, considering that cell viability is reduced by 50% after 72 h of treatment with 1xIC50 concentrations. For assays studying the impact of the treatments on cancer cell phenotypes related to cancer cell death, such as the inhibition of cell proliferation, the induction of apoptosis and cell cycle blockage, we opted to refer to these same conditions (1xIC50, 72 h). To assess effects preceding cell death, such as impacts on clonogenicity and invasive capacities, a shorter incubation period was chosen (1xIC50, 48 h). For effects relating to gene expression, shorter incubation periods with higher drug concentrations (5xIC50, 12 h for RT-qPCRs; 10xIC50, 8 h for RNA-Seq and Chem-Map, 5xIC50, 24 h for Western Blotting and 5xIC50, 10 h for immunofluorescence and ChIP-qPCR) allowed us to study more closely the immediate and direct effects of the drugs on cancer cell transcriptomes and epigenomes. The used drug concentrations and treatment durations are stated in the respective figure legends.

Protein extraction and western blotting

For whole cell extracts, cells were rinsed once with cold PBS, before pelleting and resuspension in LSDB 0.5M buffer (500 mM KCl, 50 mM Tris pH 7.9, 20% glycerol, 1% NP-40, 1 mM DTT, phosphatase inhibitor and protease inhibitor cocktail). Afterwards, cells were fully disrupted with 3 cycles of heat shock (liquid nitrogen followed by 37 °C water bath). Then, samples were centrifugated for 15 min at 11,000g to remove cell debris. Lysates were subjected to SDS-polyacrylamide gel electrophoresis (SDS-PAGE) and proteins were transferred onto a nitrocellulose membrane. Membranes were incubated overnight 4 °C with primary antibodies in PBS + 5% milk powder + 0.01 % Tween-20. The membranes were then incubated with HRP-conjugated secondary antibody (Jackson ImmunoResearch) for 1 h at room temperature and visualized using the ECL detection system (GE Healthcare).

IC50 estimation

Cells were seeded at 5×10^3 cells/well in 96-well plates and treated with increasing concentrations of vemurafenib, dabrafenib, trametinib, lurbinectedin, ecubectedin, or PMS4. After 72 h of incubation, cells were treated with PrestoBlue reagent (ThermoFisher) according to the manufacturer's instructions. The absorbance per well was measured with a CellInsight CX5 microplate reader (ThermoFisher). Determination of IC50 values was performed by nonlinear curve fitting using the Prism9 statistical software (GraphPad). To assess the effect of IFN γ on drug sensitivities, cells were pre-treated with IFN γ (20 ng/mL) for 24 h, before being treated as mentioned above, while maintaining IFN γ (20 ng/mL) in the medium.

Clonogenicity assay

Cells were drug-treated at IC50 concentrations during 48 h before seeding 1×10^3 or 2×10^3 cells in 6-well plates without drugs, where they grew for 10 days to allow for colony formation. Afterwards, cells were washed once with PBS, then fixed for 10 min with 4% Paraformaldehyde solution, and stained with Crystal Violet solution 0.2% for 15 min. The wells were finally washed twice with deionized water, air dried, scanned and analyzed with Fiji software to count the number of colonies.

Cell proliferation, apoptosis, and cell cycle analysis by flow cytometry

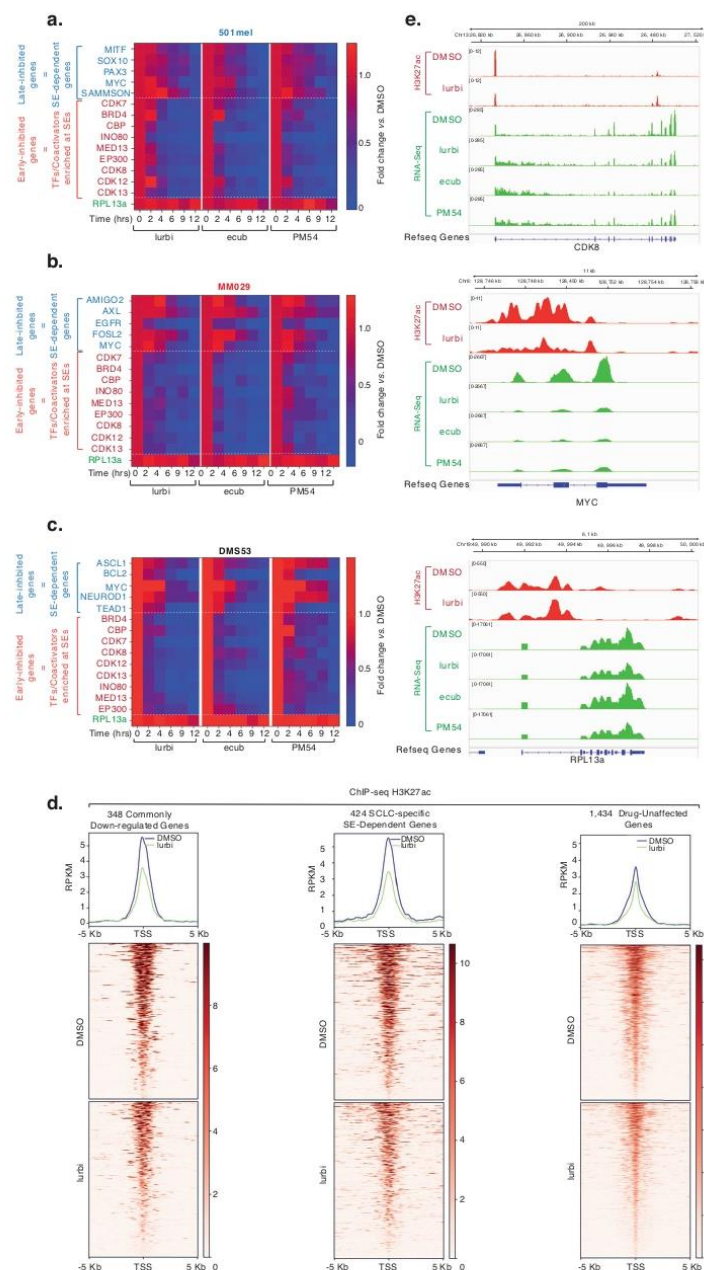
2×10^5 cells were seeded in 6-well plates and were incubated 24 h later with 1 μ M of CellTrace Violet reagent (ThermoFisher) according to the manufacturer's instructions, immediately before rinsing and drug treatment at IC50 concentrations. After 72 h of incubation, cells were rinsed and incubated with AnnexinV-APC (BD Biosciences). Cell proliferation and apoptosis were detected on a BD LSRFortessaTM Flow Cytometer. Data were analyzed with FlowJo software. To define slow proliferating or apoptotic cells, we proceeded as follows: We considered that slow proliferating cells represented the 30 % of cells with the highest concentration of CellTrace Violet signal in the DMSO control. We then calculated the % of cells that had a signal greater than or equal to this value with drug treatment. For apoptotic cells, we considered the 20% of cells with the highest signal of AnnexinV-APC in the DMSO control.

For cell cycle analysis, 2×10^5 cells were seeded in 6 well plates. After 72 h of drug treatments at IC50 concentrations, cells were pelleted and fixed with 70% ethanol for 1 h at 4 °C. After 2 washes with cold PBS, cells were incubated with RNaseA and Propidium Iodide (PI, Biolegend) for 1 h in the dark, before being analyzed on a BD LSRFortessaTM Flow Cytometer. Data were analyzed with FlowJo software.

For apoptosis assays with 3D-grown melanoma cells, TrypLe Select 10x reagent (Gibco) was used to dissociate melanospheres to obtain single-cell suspensions. These cells were incubated with AnnexinV-APC (Biolegend) and PI. With bivariate dot plots, we distinguished between viable (AnnexinV- / PI-), early apoptotic (AnnexinV+ / PI-), late apoptotic (AnnexinV+ / PI+) and necrotic cells (AnnexinV- / PI+).

Boyden chamber invasion assay

2×10^5 cells were seeded inside Boyden Chamber inserts (Fisher Scientific) with 4% Matrigel (Corning) and covered with serum-free media.



The inserts were placed in 24 well plates filled with complete medium. After 24 h, the inserts were washed once with PBS, fixed for 10 min with 4% paraformaldehyde solution, and stained with Crystal Violet solution 0.2% for 15 min. The wells were finally washed twice with deionized water, air dried, and photos were collected using an EVOS xl Core microscope. The pictures were analyzed with Fiji to assess the area of occupancy of the cells.

Melanosphere formation and viability assay

5×10^4 cells were seeded in ultra-low attachment hydrogel-layered 96 well plates (Corning 7007) in KO DMEM medium supplemented with 20 % KSR, AANE, 2mM Glutamax, Penicillin/Streptomycin and 100 μ M Beta-mercaptoethanol. To allow for melanosphere formation, cells were left to grow for 4 days before drug treatment.

Fig. 9 | Transcriptional inhibition waves induced by synthetic ecteinascidins in melanoma and SCLC cells. **a, b** Heatmap showing average 18S-normalized expression ($n = 3$) of the indicated genes in 501mel **a** and MM029 **b** cells treated with either lurbinedetin, ecubectedin or PM54 (5xIC50 concentration) for the indicated period of time. Results were obtained by RT-qPCR and are shown as relative expression compared to DMSO-treated cells. RPL13a is a housekeeping gene. **c** Heatmap showing average 18S-normalized expression ($n = 3$) of the indicated genes in DMS53 cells (SCLC) treated with synthetic ecteinascidins (5xIC50 concentration (IC50 = 0.11 nM for lurbinedetin, 0.16 nM for ecubectedin and 0.15 nM for PM54)) for the indicated period of time. Results were obtained by RT-qPCR and are shown as relative expression compared to DMSO-treated cells. RPL13a is a housekeeping gene. **d** Upper panel: This analysis ($n = 3$) focuses on three gene sets: (1) genes commonly downregulated after treatment in melanoma, SCLC, and NSCLC cells, (2) putative super-enhancer-dependent genes in DMS53 SCLC

cells, and (3) genes whose expression exhibited a fold change between 0.9 and 1.1 relative to DMSO, which we considered unaffected by the treatment (GSE195663). These sets comprised 648, 424, and 8435 genes, respectively. From these genes, we selected only the genes presenting H3K27ac peaks located at their transcription start sites (TSS), yielding 348 genes for the commonly downregulated genes across the three cancers, 424 for the SCLC super-enhancer-dependent genes, and 1434 for the unaffected genes (see Supplementary Data 7). Metaplot distribution shows H3K27ac signal in a ± 5 kb window around the TSS of these three groups of genes in mock- or lurbinedetin-treated DMS53 cells (GSE179074). Lower panel: Heatmap profiles representing the read density clusters obtained with seqMINER for the H3K27ac signal. **e** Gene tracks showing H3K27ac occupancy and RNA-Seq signals ($n = 3$) at the CDK8 (top), MYC (middle) and RPL13a (bottom) loci in mock- or lurbinedetin-treated DMS53 cells.

To analyze melanosphere viability after drug treatment, cells were treated with CellTiterGlo reagent (Promega) according to the manufacturer's instructions. Luminescence signals were measured with a Centro XS LB 960 microplate reader (Berthold).

Immunofluorescence assays

After PBS-rinsing, cells grown on coverslips were fixed with 4% paraformaldehyde for 15 min. Cells were then permeabilized with PBS and 0.1% Triton X-100. Blocking was done with 10% BSA. Primary antibodies were incubated overnight at 4 °C, after which cells were stained for 1 h at room temperature with AlexaFluor-conjugated secondary antibodies diluted in PBS + 10% FCS (Life technologies) and stained with DAPI. For BRD4 and MED1 foci quantifications, image acquisition was performed on a TCS SP5 inverted confocal microscope (Leica), and foci were counted using the Cell Counter plugin of the Fiji software.

For immunohistochemistry, tumors were grown as mentioned above and were extracted after 24 h following a single dose of placebo treatment or 1.2 mg/kg of ecubectedin or PM54. In parallel, untreated tumors were extracted. The tumors were fixed in 10% formalin and embedded in paraffin for histology. Slides prepared from 5 μ m-thick paraffin sections were processed for antigen retrieval in 10 mM sodium citrate buffer (PH = 6.0) for 45 min at 95 °C in a water bath. The slides were cooled down at room temperature (RT) for 15 min. They were rinsed in PBS and then incubated in a humidified chamber for 16 h at 4 °C, with the primary antibodies diluted in PBS containing 0.1% (v/v) Tween 20 (PBST) to detect mitotic (pHH3-positive) and apoptotic (cleaved caspase 3-positive) cells. After rinsing in PBST, detection of the bound primary antibodies was performed for 1 h at room temperature in a humidified chamber using 555-conjugated secondary rabbit IgG antibody. The sections were then counterstained with DAPI to label nuclei. Stained sections were digitalized using a slide scanner (Nanozoomer 2.0-HT, Hamamatsu) and analyzed with the corresponding ND.View2 software.

Large 8-Bits digital scanned images of tumors stained for nuclei (10,000 to 30,000 nuclei per section) and pHH3 or cleaved caspase 3 were processed through an inhouse python (v3.8) algorithm to quantify positive cells. Basically, blue channels were proposed to a Cellpose2 model (deep learning model backbone by pytorch process) to segment nuclei. Subsequently, nuclei were analyzed for specific signals. For pHH3, a nucleus was considered positive if total pixels above 50 in intensity value exceeds 20% of nuclei surface (in 8 Bits image values range from 0 [no signal] to 255). Hence, we ensured that we did not consider unspecific background signals or insignificantly bright signals. The same procedure was applied to Caspase3 with pixel value set to 50 and minimal covered surface set to 30%. For each image, a ratio of positive cells/total nuclei was returned as the experimental variable. Statistics were produced using python's pingouin library (v0.5.3) with two-way ANOVA and post hoc tests being built-in functions.

High throughput sequencing

Supplementary Data 9 provides additional information about high throughput sequencing data, including among others, sequences quality controls, preprocessing, mapping, quantification and normalization methods, as well as size-number matched shuffled regions controls for Chem-Map data.

a. Bulk RNA-Seq and analysis. Library preparation was performed at the GenomEast platform at the Institute of Genetics and Molecular and Cellular Biology using TruSeq Stranded Total RNA Reference Guide - PN 1000000040499. Total RNA-Seq libraries were generated from 700 ng of total RNA using TruSeq Stranded Total RNA Library Prep Gold kit and TruSeq RNA Single Indexes kit A and B (Illumina, San Diego, USA), according to manufacturer's instructions. Briefly, cytoplasmic and mitochondrial ribosomal RNA (rRNA) was removed using biotinylated, target-specific oligos combined with Ribo-Zero rRNA removal beads. Following purification, the depleted RNA was fragmented into small pieces using divalent cations at 94 °C for 8 min. Cleaved RNA fragments were then copied into first strand cDNA using reverse transcriptase and random primers followed by second strand cDNA synthesis using DNA Polymerase I and RNase H. Strand specificity was achieved by replacing dTTP with dUTP during second strand synthesis. The double stranded cDNA fragments were blunted using T4 DNA polymerase, Klenow DNA polymerase and T4 PNK. A single 'A' nucleotide was added to the 3' ends of the blunt DNA fragments using a Klenow fragment (3' to 5' exo minus) enzyme. The cDNA fragments were ligated to double stranded adapters using T4 DNA Ligase. The ligated products were enriched by PCR amplification. Surplus PCR primers were further removed by purification using AMPure XP beads (Beckman-Coulter, Villepinte, France) and the final cDNA libraries were checked for quality and quantified using capillary electrophoresis. Libraries were sequenced on an Illumina HiSeq 4000 sequencer as single read 50 base reads. Image analysis and base calling were performed using RTA version 2.7.7 and bcl2fastq version 2.20.0.422.

Reads were preprocessed to remove adapter and low-quality sequences (Phred quality score below 20). After this preprocessing, reads shorter than 40 bases were discarded for further analysis. These preprocessing steps were performed using cutadapt version 1.10. Reads were mapped to rRNA sequences using bowtie version 2.2.8 and reads mapping to rRNA sequences were removed for further analysis. Reads were mapped onto the hg19 assembly of Homo sapiens genome using STAR version 2.5.3a. Gene expression quantification was performed from uniquely aligned reads using htseq-count version 0.6.1p1, with annotations from Ensembl version 75 and "union" mode. Only non-ambiguously assigned reads have been retained for further analyses. Read counts have been normalized across samples with the median-of-ratios method proposed by Anders and Huber⁴² to make these counts comparable between samples. Comparisons of interest were performed using the Wald test for differential expression⁴⁹ and implemented in the Bioconductor package DESeq2 version 1.16.1.

Genes with high Cook's distance were filtered out and independent filtering based on the mean of normalized counts was performed. *P*-values were adjusted for multiple testing using the Benjamini and Hochberg method⁵⁰. Deregulated genes were defined as genes with $\log_2(\text{Fold change}) > 1$ or < -1 and adjusted *P*-value < 0.05 .

Volcano plots were generated using the Prism9 statistical software (GraphPad). Heatmaps were generated using Morpheus (<https://software.broadinstitute.org/morpheus>). Venn diagrams were generated using DeepVenn (<http://www.deepvenn.com/>) and representation factors and hypergeometric *P*-values were determined using Graeber lab software (<https://systems.crump.ucla.edu/hypergeometric/>). GO Analysis was performed using ShinyGO. Metascape and enrichr analyzes can be found in Supplementary Data 9⁵¹. The number of assigned reads for each sample exceeds 15.10^6 (Supplementary Data 9), ensuring adequate coverage of the majority of expressed genes, with the exception of very low-expressed ones.

b. Chem-map and Cut&Tag. 501mel and MM029 cells were seeded and grown to sub-confluency in 15-cm plates before treatment for 8 h with DMSO, biotinylated lurbinctedin (Bio-lurbi) or biotinylated PM54 (Bio-PM54) at a concentration equivalent to $10 \times \text{IC}_{50}$ (see Table 1). Chem-map (Biological triplicates) and CUT&TAG (Biological duplicates) were then performed using the Active Motif CUT&Tag-IT assay kit (53160, 53165), following the manufacturer's instructions. Briefly, 5×10^5 cells per condition were collected and washed twice before being bound to Concanavalin A beads and then incubated overnight at 4 °C with primary antibodies (1:50 dilutions). The following day, the corresponding guinea pig Anti-rabbit or rabbit Anti-mouse secondary antibodies were used at a 1:100 dilution in digitonin buffer and incubated at room temperature for 1 h. Subsequently, the CUT&Tag-IT Assembled pA-Tn5 Transposomes were incubated at room temperature for 1 h, and cells were resuspended in Tagmentation buffer and incubated at 37 °C for 1 h. The Tagmentation process was then stopped by adding EDTA and SDS. Protein digestion was performed by adding Proteinase K (10 mg/mL) and incubating at 55 °C for 1 h. The DNA was retrieved with DNA purification columns provided by the manufacturer and was then subjected to library preparation and PCR amplification and purified by 2 successive washes with SPRI beads. Libraries were sequenced on an Illumina NextSeq 2000 sequencer as paired-end 50 base reads. Image analysis and base calling were performed using RTA version 2.7.7 and BCL Convert version 3.8.4. The adapter sequence: CTGTCTCTTATA has been trimmed with cutadapt 1.18 with option: -a CTGTCTCTTATA -A CTGTCTCTTATA -m 5 -e 0.1 and Bowtie2⁵² parameter: -N 1 -X 1000, was used for mapping to the human genome (hg19). After the mapping, reads overlapping with ENCODE blacklist V2 were filtered. Each de-duplicated read was extended to its fragment size. Tracks were normalized with RPKM method. Peak calling was performed using Macs2 2.2.7.1⁵³ in BEDPE and narrow mode. narrowPeaks from biological triplicate samples were then merged to a single master peak set. BEDtools⁵⁴ was used to calculate the read coverage for each peak and for each sample. Peaks were annotated using Homer⁵⁵ software with ucsc 6.4 gene annotation. Promoters were defined as regions extending from 1 kb upstream to 100 bp downstream of the TSS and the "Annotate peaks" Homer tool was then employed to identify the promoters bound by the drugs. Bigwig tracks were generated using bamCoverage from deepTools 3.5.4⁵⁶ and normalized with RPKM method. The differential analysis was performed using DESeq2⁵⁷. Peak correlation analysis was performed using DiffBind⁵⁸ package. Heatmap and average profile analyzes were performed using seqMINER⁵⁹ and deepTools. For Super-Enhancer calling, ROSE algorithm version 0.1 (http://younglab.wi.mit.edu/super_enhancer_code.html) was applied with default parameters (stitch distance = 12500⁶⁰) using the BRD4 or H3K27ac peaks identified by MACS2 with the Cut&Tag experiments. TSS regions (Refseq TSS ± 1000 bp) were excluded. We defined SEs as 'bona fide' if they

were positive for both H3K27ac and BRD4 signals. ROSE-gene mapper (Default parameters, hg19) was used to link super enhancers to targeted genes based on proximity and regulation potential. We considered Bio-lurbi or Bio-PM54 binding peaks to be overlapping with bona fide SEs if there was at least 1 bp of overlap. Similarly, all other overlapping analyzes considered different peaks as overlapping if there was at least 1 bp of overlap.

c. ATAC-Seq. 501mel and MM029 cells were seeded and grown to sub-confluency in 15-cm plates, and ATAC-Seq was then performed using the Active Motif ATAC-Seq Kit (53150), following the manufacturer's instructions. Briefly, 1×10^5 nuclei were isolated by adding 100 μL ice cold ATAC-lysis buffer to the cell pellet. After centrifugation (500 g, 10 min at 4 °C), cells were washed and incubated with the tagmentation master mix in a shaking heat block at 37 °C/200 g for 30 min. Obtained DNA was taken up in DNA purification buffer, purified using the contained DNA purification columns, amplified for 10 cycles using indexed primers, and size-selected using SPRI beads. Libraries were sequenced on an Illumina NextSeq 2000 sequencer as paired-end 50 base reads. Image analysis and base calling were performed using RTA version 2.7.7 and BCL Convert version 3.8.4. Samples were analyzed using the ENCODE ATACseq pipeline release v2.0.2 with hg19 assembly. All the experiments were performed in biological duplicates.

d. Shuffled analysis. To assess the specificity of signal enrichment, a control dataset was generated by using shuffled genomic regions for Bio-Ecteinascidins, ATAC-seq, CpG islands and super-enhancer peaks. The shuffling process was implemented using "bedtools shuffle" tool, which randomly redistributed the control regions across the genome while ensuring they did not overlap with the experimental regions. These shuffled regions were subjected to the same analysis pipeline as the targeted regions to serve as a negative control in downstream enrichment analysis.

Identification of active enhancers using ABC-scoring

The Active-By-Contact (ABC) model⁴³ was used to integrate ATAC-Seq, Cut&Tag and RNA-Seq data to generate a genome-wide annotation of all active cis-candidate regulatory regions (cCRE) directly implicated in activating gene expression in 501mel cells. First, candidate cCREs were identified using the makeCandidateRegions function which integrated ATAC-Seq narrow peaks and ATAC-Seq bam alignments. Settings were changed to 250 bp extension from the summit and peak strength equal to 1.5×10^5 . cCRE activity was then measured using the run.neighborhoods function where candidate cCREs were integrated with H3K27ac bam alignments, followed by an additional removal of cCREs linked to housekeeping genes whose activity may interfere with ones linked to cell-state/identity genes. Next, we estimated the ABC power law score using the predict function. Here, the obtained cCREs were assessed for their predicted physical contacts with nearby genes based on HiC data. HiC parameters were obtained using the juicebox_dump and compute.powerlaw_fit_from_hic functions and a publicly available SKMEL-5 (differentiated melanoma cells) HiC h5 matrix (GSE105491⁴⁴), used to train the model. This HiC matrix was converted into juicer format using hic-converter (<https://github.com/4DGB/hic-converter>). HiC parameters were set as follows: --hic_gamma 0.9456060921860431, --hic_scale 5.081208553261949, --hic_gamma_reference 0.87, --hic_pseudocount_distance 5000. All putative cCREs were filtered using the filter_prediction script, and setting an ABC-score threshold of 0.02 we removed self-promoter contacts and retained only cCREs linked to expressed genes. Using R, cCREs were ranked based on their final ABC-scores measured as the sum of the ABC-score values of their related genes. Differentially expressed genes determined by RNA-Seq were used to identify their associated promoter-cCRE interactions. Plots were generated using R and GraphPad Prism.

RNA extraction and RT-qPCR

Total RNA isolation was performed according to the manufacture protocol with NucleoSpin RNA Plus kit (Macherey-Nagel). RNA was retrotranscribed with Reverse Transcriptase Superscript IV (Invitrogen), qPCR was performed with SYBR Green (Roche) and on a Light-Cycler 480 (Roche). Target gene expression was normalized using 18S as reference gene.

ChIP-qPCR

501mel and MM029 cells were seeded and grown to sub-confluency in 15-cm plates. After drug treatments, cells were fixed with 0.4 % PFA for 10 min and quenched with 2 M Glycine pH 8. Cells pellets were lysed in 25 mM HEPES pH 7.8, 10 mM NaCl, 1.5 mM MgCl₂, 0.5 % NP-40, 1 mM DTT. Nuclei were resuspended in 50 mM HEPES-KOH pH 7.8, 140 mM NaCl, 1 mM EDTA, 1% Triton X-100, 0.1 mM Na-deoxycholate, 0.1 % SDS and sonicated at 4 °C with a Q500 sonicator (Qsonica) to get DNA fragments between 100-500 bp. 50 µg of the sonicated chromatin was then diluted in Dilution buffer (1% Triton X-100, 2 mM EDTA, 20 mM Tris HCl pH 7.5, 150 mM NaCl) and incubated overnight at 4 °C with 5 µg of respective antibodies. The antibody-chromatin complex was then captured with a mix of protein A and G Dynabeads (Invitrogen) for 2 h at 4 °C, and beads were then washed twice in Low Salt Washing Buffer (1% Triton, 2 mM EDTA, 20 mM Tris HCl pH 7.5, 150 mM NaCl, 0.1 % SDS), High salt Washing Buffer (1% Triton, 2 mM EDTA, 20 mM Tris HCl pH 7.5, 500 mM NaCl, 0.1 % SDS), and TE buffer (100 mM Tris HCl pH 7.5, 10 mM EDTA). Immunoprecipitated chromatin was subsequently eluted from beads in 1% SDS and 100 mM NaHCO₃ at 65 °C for 30 min, and crosslinks were reversed by overnight incubation with Proteinase K (50 µg/ml) at 65 °C. The DNA was finally purified with the QIAquick PCR Purification kit (QIAGEN), resuspended in 200 µL of water, and analyzed by qPCR. Quantification of ChIP DNA concentrations with qPCR was performed by calculating the percent of input for each ChIP sample, calculated as $2^{(Ct_{input} - Ct_{IP})} \times 100$. Subsequently, the obtained percentage was normalized to the negative control IgG. Finally, the fold enrichment of the drug-treated samples over the DMSO-treated samples was calculated.

Animal studies. Animal studies were carried out at PharmaMar, which complies with ethical standards and principles governing the use of animal models. 4- to 6-week-old NSG (Charles River laboratory) or athymic nude female (Inotiv laboratory) mice were subcutaneously implanted into their right flank with human melanoma cell suspensions (LOX-IMVI, WM-266-4, 501mel, or 501mel^{emur}). Athymic nude mice were used for their lack of T-cell mediated immunity, which is suitable for studies requiring longer-term tumor growth observations (LOX-IMVI and WM-266-4). NSG mice were chosen for their more severely compromised immune systems, which allow for robust engraftment and growth of human melanoma cells, including those resistant to therapies (501mel and 501mel^{emur}). The experiments performed in this study is not affected by sex of the animal, consequently only females were used. When tumors began to develop, these were measured 2-3 times per week. Tumor volume was calculated with the equation $(a \times b^2)/2$, where “a” and “b” referred to the longest and shortest diameters, respectively. When tumors reached a size of 150 mm³, tumor bearing animals ($N = 8/\text{group}$) were treated with placebo (saline solution) or ecubectedin or PMS4 at 1.2 mg/kg weekly. Tumor volume and animal body weights were measured 2-3 times per week, starting from the first day of treatment. The median was determined for tumor volume/size on each measurement day. Treatment tolerability was assessed by monitoring body weight evolution, clinical signs of systemic toxicity, as well as evidences of local damage in the injection site. Differences on antitumor effect were evaluated by comparing tumor volume data as well as median survival time from the placebo-treated group with Ecubectedin or PMS4 treated groups. For this, a two-tailed Mann-Whitney U test was used. According to animal care and enforcement, the maximum allowable diameter for

subcutaneous tumors in mice is 20 mm. This limit was not exceeded at any point. All animals used in this research were housed in a specific pathogen-free (SPF) environment with a 12 h dark/light cycle, constant and appropriate room temperature (22–25 °C), with relative humidity between 55 ± 10% and had free access to food and water.

Antibodies dilutions. ACTb, WB Dilution 1/1000, Cat# 558623, RRI-D:AB1645341; ATM, WB Dilution 1/1000, Cat# 2873S, RRI-D:AB_2062659; AXL, WB Dilution 1/1000, Cat# 13196-1-AP, RRID:AB_10642006; Biotin, 2.5µg/ ChIP-CUT&Tag assay, Cat# 5597S, RRID:AB_10828011; BRD4, 2.5µg/ ChIP-CUT&Tag assay, Cat# 39909, RRID:AB_2615059; CDK12, WB Dilution 1/1000, Cat# ABE1861; CDK13, WB Dilution 1/1000, Cat# ABE1860; CDK7, WB Dilution 1/2000, Cat# 556345, RRID:AB_396374; Cleaved Caspase-3 (Asp175), WB Dilution 1/2000, Cat# 9661S, RRID:AB_2341188; EGFR, WB Dilution 1/2000 Cat# sc-373746, RRID:AB_10920395; EP300, WB Dilution 1/1000 Cat# 61401, RRID:AB_2716754; H3K27ac, 1µg/ChIP-CUT&Tag assay, Cat# 91193, RRID:AB_2793797; H3K27me3, 1 µg/ChIP-CUT&Tag assay, 9733, RRI-D:AB_2616029; IRF1, WB Dilution 1/2000, Cat# 8478S, RRI-D:AB_10949108; MED1, WB Dilution 1/1000, Cat# ab64965, AB_1142301; MITF, WB Dilution 1/2000, Cat# 12590S, RRID:AB_2616024; MYC, WB Dilution 1/1000, Cat# sc-764, RRID:AB_631276; PD-L1, WB Dilution 1/2000 Cat# 13684S, RRID:AB_2687655; Phospho-ATM (Ser1981), WB Dilution 1/2000, Cat# 13050S, RRID:AB_2798100; Phospho-Histone H3 (Ser10), WB Dilution 1/2000, Cat# 06-570, RRID:AB_310177; Phospho-Stat1 (Tyr701), WB Dilution 1/1000, Cat# 9167S, RRID:AB_561284; yH2AX, WB and IF Dilution 1/1000, Cat# AB22551, RRID:AB_447150; RPB1, 2.5µg/ ChIP-CUT&Tag assay, Cat# AF6851, RRID:AB_2847574; RPB1, 2.5µg/ ChIP-CUT&Tag assay, Cat# AF6851, RRID:AB_2847574; SOX10, WB Dilution 1/1000, Cat# sc-365692, RRID:AB_10844002; SOX9, WB Dilution 1/1000 Cat# 82630S, RRID:AB_2665492; STAT1, WB Dilution 1/1000, Cat# 14994S, RRID:AB_2737027; Vinculin, WB Dilution 1/1000, Cat# V4505-100UL, RRID:AB_477617

Statistics and reproducibility

Experimental data was plotted and analyzed using either Excel (Microsoft) or GraphPad Prism (GraphPad Software Inc.). The tests used included ordinary one-way ANOVA using Dunnett’s multiple comparisons test, Logrank (Mantel-Cox) test, Hypergeometric distribution test, One-way ANOVA with post-hoc Tukey adjustment comparisons, the Benjamini and Hochberg test method, the Fisher’s Exact Test, and the Wald test. Differences were considered significant at $P < 0.05$. Each in vitro experiment was repeated independently at least three times unless indicated differently. The number of samples and replicates are indicated in the respective figure legends. No data were excluded from the analyzes. These experiments do not require blinding of the investigator.

Resource availability

Lead contact. Further information and requests for resources and reagents should be directed to and will be fulfilled by the Lead Contact, Frédéric Coin (fredr@igbmc.fr). All data are available in the Source Data File.

Extended resource table. An extended resource table with antibodies, oligonucleotide sequences, chemicals and reagents used in this work is provided in Supplementary Data 8.

Reporting summary

Further information on research design is available in the Nature Portfolio Reporting Summary linked to this article.

Data availability

The publicly available data used in this study are available in the GEO database under the following accession codes: the RNA-seq, ChIP-seq and ATAC-seq data from SCLC cell lines; [GSE179074](https://www.ncbi.nlm.nih.gov/geo/query/acc.cgi?acc=GSE179074)³⁵ and

GSE195663³⁵, the RNA-seq data from the MM047 cell line; GSE205463⁴², the ATAC-seq and CUT&Tag data from the ECC4, A99 and DMS53 cell lines; GSE190618⁶¹, and the SKMEL-5 (differentiated melanoma cells) HiC h5 matrix GSE105491⁴⁴. The raw RNA-seq, ATAC-seq, and Cut&Tag data generated in this study have been deposited at GEO under accession numbers GSE256100 and GSE256094. The remaining data are available within the Article, Supplementary Information or Source Data file. Source data are provided with this paper.

References

- Bradner, J. E., Hnisz, D. & Young, R. A. Transcriptional Addiction in Cancer. *Cell* **168**, 629–643 (2017).
- Sengupta, S. & George, R. E. Super-Enhancer-Driven Transcriptional Dependencies in Cancer. *Trends Cancer* **3**, 269–281 (2017).
- Zanconato, F. et al. Transcriptional addiction in cancer cells is mediated by YAP/TAZ through BRD4. *Nat. Med.* **24**, 1599–1610 (2018).
- Hogg, S. J., Beavis, P. A., Dawson, M. A. & Johnstone, R. W. Targeting the epigenetic regulation of antitumour immunity. *Nat. Rev. Drug Discov.* **19**, 776–800 (2020).
- Vervoort, S. J. et al. Targeting transcription cycles in cancer. *Nat. Rev. Cancer* **22**, 5–24 (2022).
- Pott, S. & Lieb, J. D. What are super-enhancers? *Nat. Genet.* **47**, 8–12 (2015).
- Hnisz, D. et al. Super-enhancers in the control of cell identity and disease. *Cell* **155**, 934–947 (2013).
- Whyte, W. A. et al. Master transcription factors and mediator establish super-enhancers at key cell identity genes. *Cell* **153**, 307–319 (2013).
- Sabari, B. R. et al. Coactivator condensation at super-enhancers links phase separation and gene control. *Science* **361**, eaar3958 (2018).
- Boija, A., Klein, I. A. & Young, R. A. Biomolecular Condensates and Cancer. *Cancer Cell* **39**, 174–192 (2021).
- Laham-Karam, N., Pinto, G. P., Poso, A. & Kokkonen, P. Transcription and Translation Inhibitors in Cancer Treatment. *Front. Chem.* **8**, 276 (2020).
- Bushweller, J. H. Targeting transcription factors in cancer — from undruggable to reality. *Nat. Rev. Cancer* **19**, 611–624 (2019).
- Kwiatkowski, N. et al. Targeting transcription regulation in cancer with a covalent CDK7 inhibitor. *Nature* **511**, 616–620 (2014).
- Berico, P. et al. CDK7 and MITF repress a transcription program involved in survival and drug tolerance in melanoma. *EMBO Rep.* <https://doi.org/10.15252/embr.202051683> (2021).
- Fontanals-Cirera, B. et al. Harnessing BET Inhibitor Sensitivity Reveals AMIGO2 as a Melanoma Survival Gene. *Mol. Cell* **68**, 731–744.e9 (2017).
- Donati, B., Lorenzini, E. & Ciarrocchi, A. BRD4 and Cancer: going beyond transcriptional regulation. *Mol. Cancer* **17**, 164 (2018).
- Hoek, K. S. et al. In vivo switching of human melanoma cells between proliferative and invasive states. *Cancer Res.* **68**, 650–656 (2008).
- Verfaillie, A. et al. Decoding the regulatory landscape of melanoma reveals TEADS as regulators of the invasive cell state. *Nat. Commun.* **6**, 6683 (2015).
- Wouters, J. et al. Robust gene expression programs underlie recurrent cell states and phenotype switching in melanoma. *Nat. Cell Biol.* **22**, 986–998 (2020).
- Pozniak, J. et al. A TCF4-dependent gene regulatory network confers resistance to immunotherapy in melanoma. *Cell* **187**, 166–183.e25 (2024).
- Gide, T. N., Wilmott, J. S., Scolyer, R. A. & Long, G. V. Primary and Acquired Resistance to Immune Checkpoint Inhibitors in Metastatic Melanoma. *Clin. Cancer Res.* **24**, 1260–1270 (2018).
- Weiss, S. A., Wolchok, J. D. & Sznol, M. Immunotherapy of Melanoma: Facts and Hopes. *Clin. Cancer Res.* **25**, 5191–5201 (2019).
- Schadendorf, D. et al. Melanoma. *Lancet* **392**, 971–984 (2018).
- Jerby-Amon, L. et al. A Cancer Cell Program Promotes T Cell Exclusion and Resistance to Checkpoint Blockade. *Cell* **175**, 984–+ (2018).
- Tsoi, J. et al. Multi-stage Differentiation Defines Melanoma Subtypes with Differential Vulnerability to Drug-Induced Iron-Dependent Oxidative Stress. *Cancer Cell* **33**, 890–904.e5 (2018).
- Arozarena, I. & Wellbrock, C. Phenotype plasticity as enabler of melanoma progression and therapy resistance. *Nat. Rev. Cancer* **19**, 377–391 (2019).
- Benboubker, V., Boivin, F., Dalle, S. & Caramel, J. Cancer Cell Phenotype Plasticity as a Driver of Immune Escape in Melanoma. *Front. Immunol.* **13**, 873116 (2022).
- Chauhan, J. S., Hölzel, M., Lambert, J., Buffa, F. M. & Goding, C. R. The MITF regulatory network in melanoma. *Pigment Cell Melanoma Res* **35**, 517–533 (2022).
- Comandante-Lou, N., Baumann, D. G. & Fallahi-Sichani, M. AP-1 transcription factor network explains diverse patterns of cellular plasticity in melanoma cells. *Cell Rep.* **40**, 111147 (2022).
- Karras, P. et al. A cellular hierarchy in melanoma uncouples growth and metastasis. *Nature* **610**, 190–198 (2022).
- Hoek, K. S. & Goding, C. R. Cancer stem cells versus phenotype-switching in melanoma. *Pigment Cell Melanoma Res* **23**, 746–759 (2010).
- Rambow, F., Marine, J. C. & Goding, C. R. Melanoma plasticity and phenotypic diversity: therapeutic barriers and opportunities. *Genes Dev.* **33**, 1295–1318 (2019).
- Molinski, T. F., Dalisay, D. S., Lievens, S. L. & Saludes, J. P. Drug development from marine natural products. *Nat. Rev. Drug Discov.* **8**, 69–85 (2009).
- Santamaria Nunez, G. et al. Lurbinectedin Specifically Triggers the Degradation of Phosphorylated RNA Polymerase II and the Formation of DNA Breaks in Cancer Cells. *Mol. Cancer Ther.* **15**, 2399–2412 (2016).
- Costanzo, F. et al. Promoters of ASCL1- and NEUROD1-dependent genes are specific targets of lurbinectedin in SCLC cells. *EMBO Mol. Med* <https://doi.org/10.15252/emmm.202114841> (2022).
- Trigo, J. et al. Lurbinectedin as second-line treatment for patients with small-cell lung cancer: a single-arm, open-label, phase 2 basket trial. *Lancet Oncol.* **21**, 645–654 (2020).
- Widmer, D. S. et al. Systematic classification of melanoma cells by phenotype-specific gene expression mapping. *Pigment Cell Melanoma Res* **25**, 343–353 (2012).
- David-Cordonnier, M.-H. et al. DNA and Non-DNA Targets in the Mechanism of Action of the Antitumor Drug Trabectedin. *Chem. Biol.* **12**, 1201–1210 (2005).
- Couto, G. K. et al. The Melding of Drug Screening Platforms for Melanoma. *Front. Oncol.* **9**, 512 (2019).
- Casper, D. J. et al. Use of Anti-phosphohistone H3 Immunohistochemistry to Determine Mitotic Rate in Thin Melanoma. *Am. J. Dermatopathol.* **32**, 650–654 (2010).
- Yu, Z. et al. Chem-map profiles drug binding to chromatin in cells. *Nat. Biotechnol.* **41**, 1265–1271 (2023).
- Berico, P. et al. Super-enhancer-driven expression of BAHCC1 promotes melanoma cell proliferation and genome stability. *Cell Rep.* **42**, 113363 (2023).
- Fulco, C. P. et al. Activity-by-contact model of enhancer–promoter regulation from thousands of CRISPR perturbations. *Nat. Genet.* **51**, 1664–1669 (2019).
- The ENCODE Project Consortium. An integrated encyclopedia of DNA elements in the human genome. *Nature* **489**, 57–74 (2012).
- Zawistowski, J. S. et al. Enhancer Remodeling during Adaptive Bypass to MEK Inhibition Is Attenuated by Pharmacologic Targeting of the P-TEFb Complex. *Cancer Discov.* **7**, 302–321 (2017).
- Le, V. H., Inai, M., Williams, R. M. & Kan, T. Ecteinascidins. A review of the chemistry, biology and clinical utility of potent tetrahydroisoquinoline antitumor antibiotics. *Nat. Prod. Rep.* **32**, 328–347 (2015).

47. Xie, W. et al. Lurbinectedin synergizes with immune checkpoint blockade to generate anticancer immunity. *Oncolimmunology* **8**, e1656502 (2019).
48. Dumoulin, D. W. et al. Lurbinectedin shows clinical activity and immune-modulatory functions in patients with pre-treated small cell lung cancer and malignant pleural mesothelioma. *Eur. J. Cancer* **172**, 357–366 (2022).
49. Love, M. I., Huber, W. & Anders, S. Moderated estimation of fold change and dispersion for RNA-seq data with DESeq2. *Genome Biol.* **15**, 1–21 (2014).
50. Benjamini, Y. & Hochberg, Y. Controlling the False Discovery Rate: A Practical and Powerful Approach to Multiple Testing. *J. R. Stat. Soc.: Ser. B (Methodol.)* **57**, 289–300 (1995).
51. Ge, S. X., Jung, D. & Yao, R. ShinyGO: a graphical gene-set enrichment tool for animals and plants. *Bioinformatics* **36**, 2628–2629 (2020).
52. Langmead, B. & Salzberg, S. L. Fast gapped-read alignment with Bowtie 2. *Nat. Methods* **9**, 357–359 (2012).
53. Zhang, Y. et al. Model-based analysis of ChIP-Seq (MACS). *Genome Biol.* **9**, R137 (2008).
54. Quinlan, A. R. & Hall, I. M. BEDTools: a flexible suite of utilities for comparing genomic features. *Bioinformatics* **26**, 841–842 (2010).
55. Heinz, S. et al. Simple Combinations of Lineage-Determining Transcription Factors Prime cis-Regulatory Elements Required for Macrophage and B Cell Identities. *Mol. Cell* **38**, 576–589 (2010).
56. Ramírez, F. et al. deepTools2: a next generation web server for deep-sequencing data analysis. *Nucleic Acids Res.* **44**, W160–W165 (2016).
57. Love, M. I., Huber, W. & Anders, S. Moderated estimation of fold change and dispersion for RNA-seq data with DESeq2. *Genome Biol.* **15**, 550 (2014).
58. Ross-Innes, C. S. et al. Differential oestrogen receptor binding is associated with clinical outcome in breast cancer. *Nature* **481**, 389–393 (2012).
59. Ye, T. et al. seqMINER: an integrated ChIP-seq data interpretation platform. *Nucleic Acids Res.* **39**, e35–e35 (2011).
60. Loven, J. et al. Selective inhibition of tumor oncogenes by disruption of super-enhancers. *Cell* **153**, 320–334 (2013).
61. Horie, M. et al. An integrative epigenomic approach identifies *ELF3* as an oncogenic regulator in *ASCL1*-positive neuroendocrine carcinoma. *Cancer Sci.* **114**, 2596–2608 (2023).

Acknowledgements

This study was supported by the Ligue contre le cancer (Equipe Labélisée 2022–2024), the Institut National du Cancer (INCa) (INCa_18353), the grant ANR-10-LABX-0030-INRT, a French State fund managed by the Agence Nationale de la Recherche under the frame program Investissements d’Avenir ANR-10-IDEX-0002-02. This work of the Interdisciplinary Thematic Institute IMCBio+, as part of the ITI 2021–2028 program of the University of Strasbourg, CNRS and Inserm, was supported by IdEx Unistra (ANR-10-IDEX-0002), and by SFRI-STRATUS project (ANR-20-SFRI-0012) and EUR IMCBio (ANR-17-EURE-0023) under the framework of the France 2030 Program. Sequencing was performed by the IGBMC GenomEast platform, a member of the “France Génomique” consortium (ANR-10-INBS-0009). Histology and subsequent image analysis were performed by the pathology facility of the mouse clinic institute (ICS), a member of the Celphedia/Phenomin infrastructures

(ANR-10-INBS-0007). We also thank the IGBMC PluriCell East facility, Flow cytometry and Photonic microscopy services. P.B is supported by the Ligue contre le Cancer. JME was sponsored by a Mount Jade Scholar Fellow from the MOST of Taiwan and a Yonglin Chair Professor grant of National Taiwan University. We thank Dr Hsiang-Hung Huang for having initiated the work on SCLC cells.

Author contributions

Conceptualization: FC. Methodology: MC, JO, ID, C-Cuevas, FC. Investigation: MC, JO, MN, LS, PC, PB, C-Capelli, CM, AZ, CE, MJGN, TKL, EC, PA, MMD and GSN. Analysis of data: TY, GD, JME. Funding acquisition: FC. Supervision: FC. Writing – original draft: FC. Writing – review & editing: ID, EC, CC, MC, JO.

Competing interests

PA and C-Cuevas are PharmaMar S.A employees and shareholders. MJGN, MMD, GSM are PharmaMar employees. The remaining authors declare no competing interests.

Additional information

Supplementary information The online version contains supplementary material available at <https://doi.org/10.1038/s41467-024-55667-z>.

Correspondence and requests for materials should be addressed to Frédéric Coin.

Peer review information *Nature Communications* thanks the anonymous reviewers for their contribution to the peer review of this work. A peer review file is available.

Reprints and permissions information is available at <http://www.nature.com/reprints>

Publisher’s note Springer Nature remains neutral with regard to jurisdictional claims in published maps and institutional affiliations.

Open Access This article is licensed under a Creative Commons Attribution-NonCommercial-NoDerivatives 4.0 International License, which permits any non-commercial use, sharing, distribution and reproduction in any medium or format, as long as you give appropriate credit to the original author(s) and the source, provide a link to the Creative Commons licence, and indicate if you modified the licensed material. You do not have permission under this licence to share adapted material derived from this article or parts of it. The images or other third party material in this article are included in the article’s Creative Commons licence, unless indicated otherwise in a credit line to the material. If material is not included in the article’s Creative Commons licence and your intended use is not permitted by statutory regulation or exceeds the permitted use, you will need to obtain permission directly from the copyright holder. To view a copy of this licence, visit <http://creativecommons.org/licenses/by-nc-nd/4.0/>.

© The Author(s) 2025

¹IGBMC, Institut de Génétique et de Biologie Moléculaire et Cellulaire Illkirch Cedex, C.U. Equipe Labélisée Ligue contre le Cancer, Strasbourg, France. ²UMR7104, Illkirch, France. ³U1258, Illkirch, France. ⁴Université de Strasbourg, Illkirch, France. ⁵Department of Pathology, New York University Grossman School of Medicine, New York, USA. ⁶Interdisciplinary Melanoma Cooperative Group, Perlmutter Cancer Center, NYU Langone Health, New York, USA. ⁷Cell Biology Department, Research and Development, PharmaMar SA, Colmenar Vejo, Spain. ⁸Graduate Institute of Microbiology, College of Medicine, National Taiwan University, Taipei, Taiwan. ⁹College of Medicine, National Taiwan University, Taipei city, Taiwan. ¹⁰These authors contributed equally: Max Cigrang, Julian Obid. ✉ e-mail: fredr@igbmc.fr

Active mRNA degradation by EXD2 nuclease elicits recovery of transcription after genotoxic stress

Received: 20 June 2022

Accepted: 6 January 2023

Published online: 20 January 2023

 Check for updates

Jérémy Sandoz^{1,2,3,4}, Max Cigrang^{1,2,3,4}, Amélie Zachayus^{1,2,3,4},
Philippe Catez^{1,2,3,4}, Lise-Marie Donnio⁵, Clémence Elly^{1,2,3,4},
Jadwiga Nieminuszczy⁶, Pietro Berico^{1,2,3,4}, Cathy Braun^{1,2,3,4},
Sergey Alekseev^{1,2,3,4}, Jean-Marc Egly^{1,2,3,4}, Wojciech Niedzwiedz⁶,
Giuseppina Giglia-Mari⁵, Emmanuel Compe^{1,2,3,4} & Frédéric Coin^{1,2,3,4}✉

The transcriptional response to genotoxic stress involves gene expression arrest, followed by recovery of mRNA synthesis (RRS) after DNA repair. We find that the lack of the EXD2 nuclease impairs RRS and decreases cell survival after UV irradiation, without affecting DNA repair. Overexpression of wild-type, but not nuclease-dead EXD2, restores RRS and cell survival. We observe that UV irradiation triggers the relocation of EXD2 from mitochondria to the nucleus. There, EXD2 is recruited to chromatin where it transiently interacts with RNA Polymerase II (RNAPII) to promote the degradation of nascent mRNAs synthesized at the time of genotoxic attack. Reconstitution of the EXD2-RNAPII partnership on a transcribed DNA template *in vitro* shows that EXD2 primarily interacts with an elongation-blocked RNAPII and efficiently digests mRNA. Overall, our data highlight a crucial step in the transcriptional response to genotoxic attack in which EXD2 interacts with elongation-stalled RNAPII on chromatin to potentially degrade the associated nascent mRNA, allowing transcription restart after DNA repair.

Cells are regularly exposed to endogenous and exogenous genotoxic attacks that induce damage in the DNA molecule^{1,2}. The generation of DNA damage can potentially challenge several fundamental cellular processes such as transcription or replication and can ultimately cause diseases such as cancer if not repaired^{3–5}. The identification of several protective mechanisms against genotoxic stress highlights the importance of maintaining genome integrity to ensure low mutation frequencies in the genome⁶. One such mechanism, the nucleotide excision repair (NER) pathway, removes DNA adducts such as pyrimidine (6–4) pyrimidone (6–4PP) or cyclobutane pyrimidine dimers (CPD) that are produced by UV light^{7–9}. Two NER sub-pathways co-exist in cells: global genome NER (GG-NER), which removes DNA damage

from the entire genome, and transcription-coupled NER (TC-NER), which corrects lesions located on actively transcribed genes^{5,10–12}. In GG-NER, the concerted action of XPC and/or DDB2-containing complexes enables the detection of DNA damage in the genome, whereas in TC-NER, an actively transcribing RNA Polymerase II (RNAPII), which is stalled by a lesion, triggers efficient removal of cytotoxic damage^{3,14}.

To protect the integrity of gene expression under genotoxic attack, cells undergo a transcription stress response that includes global inhibition of transcription occurring in two steps: rapid and local inhibition of elongation due to the stalling of RNAPII in front of transcription-blocking DNA damage¹⁵ which is followed by a global inhibition of transcription initiation occurring on both damaged and

¹Institut de Génétique et de Biologie Moléculaire et Cellulaire Illkirch Cedex, C.U. Equipe Labellisée Ligue contre le Cancer, 2022 Strasbourg, France. ²Centre National de la Recherche Scientifique, UMR7104 Illkirch, France. ³Institut National de la Santé et de la Recherche Médicale, U1258 Illkirch, France. ⁴Université de Strasbourg, Strasbourg, France. ⁵Institut NeuroMyogène (INMG) – Laboratoire Physiopathologie et Génétique du Neurone et du Muscle, Université Claude Bernard Lyon 1, CNRS UMR 5261, INSERM U1315, Lyon, France. ⁶The Institute of Cancer Research, London SW3 6JB, UK. ✉e-mail: fredr@igbmc.fr

undamaged genes^{16,17}. Recent evidence has shown that global inhibition takes place after the degradation of the pool of RNAPII^{18,19}. After DNA repair, cells recover transcription in an active process involving transcription and chromatin remodeling factors^{20–24}. Recovery of RNA synthesis (RRS) encompasses both the re-initiation of expression at the promoters of actively transcribed genes and the restart of RNAPII molecules already in elongation. Despite recent advances in our understanding of the transcriptional stress response to genotoxic attack, the actors and mechanisms responsible for RRS after DNA repair remain largely elusive. Finding new players involved in RRS is therefore crucial to better understand this process at the molecular level and its role in genome stability.

We unveil here that EXD2, a RNA/DNA nuclease previously shown to be involved in homologous recombination and in the replication fork protection pathway^{25,26}, is essential for RRS after the genotoxic attack. Cells lacking EXD2 or expressing a nuclease-dead version of the enzyme are unable to restore global RNAPII-dependent transcription after UV irradiation, resulting in decreased resistance to genotoxic attack. Mechanistically, we demonstrated that EXD2 is not involved in the removal of UV-induced photoproducts. Instead, UV irradiation provokes the re-localization of EXD2 from mitochondria to the nucleus and its translocation to chromatin. There EXD2 transiently interacts with RNAPII and potentially promotes the degradation, during the recovery phase of transcription, of nascent mRNA being synthesized at the time of the genotoxic attack. Using a reconstituted transcription system *in vitro*, we reconstructed the dynamic association of EXD2 to RNAPII on a transcribed DNA template and demonstrated that EXD2 preferentially interacts with an elongation-blocked RNAPII. In such system, the ribonuclease activity of purified EXD2 efficiently processes mRNA. Accordingly, the interaction between EXD2 and a stalled-RNAPII was also observed *in vivo* using proximal ligation assay (PLA). These findings unveil a crucial role for EXD2 in the transcription stress response and are the first to assign a nuclear function to the ribonuclease activity of EXD2 by showing its involvement in the degradation of mRNA under synthesis at the time of the genotoxic attack. This degradation is necessary for an efficient recovery of gene expression after DNA repair.

Results

UV-induced inhibition and recovery of transcription at a defined genomic locus

In order to identify factors required for transcription recovery after a genotoxic attack, we first sought to develop a sensitive assay to easily monitor transcription inhibition and recovery after UV irradiation. As depicted in Supplementary Fig. 1a, we used a doxycyclin (dox)-inducible transcription/translation reporter system integrated at a single site on genomic DNA in the human osteosarcoma U-2 OS cell line. This system allows visualization of the genomic locus, its nascent mRNA transcript (CFP-SKL), and protein product (CPF-SKL)^{27,28}. After a 2-h dox treatment, we detected transcription of CFP-SKL in 80% of the cells (Supplementary Fig. 1b). A 2-h dox treatment followed by a recovery period in the absence of dox (1- to 4-h) triggered an accumulation of CFP-SKL protein expression (Supplementary Fig. 1c). The plasticity of this system also allowed us to measure the transcriptional activity of the cells in a specific time window after UV-irradiation. For this purpose, cells were irradiated with UV (30 J/m²) and pulsed with dox for 2 h at different times after the genotoxic attack. Under these conditions, we noticed a strong inhibition of CPF-SKL mRNA expression at early times after UV irradiation (Supplementary Fig. 1d, right panel, lanes 1 and 2). Interestingly, CPF-SKL mRNA expression recovered over time after irradiation (lane 3) and knockdown of the TC- and GG-NER factor XPA prevented this recovery (lanes 4–6 and left panel). CPF-SKL protein expression followed that of its mRNA with a strong inhibition early after irradiation and a progressive recovery that was completed 18 h after irradiation (Supplementary Fig. 1e). These data indicate that CPF-SKL expression recapitulates the rapid inhibition and

progressive recovery of global transcription that is generally completed 20 h after a genotoxic attack when DNA repair is efficient^{29,30}.

EXD2 is a critical factor for RRS

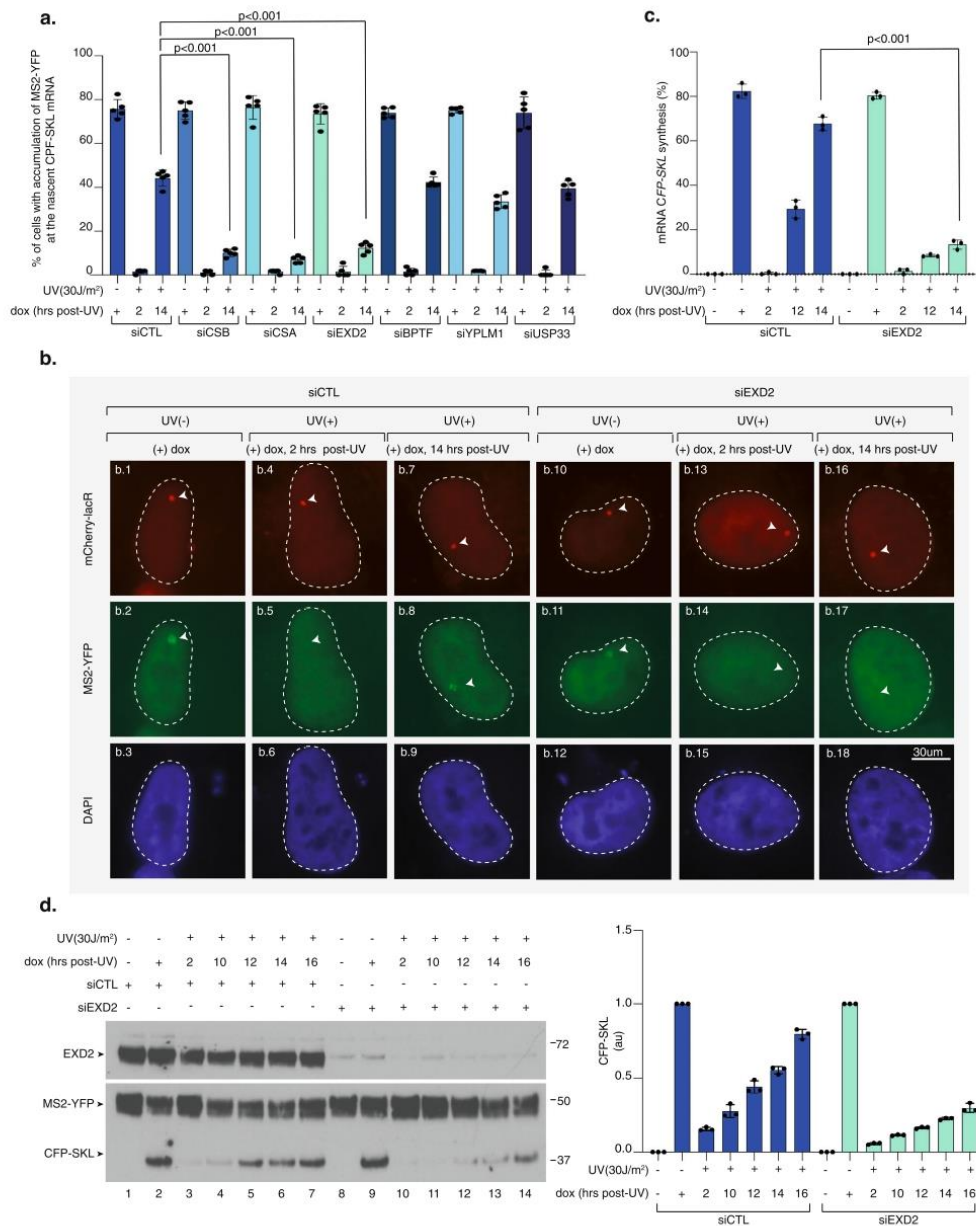
To explore the mechanism of transcription recovery after genotoxic stress, we used the reporter assay described above and tested a small number of selected candidates for their potential involvement in RRS. As expected, knockdown of the TC-NER factors CSA and CSB inhibited recovery of CFP-SKL expression (Fig. 1a). Interestingly, the 3' to 5' DNA/RNA exonuclease EXD2 emerged as a potential effector of transcription recovery after UV irradiation (Fig. 1a, b). The lack of recovery of CFP-SKL expression in the absence of EXD2 was confirmed by RT-qPCR (Fig. 1c) and resulted in 70% inhibition of *de novo* translation of CFP-SKL over time after UV irradiation (Fig. 1d, compare lanes 10–14 and 3–7). Of note, we observed that the accumulation of nascent CFP-SKL mRNA or *de novo* CFP-SKL protein was not impaired by the knockdown of EXD2 in the mock-treated cells (Fig. 1b, compare panels b1-b2-b3 with b10-b11-b12 and Fig. 1d, compare lane 2 and 9). These data suggest that EXD2 is required for RRS following a genotoxic stress.

EXD2 nuclease activity is required for RRS

We next used HeLa EXD2 CRISPR knock-out cells (EXD2^{-/-}-cl1)²⁵ (Fig. 2a, compare lanes 1 and 2) to measure the impact of EXD2 on global RRS. We pulse-labeled nascent mRNAs at various time points after UV irradiation (15 J/m²) using 5-ethynyluridine (EU)³¹. At this UV dose, all transcribed gene strands should contain at least one lesion that blocks RNAPII elongation³². We pre-treated the cells with a low concentration of actinomycin D (0.05 µg/ml) to abolish the intense nucleolar EU staining due to RNAPI-dependent ribosomal RNA synthesis. In these conditions, EU incorporation mainly reflects RNAPII-dependent RNA transcription³¹. Within the first hour after UV irradiation, we observed a strong inhibition (50%) of mRNA synthesis in both EXD2^{-/-} and EXD2^{-/-}-cl1 cells (Fig. 2b and Supplementary Fig. 2a, panels a.1-a.2 and a.5-a.6). In agreement with the above data, RRS was progressively restored in wild-type EXD2^{+/+} cells over time, whereas it remained deficient in EXD2^{-/-}-cl1 cells (Fig. 2b and Supplementary Fig. 2a panels a.3-a.4 and a.7-a.8). This defect was similar to the RRS defect observed in the CS1ANSV cell line from CS-B patient (in which the TC-NER factor CSB was deficient)³³ (Supplementary Fig. 2b).

To explore the role of the exonuclease activity of EXD2 in RRS, EXD2^{-/-}-cl1 cells were subsequently complemented with either FLAG-HA-tagged wild-type (EXD2^{-/-}+EXD2^{WT}-cl1) or dominant negative nuclease-dead EXD2 containing two substitutions at positions D108 and E110 (EXD2^{-/-}+EXD2^{D108A/E110A}-cl1). These two amino-acids are located in the active site of EXD2 and are known to be essential for its nuclease activity^{25,34}. RRS was restored in EXD2^{-/-}+EXD2^{WT}-cl1 cells but not in the nuclease-dead EXD2^{-/-}+EXD2^{D108A/E110A}-cl1 cells (Fig. 2b, c, compare panels c.1, c.2, c.3 with c.4, c.5, c.6), showing that RRS requires the nuclease activity of EXD2. We noted that the stability of the RPB1 subunit of RNAPII after UV-irradiation was not affected by the depletion of EXD2 or the lack of its exonuclease activity (Supplementary Fig. 2c). As noted above, we also observed that mRNA synthesis was indistinguishable in all four mock-treated HeLa cells, suggesting that EXD2 is not required for RNAPII-dependent transcription in the absence of genotoxic attack (Fig. 2c, panels c.1 and c.4, and Supplementary Fig. 2a, panels a.1 and a.5). Similar results were obtained with an additional set of HeLa clones (EXD2^{-/-}-cl2, EXD2^{-/-}+EXD2^{WT}-cl2 and EXD2^{-/-}+EXD2^{D108A/E110A}-cl2) (Supplementary Fig. 2d–e), but also under conditions in which cells were synchronized at G0-G1 to prevent cell division (Supplementary Fig. 2f). Thus, the knockdown as well as overexpression studies complement one another and establish that EXD2 exonuclease activity has a crucial function in RRS following UV irradiation.

In a second set of experiments, we evaluated the role of EXD2 in response to various treatments provoking transcription arrest without



generating DNA damage. We either treated the cells with the transcriptional inhibitor 5,6-dichloro-1-beta-D-ribofuranosylbenzimidazole (DRB) for 30 min³¹ or incubated them for 15 min at 4 °C to block transcription. Following the chase of DRB or the re-incubation at 37 °C, we observed similar transcriptional recovery in EXD2^{-/-} + EXD2^{WT}-c11 and EXD2^{-/-} + EXD2^{D108A/E110A}-c11 (Supplementary Fig. 3). Taken together, these results suggest that EXD2 specifically contributes to the global transcription recovery operating after a genotoxic stress such as UV irradiation.

Lack of EXD2 nuclease activity leads to mild UV sensitivity
To further examine the consequences of a lack of EXD2 activity on cell homeostasis, we measured the UV sensitivity of EXD2^{-/-}-c11, EXD2^{-/-} + EXD2^{WT}-c11, and EXD2^{-/-} + EXD2^{D108A/E110A}-c11 cells in comparison with the parental EXD2^{-/-} cells as well as the CS-B patient CS1ANSV cell line and the HeLa XPC^{-/-} (in which the GG-NER factor XPC was depleted)³⁵. Upon increasing doses of UV irradiation, knockdown of EXD2 activity resulted in hypersensitivity of EXD2^{-/-}-c11 and EXD2^{-/-} + EXD2^{D108A/E110A}-c11 cells, compared to EXD2^{-/-} and EXD2^{-/-} + EXD2^{WT}.

Fig. 1 | Knockdown of EXD2 impairs RRS of CFP-SKL. **a** U-2 OS cells were transfected with siRNA for 24 h, then with a construct expressing mCherry-lacR for 24 h before UV irradiation (30 J/m²) and 2-h pulse-incubation with dox starting at various time points post-UV. Nascent CFP-SKL mRNAs were detected at the reporter locus by accumulation of the MS2-YFP protein to the MS2 RNA loop. Quantification of the transcribing locus is expressed as % of cells showing YFP-MS2 accumulation at a single locus ($n =$ at least 250 cells in five independent experiments). Bars represent mean values of three different experiments (Biological triplicates) (\pm SD). One-way ANOVA with post-hoc Tukey adjustment comparisons were used to determine the p -values. Source data are provided as a Source Data file. **b** Representative confocal images of cells treated with siCTL or siEXD2. Images of the cells were obtained with the same microscopy system and constant acquisition parameters. **c** Cells were treated as described above and after the 2-h pulse-incubation with dox, the relative amount of CFP-SKL mRNA was quantified by RT-qPCR. Bars represent

mean values of three different experiments (Biological triplicates) (\pm SEM). One-way ANOVA with post-hoc Tukey adjustment comparisons were used to determine the p -values. Source data are provided as a Source Data file. **d** U-2 OS cells were treated as described above. After the 2-h pulse-incubation with dox, the cells were let to recover for 4 h before lysis. Extracts were resolved by SDS-PAGE and immunoblotted with anti-GFP (recognizing both the MS2-YFP and CFP-SKL proteins) and anti-EXD2. Lanes 1 and 8 are negative controls in which cells were not treated with dox. Lanes 2 and 9 are positive controls in which cells were treated with dox for 2 h before to recover 4 h in the absence of dox. Molecular sizes are indicated (kDa). CFP-SKL signals were quantified using ImageJ software (NIH), normalized with YFP-MS2 signals and reported on the graph (1 is the value for dox (+) for siCTL or siEXD2). Bars represent mean values of three different experiments (Biological triplicates) (\pm SEM). Source data are provided as a Source Data file.

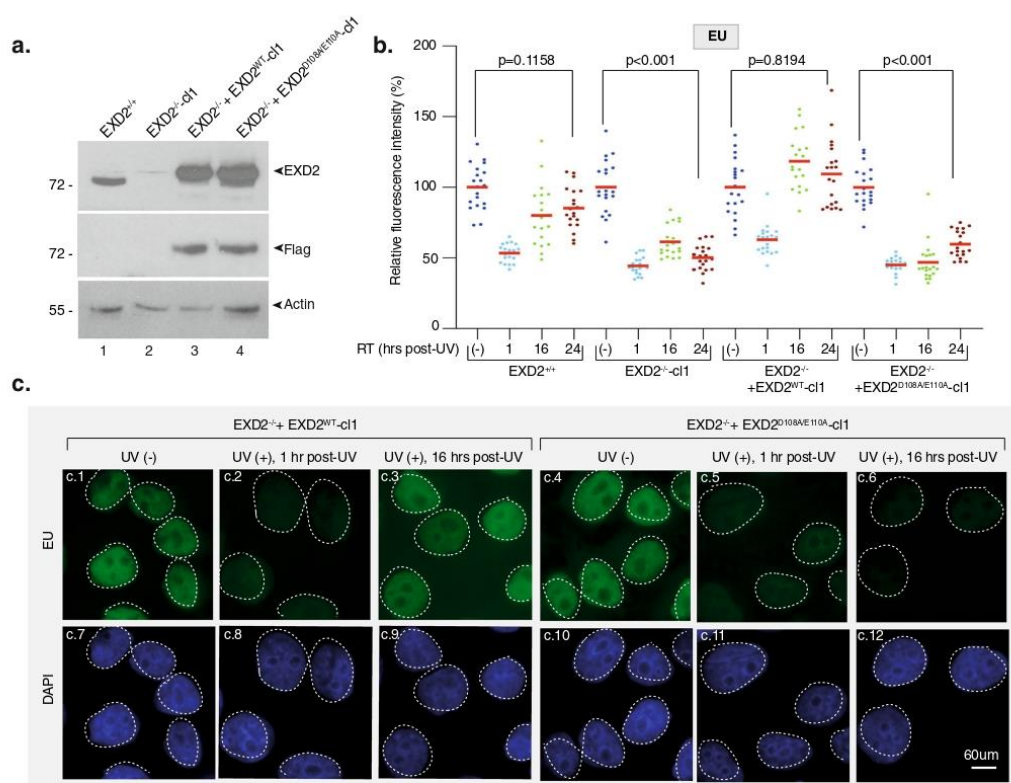


Fig. 2 | Knockdown of EXD2 nuclease activity impairs global RRS. **a** Protein lysates from EXD2^{+/+}, EXD2^{-/-}-cl1, EXD2^{-/-} + EXD2^{WT}-cl1 and EXD2^{-/-} + EXD2^{D108A/E110A}-cl1 cells were immuno-blotted for proteins as indicated. Molecular mass of the proteins is indicated (kDa). Source data are provided as a Source Data file. **b** Cells were mock- or UV-irradiated (15 J/m²) and mRNA was labeled with EU at the indicated time points post-UV. EU signal was quantified by ImageJ and relative integrated densities, normalized to mock-treated level set to 100%, are reported on the

graph ($n =$ at least 20 cells per conditions). Red bars indicate mean integrated density. RT recovery time. One-way ANOVA with post-hoc Tukey adjustment comparisons were used to determine the p -values. Source data are provided as a Source Data file. **c** Representative confocal images of EXD2^{+/+} + EXD2^{WT}-cl1 and EXD2^{-/-} + EXD2^{D108A/E110A}-cl1 treated like in **b**. Images of the cells were obtained with the same microscopy system and constant acquisition parameters.

cl1 cells (Fig. 3a). Interestingly, UV sensitivity of EXD2^{-/-}-cl1 and EXD2^{-/-} + EXD2^{D108A/E110A}-cl1 cells was similar to that found in the TC-NER deficient CS-B cells but not as pronounced as the one found in the highly sensitive GG-NER deficient XPC^{-/-} cells.

To determine whether EXD2 was involved in the removal of UV-induced DNA damage by NER, we measured GG- and TC-NER in cells depleted of EXD2 activity. To this end, we first performed immunofluorescence-based quantification of UV lesions directly in cell

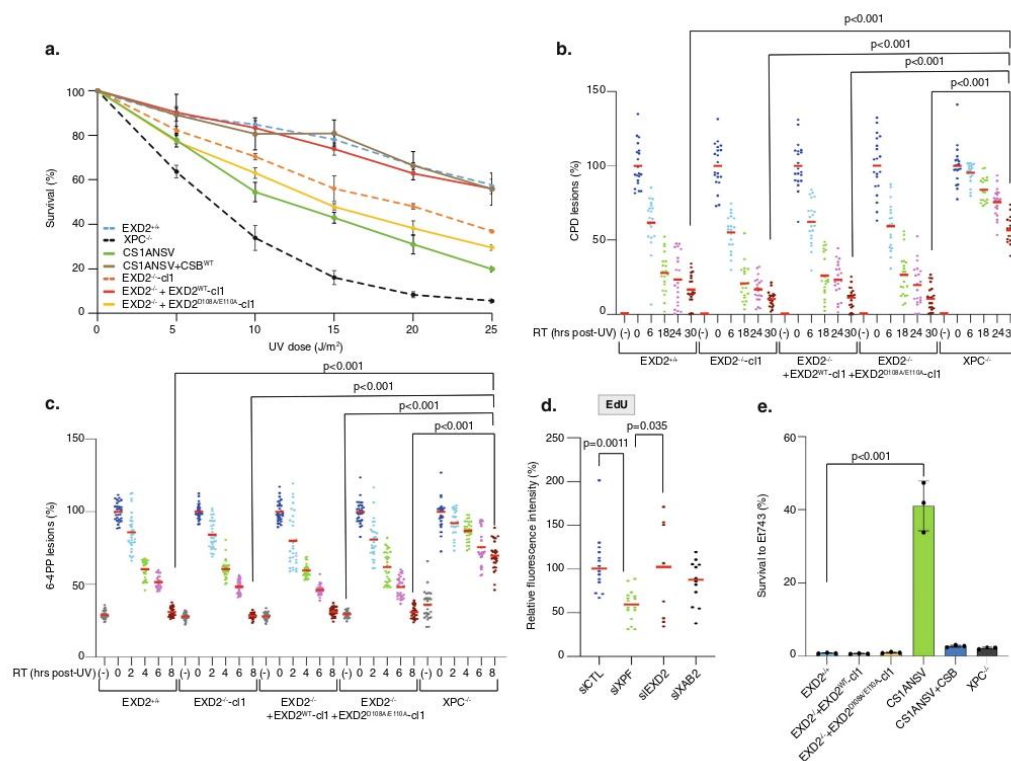


Fig. 3 | Knockdown of EXD2 nuclease activity sensitizes cells to UV irradiation.

a Cells were treated with increasing doses of UV irradiation and survival was determined 48 h later. Data were normalized to the mock treatment controls (as value of 100). The values are the means of three independent experiments (\pm SEM) (Technical triplicates). Source data are provided as a Source Data file. **b, c** Removal of UV lesions was measured in cells, harvested at different time points post-UV (15 J/m²) as indicated. Cells were labeled with anti-CPD (**b**) or anti-6-4PP (**c**) antibodies and signals were quantified using ImageJ at the different times indicated in the figure. Graph represents the % of lesions remaining in the genome at different time points normalized to the amounts of lesions measured immediately after UV irradiation (as a value of 100%). For each time point, a mean of 30 cells has been analyzed. Red bars indicate mean integrated density. RT; recovery time. (-); cells were mock-irradiated. 0; cells were irradiated and fixed immediately. One-way ANOVA with post-hoc Tukey adjustment comparisons were used to determine the

p -values. Source data are provided as a Source Data file. **d** GG-NER deficient XPC^{-/-} cells were treated either with siRNA against the TC-NER factor XAB2, the TC- and GG-NER factor XPF or against EXD2 for 24 h before local UV irradiation (50 J/m²) and EdU staining. The local TCR-UDS signals were quantified by ImageJ and reported on the graph. At least 15 cells were quantified for each situation. Red bars indicate mean integrated density. One-way ANOVA with post-hoc Tukey adjustment comparisons were used to determine the p -values. Source data are provided as a Source Data file. **e** Cells were treated with Et743 (0.5 nM) and survival was determined 48 h later. Data were normalized to the mock treatment controls (as a value of 100). The values are the means of three independent experiments (\pm SEM) (Biological triplicates). One-way ANOVA with post-hoc Tukey adjustment comparisons were used to determine the p -values. Source data are provided as a Source Data file.

nuclei³¹. The removal rate of the two main types of UV lesions in EXD2^{-/-}-c1 and EXD2^{-/-}+EXD2^{D108A/E110A}-c1 cells was higher to that of HeLa XPC^{-/-} cells and identical to that of EXD2^{+/+} or EXD2^{-/-}+EXD2^{WT}-c1 cells, implying that GG-NER was efficient in cells lacking EXD2 nuclease activity (Fig. 3b, c). We used two different assays to measure TC-NER. We first performed unscheduled DNA repair synthesis (UDS) during TC-NER (TCR-UDS)³⁶. Using GG-NER deficient XPC^{-/-} cells to ensure that repair replication in the UV-damage area was due to ongoing TC-NER, we measured repair replication via incorporation of EdU into newly synthesized DNA after local UV irradiation. Loss of the TC-NER specific factor XAB2 or TC/GG-NER factor XPF using siRNA knockdown induced similar deficiency in TCR-UDS, while loss of EXD2 had no impact (Fig. 3d). We next used the particularity of TC-NER deficient cells to be resistant to the DNA binder and anti-cancer drug Ecteinascidin 743 (Et743)³⁷. Indeed, the TC-NER deficient CS1ANSV cells showed high resistance to Et743 that was abolished in the

recovered CS1ANSV+CSB cells (Fig. 3e). In contrast, knockdown of EXD2 exonuclease activity did not impact the sensitivity of the corresponding cells to Et743. Finally, while γ H2AX accumulated after UV-irradiation and persisted in NER deficient cells³⁸, no accumulation of γ H2AX after knockdown of EXD2 was observed over time after UV irradiation (Supplementary Fig. 4). Altogether, these results suggest that while the knockdown of EXD2 sensitizes cells to UV irradiation, the nuclease is not involved in GG- or TC-NER.

EXD2 degrades nascent mRNA under synthesis at the time of UV irradiation

The above data point to a direct processing of mRNA by EXD2 nuclease activity during transcription recovery. To study this function, we first wanted to analyze the fate of mRNA under synthesis at the time of UV irradiation and developed the assay described in Fig. 4a, upper panel. We inhibited ribosomal RNA synthesis with a low

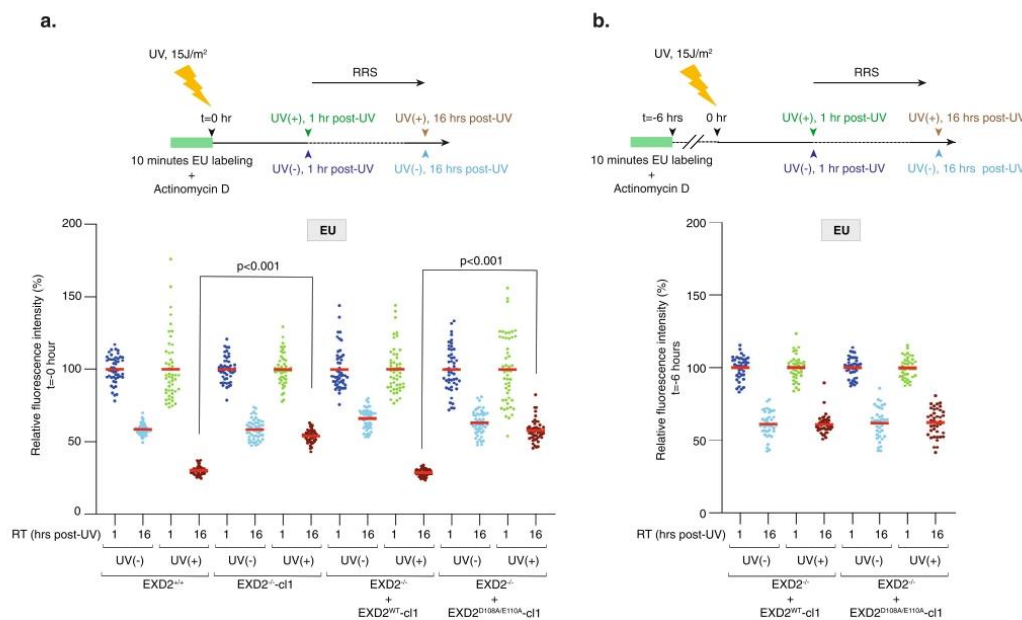


Fig. 4 | EXD2 degrades mRNA under synthesis at the time of UV irradiation.
a Upper panel; Scheme of the EU pulse-chase method used to analyze the fate of mRNA being synthesized at the moment of UV irradiation. Cells were incubated for 30 min with Actinomycin D (0.05 µg/ml) to specifically inhibit RNAPII transcription and mRNAs were pulse-labeled with EU for 10 min prior to UV irradiation (15 J/m²). Cells were let to recover for 1 h or 16 h post-UV before fixation. Actinomycin D was maintained during the experiment. Lower panel; Cells were treated as indicated in the upper panel and EU signals were quantified using ImageJ and normalized to the value obtained at 1 h set to 100%. Values are reported on the graph ($n =$ at least 50 cells). Red bars indicate mean integrated density. RT; recovery time. One-way ANOVA with post-hoc Tukey adjustment comparisons were used to determine the

p -values. Source data are provided as a Source Data file. **b** Upper panel; Compare to panel a, UV irradiation (15 J/m²) was performed 6 h after EU labeling and cells were let to recover for either 1 h or 16 h post-UV before fixation. Actinomycin D was maintained during the experiment. Lower panel; Cells were treated as indicated in upper panel and EU signals were quantified using ImageJ. Values are reported on the graph ($n =$ at least 50 cells). Red bars indicate mean integrated density. RT recovery time. One-way ANOVA with post-hoc Tukey adjustment comparisons were used to determine the p -values. No statistically significant differences were detected at 16 h post-UV between $EXD2^{-/-} + EXD2^{WT-c1l}$ and $EXD2^{-/-} + EXD2^{D108A/E110A-c1l}$ cells. Source data are provided as a Source Data file.

concentration of actinomycin D and subsequently labeled nascent mRNAs with a 10 min EU pulse. We then chased EU and immediately UV-irradiated the cells (15 J/m²). Fixing them 1 or 16 h post-chase, we were able to follow, during the recovery phase, the fate of mRNAs under synthesis when cells were subject to a genotoxic attack. In the four mock-treated cells, we observed a 50–40% reduced fraction size of EU-labeled mRNAs between 1 and 16 h of culture (probably reflecting both the turn-over of mRNAs and their dilution during cell division) (Fig. 4a and Supplementary Fig. 5a). Interestingly, UV irradiation of wild-type $EXD2^{+/+}$ and $EXD2^{-/-} + EXD2^{WT-c1l}$ cells provoked a 70% reduced fraction size of EU-labeled mRNAs between 1 and 16 h of culture, while $EXD2^{-/-c1l}$ and $EXD2^{-/-} + EXD2^{D108A/E110A-c1l}$ cells were refractory to this reduction and showed a situation similar to mock-treated cells with a 50–40% reduced fraction size of EU-labeled mRNAs (Fig. 4a and Supplementary Fig. 5a). Similarly, TCR-deficient CS-B cells were refractory to UV-induced reduction of EU-labeled mRNAs, which was restored after CSB^{WT} expression (Supplementary Fig. 5b). In another set of experiments, we performed UV-irradiation long after EU labeling (6 h) so that the labeled mRNAs were synthesized long before the UV treatment (Fig. 4b, upper panel). In these conditions, the reduced fraction size of labeled mRNAs between 1 and 16 h after irradiation was 50–40% for the four cell lines, regardless of whether EXD2 nuclease activity was present or not, a situation that resembles that of the mock treatment (Fig. 4b). These experiments suggest that the EXD2 nuclease degrades, during the recovery

phase, a large fraction of the nascent mRNAs (30%) that were being synthesized at the time of UV irradiation.

EXD2 translocates to nucleus to interact with RNAPII after UV irradiation

After having established the involvement of EXD2, during the recovery phase, in the degradation of mRNA under synthesis at the time of UV irradiation, we studied the potential connection of the nuclease with RNAPII. Since the literature on EXD2 suggests that the protein has a mitochondrial localization that seems incompatible with a potential nuclear role, we first determined the localization of EXD2 in wild-type $EXD2^{+/+}$ cells in normal conditions and after UV irradiation. Interestingly, whereas the localization of endogenous EXD2 appeared mostly mitochondrial in the absence of genotoxic stress, UV irradiation triggered the re-localization of a large fraction of the endogenous protein from the mitochondria to the nucleus (Fig. 5a, panels a.1–a.10). Similarly, the exogenous flag-tagged EXD2 protein in $EXD2^{-/-} + EXD2^{WT-c1l}$ cells also appeared to partially re-localize to the nucleus after irradiation, although a fraction appeared to localize to the nucleus even in the absence of genotoxic stress (Fig. 5a, panels a.21–a.30). To confirm these observations, we also performed a cell fractionation experiment on $EXD2^{-/-}$ cells. We observed that while EXD2 was mainly localized in mitochondria in the absence of genotoxic stress (although a small fraction was found in the chromatin), a decrease in the amount of EXD2 in this organelle was observed after UV irradiation, coupled

with an increase in the amount of EXD2 associated with chromatin (Fig. 5b). Next, we analyzed the potential interaction between EXD2 and RNAPII and its timing in EXD2^{-/-} + EXD2^{WT}-c1 cells. Following UV irradiation (15 J/m²), we observed transient coprecipitation between flag-EXD2 and the RPB1 subunit of RNAPII, which was maximal at 1 h after treatment (Fig. 5c, lanes 9–12) and then begins to decrease at later time points to reach the level of mock-treated cells 24 h after UV irradiation (compare lanes 12–14–16). Note that an interaction between endogenous EXD2 and RNAPII was also observed in HeLa EXD2^{+/+}, 1 h after UV irradiation (Fig. 5d). We next expressed the full-length GST-tagged EXD2^{WT} in bacteria and performed a GST pull-down assay with purified RNAPII from HeLa cells³⁹. GST-EXD2^{WT} pull-down coprecipitated RPB1, suggesting a direct interaction between EXD2 and RNAPII (Fig. 5e). These data highlight a transient direct interaction between EXD2 and RNAPII taking place quickly after UV irradiation and persisting during the recovery phase.

EXD2 interacts with a subset of RNAPII that stalls persistently on DNA

We then asked whether we could reconstitute EXD2 recruitment in vitro on an elongation-blocked RNAPII. We approached this question using a protein/DNA binding assay consisting of a biotinylated DNA template containing the AdMLP promoter and a transcribed region of 309 base pairs. The template was immobilized to streptavidin beads and incubated with purified RNAPII fraction from HeLa cells as well as with the recombinant general transcription factors (GTF: TFIIB, TBP, TFIIE, TFIIF, TFIIH) to form the pre-initiation complex (PIC). Bacterially purified recombinant EXD2 (rEXD2, without GST) was added at different stages of the assay (Fig. 6a, left panel). Addition of NTP induced transcription initiation, whereas their subsequent chase induced RNAPII elongation arrest⁴⁰ (Fig. 6a, middle panel). While western blot analysis of the remaining DNA-bound proteins revealed a very weak background signal of EXD2 to the DNA template in the absence of RNAPII and its GTF (Fig. 6a, right panel, lane 1), a clear recruitment of EXD2 occurred to the PIC in the absence of NTP (lane 3). In contrast, the presence of EXD2 did not improve the recruitment of RNAPII or GTFs (as observed for TFIIE α) (compare lane 2 and 3). The addition of NTP (lane 4) induced the initiation of transcription and the beginning of the elongation step characterized by the emergence of RNAPIIO as well as the release of the basal transcription factor TFIIE α from the DNA template (Fig. 6a, middle panel)⁴⁰. Under these conditions of transcription elongation, EXD2 was released from the RNAPII complex (compare lane 3 with lane 5). Interestingly, the chase of NTP, which blocks RNAPII in elongation, caused EXD2 to be recruited again to the DNA template (compare lane 5 with lane 7). In another set of experiments, we determined whether NTP or ATP were required to induce EXD2 release from RNAPII during initiation. The addition of ATP triggered EXD2 release that was clearly enhanced by the presence of the four NTP (Fig. 6b).

To further demonstrate the association of EXD2 with stalled RNAPII in vivo, we used the proximity-ligation assay (PLA). U-2 OS cells stably expressing C-terminally tagged EXD2-GFP, in which EXD2 localized mainly in mitochondria (Supplementary Fig. 6a), were treated with Flavopiridol, which inhibits RNAPII elongation and causes a slight relocation of EXD2-GFP to the nucleus (Supplementary Fig. 6a, b). After Flavopiridol treatment, we detected a nuclear PLA signal indicating EXD2-RNAPII interaction, which was significantly enriched compared to untreated cells and did not occur with GFP alone (Fig. 6c). These data indicate that EXD2 preferentially interacts with an elongation-blocked RNAPII.

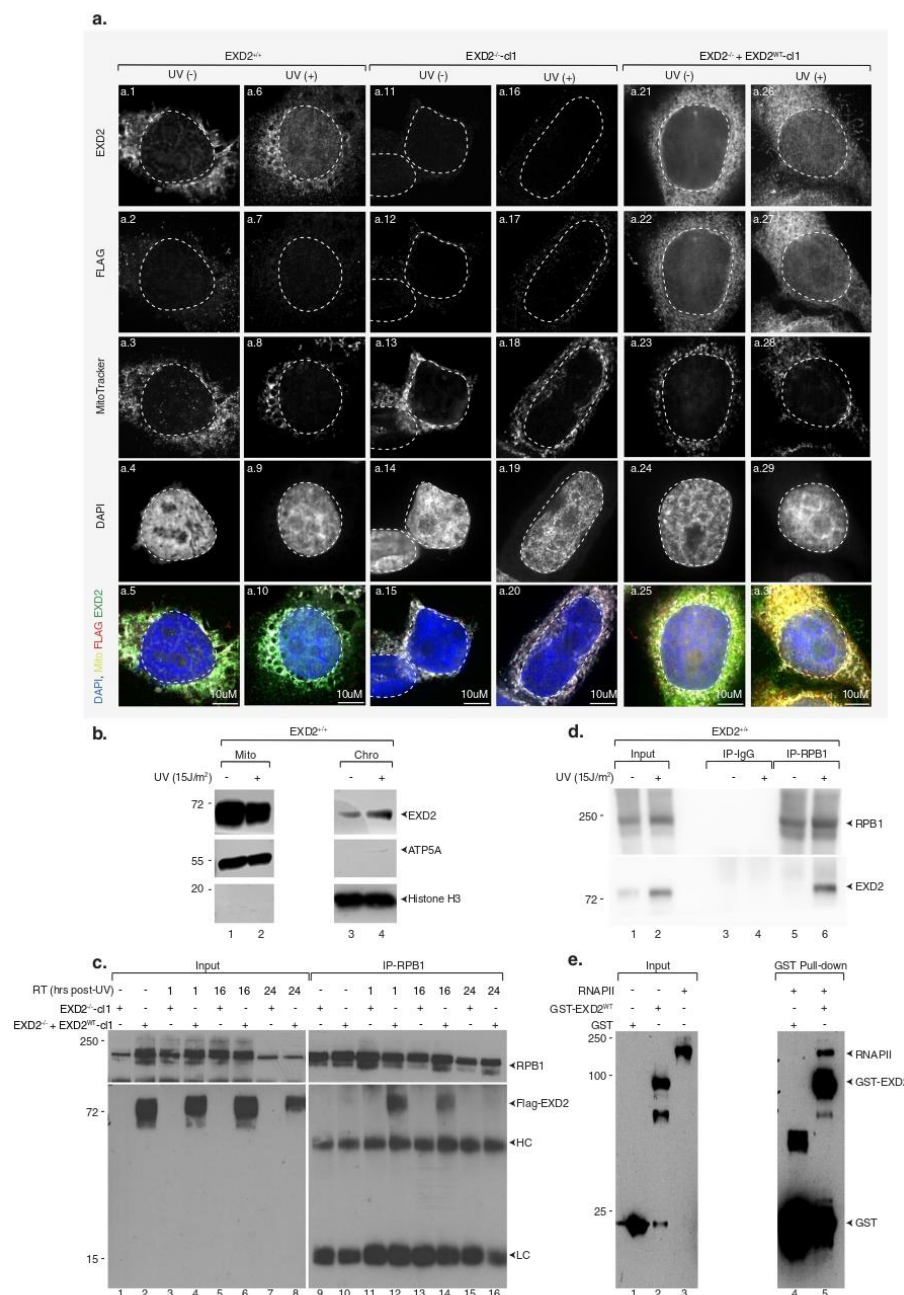
We subsequently examined the impact of the exonuclease activity of EXD2 on newly synthesized mRNA. To detect mRNA, we complemented the above in vitro system with radio-labeled CTP³¹. Note that the purified RNAPII fraction from HeLa cells was devoid of EXD2

(Fig. 6d, left panel). Recombinant human EXD2^{WT} and nuclease-dead EXD2^{D108A/E110A} were purified from insect cells in parallel (Fig. 6d, right panel). Transcription of the AdMLP-containing DNA template led to the production of an mRNA transcript of 309 nucleotides length in 30 min (Fig. 6e, lane 1). The addition of increasing amounts of recombinant purified EXD2^{WT} for the last 10 min of the reaction induced the degradation of the mRNA transcript whereas EXD2^{D108A/E110A} had no impact (compare lanes 3–5 to 6–8). Taken together, these data suggest that a fraction of EXD2 is recruited to chromatin after UV irradiation to directly interact with elongation-blocked RNAPII and degrade mRNA under synthesis.

Discussion

Transcription is controlled in time and space by complex epigenetic and signaling-mediated regulatory networks at each step of the process. When cells are subjected to genotoxic attack, DNA damage impacts several crucial cellular functions, including transcription. Indeed, if these lesions are bulky and located in the transcribed strand of an active gene, they become a major complication during its transcription because they constitute a strong barrier to RNAPII forward translocation and result in its blockage, generating transcriptional genotoxic stress^{41,42}. Cells cope with this stress firstly by inhibiting global gene expression, then by removing lesions that block RNAPII progression using the TC-NER pathway, and finally by initiating RRS at both promoters and damaged sites. How cells resume transcription after an acute genotoxic attack is crucial because inappropriate restarting is toxic and leads to cellular dysfunction and apoptosis, as observed in cells from patients with CS, which show intermediate sensitivity to UV irradiation coupled with a defect in RRS⁴³. With this in mind, we sought to find new players involved in RNAPII-dependent gene expression recovery after genotoxic attack and unveiled a key role for the 3'–5' exonuclease activity of EXD2 in this process. Recent studies have shown that RNAPI-dependent ribosomal gene transcription is also blocked shortly after a genotoxic stress and recovers over time. A TC-NER machinery removes lesions in ribosomal genes with the participation of CSA and CSB⁴⁴. We tested whether EXD2 was involved in RNAPI-dependent transcription recovery but did not detect a defect in this process in cells lacking EXD2 (Dr. Mari-Giglia, personal information), suggesting a specific involvement of EXD2 in RNAPI-dependent transcription recovery after UV irradiation.

Cells lacking EXD2 nuclease activity exhibited deficient in RRS and intermediate sensitivity to UV irradiation, reminiscent of the phenotype observed in TC-NER deficient cells^{40,42}, including CS-B cells in our study. At first glance, this could indicate that EXD2 is involved in TC-NER and in the removal of DNA lesions that block RNAPII during elongation. However, sensitivity to Et743, which required an active TC-NER pathway³⁷, and the TCR-UDS assay indicate that TC-NER is unaffected by the absence of EXD2, suggesting an uncoupling of efficient TC-NER from deficient RRS in these conditions. Recently, regulation of the RNAPII pool by ubiquitination was shown to be central in the inhibition and restart of transcription in response to genotoxic stress^{18,19}. Persistent depletion of RNAPII was shown to be largely responsible for the lack of transcriptional recovery observed in CS-B cells. Under our conditions, the RNAPII pool was not affected after UV irradiation by the lack of EXD2 nuclease activity, and we ruled out that a direct impact of EXD2 on RNAPII stability was involved in the RRS defect observed in EXD2-deficient cells. Instead, our observations suggest that EXD2 nuclease acts on mRNA, which was observed both in vivo, using pulse-labeling of nascent mRNA, and in vitro, using the transcription/nuclease run-off assay. These assays suggest that the EXD2 nuclease processes, during the recovery phase, a fraction of mRNA representing 30% of the nascent mRNA being synthesized at the time of the genotoxic attack. During RNAPII backtracking, the ability of RNAPII to cleave its transcript potentially allows transcription to resume and cells to survive when the lesions are removed. A plethora



of transcription factors, such as TFIIIS, are known to stimulate transcript cleavage⁴⁵. Similarly, it seems reasonable to suggest that the exonuclease activity of EXD2 is involved in the mRNA processing associated with RNAPII backtracking in front of DNA lesion as illustrated by the dynamic interaction we observed between them, which transiently kicks in after the genotoxic attack. Moreover, this activity is

likely limited to a genotoxic attack situation because mRNA transcription was efficiently recovered after cold-shock treatment in cells lacking EXD2. Our observations also suggest that EXD2 is probably not involved in transcription per se, as EU incorporation or reporter expression was hardly affected in mock-treated cells in our assay and cell viability was largely not affected by EXD2 knockdown in the

Fig. 5 | EXD2 transiently interacts with RNAPII after UV irradiation.

a Representative confocal images of HeLa EXD2^{+/+}, EXD2^{-/-} and EXD2^{-/-} + EXD2^{WT}-c1 mock- or UV-irradiated (15 J/m²) and left to recover for an hour. Cells were labeled with anti-EXD2 and anti-FLAG and stained with MitoTracker. Images of the cells were obtained with the same microscopy system and constant acquisition parameters for a given labeling/staining. **b** EXD2^{+/+} cells were mock- or UV-irradiated (15 J/m²) and left to recover for 1 h. Cells were fractionated in mitochondria (Mito) and chromatin (Chro) fractions, which were resolved by SDS-PAGE and immunoblotted against the indicated proteins. Molecular sizes are indicated (kDa). ATP5A is a marker of mitochondria. Histone H3 is a marker of chromatin. Source data are provided as a Source Data file. **c** EXD2^{-/-}-c1 or EXD2^{-/-} + EXD2^{WT}-c1 cells were mock- or UV-irradiated (15 J/m²) and left to recover for the indicated period of time post-UV (RT). RNAPII was immunoprecipitated using anti-RPB1 from total extracts and

protein were resolved by SDS-PAGE and immunoblotted using anti-RPB1 or anti-EXD2 antibodies. HC antibody heavy chain, LC antibody light chain, RT recovery time. Molecular sizes are indicated (kDa). Source data are provided as a Source Data file. **d**. RNAPII was immunoprecipitated from chromatin fractions obtained in panel **b**, using anti-RPB1 in the presence of Benzonase. IP using IgG was performed as controls. Proteins were resolved by SDS-PAGE and immunoblotted using anti-RPB1 or anti-EXD2 antibodies. RT recovery time. Molecular sizes are indicated (kDa). Source data are provided as a Source Data file. **e** Purified RNAPII from HeLa cells¹⁹ was incubated with recombinant pulldown GST-EXD2^{WT}. Following washes, fractions were resolved by SDS-PAGE and immunoblotted against the indicated proteins. Controls IP was performed with GST alone (lane 4). Molecular sizes are indicated (kDa). Source data are provided as a Source Data file.

absence of genotoxic stress (our data and ref.²⁵). This is similar to other genes encoding transcript cleavage stimulatory factors, such as TFIS, that becomes essential for cell viability only in the presence of a genotoxic stress⁴⁶, which may reflect a potential redundancy in the function of these factors in the absence of stress. The involvement of EXD2 in the recovery of transcription after a genotoxic attack, as well as its role in the repair of double-strand breaks^{25,26} seems to contradict its mitochondrial location^{47,48} that we confirmed in this work. However, our results may potentially reconcile these observations as they suggest that a genotoxic stress such as UV-irradiation leads to a significant re-location of EXD2 from the mitochondria to the nucleus. The molecular aspects of this relocation, and the generalization of this observation to other genotoxic attacks, are not yet known but it suggests post-translational modifications or new protein interactions allowing EXD2 to travel from the mitochondria to the nucleus.

Because EXD2 is known to be a regulator of homologous recombination in double-strand break repair²⁶ and double-strand breaks can occur following replication stress, we were also concerned that the lack of RRS might be due to replication stress and not directly to UV irradiation-induced DNA damage. However, we observed first that confluent EXD2-deficient cells synchronized in G0-G1 were also unable to recover transcription after UV irradiation and second that RNAPII-EXD2 interaction occurred when RNAPII is blocked in elongation, even in the absence of genotoxic stress. These data argue for a direct role of EXD2 in transcription recovery in relation to its interaction with RNAPII.

RNAPII backtracking in front of a lesion likely occurs over several nucleotides, such that the 3' end of the RNA is no longer aligned with the RNAPII active site, preventing transcription restart. Therefore, the data presented here advocate for a scenario in which EXD2, after its relocation to the nucleus, transiently associates with an RNAPII that is stopped persistently on a gene during elongation by the presence of a transcription-blocking lesion, to potentially assist RNAPII in degrading mRNA from 3' to 5' when backtracking occurs^{41,49}. This activity, alone or in combination with that of RNAPII, could reactivate backtracked RNAPII by providing a new 3' end to the mRNA to realign RNAPII active site with the ongoing mRNA. Why cells would require the 3' to 5' exonuclease activities of RNAPII and EXD2 to process mRNA at a damaged site is unclear, but consistent with this scenario, EXD2 is essential for cell viability after UV irradiation but is not required for NER to occur, demonstrating that UV sensitivity reflects the toxicity of the absence of RRS rather than a defect in DNA damage removal. To better understand the molecular mechanism of EXD2 involvement in RRS, the association of EXD2 with RNAPII was reconstituted in vitro using a transcribed DNA template and highly purified and recombinant transcription factors. Consistent with our hypothesis, we observed that elongation-active RNAPII associated less with EXD2 than elongation-blocked RNAPII on transcribed DNA. It is known that EXD2 discriminates RNA and DNA substrates via metal coordination (Mn2+ vs Mg2+)³⁴. We show that under the physicochemical conditions allowing in vitro transcription and the presence of Mg2+, EXD2

exonuclease activity processes newly synthesized long mRNA molecules (309nts length), reinforcing our model of UV-induced recruitment of EXD2 to stalled RNAPII, followed by degradation of nascent mRNA before transcription resumes. Interestingly, these data are also the only ones to assign a ribonuclease function to EXD2 in the nucleus since previous work implicated it in the degradation of nuclear DNA either during DNA double strand break resection in non-homologous end joining or in the protection of stressed replication forks^{25,26,50}.

Methods

Cell culture

U-2 OS cells were cultured in DMEM (1 g/l Glucose) containing 10% FCS and gentamycin. U-2 OS pTuner 263 cells were cultured in DMEM (1 g/l Glucose) containing 10% Tet-system approved FBS, 1% Penicillin/Streptomycin, 400 µg/ml G418, and 100 µg/ml hygromycin B and 2 µg/ml puromycin. The clones of each cell type (HeLa EXD2^{-/-}-c1 and 2, HeLa EXD2^{-/-} + EXD2^{WT}-c1 and 2 and HeLa EXD2^{-/-} + EXD2^{D108A/E110A}-c1 and 2) were cultured in DMEM (1 g/l Glucose) containing 10% FCS and gentamycin supplemented with 0.25 µg/ml of puromycin for HeLa EXD2^{-/-} + EXD2^{WT}-c1 and 2 and HeLa EXD2^{-/-} + EXD2^{D108A/E110A}-c1 and 2. XP4PA-SV, CS1ANSV, CS1ANSV + CSB, and XPC Hela Silencix were cultured as described^{33,36,51} in Dulbecco/HamF10 medium containing 10% FCS. U-2 OS^{EXD2-GFP} and U-2 OS^{GFP} cells were cultured as described²⁵ in DMEM medium containing 10% FCS.

Quantification of actively transcribing cells

U-2 OS pTuner 263 cells were induced by 1 µg/ml of dox for the indicated time intervals. Cells were fixed and the number of cells harboring an YFP-MS2 spot counted.

CFP-SKL mRNA quantification

Total RNA was purified using TriReagent following the manufacturer's protocol (Molecular Research Center, TRI18) and cDNA was prepared by the SuperScript IV kit (Invitrogen, 18090050). qPCR reactions were carried out using the LightCycler480 (Roche) machine and the LightCycler 480 SYBR Green I Master (Roche, 04887352001).

EU incorporation assay/RRS assay

RNA labeling by EU incorporation was performed with Click-IT RNA Alexa Fluor 488 Imaging Kit (Invitrogen, C10329) following the manufacturer protocol with the following modifications; SEU was used at 0.1 mM and labeling was performed during 1 h (with the exception of the RNA degradation assay in which mRNAs were labeled during 10 min) to obtain a good linear EU signal as a function of the incubation time³¹. Microscopy pictures were taken with Leica DM 4000 B equipped with a CoolSnap FX monochrome camera and EU signal intensity was quantified by ImageJ software.

Immunofluorescence-based DNA lesion quantification

Cells were plated in a 24-well plate. 24 h later, cells were UV-irradiated with UV-C lamp (15 J/m²) and recovered for different recovery time

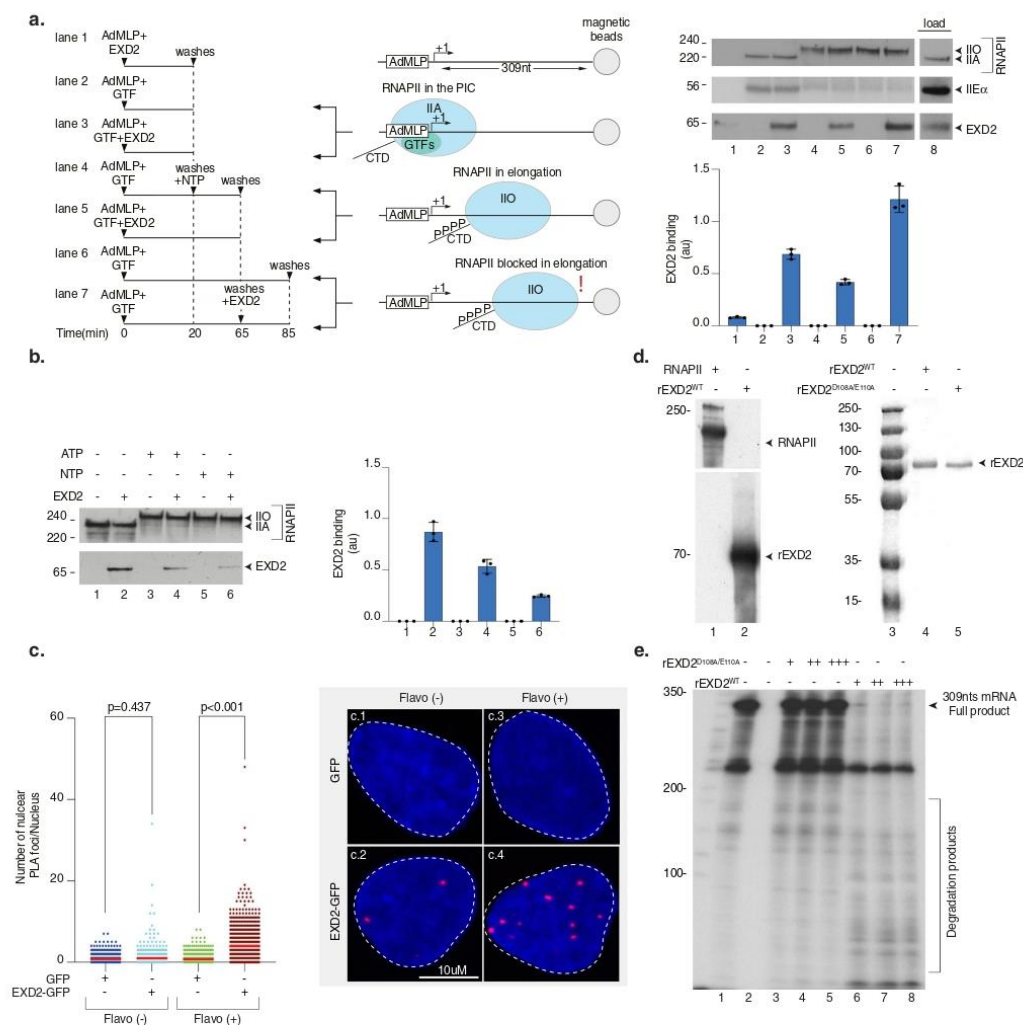


Fig. 6 | EXD2 preferentially interacts with RNAPII stopped in elongation. **a** Left panel; biotinylated DNA template was bound to streptavidin magnetic beads and incubated for 20 min with purified RNAPII and GTFs. After washes, NTPs were added to initiate RNAPII elongation for 45 min. Middle panel; Three conditions were used: in the absence of NTPs where PIC is formed, in the presence of NTPs in which RNAPII is in elongation, and after the chase of NTPs in which RNAPII is blocked from elongating. Right panel; the binding of different factors was evaluated by immunoblotting. The signals for rEXD2 were quantified and plotted in arbitrary units (au). The values are the means of three independent experiments (\pm SD) (Technical triplicates). Molecular sizes are indicated (KDa). Source data are provided as a Source Data file. **b** The biotinylated DNA template was bound to streptavidin magnetic beads and incubated for 20 min with purified RNAPII and GTFs with or without EXD2 as indicated. After washes, ATP or NTPs were added for 45 min. The binding of different factors was evaluated by immunoblotting and the signals for EXD2 were quantified and plotted in arbitrary units (au). The values are the means of three independent experiments (\pm SD) (Technical triplicates).

Molecular sizes are indicated (KDa). Source data are provided as a Source Data file. **c** Number of nuclear GFP/RNAPII PLA foci in U-2 OS cells expressing either GFP or EXD2-GFP with or without Flavopiridol treatment ($n = \text{at least 100 cells per condition}$ from three independent experiments). Red bars indicate mean integrated density. One-way ANOVA with post-hoc Tukey adjustment comparisons were used to determine the p -values. **d** Left panel; rEXD2^{WT} and purified RNAPII were resolved by SDS-PAGE and immunoblotted with anti-EXD2 and anti-RPB1 antibodies. Molecular sizes are indicated (KDa). Right panel; Coomassie staining of recombinant EXD2^{WT} and EXD2^{D108A/E110A}. Lane 3 is the protein markers. Source data are provided as a Source Data file. **e** RNA (309nts) was transcribed from a linear template containing the AdML promoter using a reconstituted RNAPII run-off transcription assay. Then, increasing amount of recombinant EXD2^{WT} or EXD2^{D108A/E110A} (10, 20 and 30 ng) was added to the reaction for an additional 10 min incubation period before the reaction was stopped. Molecular sizes are indicated (Nucleotides). Source data are provided as a Source Data file.

intervals at 37 °C, 5% CO₂. Immuno-labeling of cyclobutane pyrimidine dimers (CPD) and 6–4 photoproducts (6–4PP) was performed using mouse anti-CPD and anti-6–4PP antibodies. DNA was denatured with 2 M HCl for 20 min at RT and blocked in 10% FCS in PBS for 30 min prior to labeling. Microscopy pictures were taken with Leica DM 4000 B equipped with a CoolSnap FX monochrome camera and EU signal intensity was quantified by ImageJ software to determine the percentage of CPD and 6–4PP removal (100% represents the % of lesions measured just after UV irradiation).

Immunofluorescence

Twenty-four hours after plating, cells were irradiated with UV-C lamps (15 J/m²) and recovered for 1 h at 37 °C, 5% CO₂. Thirty minutes before fixation, cells were treated with MitoTracker Red CMXRos according to the manufacturer's instructions. After permeabilization (0.02% Triton X-100 for 10 min) and blocking (4% bovine serum albumin, 20 min), cells were immuno-labeled to visualize either endogenous or tag-FLAG EXD2 using rabbit anti-EXD2 (HPA005848, 1/2000) and mouse anti-FLAG M2 antibodies. Slides were mounted with Vectashield containing DAPI. Microscopy pictures were taken with Leica Spinning Disk CSU-W1 and processed with ImageJ software.

Proximity-ligation assay

U-2 OS cells stably expressing GFP or EXD2-GFP were treated with Flavopiridol (1 μM for 1 h) before permeabilization in 0.5% Triton in PBS for 10 min at 4 °C followed by two washes with PBS, fixation with 3% formaldehyde, 2% sucrose in PBS for 10 min at room temperature and two washes with PBS. Blocking, primary antibody incubation and the PLA assay were then carried out as described²⁵. Antibodies employed for the PLA assay were as follows: GFP (Roche, 11814460001, 1:500) and RNAPII (Bethyl, A300-653A, 1:1000). Images were acquired with Zeiss Axio Observer Z1 Marianas™ Microscope attached with a CSU-W spinning disk unit (built by Intelligent Imaging Innovations (3i)) using a 63x objective. Image analysis was carried out with FIJI (ImageJ) and CellProfiler (Broad Institute) software.

Transfections

Plasmid transfections were conducted using X-tremeGene DNA Transfection Reagent (Roche) according to the manufacturer's protocols. siRNA transfections were conducted using Lipofectamine RNAiMAX Transfection Reagent (Invitrogen) according to the manufacturer's protocols.

TCR-Unscheduled DNA synthesis (TCR-UDS)

GG-NER-deficient XP4PA-SV cells (XP-C) were grown on 18 mm coverslips. siRNA transfections were performed 24 h and 48 h before TCR-UDS assays. After local irradiation at 50 J/m² with UV-C through a 5 μm pore polycarbonate membrane filter, cells were incubated for 8 h with 5-ethynyl-2'-deoxyuridine (EdU), fixed and permeabilized with PBS and 0.5% triton X-100. Then, cells were blocked with PBS + solution (PBS containing 0.15% glycine and 0.5% bovine serum albumin) for 30 min and subsequently incubated for 1 h with mouse monoclonal anti-yH2AX antibody 1:500 diluted in PBS. After extensive washes with PBS containing 0.5% Triton X100, cells were incubated for 45 min with secondary antibodies conjugated with Alexa Fluor 594 fluorescent dyes (Molecular Probes, 1:400 dilution in PBS). Next, cells were washed several times and then incubated for 30 min with the Click-iT reaction cocktail containing Alexa Fluor Azide 488. After washing, the coverslips were mounted with Vectashield containing DAPI (Vector). Images of the cells were obtained with the same microscopy system and constant acquisition parameters. Images were analyzed as follows using ImageJ and a circle of constant size for all images: (i) the background signal was estimated in the nucleus (avoiding the damage, nucleoli and other non-specific signal) and subtracted, (ii) the locally damaged area was defined by using the yH2AX staining, (iii) the mean

fluorescence correlated to the EdU incorporation was then measured and thus an estimate of DNA synthesis after the repair was obtained. For each sample, three independent experiments were performed.

Cell sub-fractionation and IP

Cell fractionation was performed by using the Qproteome Mitochondria Isolation Kit (Qiagen) with some modifications. 2 × 10⁷ HeLa cells were collected 1-h post UV irradiation (20 J/m²) and resuspended in cold lysis buffer. Following centrifugation (1000 × g, 4 °C), the supernatant was removed and the pellet was resuspended in cold disruption buffer using dounce homogenizer. After centrifugation (1000 × g, 4 °C), while the supernatant was treated according to the manufacturer's instruction to collect mitochondrial fraction, the pellet has been washed three times with PBS and resuspended in sucrose buffer (20 mM Tris pH 7.6, 15 mM KCl, 60 mM NaCl, 0.34 M sucrose). Under vortex agitation, high salt buffer (20 mM Tris pH 7.6, 25% glycerol, 1.5 mM MgCl₂, 0.1 mM EDTA, 300 mM NaCl final concentration) was added (30 min at 4 °C). Following centrifugation (2500 × g, 4 °C), the supernatant was removed and the pellet (containing the chromatin fraction) was resuspended in sucrose buffer supplemented with 1 mM CaCl₂. Digestion with Micrococcal Nuclease (25 u, Biolabs) was next performed 5 min at 37 °C and stopped by adding 4 mM EDTA. Sonication was carried out with a Q800R2 sonicator (Qsonica, 3 s on/2 s off during 3 min). The chromatin fraction was collected after centrifugation (16,000 × g, 30 min at 4 °C). Bradford protein assays were used to measure the final concentration of the mitochondrial and chromatin fraction. IP experiments were performed with the chromatin fraction using anti-RPB1 monoclonal antibody in the presence or not of Benzonase.

Protein-DNA binding assay

Biotinylated AdMLP DNA template bound to streptavidin magnetic beads was incubated 20 min at 25 °C with purified RNAPII, TFIIA, IIB, IIF, TBP, IIH and EXD2 in transcription buffer (20 mM HEPES (pH 7.9), 7 mM MgCl₂, 55 mM KCl). After three washings at 50 mM NaCl, bound fractions were resolved by SDS-PAGE for immunoblottings and others were incubated 45 min at 25 °C with NTP (200 μM). After washings, these fractions were in turn resolved by SDS-PAGE or were further incubated 20 min with EXD2. The abundance of EXD2 was assessed by immunoblot densitometry analysis (using ImageJ software). Each signal was quantified three times and plotted in arbitrary units (au).

Reconstituted run-off transcription

Reaction mixtures of 12 μL containing 50 ng of linear AdMLP DNA template and recombinant TFIIH, TFIIIB, TFIIIE, TFIIF, TBP together with purified RNA pol II as described⁵² were pre-incubated for 20 min at 25 °C in transcription buffer (20 mM HEPES (pH7.9), 7 mM MgCl₂, 55 mM KCl) and transcription was initiated by the addition of 2 μL nucleotide solution to final concentrations of 600 μM UTP, ATP, GTP and 0.6 μM (α-³²P) CTP. Reactions were carried out for 30 min and recombinant EXD2 was added for another 10 min. Reaction was stopped by the addition of 0.5 μL of 0.5 M EDTA (pH 8). The resulting RNA transcripts were analyzed on an 8% denaturing polyacrylamide gel.

Statistics and reproducibility

Experimental data were plotted and analyzed using GraphPad Prism (GraphPad Software Inc.). The number of samples and replicates are indicated in the respective figure legends. Each experiment was repeated a least three times with similar results.

Extended resource table

An extended resource table with antibodies, oligonucleotide sequences, chemicals, and reagents used in this work is provided in Supplementary Table 1.

Reporting summary

Further information on research design is available in the Nature Portfolio Reporting Summary linked to this article.

Data availability

All data generated or analyzed during this study are included in this published article (and its supplementary information files) and are available from the corresponding author on request. An extended resource table with antibodies, oligonucleotide sequences, chemicals and reagents used in this work is provided in Supplemental Table 1. Source data are provided with this paper.

References

- Hoeijmakers, J. H. J. DNA damage, aging, and cancer. *N. Engl. J. Med.* **361**, 1475–1485 (2009).
- Vermeij, W. P., Hoeijmakers, J. H. & Pothof, J. Aging: not all DNA damage is equal. *Curr. Opin. Genet. Dev.* **26**, 124–130 (2014).
- Kotsantis, P., Petermann, E. & Boulton, S. J. Mechanisms of oncogene-induced replication stress: Jigsaw falling into place. *Cancer Discov.* **8**, 537–555 (2018).
- Lee, T. I. & Young, R. A. Transcriptional regulation and its misregulation in disease. *Cell* **152**, 1237–1251 (2013).
- Jackson, S. P. & Bartek, J. The DNA-damage response in human biology and disease. *Nature* **461**, 1071–1078 (2009).
- Edifizi, D. & Schumacher, B. Genome instability in development and aging: insights from nucleotide excision repair in humans, mice, and worms. *Biomolecules* **5**, 1855–1869 (2015).
- Sancar, A. & Reardon, J. T. Nucleotide excision repair in *E. Coli* and man. *Adv. Protein Chem.* **69**, 43–71 (2004).
- Marteijn, J. A., Lans, H., Vermeulen, W. & Hoeijmakers, J. H. Understanding nucleotide excision repair and its roles in cancer and ageing. *Nat. Rev. Mol. Cell Biol.* **15**, 465–481 (2014).
- Scharer, O. D. Nucleotide excision repair in eukaryotes. *Cold Spring Harb. Perspect. Biol.* **5**, a012609 (2013).
- van den Heuvel, D., van der Weegen, Y., Boer, D. E. C., Ogi, T. & Luijsterburg, M. S. Transcription-coupled DNA repair: from mechanism to human disorder. *Trends Cell Biol.* **31**, 359–371 (2021).
- Ljungman, M. & Lane, D. P. Transcription—guarding the genome by sensing DNA damage. *Nat. Rev. Cancer* **4**, 727–737 (2004).
- Hanawalt, P. C. & Spivak, G. Transcription-coupled DNA repair: two decades of progress and surprises. *Nat. Rev. Mol. Cell Biol.* **9**, 958–970 (2008).
- Foster, M. & Mullenders, L. H. Transcription-coupled nucleotide excision repair in mammalian cells: molecular mechanisms and biological effects. *Cell Res.* **18**, 73–84 (2008).
- Lans, H., Hoeijmakers, J. H. J., Vermeulen, W. & Marteijn, J. A. The DNA damage response to transcription stress. *Nat. Rev. Mol. Cell Biol.* **20**, 766–784 (2019).
- Lavigne, M. D., Konstantopoulos, D., Ntakou-Zamplara, K. Z., Liakos, A. & Foster, M. Global unleashing of transcription elongation waves in response to genotoxic stress restricts somatic mutation rate. *Nat. Commun.* **8**, 2076 (2017).
- Gyenis, Á. et al. UVB induces a genome-wide acting negative regulatory mechanism that operates at the level of transcription initiation in human cells. *PLoS Genet.* **10**, e1004483 (2014).
- Rockx, D. A. et al. UV-induced inhibition of transcription involves repression of transcription initiation and phosphorylation of RNA polymerase II. *Proc. Natl Acad. Sci. USA* **97**, 10503–10508 (2000).
- Tufegdžić Vidaković, A. et al. Regulation of the RNAPII pool is integral to the DNA damage response. *Cell* **180**, 1245–1261.e21 (2020).
- Nakazawa, Y. et al. Ubiquitination of DNA damage-stalled RNAPII promotes transcription-coupled repair. *Cell* **180**, 1228–1244.e24 (2020).
- Oksenyich, V. et al. Histone methyltransferase DOT1L drives recovery of gene expression after a genotoxic attack. *PLoS Genet.* **9**, e1003611 (2013).
- Mourgues, S. et al. ELL, a novel TFIIF partner, is involved in transcription restart after DNA repair. *Proc. Natl Acad. Sci. USA* **110**, 17927–17932 (2013).
- Adam, S., Polo, S. E. & Almouzni, G. Transcription recovery after DNA damage requires chromatin priming by the H3.3 histone chaperone HIRA. *Cell* **155**, 94–106 (2013).
- Dinant, C. et al. Enhanced chromatin dynamics by FACT promotes transcriptional restart after UV-induced DNA damage. *Mol. Cell* **51**, 469–479 (2013).
- Geijer, M. E. et al. Elongation factor ELOF1 drives transcription-coupled repair and prevents genome instability. *Nat. Cell Biol.* **23**, 608–619 (2021).
- Nieminuszczy, J. et al. EXD2 protects stressed replication forks and is required for cell viability in the absence of BRCA1/2. *Mol. Cell* **75**, 605–619.e6 (2019).
- Broderick, R. et al. EXD2 promotes homologous recombination by facilitating DNA end resection. *Nat. Cell Biol.* **18**, 271–280 (2016).
- Janicki, S. M. et al. From silencing to gene expression: real-time analysis in single cells. *Cell* **116**, 683–698 (2004).
- Shanbhag, N. M., Rafalska-Metcalfe, I. U., Balane-Bolivar, C., Janicki, S. M. & Greenberg, R. A. ATM-dependent chromatin changes silence transcription in cis to DNA double-strand breaks. *Cell* **141**, 970–981 (2010).
- Mayne, L. V. & Lehmann, A. R. Failure of RNA synthesis to recover after UV radiation: an early defect in cells from individuals with Cockayne's syndrome and xeroderma pigmentosum. *Cancer Res.* **42**, 1473–1478 (1982).
- Williamson, L. et al. UV irradiation induces a non-coding RNA that functionally opposes the protein encoded by the same gene. *Cell* **168**, 843–855.e13 (2017).
- Alekseev, S. et al. Transcription without XPB establishes a unified helicase-independent mechanism of promoter opening in eukaryotic gene expression. *Mol. Cell* **65**, 504–514.e4 (2017).
- van Hoffen, A., Venema, J., Meschini, R., van Zeeland, A. A. & Mullenders, L. H. Transcription-coupled repair removes both cyclobutane pyrimidine dimers and 6-4 photoproducts with equal efficiency and in a sequential way from transcribed DNA in xeroderma pigmentosum group C fibroblasts. *Embo J.* **14**, 360–367 (1995).
- Kristensen, U. et al. Regulatory interplay of Cockayne syndrome B ATPase and stress-response gene ATF3 following genotoxic stress. *Proc. Natl Acad. Sci. U.S.A.* **110**, E2261–E2270 (2013).
- Park, J. et al. The structure of human EXD2 reveals a chimeric 3' to 5' exonuclease domain that discriminates substrates via metal coordination. *Nucleic Acids Res.* **47**, 7078–7093 (2019).
- Biard, D. S. F., Despras, E., Sarasin, A. & Angulo, J. F. Development of new EBV-based vectors for stable expression of small interfering RNA to mimic human syndromes: application to NER gene silencing. *Mol. Cancer Res.* **3**, 519–529 (2005).
- Donnio, L.-M., Lagarou, A., Sœur, G., Mari, P.-O. & Giglia-Mari, G. CSB-dependent cyclin-dependent kinase 9 degradation and RNA polymerase II phosphorylation during transcription-coupled repair. *Mol. Cell Biol.* **39**, e00225-18 (2019).
- Takebayashi, Y. et al. Antiproliferative activity of ecteinascidin 743 is dependent upon transcription-coupled nucleotide-excision repair. *Nat. Med.* **7**, 961–966 (2001).
- Oh, K.-S., Bustin, M., Mazur, S. J., Appella, E. & Kraemer, K. H. UV-induced histone H2AX phosphorylation and DNA damage related proteins accumulate and persist in nucleotide excision repair-deficient XP-B cells. *DNA Repair* **10**, 5–15 (2011).

39. Gerard, M. et al. Purification and interaction properties of the human RNA polymerase B(II) general transcription factor BTF2. *J. Biol. Chem.* **266**, 20940–20945 (1991).
40. Compe, E., Genes, C. M., Braun, C., Coin, F. & Egly, J. M. TFIIIE orchestrates the recruitment of the TFIIH kinase module at promoter before release during transcription. *Nat. Commun.* **10**, 2084 (2019).
41. Noe Gonzalez, M., Blears, D. & Svejstrup, J. Q. Causes and consequences of RNA polymerase II stalling during transcript elongation. *Nat. Rev. Mol. Cell Biol.* **22**, 3–21 (2021).
42. Jia, N. et al. Dealing with transcription-blocking DNA damage: repair mechanisms, RNA polymerase II processing and human disorders. *DNA Repair* **106**, 103192 (2021).
43. Gregersen, L. H. & Svejstrup, J. Q. The cellular response to transcription-blocking DNA damage. *Trends Biochem. Sci.* **43**, 327–341 (2018).
44. Daniel, L. et al. Mechanistic insights in transcription-coupled nucleotide excision repair of ribosomal DNA. *Proc. Natl Acad. Sci. USA* **115**, E6770–E6779 (2018).
45. Sigurdsson, S., Dirac-Svejstrup, A. B. & Svejstrup, J. Q. Evidence that transcript cleavage is essential for RNA polymerase II transcription and cell viability. *Mol. Cell* **38**, 202–210 (2010).
46. Jensen, A. & Mullenders, L. H. F. Transcription factor IIS impacts UV-inhibited transcription. *DNA Repair* **9**, 1142–1150 (2010).
47. Hensen, F., Moreton, A., van Esvelde, S., Farge, G. & Spelbrink, J. N. The mitochondrial outer-membrane location of the EXD2 exonuclease contradicts its direct role in nuclear DNA repair. *Sci. Rep.* **8**, 5368 (2018).
48. Silva, J. et al. EXD2 governs germ stem cell homeostasis and lifespan by promoting mitochondria integrity and translation. *Nat. Cell Biol.* **20**, 162–174 (2018).
49. Geijer, M. E. & Martijn, J. A. What happens at the lesion does not stay at the lesion: Transcription-coupled nucleotide excision repair and the effects of DNA damage on transcription in cis and trans. *DNA Repair* **71**, 56–68 (2018).
50. Biehls, R. et al. DNA double-strand break resection occurs during non-homologous end joining in G1 but is distinct from resection during homologous recombination. *Mol. Cell* **65**, 671–684.e5 (2017).
51. Le May, N. et al. NER factors are recruited to active promoters and facilitate chromatin modification for transcription in the absence of exogenous genotoxic attack. *Mol. Cell* **38**, 54–66 (2010).
52. Coin, F. et al. p8/TTD-A as a repair-specific TFIIH subunit. *Mol. Cell* **21**, 215–226 (2006).

Acknowledgements

We thank Dr. Patrick Reilly for the critical reading of the article and Dr. Roger Greenberg (University of Pennsylvania) for the U-2 OS-pTuner263 cells and Karolina Chabowska (ICR London) for recombinant EXD2^{WT} and EXD2^{D108A/E110A} proteins expressed in and purified from insect cells. We thank Amélie Freismuth and the cell culture service of IGBMC. This study was supported by ANR (TFIIH-2021), by the Ligue contre le cancer (Equipe Labélisée 2022-2024) and the grant ANR-10-LABX-0030-INRT, a French State fund managed by the Agence Nationale de la Recherche

under the frame program Investissements d'Avenir ANR-10-IDEX-0002-02. M.C. is supported by the "Ligue contre le Cancer". C.E. by the "Région Réunion". LMD is supported by Agence Nationale de la Recherche (ANR-14-CE10-0009) and Institut National du Cancer (PLBIO17-043 and PLBIO19-126). Work in WN's laboratory is funded by Cancer Research UK Programme (A24881).

Author contributions

J.S. (EU, WB, mRNA degradation), M.C. (EU, mRNA degradation), A.Z., (Confocal microscopy), P.C. (IP, Fractionation assay), L.-M.D. (TCR-UDS), P.B. (WB), C.E. (CFP-SKL reporter assay), J.N. (PLA assay), C.B. (In vitro binding assay) and S.A. (CFP-SKL assay) conducted the experiments. J.S., W.N., J.M.-E., G.G.-M., E.C., and F.C. analyzed the results and/or provided valuable material. F.C. designed the experiments and wrote the paper.

Competing interests

The authors declare no competing interests.

Additional information

Supplementary information The online version contains supplementary material available at

<https://doi.org/10.1038/s41467-023-35922-5>.

Correspondence and requests for materials should be addressed to Frédéric Coin.

Peer review information *Nature Communications* thanks Björn Schumacher and the other, anonymous, reviewer(s) for their contribution to the peer review of this work.

Reprints and permissions information is available at

<http://www.nature.com/reprints>

Publisher's note Springer Nature remains neutral with regard to jurisdictional claims in published maps and institutional affiliations.

Open Access This article is licensed under a Creative Commons Attribution 4.0 International License, which permits use, sharing, adaptation, distribution and reproduction in any medium or format, as long as you give appropriate credit to the original author(s) and the source, provide a link to the Creative Commons license, and indicate if changes were made. The images or other third party material in this article are included in the article's Creative Commons license, unless indicated otherwise in a credit line to the material. If material is not included in the article's Creative Commons license and your intended use is not permitted by statutory regulation or exceeds the permitted use, you will need to obtain permission directly from the copyright holder. To view a copy of this license, visit <http://creativecommons.org/licenses/by/4.0/>.

© The Author(s) 2023

Bibliography

Abdulrahman, Wassim, Izarn Iltis, Laura Radu, et al. 2013. « ARCH Domain of XPD, an Anchoring Platform for CAK That Conditions TFIIH DNA Repair and Transcription Activities ». *Proceedings of the National Academy of Sciences* 110 (8). <https://doi.org/10.1073/pnas.1213981110>.

Abeti, Rosella, Anna Zeitlberger, Colm Peelo, et al. 2019. « Xeroderma Pigmentosum: Overview of Pharmacology and Novel Therapeutic Strategies for Neurological Symptoms ». *British Journal of Pharmacology* 176 (22): 4293-301. <https://doi.org/10.1111/bph.14557>.

Aguilar-Fuentes, Javier, Mariana Fregoso, Mariana Herrera, et al. 2008. « P8/TTDA Overexpression Enhances UV-Irradiation Resistance and Suppresses TFIIH Mutations in a Drosophila Trichothiodystrophy Model ». *PLoS Genetics* 4 (11): e1000253. <https://doi.org/10.1371/journal.pgen.1000253>.

Amaral, Paulo, Silvia Carbonell-Sala, Francisco M. De La Vega, et al. 2023. « The Status of the Human Gene Catalogue ». *Nature* 622 (7981): 41-47. <https://doi.org/10.1038/s41586-023-06490-x>.

Amasino, Audra L., Shalini Gupta, Larry J. Friedman, Jeff Gelles, et Stephen P. Bell. 2023. « Regulation of Replication Origin Licensing by ORC Phosphorylation Reveals a Two-Step Mechanism for Mcm2-7 Ring Closing ». *Proceedings of the National Academy of Sciences of the United States of America* 120 (29): e2221484120. <https://doi.org/10.1073/pnas.2221484120>.

Andersson, Robin, et Albin Sandelin. 2020. « Determinants of Enhancer and Promoter Activities of Regulatory Elements ». *Nature Reviews Genetics* 21 (2): 71-87. <https://doi.org/10.1038/s41576-019-0173-8>.

André, Kévin M., Eliet H. Sipos, et Julie Soutourina. 2021. « Mediator Roles Going Beyond Transcription ». *Trends in Genetics* 37 (3): 224-34. <https://doi.org/10.1016/j.tig.2020.08.015>.

Antonin, Wolfram, et Heinz Neumann. 2016. « Chromosome Condensation and Decondensation during Mitosis ». *Current Opinion in Cell Biology* 40 (juin): 15-22. <https://doi.org/10.1016/j.ceb.2016.01.013>.

Ashton, Nicholas W., Nancy Jaiswal, Natália Cestari Moreno, et al. 2023. « A Novel Interaction Between RAD23A/B and Y-Family DNA Polymerases ». *Journal of Molecular Biology* 435 (24): 168353. <https://doi.org/10.1016/j.jmb.2023.168353>.

Assfalg, Robin, Anton Lebedev, Omar Garcia Gonzalez, Adrian Schelling, Sylvia Koch, et Sebastian Iben. 2012. « TFIIH Is an Elongation Factor of RNA Polymerase I ». *Nucleic Acids Research* 40 (2): 650-59. <https://doi.org/10.1093/nar/gkr746>.

Bae, Sunhee, et Bluma J. Lesch. 2020. « H3K4me1 Distribution Predicts Transcription State and Poising at Promoters ». *Frontiers in Cell and Developmental Biology* 8: 289. <https://doi.org/10.3389/fcell.2020.00289>.

Barba-Aliaga, Marina, Paula Alepuz, et José E. Pérez-Ortín. 2021. « Eukaryotic RNA Polymerases: The Many Ways to Transcribe a Gene ». *Frontiers in Molecular Biosciences* 8 (avril): 663209. <https://doi.org/10.3389/fmolb.2021.663209>.

Barnett, Jamie T, Jochen Kuper, Wolfgang Koelmel, Caroline Kisker, et Neil M Kad. 2020. « The TFIIH Subunits P44/P62 Act as a Damage Sensor during Nucleotide Excision Repair ». *Nucleic Acids Research* 48 (22): 12689-96. <https://doi.org/10.1093/nar/gkaa973>.

Barshad, Gilad, James J. Lewis, Alexandra G. Chivu, et al. 2023. « RNA Polymerase II Dynamics Shape Enhancer–Promoter Interactions ». *Nature Genetics* 55 (8): 1370-80. <https://doi.org/10.1038/s41588-023-01442-7>.

Basu, Alakananda, et Soumya Krishnamurthy. 2010. « Cellular Responses to Cisplatin-Induced DNA Damage ». *Journal of Nucleic Acids* 2010 (1): 201367. <https://doi.org/10.4061/2010/201367>.

Benkhaira, N., N. Kerouaz, et Y. Kitouni. 2021. « Syndrome de Cockayne type 3 ; à propos d'un cas ». *La Revue de Médecine Interne* 42 (décembre): A420. <https://doi.org/10.1016/j.revmed.2021.10.142>.

Bentley, David L. 2014. « Coupling mRNA Processing with Transcription in Time and Space ». *Nature Reviews. Genetics* 15 (3): 163-75. <https://doi.org/10.1038/nrg3662>.

Bhandari, Seema Khattri, Nathaniel Wiest, Annahita Sallmyr, et al. 2023. « Unchanged PCNA and DNMT1 Dynamics during Replication in DNA Ligase I-Deficient Cells but Abnormal Chromatin Levels of Non-Replicative Histone H1 ». *Scientific Reports* 13 (1): 4363. <https://doi.org/10.1038/s41598-023-31367-4>.

Bhuiyan, Tanja, et H.Th. Marc Timmers. 2019. « Promoter Recognition: Putting TFIID on the Spot ». *Trends in Cell Biology* 29 (9): 752-63. <https://doi.org/10.1016/j.tcb.2019.06.004>.

- Blackford, Andrew N., et Stephen P. Jackson. 2017. « ATM, ATR, and DNA-PK: The Trinity at the Heart of the DNA Damage Response ». *Molecular Cell* 66 (6): 801-17. <https://doi.org/10.1016/j.molcel.2017.05.015>.
- Borukhov, Sergei, et Evgeny Nudler. 2003. « RNA Polymerase Holoenzyme: Structure, Function and Biological Implications ». *Current Opinion in Microbiology* 6 (2): 93-100. [https://doi.org/10.1016/S1369-5274\(03\)00036-5](https://doi.org/10.1016/S1369-5274(03)00036-5).
- Boutin, Joël, Frédéric Lessard, Michel G. Tremblay, et Tom Moss. 2019. « The Short N-Terminal Repeats of Transcription Termination Factor 1 Contain Semi-Redundant Nucleolar Localization Signals and P19-ARF Tumor Suppressor Binding Sites ». *The Yale Journal of Biology and Medicine* 92 (3): 385-96.
- Boyle, Jennifer, Takahiro Ueda, Kyu-Seon Oh, et al. 2008. « Persistence of Repair Proteins at Unrepaired DNA Damage Distinguishes Diseases with *ERCC2* (*XPD*) Mutations: Cancer-Prone Xeroderma Pigmentosum vs. Non-Cancer-Prone Trichothiodystrophy ». *Human Mutation* 29 (10): 1194-208. <https://doi.org/10.1002/humu.20768>.
- Brambullo, Tito, Michele Rosario Colonna, Vincenzo Vindigni, et al. 2022. « Xeroderma Pigmentosum: A Genetic Condition Skin Cancer Correlated—A Systematic Review ». *BioMed Research International* 2022 (1): 8549532. <https://doi.org/10.1155/2022/8549532>.
- Brannan, Kris, Hyunmin Kim, Benjamin Erickson, et al. 2012. « mRNA Decapping Factors and the Exonuclease Xrn2 Function in Widespread Premature Termination of RNA Polymerase II Transcription ». *Molecular Cell* 46 (3): 311-24. <https://doi.org/10.1016/j.molcel.2012.03.006>.
- Brooker, Amanda S., et Karen M. Berkowitz. 2014. « The Roles of Cohesins in Mitosis, Meiosis, and Human Health and Disease ». *Methods in Molecular Biology (Clifton, N.J.)* 1170: 229-66. https://doi.org/10.1007/978-1-4939-0888-2_11.
- Brown, Jay C. 2018. « Control of Human Gene Expression: High Abundance of Divergent Transcription in Genes Containing Both INR and BRE Elements in the Core Promoter ». *PloS One* 13 (8): e0202927. <https://doi.org/10.1371/journal.pone.0202927>.
- Bruskov, V. I. 2002. « Heat-induced formation of reactive oxygen species and 8-oxoguanine, a biomarker of damage to DNA ». *Nucleic Acids Research* 30 (6): 1354-63. <https://doi.org/10.1093/nar/30.6.1354>.

- Busso, D., A. Keriél, B. Sandrock, A. Poterszman, O. Gileadi, et J. M. Egly. 2000. « Distinct Regions of MAT1 Regulate Cdk7 Kinase and TFIIH Transcription Activities ». *The Journal of Biological Chemistry* 275 (30): 22815-23. <https://doi.org/10.1074/jbc.M002578200>.
- Byrd, Alicia K., et Kevin D. Raney. 2012. « Superfamily 2 Helicases ». *Frontiers in Bioscience (Landmark Edition)* 17 (6): 2070-88. <https://doi.org/10.2741/4038>.
- Calvo, Olga. 2020. « RNA Polymerase II Phosphorylation and Gene Looping: New Roles for the Rpb4/7 Heterodimer in Regulating Gene Expression ». *Current Genetics* 66 (5): 927-37. <https://doi.org/10.1007/s00294-020-01084-w>.
- Chadha, Yagya, Arohi Khurana, et Kurt M. Schmoller. 2024. « Eukaryotic Cell Size Regulation and Its Implications for Cellular Function and Dysfunction ». *Physiological Reviews* 104 (4): 1679-717. <https://doi.org/10.1152/physrev.00046.2023>.
- Chauhan, Anil K., Ping Li, Yingming Sun, Gulzar Wani, Qianzheng Zhu, et Altaf A. Wani. 2021. « Spironolactone-Induced XPB Degradation Requires TFIIH Integrity and Ubiquitin-Selective Segregase VCP/P97 ». *Cell Cycle* 20 (1): 81-95. <https://doi.org/10.1080/15384101.2020.1860559>.
- Chen, Jia, Jianping Xiong, Jiejun Wang, Leizhen Zheng, YanFei Gao, et Zhongzhen Guan. 2018. « Capecitabine/Cisplatin versus 5-Fluorouracil/Cisplatin in Chinese Patients with Advanced and Metastatic Gastric Cancer: Re-Analysis of Efficacy and Safety Data from the ML17032 Phase III Clinical Trial ». *Asia-Pacific Journal of Clinical Oncology* 14 (5): e310-16. <https://doi.org/10.1111/ajco.12832>.
- Cheon, Na Young, Hyun-Suk Kim, Jung-Eun Yeo, Orlando D Schärer, et Ja Yil Lee. 2019. « Single-Molecule Visualization Reveals the Damage Search Mechanism for the Human NER Protein XPC-RAD23B ». *Nucleic Acids Research* 47 (16): 8337-47. <https://doi.org/10.1093/nar/gkz629>.
- Chhetri, Khadka B. 2025. « DNA Compaction and Chromatin Dynamics: The Role of Cationic Polyamines and Proteins ». *Biochemical and Biophysical Research Communications* 756 (avril): 151538. <https://doi.org/10.1016/j.bbrc.2025.151538>.
- Choi, Eui-Hwan, Seobin Yoon, Young Eun Koh, et al. 2022. « Meiosis-Specific Cohesin Complexes Display Essential and Distinct Roles in Mitotic Embryonic Stem Cell Chromosomes ». *Genome Biology* 23 (1): 70. <https://doi.org/10.1186/s13059-022-02632-y>.

- Chon, James, Patrick J. Stover, et Martha S. Field. 2017. « Targeting Nuclear Thymidylate Biosynthesis ». *Molecular Aspects of Medicine* 53 (février): 48-56. <https://doi.org/10.1016/j.mam.2016.11.005>.
- Chung, Mingyu, Chad Liu, Hee Won Yang, Marielle S. Köberlin, Steven D. Cappell, et Tobias Meyer. 2019. « Transient Hysteresis in CDK4/6 Activity Underlies Passage of the Restriction Point in G1 ». *Molecular Cell* 76 (4): 562-573.e4. <https://doi.org/10.1016/j.molcel.2019.08.020>.
- Coin, Frédéric, Luca Proietti De Santis, Tiziana Nardo, Olga Zlobinskaya, Miria Stefanini, et Jean-Marc Egly. 2006. « P8/TTD-A as a Repair-Specific TFIIH Subunit ». *Molecular Cell* 21 (2): 215-26. <https://doi.org/10.1016/j.molcel.2005.10.024>.
- Coin, Frédéric, Jean-Christophe Marinoni, Carlo Rodolfo, Sébastien Fribourg, Antonia Maria Pedrini, et Jean-Marc Egly. 1998. « Mutations in the XPD Helicase Gene Result in XP and TTD Phenotypes, Preventing Interaction between XPD and the P44 Subunit of TFIIH ». *Nature Genetics* 20 (2): 184-88. <https://doi.org/10.1038/2491>.
- Coin, Frédéric, Valentyn Oksenysh, et Jean-Marc Egly. 2007. « Distinct Roles for the XPB/P52 and XPD/P44 Subcomplexes of TFIIH in Damaged DNA Opening during Nucleotide Excision Repair ». *Molecular Cell* 26 (2): 245-56. <https://doi.org/10.1016/j.molcel.2007.03.009>.
- Coin, Frédéric, Valentyn Oksenysh, Vincent Mocquet, Stefanie Groh, Christine Blattner, et Jean-Marc Egly. 2008. « Nucleotide Excision Repair Driven by the Dissociation of CAK from TFIIH ». *Molecular Cell* 31 (1): 9-20. <https://doi.org/10.1016/j.molcel.2008.04.024>.
- Compe, Emmanuel, et Jean-Marc Egly. 2007. « Troubles neurologiques et trichothiodystrophie: Sans TFIIH, les hormones thyroïdiennes défontent ». *médecine/sciences* 23 (12): 1171-72. <https://doi.org/10.1051/medsci/200723121171>.
- Compe, Emmanuel, et Jean-Marc Egly. 2012. « TFIIH: When Transcription Met DNA Repair ». *Nature Reviews Molecular Cell Biology* 13 (6): 343-54. <https://doi.org/10.1038/nrm3350>.
- Compe, Emmanuel, et Jean-Marc Egly. 2016. « Nucleotide Excision Repair and Transcriptional Regulation: TFIIH and Beyond ». *Annual Review of Biochemistry* 85 (1): 265-90. <https://doi.org/10.1146/annurev-biochem-060815-014857>.
- Compe, Emmanuel, Carlos M. Genes, Cathy Braun, Frederic Coin, et Jean-Marc Egly. 2019. « TFIIH Orchestrates the Recruitment of the TFIIH Kinase Module at Promoter before Release during Transcription ». *Nature Communications* 10 (1): 2084. <https://doi.org/10.1038/s41467-019-10131-1>.

- Compe, Emmanuel, Evanthia Pangou, Nicolas Le May, et al. 2022. « Phosphorylation of XPD Drives Its Mitotic Role Independently of Its DNA Repair and Transcription Functions ». *Science Advances* 8 (33): eabp9457. <https://doi.org/10.1126/sciadv.abp9457>.
- Core, Leighton, et Karen Adelman. 2019. « Promoter-Proximal Pausing of RNA Polymerase II: A Nexus of Gene Regulation ». *Genes & Development* 33 (15-16): 960-82. <https://doi.org/10.1101/gad.325142.119>.
- Cortazar, Michael A., Benjamin Erickson, Nova Fong, Sarala J. Pradhan, Evgenia Ntini, et David L. Bentley. 2022. « Xrn2 Substrate Mapping Identifies Torpedo Loading Sites and Extensive Premature Termination of RNA Pol II Transcription ». *Genes & Development* 36 (19-20): 1062-78. <https://doi.org/10.1101/gad.350004.122>.
- Cramer, P., K.-J. Armache, S. Baumli, et al. 2008. « Structure of Eukaryotic RNA Polymerases ». *Annual Review of Biophysics* 37 (1): 337-52. <https://doi.org/10.1146/annurev.biophys.37.032807.130008>.
- Cramer, Patrick. 2002. « Multisubunit RNA Polymerases ». *Current Opinion in Structural Biology* 12 (1): 89-97. [https://doi.org/10.1016/S0959-440X\(02\)00294-4](https://doi.org/10.1016/S0959-440X(02)00294-4).
- Cramer, Patrick. 2019. « Organization and Regulation of Gene Transcription ». *Nature* 573 (7772): 45-54. <https://doi.org/10.1038/s41586-019-1517-4>.
- Crncec, Adrijana, et Helfrid Hocheegger. 2019. « Triggering Mitosis ». *FEBS Letters* 593 (20): 2868-88. <https://doi.org/10.1002/1873-3468.13635>.
- Cruz-Becerra, Grisel, Mandy Juárez, Viviana Valadez-Graham, et Mario Zurita. 2016. « Analysis of *Drosophila* P8 and P52 Mutants Reveals Distinct Roles for the Maintenance of TFIIH Stability and Male Germ Cell Differentiation ». *Open Biology* 6 (10): 160222. <https://doi.org/10.1098/rsob.160222>.
- Dasari, Shaloam, et Paul Bernard Tchounwou. 2014. « Cisplatin in Cancer Therapy: Molecular Mechanisms of Action ». *European Journal of Pharmacology* 740 (octobre): 364-78. <https://doi.org/10.1016/j.ejphar.2014.07.025>.
- De Marco Zompit, Mara, et Manuel Stucki. 2021. « Mechanisms of Genome Stability Maintenance during Cell Division ». *DNA Repair* 108 (décembre): 103215. <https://doi.org/10.1016/j.dnarep.2021.103215>.

- Dehm, Scott M., et Donald J. Tindall. 2007. « Androgen Receptor Structural and Functional Elements: Role and Regulation in Prostate Cancer ». *Molecular Endocrinology* 21 (12): 2855-63. <https://doi.org/10.1210/me.2007-0223>.
- Demin, Annie A., Kouji Hirota, Masataka Tsuda, et al. 2021. « XRCC1 Prevents Toxic PARP1 Trapping during DNA Base Excision Repair ». *Molecular Cell* 81 (14): 3018-3030.e5. <https://doi.org/10.1016/j.molcel.2021.05.009>.
- Diaz, Ulises, Zane J. Bergman, Brittany M. Johnson, et al. 2019. « Microtubules Are Necessary for Proper Reticulon Localization during Mitosis ». *PloS One* 14 (12): e0226327. <https://doi.org/10.1371/journal.pone.0226327>.
- Dirar, Qais S., Hebah M. Musalem, Selwa A.F. Al-Hazzaa, Abdulaziz A. Al Zoba, et Amal A. Almalki. 2020. « Effect of Pegylated Interferon and Mitomycin C on Ocular Surface Squamous Neoplasia in Xeroderma Pigmentosum: A Case Series ». *American Journal of Case Reports* 21 (avril). <https://doi.org/10.12659/AJCR.921301>.
- Dubaele, Sandy, Luca Proietti De Santis, Rachelle J Bienstock, et al. 2003. « Basal Transcription Defect Discriminates between Xeroderma Pigmentosum and Trichothiodystrophy in XPD Patients ». *Molecular Cell* 11 (6): 1635-46. [https://doi.org/10.1016/S1097-2765\(03\)00182-5](https://doi.org/10.1016/S1097-2765(03)00182-5).
- Egly, Jean-Marc, et Frédéric Coin. 2011. « A History of TFIIH: Two Decades of Molecular Biology on a Pivotal Transcription/Repair Factor ». *DNA Repair* 10 (7): 714-21. <https://doi.org/10.1016/j.dnarep.2011.04.021>.
- Elowe, Sabine, et Victor M. Bolanos-Garcia. 2022. « The Spindle Checkpoint Proteins BUB1 and BUBR1: (SLiM)Ming down to the Basics ». *Trends in Biochemical Sciences* 47 (4): 352-66. <https://doi.org/10.1016/j.tibs.2022.01.004>.
- Emmert, Steffen, Takahiro Ueda, Urs Zumsteg, et al. 2009. « Strict Sun Protection Results in Minimal Skin Changes in a Patient with Xeroderma Pigmentosum and a Novel c.2009delG Mutation in XPD (ERCC2) ». *Experimental Dermatology* 18 (1): 64-68. <https://doi.org/10.1111/j.1600-0625.2008.00763.x>.
- Engel, Christoph, Tobias Gubbey, Simon Neyer, et al. 2017. « Structural Basis of RNA Polymerase I Transcription Initiation ». *Cell* 169 (1): 120-131.e22. <https://doi.org/10.1016/j.cell.2017.03.003>.
- Eykelenboom, John K., Marek Gierliński, Zuojun Yue, et Tomoyuki U. Tanaka. 2024. « Exclusion of Condensin I from the Nucleus during Prophase Coordinates Mitotic Chromosome

Reorganization to Complete Sister Chromatid Resolution ». Prépublication, avril 27. <https://doi.org/10.1101/2024.04.26.591320>.

Eykelenboom, John Kenneth, Emma Christina Harte, Lynn Canavan, et al. 2013. « ATR Activates the S-M Checkpoint during Unperturbed Growth to Ensure Sufficient Replication Prior to Mitotic Onset ». *Cell Reports* 5 (4): 1095-107. <https://doi.org/10.1016/j.celrep.2013.10.027>.

Fagundes, Rafaela, et Leonardo K. Teixeira. 2021. « Cyclin E/CDK2: DNA Replication, Replication Stress and Genomic Instability ». *Frontiers in Cell and Developmental Biology* 9: 774845. <https://doi.org/10.3389/fcell.2021.774845>.

Fan, Li, et Kevin T. DuPrez. 2015. « XPB: An Unconventional SF2 DNA Helicase ». *Progress in Biophysics and Molecular Biology* 117 (2-3): 174-81. <https://doi.org/10.1016/j.pbiomolbio.2014.12.005>.

Fan, Li, Jill O. Fuss, Quen J. Cheng, et al. 2008. « XPD Helicase Structures and Activities: Insights into the Cancer and Aging Phenotypes from XPD Mutations ». *Cell* 133 (5): 789-800. <https://doi.org/10.1016/j.cell.2008.04.030>.

Faridounnia, Maryam, Gert E. Folkers, et Rolf Boelens. 2018. « Function and Interactions of ERCC1-XPF in DNA Damage Response ». *Molecules (Basel, Switzerland)* 23 (12): 3205. <https://doi.org/10.3390/molecules23123205>.

Ferreira, Luísa T., et Helder Maiato. 2021. « Prometaphase ». *Seminars in Cell & Developmental Biology* 117 (septembre): 52-61. <https://doi.org/10.1016/j.semcd.2021.06.004>.

Fu, Iwen, Hong Mu, Nicholas E Geacintov, et Suse Broyde. 2022. « Mechanism of Lesion Verification by the Human XPD Helicase in Nucleotide Excision Repair ». *Nucleic Acids Research* 50 (12): 6837-53. <https://doi.org/10.1093/nar/gkac496>.

Fujimoto, Mitsuo, Suzanne N. Leech, Therina Theron, et al. 2005. « Two New XPD Patients Compound Heterozygous for the Same Mutation Demonstrate Diverse Clinical Features ». *Journal of Investigative Dermatology* 125 (1): 86-92. <https://doi.org/10.1111/j.0022-202X.2005.23745.x>.

Garcia-Luis, Jonay, Hélène Bordelet, Agnès Thierry, Romain Koszul, et Luis Aragon. 2022. « Depletion or Cleavage of Cohesin during Anaphase Differentially Affects Chromatin Structure and Segregation ». *eLife* 11 (octobre): e80147. <https://doi.org/10.7554/eLife.80147>.

Garon, Laurence, Victor Kokta, et Jérôme Coulombe. 2023. « Trichothiodystrophy ». *JAMA Dermatology* 159 (8): 877. <https://doi.org/10.1001/jamadermatol.2023.0913>.

- Gavet, Olivier, et Jonathon Pines. 2010. « Progressive Activation of CyclinB1-Cdk1 Coordinates Entry to Mitosis ». *Developmental Cell* 18 (4): 533-43. <https://doi.org/10.1016/j.devcel.2010.02.013>.
- Geacintov, Nicholas E., et Suse Broyde. 2017. « Repair-Resistant DNA Lesions ». *Chemical Research in Toxicology* 30 (8): 1517-48. <https://doi.org/10.1021/acs.chemrestox.7b00128>.
- Gervais, Virginie, Isabelle Muller, Pierre-Olivier Mari, et al. 2018. « Small Molecule-Based Targeting of TTD-A Dimerization to Control TFIID Transcriptional Activity Represents a Potential Strategy for Anticancer Therapy ». *Journal of Biological Chemistry* 293 (39): 14974-88. <https://doi.org/10.1074/jbc.RA118.003444>.
- Gibcus, Johan H., Kumiko Samejima, Anton Goloborodko, et al. 2018. « A Pathway for Mitotic Chromosome Formation ». *Science (New York, N.Y.)* 359 (6376): eaao6135. <https://doi.org/10.1126/science.aao6135>.
- Giglia-Mari, Giuseppina, Catherine Miquel, Arjan F Theil, et al. 2006. « Dynamic Interaction of TTDA with TFIID Is Stabilized by Nucleotide Excision Repair in Living Cells ». *PLoS Biology* 4 (6): e156. <https://doi.org/10.1371/journal.pbio.0040156>.
- Girbig, Mathias, Agata D. Misiaszek, et Christoph W. Müller. 2022. « Structural Insights into Nuclear Transcription by Eukaryotic DNA-Dependent RNA Polymerases ». *Nature Reviews Molecular Cell Biology*, mai 3, 1-20. <https://doi.org/10.1038/s41580-022-00476-9>.
- Godon, Camille, Sophie Mourgues, Julie Nonnekens, et al. 2012. « Generation of DNA Single-Strand Displacement by Compromised Nucleotide Excision Repair: UV-Induced Strand Displacement in TFIID^{XP/CS} Cells ». *The EMBO Journal* 31 (17): 3550-63. <https://doi.org/10.1038/emboj.2012.193>.
- Gomes, Edward, et James Shorter. 2019. « The Molecular Language of Membraneless Organelles ». *The Journal of Biological Chemistry* 294 (18): 7115-27. <https://doi.org/10.1074/jbc.TM118.001192>.
- Goodfellow, Sarah J., et Joost C. B. M. Zomerdijs. 2013. « Basic Mechanisms in RNA Polymerase I Transcription of the Ribosomal RNA Genes ». *Sub-Cellular Biochemistry* 61: 211-36. https://doi.org/10.1007/978-94-007-4525-4_10.
- Goodson, Holly V., et Erin M. Jonasson. 2018. « Microtubules and Microtubule-Associated Proteins ». *Cold Spring Harbor Perspectives in Biology* 10 (6): a022608. <https://doi.org/10.1101/cshperspect.a022608>.

Greber, Basil J., Thi Hoang Duong Nguyen, Jie Fang, Pavel V. Afonine, Paul D. Adams, et Eva Nogales. 2017. « The Cryo-Electron Microscopy Structure of Human Transcription Factor IIH ». *Nature* 549 (7672): 414-17. <https://doi.org/10.1038/nature23903>.

Greber, Basil J., Juan M. Perez-Bertoldi, Kif Lim, Anthony T. Iavarone, Daniel B. Toso, et Eva Nogales. 2020. « The Cryoelectron Microscopy Structure of the Human CDK-Activating Kinase ». *Proceedings of the National Academy of Sciences* 117 (37): 22849-57. <https://doi.org/10.1073/pnas.2009627117>.

Greber, Basil J, Daniel B Toso, Jie Fang, et Eva Nogales. 2019. « The Complete Structure of the Human TFIID Core Complex ». *eLife* 8 (mars): e44771. <https://doi.org/10.7554/eLife.44771>.

Gregersen, Lea H., et Jesper Q. Svejstrup. 2018. « The Cellular Response to Transcription-Blocking DNA Damage ». *Trends in Biochemical Sciences* 43 (5): 327-41. <https://doi.org/10.1016/j.tibs.2018.02.010>.

Gruber, R., A. Zschocke, H. Zellner, et M. Schmuth. 2021. « Successful Treatment of Trichothiodystrophy with Dupilumab ». *Clinical and Experimental Dermatology* 46 (7): 1381-83. <https://doi.org/10.1111/ced.14642>.

Guo, Jia, Guilan Zhou, Wenfeng Zhang, Yaling Song, et Zhuan Bian. 2013. « A Novel POLH Mutation Causes XP-V Disease and XP-V Tumor Proneness May Involve Imbalance of Numerous DNA Polymerases ». *Oncology Letters* 6 (6): 1583-90. <https://doi.org/10.3892/ol.2013.1604>.

Haberle, Vanja, et Alexander Stark. 2018. « Eukaryotic Core Promoters and the Functional Basis of Transcription Initiation ». *Nature Reviews Molecular Cell Biology* 19 (10): 621-37. <https://doi.org/10.1038/s41580-018-0028-8>.

Hamdan, Samir M., et Alfredo De Biasio. 2023. « Functional Hierarchy of PCNA-Interacting Motifs in DNA Processing Enzymes ». *BioEssays: News and Reviews in Molecular, Cellular and Developmental Biology* 45 (6): e2300020. <https://doi.org/10.1002/bies.202300020>.

Han, Zhong, George A. Moore, Richard Mitter, et al. 2023. « DNA-Directed Termination of RNA Polymerase II Transcription ». *Molecular Cell* 83 (18): 3253-3267.e7. <https://doi.org/10.1016/j.molcel.2023.08.007>.

Hashimoto, Yoshitami, et Hirofumi Tanaka. 2021. « Ongoing Replication Forks Delay the Nuclear Envelope Breakdown upon Mitotic Entry ». *The Journal of Biological Chemistry* 296: 100033. <https://doi.org/10.1074/jbc.RA120.015142>.

- Hirai, Yuko, Yoshiaki Kodama, Shin-Ichi Moriwaki, et al. 2006. « Heterozygous Individuals Bearing a Founder Mutation in the XPA DNA Repair Gene Comprise Nearly 1% of the Japanese Population ». *Mutation Research/Fundamental and Molecular Mechanisms of Mutagenesis* 601 (1-2): 171-78. <https://doi.org/10.1016/j.mrfmmm.2006.06.010>.
- Hoogstraten, Deborah, Alex L Nigg, Helen Heath, et al. 2002. « Rapid Switching of TFIIH between RNA Polymerase I and II Transcription and DNA Repair In Vivo ». *Molecular Cell* 10 (5): 1163-74. [https://doi.org/10.1016/S1097-2765\(02\)00709-8](https://doi.org/10.1016/S1097-2765(02)00709-8).
- Horibata, Katsuyoshi, Sayaka Kono, Chie Ishigami, et al. 2015. « Constructive Rescue of TFIIH Instability by an Alternative Isoform of XPD Derived from a Mutated XPD Allele in Mild but Not Severe XP-D/CS ». *Journal of Human Genetics* 60 (5): 259-65. <https://doi.org/10.1038/jhg.2015.18>.
- Hossain, Mozammel, Ashraful Hasan, Mohammad Mahfuz Ali Khan Shawan, Subrata Banik, et Iffat Jahan. 2021. « Current Therapeutic Strategies of Xeroderma Pigmentosum ». *Indian Journal of Dermatology* 66 (6): 660-67. https://doi.org/10.4103/ijd.ijd_329_21.
- House, Isabelle, Mari Valore-Caplan, Elijah Maris, et Gerald S. Falchook. 2025. « Cyclin Dependent Kinase 2 (CDK2) Inhibitors in Oncology Clinical Trials: A Review ». *Journal of Immunotherapy and Precision Oncology* 8 (1): 47-54. <https://doi.org/10.36401/JIPO-24-22>.
- Houten, Bennett Van, Jochen Kuper, et Caroline Kisker. 2016. « Role of XPD in Cellular Functions: To TFIIH and Beyond ». *DNA Repair* 44 (août): 136-42. <https://doi.org/10.1016/j.dnarep.2016.05.019>.
- Hu, Xiangdong, Xuejiao Jin, Xiuling Cao, et Beidong Liu. 2022. « The Anaphase-Promoting Complex/Cyclosome Is a Cellular Ageing Regulator ». *International Journal of Molecular Sciences* 23 (23): 15327. <https://doi.org/10.3390/ijms232315327>.
- Huang, Di, Hanna M. Petrykowska, Brendan F. Miller, Laura Elnitski, et Ivan Ovcharenko. 2019. « Identification of Human Silencers by Correlating Cross-Tissue Epigenetic Profiles and Gene Expression ». *Genome Research* 29 (4): 657-67. <https://doi.org/10.1101/gr.247007.118>.
- Hwang, Ji-Hyun, Linh Thuong Vuong, et Kwang-Wook Choi. 2020. « Crumbs, Galla and Xpd Are Required for Kinesin-5 Regulation in Mitosis and Organ Growth in *Drosophila* ». *Journal of Cell Science* 133 (12): jcs246801. <https://doi.org/10.1242/jcs.246801>.

- Iben, Sebastian, Herbert Tschochner, Mirko Bier, et al. 2002. « TFIIF Plays an Essential Role in RNA Polymerase I Transcription ». *Cell* 109 (3): 297-306. [https://doi.org/10.1016/S0092-8674\(02\)00729-8](https://doi.org/10.1016/S0092-8674(02)00729-8).
- Ito, Shinsuke, Li Jing Tan, Daisuke Andoh, et al. 2010. « MMXD, a TFIIF-Independent XPD-MMS19 Protein Complex Involved in Chromosome Segregation ». *Molecular Cell* 39 (4): 632-40. <https://doi.org/10.1016/j.molcel.2010.07.029>.
- Jawhari, Anass, Jean-Philippe Lainé, Sandy Dubaele, et al. 2002. « P52 Mediates XPB Function within the Transcription/Repair Factor TFIIF ». *The Journal of Biological Chemistry* 277 (35): 31761-67. <https://doi.org/10.1074/jbc.M203792200>.
- Jiao, Lijuan, Yuzhe Liu, Xi-Yong Yu, et al. 2023. « Ribosome Biogenesis in Disease: New Players and Therapeutic Targets ». *Signal Transduction and Targeted Therapy* 8 (1): 15. <https://doi.org/10.1038/s41392-022-01285-4>.
- Jones, Matthew C., Janet A. Askari, Jonathan D. Humphries, et Martin J. Humphries. 2018. « Cell Adhesion Is Regulated by CDK1 during the Cell Cycle ». *The Journal of Cell Biology* 217 (9): 3203-18. <https://doi.org/10.1083/jcb.201802088>.
- Jonkers, Iris, et John T. Lis. 2015. « Getting up to Speed with Transcription Elongation by RNA Polymerase II ». *Nature Reviews Molecular Cell Biology* 16 (3): 167-77. <https://doi.org/10.1038/nrm3953>.
- Ju, Jia-Qian, Xiao-Han Li, Meng-Hao Pan, et al. 2021. « Mps1 Controls Spindle Assembly, SAC, and DNA Repair in the First Cleavage of Mouse Early Embryos ». *Journal of Cellular Biochemistry* 122 (2): 290-300. <https://doi.org/10.1002/jcb.29858>.
- Kaldis, P. 1999. « The Cdk-Activating Kinase (CAK): From Yeast to Mammals ». *Cellular and Molecular Life Sciences: CMLS* 55 (2): 284-96. <https://doi.org/10.1007/s000180050290>.
- Kapanidou, Maria, Natalie L. Curtis, et Victor M. Bolanos-Garcia. 2017. « Cdc20: At the Crossroads between Chromosome Segregation and Mitotic Exit ». *Trends in Biochemical Sciences* 42 (3): 193-205. <https://doi.org/10.1016/j.tibs.2016.12.001>.
- Kappenberger, Jeannette, Wolfgang Koelmel, Elisabeth Schoenwetter, et al. 2020. « How to Limit the Speed of a Motor: The Intricate Regulation of the XPB ATPase and Translocase in TFIIF ». *Nucleic Acids Research* 48 (21): 12282-96. <https://doi.org/10.1093/nar/gkaa911>.

Karikkineth, Ajoy C., Morten Scheibye-Knudsen, Elayne Fivenson, Deborah L. Croteau, et Vilhelm A. Bohr. 2017. « Cockayne Syndrome: Clinical Features, Model Systems and Pathways ». *Ageing Research Reviews* 33 (janvier): 3-17. <https://doi.org/10.1016/j.arr.2016.08.002>.

Karnuta, Jaret M., et Peter C. Scacheri. 2018. « Enhancers: Bridging the Gap between Gene Control and Human Disease ». *Human Molecular Genetics* 27 (R2): R219-27. <https://doi.org/10.1093/hmg/ddy167>.

Kim, Jin Seok, Charlotte Saint-André, Hye Seong Lim, Cheol-Sang Hwang, Jean Marc Egly, et Yunje Cho. 2015. « Crystal Structure of the Rad3/XPD Regulatory Domain of Ssl1/P44 ». *The Journal of Biological Chemistry* 290 (13): 8321-30. <https://doi.org/10.1074/jbc.M115.636514>.

Kim, Jinseok, Chia-Lung Li, Xuemin Chen, et al. 2023. « Lesion Recognition by XPC, TFIIH and XPA in DNA Excision Repair ». *Nature* 617 (7959): 170-75. <https://doi.org/10.1038/s41586-023-05959-z>.

Kim, Seon Hee, Geun Hoe Kim, Michael G Kemp, et Jun-Hyuk Choi. 2022. « TREX1 Degrades the 3' End of the Small DNA Oligonucleotide Products of Nucleotide Excision Repair in Human Cells ». *Nucleic Acids Research* 50 (7): 3974-84. <https://doi.org/10.1093/nar/gkac214>.

Kim, Sungsoo, Alessandra Leong, Minah Kim, et Hee Won Yang. 2022. « CDK4/6 Initiates Rb Inactivation and CDK2 Activity Coordinates Cell-Cycle Commitment and G1/S Transition ». *Scientific Reports* 12 (1): 16810. <https://doi.org/10.1038/s41598-022-20769-5>.

Kim, Taekyung, et Anton Gartner. 2021. « Bub1 Kinase in the Regulation of Mitosis ». *Animal Cells and Systems* 25 (1): 1-10. <https://doi.org/10.1080/19768354.2021.1884599>.

Kim, Young Kyeung, Cyril F. Bourgeois, Catherine Isel, Mark J. Churcher, et Jonathan Karn. 2002. « Phosphorylation of the RNA Polymerase II Carboxyl-Terminal Domain by CDK9 Is Directly Responsible for Human Immunodeficiency Virus Type 1 Tat-Activated Transcriptional Elongation ». *Molecular and Cellular Biology* 22 (13): 4622-37. <https://doi.org/10.1128/MCB.22.13.4622-4637.2002>.

Knutson, Bruce A., Rachel McNamar, et Lawrence I. Rothblum. 2020. « Dynamics of the RNA Polymerase I TFIIF/TFIIE-like Subcomplex: A Mini-Review ». *Biochemical Society Transactions* 48 (5): 1917-27. <https://doi.org/10.1042/BST20190848>.

Koch, Sandra C., Nina Simon, Charlotte Ebert, et Thomas Carell. 2016. « Molecular Mechanisms of Xeroderma Pigmentosum (XP) Proteins ». *Quarterly Reviews of Biophysics* 49: e5. <https://doi.org/10.1017/S0033583515000268>.

Kokic, Goran, George Yakoub, Diana van den Heuvel, et al. 2024. « Structural Basis for RNA Polymerase II Ubiquitylation and Inactivation in Transcription-Coupled Repair ». *Nature Structural & Molecular Biology* 31 (3): 536-47. <https://doi.org/10.1038/s41594-023-01207-0>.

Kornberg, Roger D. 2007. « The Molecular Basis of Eukaryotic Transcription ». *Proceedings of the National Academy of Sciences of the United States of America* 104 (32): 12955-61. <https://doi.org/10.1073/pnas.0704138104>.

Kralund, Henrik H., Lilian Ousager, Nicolaas G. Jaspers, et al. 2013. « Xeroderma Pigmentosum-Trichothiodystrophy Overlap Patient with Novel XPD/ERCC2 Mutation ». *Rare Diseases* 1 (1): e24932. <https://doi.org/10.4161/rdis.24932>.

Kreibich, Elisa, et Arnaud R. Krebs. 2022. « Cofactors: A New Layer of Specificity to Enhancer Regulation ». *Trends in Biochemical Sciences* 47 (12): 993-95. <https://doi.org/10.1016/j.tibs.2022.07.008>.

Kumar, Namrata, Arjan F. Theil, Vera Roginskaya, et al. 2022. « Global and Transcription-Coupled Repair of 8-oxoG Is Initiated by Nucleotide Excision Repair Proteins ». *Nature Communications* 13 (1): 974. <https://doi.org/10.1038/s41467-022-28642-9>.

Kuper, Jochen, Cathy Braun, Agnes Elias, et al. 2014. « In TFIIH, XPD Helicase Is Exclusively Devoted to DNA Repair ». *PLoS Biology* 12 (9): e1001954. <https://doi.org/10.1371/journal.pbio.1001954>.

Kuper, Jochen, Tamsanqa Hove, Sarah Maidl, Florian Sauer, et al. 2024. *Trapped in Translocation – Stalling of XPD on a Crosslinked DNA Substrate*. Preprint. Biochemistry. <https://doi.org/10.1101/2024.02.20.581127>.

Kuper, Jochen, Tamsanqa Hove, Sarah Maidl, Hermann Neitz, et al. 2024. « XPD Stalled on Cross-Linked DNA Provides Insight into Damage Verification ». *Nature Structural & Molecular Biology* 31 (10): 1580-88. <https://doi.org/10.1038/s41594-024-01323-5>.

Kuper, Jochen, et Caroline Kisker. 2021. « Three Targets in One Complex: A Molecular Perspective of TFIIH in Cancer Therapy ». *DNA Repair* 105 (septembre): 103143. <https://doi.org/10.1016/j.dnarep.2021.103143>.

Kusakabe, Masayuki, Yuki Onishi, Haruto Tada, et al. 2019. « Mechanism and Regulation of DNA Damage Recognition in Nucleotide Excision Repair ». *Genes and Environment* 41 (1): 2. <https://doi.org/10.1186/s41021-019-0119-6>.

- Lambert, W. Clark, Claude E. Gagna, et Muriel W. Lambert. 2010. « Trichothiodystrophy: Photosensitive, TTD-P, TTD, Tay Syndrome ». In *Diseases of DNA Repair*, Nathan Back, Irun R. Cohen, Abel Lajtha, John D. Lambris, et Rodolfo Paoletti, vol. 685, édité par Shamim I. Ahmad. Advances in Experimental Medicine and Biology. Springer New York. https://doi.org/10.1007/978-1-4419-6448-9_10.
- Lansiaux, Amélie. 2011. « [Antimetabolites] ». *Bulletin Du Cancer* 98 (11): 1263-74. <https://doi.org/10.1684/bdc.2011.1476>.
- Laugel, Vincent. s. d. *Cockayne Syndrome*.
- Lee, Tong Ihn, et Richard A. Young. 2000. « TRANSCRIPTION OF EUKARYOTIC PROTEIN-CODING GENES ». *Annual Review of Genetics* 34 (1): 77-137. <https://doi.org/10.1146/annurev.genet.34.1.77>.
- Lehmann, Alan R. 2001. « The Xeroderma Pigmentosum Group D (XPD) Gene: One Gene, Two Functions, Three Diseases ». *Genes & Development* 15 (1): 15-23. <https://doi.org/10.1101/gad.859501>.
- Lehmann, Alan R. 2008. « XPD Structure Reveals Its Secrets ». *DNA Repair* 7 (11): 1912-15. <https://doi.org/10.1016/j.dnarep.2008.07.008>.
- Lehmann, Alan R. 2011. « DNA Polymerases and Repair Synthesis in NER in Human Cells ». *DNA Repair* 10 (7): 730-33. <https://doi.org/10.1016/j.dnarep.2011.04.023>.
- Leung, Alexander Kc, Benjamin Barankin, Joseph M Lam, Kin Fon Leong, et Kam Lun Hon. 2022. « Xeroderma Pigmentosum: An Updated Review ». *Drugs in Context* 11 (avril): 1-17. <https://doi.org/10.7573/dic.2022-2-5>.
- Li, Jian, Xinli Ma, Xiaoyu Wang, et al. 2024. « Mutations Found in Cancer Patients Compromise DNA Binding of the Winged Helix Protein STK19 ». *Scientific Reports* 14 (1): 14098. <https://doi.org/10.1038/s41598-024-64840-9>.
- Li, Yan, Qianmin Wang, Yanhui Xu, et Ze Li. 2024. « Structures of Co-Transcriptional RNA Capping Enzymes on Paused Transcription Complex ». *Nature Communications* 15 (1): 4622. <https://doi.org/10.1038/s41467-024-48963-1>.
- Lim, Rongxuan, Mieran Sethi, et Ana M.S. Morley. 2017. « Ophthalmic Manifestations of Xeroderma Pigmentosum ». *Ophthalmology* 124 (11): 1652-61. <https://doi.org/10.1016/j.opthta.2017.04.031>.

Lima-Bessa, Keronninn Moreno De, Melissa Gava Armelini, Vanessa Chiganças, et al. 2008. « CPDs and 6-4PPs Play Different Roles in UV-Induced Cell Death in Normal and NER-Deficient Human Cells ». *DNA Repair* 7 (2): 303-12. <https://doi.org/10.1016/j.dnarep.2007.11.003>.

Limas, Juanita C., et Jeanette Gowen Cook. 2019. « Preparation for DNA Replication: The Key to a Successful S Phase ». *FEBS Letters* 593 (20): 2853-67. <https://doi.org/10.1002/1873-3468.13619>.

Linhartova, Katerina, Francesco Luca Falginella, Martin Matl, Marek Sebesta, Robert Vácha, et Richard Stefl. 2024. « Sequence and Structural Determinants of RNAPII CTD Phase-Separation and Phosphorylation by CDK7 ». *Nature Communications* 15 (1): 9163. <https://doi.org/10.1038/s41467-024-53305-2>.

Liu, Huanting, Jana Rudolf, Kenneth A. Johnson, et al. 2008. « Structure of the DNA Repair Helicase XPD ». *Cell* 133 (5): 801-12. <https://doi.org/10.1016/j.cell.2008.04.029>.

Liu, Jingwen, et Falong Lu. 2024. « Beyond Simple Tails: Poly(A) Tail-Mediated RNA Epigenetic Regulation ». *Trends in Biochemical Sciences* 49 (10): 846-58. <https://doi.org/10.1016/j.tibs.2024.06.013>.

Liu, Xinglei, Lu Rao, Weihong Qiu, Florian Berger, et Arne Gennerich. 2024. « Kinesin-14 HSET and KlpA Are Non-Processive Microtubule Motors with Load-Dependent Power Strokes ». *Nature Communications* 15 (1). <https://doi.org/10.1038/s41467-024-50990-x>.

Llerena Schiffmacher, Diana A., Katarzyna W. Kliza, Arjan F. Theil, et al. 2023. « Live Cell Transcription-Coupled Nucleotide Excision Repair Dynamics Revisited ». *DNA Repair* 130 (octobre): 103566. <https://doi.org/10.1016/j.dnarep.2023.103566>.

Llerena Schiffmacher, Diana A., Shun-Hsiao Lee, Katarzyna W. Kliza, et al. 2024. « The Small CRL4CSA Ubiquitin Ligase Component DDA1 Regulates Transcription-Coupled Repair Dynamics ». *Nature Communications* 15 (1): 6374. <https://doi.org/10.1038/s41467-024-50584-7>.

Lolli, Graziano, et Louise N. Johnson. 2005. « CAK—Cyclin-Dependent Activating Kinase: A Key Kinase in Cell Cycle Control and a Target for Drugs? » *Cell Cycle* 4 (4): 565-70. <https://doi.org/10.4161/cc.4.4.1607>.

Long, Alexandra F, Jonathan Kuhn, et Sophie Dumont. 2019. « The Mammalian Kinetochore—Microtubule Interface: Robust Mechanics and Computation with Many Microtubules ». *Current Opinion in Cell Biology* 60 (octobre): 60-67. <https://doi.org/10.1016/j.ceb.2019.04.004>.

Long, Hannah K., Marco Osterwalder, Ian C. Welsh, et al. 2020. « Loss of Extreme Long-Range Enhancers in Human Neural Crest Drives a Craniofacial Disorder ». *Cell Stem Cell* 27 (5): 765-783.e14. <https://doi.org/10.1016/j.stem.2020.09.001>.

Lu, H., L. Zawel, L. Fisher, J. M. Egly, et D. Reinberg. 1992. « Human General Transcription Factor IIH Phosphorylates the C-Terminal Domain of RNA Polymerase II ». *Nature* 358 (6388): 641-45. <https://doi.org/10.1038/358641a0>.

Mahpour, Amin, Benjamin S. Scruggs, Dominic Smiraglia, Toru Ouchi, et Irwin H. Gelman. 2018. « A Methyl-Sensitive Element Induces Bidirectional Transcription in TATA-Less CpG Island-Associated Promoters ». *PloS One* 13 (10): e0205608. <https://doi.org/10.1371/journal.pone.0205608>.

Maiato, Helder. 2021. « Mitosis under the Microscope ». *Seminars in Cell & Developmental Biology* 117 (septembre): 1-5. <https://doi.org/10.1016/j.semcdb.2021.06.014>.

Mailand, Niels, et John F.X. Diffley. 2005. « CDKs Promote DNA Replication Origin Licensing in Human Cells by Protecting Cdc6 from APC/C-Dependent Proteolysis ». *Cell* 122 (6): 915-26. <https://doi.org/10.1016/j.cell.2005.08.013>.

Malfatti, Matilde Clarissa, Giulia Antoniali, Marta Codrich, et Gianluca Tell. 2021. « Coping with RNA Damage with a Focus on APE1, a BER Enzyme at the Crossroad between DNA Damage Repair and RNA Processing/Decay ». *DNA Repair* 104 (août): 103133. <https://doi.org/10.1016/j.dnarep.2021.103133>.

Mao, Chunfeng, et Maria Mills. 2024. « Characterization of Human XPD Helicase Activity with Single-Molecule Magnetic Tweezers ». *Biophysical Journal* 123 (2): 260-71. <https://doi.org/10.1016/j.bpj.2023.12.014>.

Marescal, Océane, et Iain M. Cheeseman. 2020. « Cellular Mechanisms and Regulation of Quiescence ». *Developmental Cell* 55 (3): 259-71. <https://doi.org/10.1016/j.devcel.2020.09.029>.

Matthews, Helen K., Cosetta Bertoli, et Robertus A. M. de Bruin. 2022. « Cell Cycle Control in Cancer ». *Nature Reviews Molecular Cell Biology* 23 (1): 74-88. <https://doi.org/10.1038/s41580-021-00404-3>.

Mayer, Christine, et Ingrid Grummt. 2005. « Cellular Stress and Nucleolar Function ». *Cell Cycle (Georgetown, Tex.)* 4 (8): 1036-38. <https://doi.org/10.4161/cc.4.8.1925>.

- McNamar, Rachel, Emma Freeman, Kairo N. Baylor, et al. 2023. « PAF49: An RNA Polymerase I Subunit Essential for rDNA Transcription and Stabilization of PAF53 ». *The Journal of Biological Chemistry* 299 (8): 104951. <https://doi.org/10.1016/j.jbc.2023.104951>.
- Mehta, Virja, Delphine Chamousset, Jennifer Law, et al. 2022. « Subcellular Distribution of PP1 Isoforms in Holoenzyme Complexes ». Prépublication, septembre 10. <https://doi.org/10.1101/2022.09.09.507380>.
- Meng, Yang, Lei Qiu, Xinyi Zeng, et al. 2022. « Targeting CRL4 Suppresses Chemoresistant Ovarian Cancer Growth by Inducing Mitophagy ». *Signal Transduction and Targeted Therapy* 7 (1): 388. <https://doi.org/10.1038/s41392-022-01253-y>.
- Merkl, Philipp E., Michael Pilsl, Tobias Fremter, et al. 2020. « RNA Polymerase I (Pol I) Passage through Nucleosomes Depends on Pol I Subunits Binding Its Lobe Structure ». *Journal of Biological Chemistry* 295 (15): 4782-95. <https://doi.org/10.1074/jbc.RA119.011827>.
- Mishal, Rabia, et Juan Pedro Luna-Arias. 2022. « Role of the TATA-Box Binding Protein (TBP) and Associated Family Members in Transcription Regulation ». *Gene* 833 (juillet): 146581. <https://doi.org/10.1016/j.gene.2022.146581>.
- Misteli, Tom. 2020. « The Self-Organizing Genome: Principles of Genome Architecture and Function ». *Cell* 183 (1): 28-45. <https://doi.org/10.1016/j.cell.2020.09.014>.
- Morrison, Olivia, et Jitendra Thakur. 2021. « Molecular Complexes at Euchromatin, Heterochromatin and Centromeric Chromatin ». *International Journal of Molecular Sciences* 22 (13): 6922. <https://doi.org/10.3390/ijms22136922>.
- Moss, Tom, Mark S. LeDoux, et Colyn Crane-Robinson. 2023. « HMG-boxes, ribosomopathies and neurodegenerative disease ». *Frontiers in Genetics* 14 (août): 1225832. <https://doi.org/10.3389/fgene.2023.1225832>.
- Muniz, Lisa, Estelle Nicolas, et Didier Trouche. 2021. « RNA Polymerase II Speed: A Key Player in Controlling and Adapting Transcriptome Composition ». *The EMBO Journal* 40 (15): e105740. <https://doi.org/10.15252/embj.2020105740>.
- Nakazawa, Yuka, Yuichiro Hara, Yasuyoshi Oka, et al. 2020. « Ubiquitination of DNA Damage-Stalled RNAPII Promotes Transcription-Coupled Repair ». *Cell* 180 (6): 1228-1244.e24. <https://doi.org/10.1016/j.cell.2020.02.010>.

- Nance, Connor, Chunfeng Mao, et K. Maria Mills. 2025. « BPS2025 - Single-Molecule Measurements of P44-Enhanced XPD Helicase Activity ». *Biophysical Journal* 124 (3): 253a. <https://doi.org/10.1016/j.bpj.2024.11.1377>.
- Nance, M. A., et S. A. Berry. 1992. « Cockayne Syndrome: Review of 140 Cases ». *American Journal of Medical Genetics* 42 (1): 68-84. <https://doi.org/10.1002/ajmg.1320420115>.
- Natale, Valerie, et Hayley Raquer. 2017. « Xeroderma Pigmentosum-Cockayne Syndrome Complex ». *Orphanet Journal of Rare Diseases* 12 (1): 65. <https://doi.org/10.1186/s13023-017-0616-2>.
- Ng, Lau Yan, Hoi Tang Ma, et Randy Y. C. Poon. 2023. « Cyclin A-CDK1 Suppresses the Expression of the CDK1 Activator CDC25A to Safeguard Timely Mitotic Entry ». *The Journal of Biological Chemistry* 299 (3): 102957. <https://doi.org/10.1016/j.jbc.2023.102957>.
- Nieto Moreno, Nicolás, Anouk M. Olthof, et Jesper Q. Svejstrup. 2023. « Transcription-Coupled Nucleotide Excision Repair and the Transcriptional Response to UV-Induced DNA Damage ». *Annual Review of Biochemistry* 92 (1): 81-113. <https://doi.org/10.1146/annurev-biochem-052621-091205>.
- Nikolaev, Sergey, Andrey A. Yurchenko, et Alain Sarasin. 2022. « Increased Risk of Internal Tumors in DNA Repair-Deficient Xeroderma Pigmentosum Patients: Analysis of Four International Cohorts ». *Orphanet Journal of Rare Diseases* 17 (1): 104. <https://doi.org/10.1186/s13023-022-02203-1>.
- Nishigori, Chikako, Eiji Nakano, Taro Masaki, et al. 2019. « Characteristics of Xeroderma Pigmentosum in Japan: Lessons From Two Clinical Surveys and Measures for Patient Care ». *Photochemistry and Photobiology* 95 (1): 140-53. <https://doi.org/10.1111/php.13052>.
- O'Brien, Michael J., et Athar Ansari. 2022. « Beyond the Canonical Role of TFIIB in Eukaryotic Transcription ». *Current Genetics* 68 (1): 61-67. <https://doi.org/10.1007/s00294-021-01223-x>.
- Ogi, Tomoo, Siripan Limsirichaikul, René M. Overmeer, et al. 2010. « Three DNA Polymerases, Recruited by Different Mechanisms, Carry Out NER Repair Synthesis in Human Cells ». *Molecular Cell* 37 (5): 714-27. <https://doi.org/10.1016/j.molcel.2010.02.009>.
- Okuda, Masahiko, Toru Ekimoto, Jun-ichi Kurita, Mitsunori Ikeguchi, et Yoshifumi Nishimura. 2021. « Structural and Dynamical Insights into the PH Domain of P62 in Human TFIIF ». *Nucleic Acids Research* 49 (5): 2916-30. <https://doi.org/10.1093/nar/gkaa1045>.

- Okur, Mustafa N., Evandro F. Fang, Elayne M. Fivenson, Vinod Tiwari, Deborah L. Croteau, et Vilhelm A. Bohr. 2020. « Cockayne Syndrome Proteins CSA and CSB Maintain Mitochondrial Homeostasis through NAD⁺ Signaling ». *Aging Cell* 19 (12): e13268. <https://doi.org/10.1111/accel.13268>.
- Oriola, David, Daniel J. Needleman, et Jan Brugués. 2018. « The Physics of the Metaphase Spindle ». *Annual Review of Biophysics* 47 (mai): 655-73. <https://doi.org/10.1146/annurev-biophys-060414-034107>.
- Ota, Ryoko, Takumi Watanabe, Yuuki Wazawa, et al. 2023. « V-Src Delocalizes Aurora B by Suppressing Aurora B Kinase Activity during Monopolar Cytokinesis ». *Cellular Signalling* 109 (septembre): 110764. <https://doi.org/10.1016/j.cellsig.2023.110764>.
- Paccosi, Elena, Federico Costanzo, Michele Costantino, et al. 2020. « The Cockayne Syndrome Group A and B Proteins Are Part of a Ubiquitin–Proteasome Degradation Complex Regulating Cell Division ». *Proceedings of the National Academy of Sciences* 117 (48): 30498-508. <https://doi.org/10.1073/pnas.2006543117>.
- Pachis, Spyridon T., et Geert J. P. L. Kops. 2018. « Leader of the SAC: Molecular Mechanisms of Mps1/TTK Regulation in Mitosis ». *Open Biology* 8 (8): 180109. <https://doi.org/10.1098/rsob.180109>.
- Panchal, Nagesh Kishan, Aishwarya Bhale, Vinod Kumar Verma, et Syed Sultan Beevi. 2020. « Computational and Molecular Dynamics Simulation Approach To Analyze the Impact of XPD Gene Mutation on Protein Stability and Function ». Prépublication, juillet 18. <https://doi.org/10.1101/2020.07.18.209841>.
- Pang, Baoxu, et Michael P. Snyder. 2020. « Systematic Identification of Silencers in Human Cells ». *Nature Genetics* 52 (3): 254-63. <https://doi.org/10.1038/s41588-020-0578-5>.
- Park, HaJeung, Kaijiang Zhang, Yingjie Ren, et al. 2002. « Crystal Structure of a DNA Decamer Containing a Cis-Syn Thymine Dimer ». *Proceedings of the National Academy of Sciences of the United States of America* 99 (25): 15965-70. <https://doi.org/10.1073/pnas.242422699>.
- Pascucci, Barbara, Alessandra Fragale, Veronica Marabitti, et al. 2018. « CSA and CSB Play a Role in the Response to DNA Breaks ». *Oncotarget* 9 (14): 11581-91. <https://doi.org/10.18632/oncotarget.24342>.

- Passmore, Lori A., et Jeff Collier. 2022. « Roles of mRNA Poly(A) Tails in Regulation of Eukaryotic Gene Expression ». *Nature Reviews Molecular Cell Biology* 23 (2): 93-106. <https://doi.org/10.1038/s41580-021-00417-y>.
- Pawlonka, Jan, Beata Rak, et Urszula Ambroziak. 2021. « The Regulation of Cyclin D Promoters – Review ». *Cancer Treatment and Research Communications* 27: 100338. <https://doi.org/10.1016/j.ctarc.2021.100338>.
- Peissert, Stefan, Florian Sauer, Daniel B. Grabarczyk, et al. 2020. « In TFIIH the Arch Domain of XPD Is Mechanistically Essential for Transcription and DNA Repair ». *Nature Communications* 11 (1): 1667. <https://doi.org/10.1038/s41467-020-15241-9>.
- Pellarin, Ilenia, Alessandra Dall'Acqua, Andrea Favero, et al. 2025. « Cyclin-Dependent Protein Kinases and Cell Cycle Regulation in Biology and Disease ». *Signal Transduction and Targeted Therapy* 10 (1): 11. <https://doi.org/10.1038/s41392-024-02080-z>.
- Pennycook, Betheney R., et Alexis R. Barr. 2020. « Restriction Point Regulation at the Crossroads between Quiescence and Cell Proliferation ». *FEBS Letters* 594 (13): 2046-60. <https://doi.org/10.1002/1873-3468.13867>.
- Peterson, Craig L, et Marc-André Laniel. 2004. « Histones and Histone Modifications ». *Current Biology* 14 (14): R546-51. <https://doi.org/10.1016/j.cub.2004.07.007>.
- Petruseva, Irina, Natalia Naumenko, Jochen Kuper, et al. 2021. « The Interaction Efficiency of XPD-P44 With Bulky DNA Damages Depends on the Structure of the Damage ». *Frontiers in Cell and Developmental Biology* 9 (mars): 617160. <https://doi.org/10.3389/fcell.2021.617160>.
- Piovesan, Allison, Maria Chiara Pelleri, Francesca Antonaros, Pierluigi Strippoli, Maria Caracausi, et Lorenza Vitale. 2019. « On the Length, Weight and GC Content of the Human Genome ». *BMC Research Notes* 12 (1): 106. <https://doi.org/10.1186/s13104-019-4137-z>.
- Ponjavic, Jasmina, Boris Lenhard, Chikatoshi Kai, et al. 2006. « Transcriptional and Structural Impact of TATA-Initiation Site Spacing in Mammalian Core Promoters ». *Genome Biology* 7 (8): R78. <https://doi.org/10.1186/gb-2006-7-8-r78>.
- Raaijmakers, J. A., et R. H. Medema. 2014. « Function and Regulation of Dynein in Mitotic Chromosome Segregation ». *Chromosoma* 123 (5): 407-22. <https://doi.org/10.1007/s00412-014-0468-7>.

Radu, Laura, Elisabeth Schoenwetter, Cathy Braun, et al. 2017. « The Intricate Network between the P34 and P44 Subunits Is Central to the Activity of the Transcription/DNA Repair Factor TFIIH ». *Nucleic Acids Research* 45 (18): 10872-83. <https://doi.org/10.1093/nar/gkx743>.

Rastogi, Rajesh P., Richa, Ashok Kumar, Madhu B. Tyagi, et Rajeshwar P. Sinha. 2010. « Molecular Mechanisms of Ultraviolet Radiation-Induced DNA Damage and Repair ». *Journal of Nucleic Acids* 2010 (1): 592980. <https://doi.org/10.4061/2010/592980>.

Ravarani, Charles N. J., Guilhem Chalancon, Michal Breker, Natalia Sanchez De Groot, et M. Madan Babu. 2016. « Affinity and Competition for TBP Are Molecular Determinants of Gene Expression Noise ». *Nature Communications* 7 (1): 10417. <https://doi.org/10.1038/ncomms10417>.

Rayêe, Danielle, U. Thomas Meier, Carolina Eliscovich, et Aleš Cvekl. 2025. « Nucleolar Ribosomal RNA Synthesis Continues in Differentiating Lens Fiber Cells until Abrupt Nuclear Degradation Required for Ocular Lens Transparency ». *RNA Biology* 22 (1): 1-16. <https://doi.org/10.1080/15476286.2025.2483118>.

Rechkoblit, Olga, Alexander Kolbanovskiy, Hannah Landes, Nicholas E. Geacintov, et Aneel K. Aggarwal. 2017. « Mechanism of Error-Free Replication across Benzo[a]Pyrene Stereoisomers by Rev1 DNA Polymerase ». *Nature Communications* 8 (1): 965. <https://doi.org/10.1038/s41467-017-01013-5>.

Rengachari, Srinivasan, Sandra Schilbach, Shintaro Aibara, Christian Dienemann, et Patrick Cramer. 2021. « Structure of the Human Mediator–RNA Polymerase II Pre-Initiation Complex ». *Nature* 594 (7861): 129-33. <https://doi.org/10.1038/s41586-021-03555-7>.

Ribeiro-Silva, Cristina, Mariangela Sabatella, Angela Helfricht, et al. 2020. « Ubiquitin and TFIIH-Stimulated DDB2 Dissociation Drives DNA Damage Handover in Nucleotide Excision Repair ». *Nature Communications* 11 (1): 4868. <https://doi.org/10.1038/s41467-020-18705-0>.

Richard, Aurélie, Jérémy Berthelet, Delphine Judith, et al. 2024. « Methylation of ESCRT-III Components Regulates the Timing of Cytokinetic Abscission ». *Nature Communications* 15 (1): 4023. <https://doi.org/10.1038/s41467-024-47717-3>.

Rimel, Jenna K., et Dylan J. Taatjes. 2018. « The Essential and Multifunctional TFIIH Complex ». *Protein Science: A Publication of the Protein Society* 27 (6): 1018-37. <https://doi.org/10.1002/pro.3424>.

Roeder, Robert G. 2019. « 50+ Years of Eukaryotic Transcription: An Expanding Universe of Factors and Mechanisms ». *Nature Structural & Molecular Biology* 26 (9): 783-91. <https://doi.org/10.1038/s41594-019-0287-x>.

Rosa, Mariarosaria De, Ryan P. Barnes, Prasanth R. Nyalapatla, Peter Wipf, et Patricia L. Opresko. 2023. « OGG1 and MUTYH Repair Activities Promote Telomeric 8-Oxoguanine Induced Cellular Senescence ». Prépublication, avril 10. <https://doi.org/10.1101/2023.04.10.536247>.

Rubin, Seth M., Julien Sage, et Jan M. Skotheim. 2020. « Integrating Old and New Paradigms of G1/S Control ». *Molecular Cell* 80 (2): 183-92. <https://doi.org/10.1016/j.molcel.2020.08.020>.

Rudolf, Jana, Vasso Makrantonis, W. John Ingledew, Michael J.R. Stark, et Malcolm F. White. 2006. « The DNA Repair Helicases XPD and FancJ Have Essential Iron-Sulfur Domains ». *Molecular Cell* 23 (6): 801-8. <https://doi.org/10.1016/j.molcel.2006.07.019>.

Russell, P. 1998. « Checkpoints on the Road to Mitosis ». *Trends in Biochemical Sciences* 23 (10): 399-402. [https://doi.org/10.1016/s0968-0004\(98\)01291-2](https://doi.org/10.1016/s0968-0004(98)01291-2).

Ryu, Jihye, et Chaeyoung Lee. 2024. « RNA Polymerase Subunits and Ribosomal Proteins: An Overview and Their Genetic Impact on Complex Human Traits ». *Frontiers in Bioscience-Landmark* 29 (5): 185. <https://doi.org/10.31083/j.fbl2905185>.

Sainsbury, Sarah, Carrie Bernecky, et Patrick Cramer. 2015. « Structural Basis of Transcription Initiation by RNA Polymerase II ». *Nature Reviews Molecular Cell Biology* 16 (3): 129-43. <https://doi.org/10.1038/nrm3952>.

Sapra, K. Tanuj, Zhao Qin, Anna Dubrovsky-Gaupp, et al. 2020. « Nonlinear Mechanics of Lamin Filaments and the Meshwork Topology Build an Emergent Nuclear Lamina ». *Nature Communications* 11 (1): 6205. <https://doi.org/10.1038/s41467-020-20049-8>.

Savina, Ekaterina A., Tatiana G. Shumilina, Vladimir G. Tumanyan, Anastasia A. Anashkina, et Irina A. Il'icheva. 2023. « Core Promoter Regions of Antisense and Long Intergenic Non-Coding RNAs ». *International Journal of Molecular Sciences* 24 (9): 8199. <https://doi.org/10.3390/ijms24098199>.

Schier, Allison C, et Dylan J Taatjes. s. d. *Structure and Mechanism of the RNA Polymerase II Transcription Machinery*.

Schnyder, Simon K., John J. Molina, et Ryoichi Yamamoto. 2020. « Control of Cell Colony Growth by Contact Inhibition ». *Scientific Reports* 10 (1): 6713. <https://doi.org/10.1038/s41598-020-62913-z>.

Schrecker, Marina, Juan C. Castaneda, Sujan Devbhandari, Charanya Kumar, Dirk Remus, et Richard K. Hite. 2022. « Multistep Loading of a DNA Sliding Clamp onto DNA by Replication Factor C ». *eLife* 11 (août): e78253. <https://doi.org/10.7554/eLife.78253>.

Schwayer, Cornelia, Mateusz Sikora, Jana Slovákova, Roland Kardos, et Carl-Philipp Heisenberg. 2016. « Actin Rings of Power ». *Developmental Cell* 37 (6): 493-506. <https://doi.org/10.1016/j.devcel.2016.05.024>.

Segert, Julian A., Stephen S. Gisselbrecht, et Martha L. Bulyk. 2021. « Transcriptional Silencers: Driving Gene Expression with the Brakes On ». *Trends in Genetics: TIG* 37 (6): 514-27. <https://doi.org/10.1016/j.tig.2021.02.002>.

Shafirovich, Vladimir, et Nicholas E. Geacintov. 2021. « Excision of Oxidatively Generated Guanine Lesions by Competitive DNA Repair Pathways ». *International Journal of Molecular Sciences* 22 (5): 2698. <https://doi.org/10.3390/ijms22052698>.

Shao, Wanqing, et Julia Zeitlinger. 2017. « Paused RNA Polymerase II Inhibits New Transcriptional Initiation ». *Nature Genetics* 49 (7): 1045-51. <https://doi.org/10.1038/ng.3867>.

She, Zhen-Yu, Ning Zhong, Kai-Wei Yu, et al. 2020. « Kinesin-5 Eg5 Is Essential for Spindle Assembly and Chromosome Alignment of Mouse Spermatocytes ». *Cell Division* 15 (1): 6. <https://doi.org/10.1186/s13008-020-00063-4>.

Silva, Patrícia M. A., et Hassan Bousbaa. 2022. « BUB3, beyond the Simple Role of Partner ». *Pharmaceutics* 14 (5): 1084. <https://doi.org/10.3390/pharmaceutics14051084>.

Sinha, Debottam, Pascal H. G. Duijf, et Kum Kum Khanna. 2019. « Mitotic Slippage: An Old Tale with a New Twist ». *Cell Cycle (Georgetown, Tex.)* 18 (1): 7-15. <https://doi.org/10.1080/15384101.2018.1559557>.

Sloutskin, Anna, Dekel Itzhak, Georg Vogler, et al. 2023. « A Single DPE Core Promoter Motif Contributes to *in Vivo* Transcriptional Regulation and Affects Cardiac Function ». Prépublication, juin 12. <https://doi.org/10.1101/2023.06.11.544490>.

Smale, Stephen T. 1997. « Transcription Initiation from TATA-Less Promoters within Eukaryotic Protein-Coding Genes ». *Biochimica et Biophysica Acta (BBA) - Gene Structure and Expression* 1351 (1-2): 73-88. [https://doi.org/10.1016/S0167-4781\(96\)00206-0](https://doi.org/10.1016/S0167-4781(96)00206-0).

So, Byung Ran, Chao Di, Zhiqiang Cai, et al. 2019. « A Complex of U1 snRNP with Cleavage and Polyadenylation Factors Controls Telescripting, Regulating mRNA Transcription in Human Cells ». *Molecular Cell* 76 (4): 590-599.e4. <https://doi.org/10.1016/j.molcel.2019.08.007>.

- Spencer, C. A., et M. Groudine. 1990. « Transcription Elongation and Eukaryotic Gene Regulation ». *Oncogene* 5 (6): 777-85.
- Stefanini, M., E. Botta, M. Lanzafame, et D. Orioli. 2010. « Trichothiodystrophy: From Basic Mechanisms to Clinical Implications ». *DNA Repair* 9 (1): 2-10. <https://doi.org/10.1016/j.dnarep.2009.10.005>.
- Stokes, Katy, Alicja Winczura, Boyuan Song, Giacomo De Piccoli, et Daniel B Grabarczyk. 2020. « Ctf18-RFC and DNA Pol ϵ Form a Stable Leading Strand Polymerase/Clamp Loader Complex Required for Normal and Perturbed DNA Replication ». *Nucleic Acids Research* 48 (14): 8128-45. <https://doi.org/10.1093/nar/gkaa541>.
- Summers, Matthew K. 2020. « The DNA Damage Response in Telophase: Challenging Dogmas ». *BioEssays* 42 (7): 2000085. <https://doi.org/10.1002/bies.202000085>.
- Sun, Yadong, Keith Hamilton, et Liang Tong. 2020. « Recent Molecular Insights into Canonical Pre-mRNA 3'-End Processing ». *Transcription* 11 (2): 83-96. <https://doi.org/10.1080/21541264.2020.1777047>.
- Sun, Yadong, Yixiao Zhang, Keith Hamilton, et al. 2018. « Molecular Basis for the Recognition of the Human AAUAAA Polyadenylation Signal ». *Proceedings of the National Academy of Sciences* 115 (7). <https://doi.org/10.1073/pnas.1718723115>.
- Takahashi, Hidehisa, Amol Ranjan, Shiyuan Chen, et al. 2020. « The Role of Mediator and Little Elongation Complex in Transcription Termination ». *Nature Communications* 11 (1): 1063. <https://doi.org/10.1038/s41467-020-14849-1>.
- Takaoka, Yutaka, Mika Ohta, Satoshi Tateishi, et al. 2021. « In Silico Drug Repurposing by Structural Alteration after Induced Fit: Discovery of a Candidate Agent for Recovery of Nucleotide Excision Repair in Xeroderma Pigmentosum Group D Mutant (R683W) ». *Biomedicines* 9 (3): 249. <https://doi.org/10.3390/biomedicines9030249>.
- Tandon, Divya, et Monisha Banerjee. 2020. « Centrosomal Protein 55: A New Paradigm in Tumorigenesis ». *European Journal of Cell Biology* 99 (5): 151086. <https://doi.org/10.1016/j.ejcb.2020.151086>.
- Tang, Xiaoyou, Tingyi Yang, Daojiang Yu, Hai Xiong, et Shuyu Zhang. 2024. « Current Insights and Future Perspectives of Ultraviolet Radiation (UV) Exposure: Friends and Foes to the Skin and beyond the Skin ». *Environment International* 185 (mars): 108535. <https://doi.org/10.1016/j.envint.2024.108535>.

- Tavasoli, Ali Reza, Arastoo Kaki, Maedeh Ganji, et al. 2025. « Trichothiodystrophy Due to *ERCC2* Variants: Uncommon Contributor to Progressive Hypomyelinating Leukodystrophy ». *Molecular Genetics & Genomic Medicine* 13 (2): e70067. <https://doi.org/10.1002/mgg3.70067>.
- Titova, Ekaterina, Galina Shagieva, Vera Dugina, et Pavel Kopnin. 2023. « The Role of Aurora B Kinase in Normal and Cancer Cells ». *Biochemistry. Biokhimiia* 88 (12): 2054-62. <https://doi.org/10.1134/S0006297923120088>.
- Topolska-Woś, Agnieszka M, Norie Sugitani, John J Cordoba, et al. 2020. « A Key Interaction with RPA Orients XPA in NER Complexes ». *Nucleic Acids Research* 48 (4): 2173-88. <https://doi.org/10.1093/nar/gkz1231>.
- Tremblay, Michel G., Dany S. Sibai, Melissa Valère, et al. 2021. « Bidirectional Cooperation between Ubtfl1 and SL1 Determines RNA Polymerase I Promoter Recognition in Cell and Is Negatively Affected in the UBTF-E210K Neuroregression Syndrome ». Prépublication, juin 7. <https://doi.org/10.1101/2021.06.07.447350>.
- Tsang, Mary-Jane, et Iain M. Cheeseman. 2023. « Alternative CDC20 Translational Isoforms Tune Mitotic Arrest Duration ». *Nature* 617 (7959): 154-61. <https://doi.org/10.1038/s41586-023-05943-7>.
- Ueda, Takahiro, Emmanuel Compe, Philippe Catez, Kenneth H. Kraemer, et Jean-Marc Egly. 2009. « Both XPD Alleles Contribute to the Phenotype of Compound Heterozygote Xeroderma Pigmentosum Patients ». *Journal of Experimental Medicine* 206 (13): 3031-46. <https://doi.org/10.1084/jem.20091892>.
- Ustinov, N. B., A. V. Korshunova, et N. B. Gudimchuk. 2020. « Protein Complex NDC80: Properties, Functions, and Possible Role in Pathophysiology of Cell Division ». *Biochemistry (Moscow)* 85 (4): 448-62. <https://doi.org/10.1134/s0006297920040057>.
- Van Der Weegen, Yana, Klaas De Lint, Diana Van Den Heuvel, et al. 2021. « ELOF1 Is a Transcription-Coupled DNA Repair Factor That Directs RNA Polymerase II Ubiquitylation ». *Nature Cell Biology* 23 (6): 595-607. <https://doi.org/10.1038/s41556-021-00688-9>.
- Van Eeuwen, Trevor, Yoonjung Shim, Hee Jong Kim, et al. 2021. « Cryo-EM Structure of TFIIH/Rad4–Rad23–Rad33 in Damaged DNA Opening in Nucleotide Excision Repair ». *Nature Communications* 12 (1): 3338. <https://doi.org/10.1038/s41467-021-23684-x>.

Van Sluis, Marjolein, Qing Yu, Melanie Van Der Woude, et al. 2024. « Transcription-Coupled DNA-Protein Crosslink Repair by CSB and CRL4CSA-Mediated Degradation ». *Nature Cell Biology* 26 (5): 770-83. <https://doi.org/10.1038/s41556-024-01394-y>.

Van Toorn, Marvin, Yasemin Turkyilmaz, Sueji Han, et al. 2022. « Active DNA Damage Eviction by HLTF Stimulates Nucleotide Excision Repair ». *Molecular Cell* 82 (7): 1343-1358.e8. <https://doi.org/10.1016/j.molcel.2022.02.020>.

Vashisht, Ajay A., Clarissa C. Yu, Tanu Sharma, Kevin Ro, et James A. Wohlschlegel. 2015. « The Association of the Xeroderma Pigmentosum Group D DNA Helicase (XPD) with Transcription Factor IIH Is Regulated by the Cytosolic Iron-Sulfur Cluster Assembly Pathway ». *The Journal of Biological Chemistry* 290 (22): 14218-25. <https://doi.org/10.1074/jbc.M115.650762>.

Vasquez-Limeta, Alejandra, et Jadranka Loncarek. 2021. « Human Centrosome Organization and Function in Interphase and Mitosis ». *Seminars in Cell & Developmental Biology* 117 (septembre): 30-41. <https://doi.org/10.1016/j.semcdb.2021.03.020>.

Vélez-Cruz, Renier, Anton S. Zadorin, Frédéric Coin, et Jean-Marc Egly. 2013. « Sirt1 Suppresses RNA Synthesis after UV Irradiation in Combined Xeroderma Pigmentosum Group D/Cockayne Syndrome (XP-D/CS) Cells ». *Proceedings of the National Academy of Sciences of the United States of America* 110 (3): E212-220. <https://doi.org/10.1073/pnas.1213076110>.

Velychko, Taras, Eusra Mohammad, Ivan Ferrer-Vicens, et al. 2024. « CDK7 Kinase Activity Promotes RNA Polymerase II Promoter Escape by Facilitating Initiation Factor Release ». *Molecular Cell* 84 (12): 2287-2303.e10. <https://doi.org/10.1016/j.molcel.2024.05.007>.

Villarroya-Beltri, Carolina, et Marcos Malumbres. 2022. « Mitotic Checkpoint Imbalances in Familial Cancer ». *Cancer Research* 82 (19): 3432-34. <https://doi.org/10.1158/0008-5472.CAN-22-2400>.

Vo Ngoc, Long, California Jack Cassidy, Cassidy Yunjing Huang, Sascha H. C. Duttke, et James T. Kadonaga. 2017. « The Human Initiator Is a Distinct and Abundant Element That Is Precisely Positioned in Focused Core Promoters ». *Genes & Development* 31 (1): 6-11. <https://doi.org/10.1101/gad.293837.116>.

Vukušić, Kruno, et Iva M. Tolić. 2021. « Anaphase B: Long-Standing Models Meet New Concepts ». *Seminars in Cell & Developmental Biology* 117 (septembre): 127-39. <https://doi.org/10.1016/j.semcdb.2021.03.023>.

- Waldman, Todd. 2020. « Emerging Themes in Cohesin Cancer Biology ». *Nature Reviews Cancer* 20 (9): 504-15. <https://doi.org/10.1038/s41568-020-0270-1>.
- Wang, Juan, Kaituo Shi, Zihui Wu, et al. 2020. « Disruption of the Interaction between TFIIA $\alpha\beta$ and TFIIA Recognition Element Inhibits RNA Polymerase II Gene Transcription in a Promoter Context-Dependent Manner ». *Biochimica et Biophysica Acta (BBA) - Gene Regulatory Mechanisms* 1863 (10): 194611. <https://doi.org/10.1016/j.bbagr.2020.194611>.
- Wang, Mai, Steven Phan, Brandon H. Hayes, et Dennis E. Discher. 2024. « Genetic Heterogeneity in P53-Null Leukemia Increases Transiently with Spindle Assembly Checkpoint Inhibition and Is Not Rescued by P53 ». *Chromosoma* 133 (1): 77-92. <https://doi.org/10.1007/s00412-023-00800-y>.
- Wang, Minmin, Tianyu Wang, Xiangyu Zhang, Xiaoxing Wu, et Sheng Jiang. 2020. « Cyclin-Dependent Kinase 7 Inhibitors in Cancer Therapy ». *Future Medicinal Chemistry* 12 (9): 813-33. <https://doi.org/10.4155/fmc-2019-0334>.
- Wang, Zhixiang. 2021. « Regulation of Cell Cycle Progression by Growth Factor-Induced Cell Signaling ». *Cells* 10 (12): 3327. <https://doi.org/10.3390/cells10123327>.
- Wang, Zhixiang. 2022. « Cell Cycle Progression and Synchronization: An Overview ». In *Cell-Cycle Synchronization*, édité par Zhixiang Wang, vol. 2579. Methods in Molecular Biology. Springer US. https://doi.org/10.1007/978-1-0716-2736-5_1.
- Watson, J. D., et F. H. C. Crick. 1953. « Molecular Structure of Nucleic Acids: A Structure for Deoxyribose Nucleic Acid ». *Nature* 171 (4356): 737-38. <https://doi.org/10.1038/171737a0>.
- Watt, Kristin En, Julia Macintosh, Geneviève Bernard, et Paul A. Trainor. 2023. « RNA Polymerases I and III in Development and Disease ». *Seminars in Cell & Developmental Biology* 136 (février): 49-63. <https://doi.org/10.1016/j.semcdb.2022.03.027>.
- Wei, Lei, et Xiaolan Zhao. 2016. « A New MCM Modification Cycle Regulates DNA Replication Initiation ». *Nature Structural & Molecular Biology* 23 (3): 209-16. <https://doi.org/10.1038/nsmb.3173>.
- West, Steven, Natalia Gromak, et Nick J. Proudfoot. 2004. « Human 5' \rightarrow 3' Exonuclease Xrn2 Promotes Transcription Termination at Co-Transcriptional Cleavage Sites ». *Nature* 432 (7016): 522-25. <https://doi.org/10.1038/nature03035>.

Winkler, G. Sebastiaan, Sofia J. Araújo, Ulrike Fiedler, et al. 2000. « TFIIF with Inactive XPD Helicase Functions in Transcription Initiation but Is Defective in DNA Repair ». *Journal of Biological Chemistry* 275 (6): 4258-66. <https://doi.org/10.1074/jbc.275.6.4258>.

Wood, Andrew J., Aaron F. Severson, et Barbara J. Meyer. 2010. « Condensin and Cohesin Complexity: The Expanding Repertoire of Functions ». *Nature Reviews. Genetics* 11 (6): 391-404. <https://doi.org/10.1038/nrg2794>.

Wu, Ji, Huacheng Luo, et Hu Wang. 2013. « Germline Stem Cells ». In *Current Topics in Developmental Biology*, vol. 102. Elsevier. <https://doi.org/10.1016/B978-0-12-416024-8.00004-0>.

Wu, Y., A. N. Suhasini, et R. M. Brosh. 2009. « Welcome the Family of FANCD1-like Helicases to the Block of Genome Stability Maintenance Proteins ». *Cellular and Molecular Life Sciences: CMLS* 66 (7): 1209-22. <https://doi.org/10.1007/s00018-008-8580-6>.

Yam, Candice Qiu Xia, Hong Hwa Lim, et Uttam Surana. 2022. « DNA damage checkpoint execution and the rules of its disengagement ». *Frontiers in Cell and Developmental Biology* 10 (octobre): 1020643. <https://doi.org/10.3389/fcell.2022.1020643>.

Yan, Chunli, Thomas Dodd, Yuan He, John A. Tainer, Susan E. Tsutakawa, et Ivaylo Ivanov. 2019. « Transcription Preinitiation Complex Structure and Dynamics Provide Insight into Genetic Diseases ». *Nature Structural & Molecular Biology* 26 (6): 397-406. <https://doi.org/10.1038/s41594-019-0220-3>.

Yanagida, Mitsuhiro, Nobuyasu Ikai, Mizuki Shimanuki, et Kenichi Sajiki. 2011. « Nutrient Limitations Alter Cell Division Control and Chromosome Segregation through Growth-Related Kinases and Phosphatases ». *Philosophical Transactions of the Royal Society of London. Series B, Biological Sciences* 366 (1584): 3508-20. <https://doi.org/10.1098/rstb.2011.0124>.

Yang, Vincent W. 2018. « The Cell Cycle ». In *Physiology of the Gastrointestinal Tract*. Elsevier. <https://doi.org/10.1016/B978-0-12-809954-4.00008-6>.

Yeom, E, S-T Hong, et K-W Choi. 2015. « Crumbs Interacts with Xpd for Nuclear Division Control in Drosophila ». *Oncogene* 34 (21): 2777-89. <https://doi.org/10.1038/onc.2014.202>.

Yeom, Kyu-Hyeon, Zhicheng Pan, Chia-Ho Lin, et al. 2021. « Tracking Pre-mRNA Maturation across Subcellular Compartments Identifies Developmental Gene Regulation through Intron Retention and Nuclear Anchoring ». *Genome Research* 31 (6): 1106-19. <https://doi.org/10.1101/gr.273904.120>.

- Yimit, Askar, Ogun Adebali, Aziz Sancar, et Yuchao Jiang. 2019. « Differential Damage and Repair of DNA-Adducts Induced by Anti-Cancer Drug Cisplatin across Mouse Organs ». *Nature Communications* 10 (1): 309. <https://doi.org/10.1038/s41467-019-08290-2>.
- You, Qinglong, Xiang Feng, Yi Cai, Stephen B. Baylin, et Huilin Li. 2024. « Human 8-Oxoguanine Glycosylase OGG1 Binds Nucleosome at the dsDNA Ends and the Super-Helical Locations ». *Communications Biology* 7 (1): 1202. <https://doi.org/10.1038/s42003-024-06919-7>.
- Yu, Jina, Chunli Yan, Thomas Dodd, et al. 2023. « Dynamic Conformational Switching Underlies TFIIH Function in Transcription and DNA Repair and Impacts Genetic Diseases ». *Nature Communications* 14 (1): 2758. <https://doi.org/10.1038/s41467-023-38416-6>.
- Yuan, Jianwei, Guoying Ni, Tianfang Wang, et al. 2018. « Genital Warts Treatment: Beyond Imiquimod ». *Human Vaccines & Immunotherapeutics* 14 (7): 1815-19. <https://doi.org/10.1080/21645515.2018.1445947>.
- Yurchenko, Andrey A., Fatemeh Rajabi, Tirzah Braz-Petta, et al. 2023. « Genomic Mutation Landscape of Skin Cancers from DNA Repair-Deficient Xeroderma Pigmentosum Patients ». *Nature Communications* 14 (1): 2561. <https://doi.org/10.1038/s41467-023-38311-0>.
- Zatreanu, Diana, Zhong Han, Richard Mitter, et al. 2019. « Elongation Factor TFIIS Prevents Transcription Stress and R-Loop Accumulation to Maintain Genome Stability ». *Molecular Cell* 76 (1): 57-69.e9. <https://doi.org/10.1016/j.molcel.2019.07.037>.
- Zhang, Heqiao, Dong-Hua Chen, Rayees U.H. Mattoo, et al. 2021. « Mediator Structure and Conformation Change ». *Molecular Cell* 81 (8): 1781-1788.e4. <https://doi.org/10.1016/j.molcel.2021.01.022>.
- Zhang, Tian-Miao, Xiao-Nian Zhu, Shao-Wei Qin, et al. 2024. « Potential and Application of Abortive Transcripts as a Novel Molecular Marker of Cancers ». *World Journal of Experimental Medicine* 14 (2): 92343. <https://doi.org/10.5493/wjem.v14.i2.92343>.
- Zheng, Jie, Weiyang Liu, Zhongxia Zhou, et al. 2023. « Successful Treatment of Non-Melanoma Skin Cancer in Three Patients with Xeroderma Pigmentosum by Modified ALA-PDT ». *Photodiagnosis and Photodynamic Therapy* 43 (septembre): 103694. <https://doi.org/10.1016/j.pdpdt.2023.103694>.
- Zhou, Ming, et Julie A. Law. 2015. « RNA Pol IV and V in Gene Silencing: Rebel Polymerases Evolving Away from Pol II's Rules ». *Current Opinion in Plant Biology* 27 (octobre): 154-64. <https://doi.org/10.1016/j.pbi.2015.07.005>.

Clémence ELLY

Consequences of XPD mutations on DNA repair, transcription and cell division, leading to the development of rare genetic diseases

Résumé

XPD hélicase 5'-3' du complexe TFIIH, participe à la transcription, à la réparation des lésions UV (NER) et à la ségrégation chromosomique. Des mutations de XPD sont associées à des pathologies récessives rares comme XP, XP/CS et TTD. Longtemps attribuées à des défauts de NER, ces maladies pourraient aussi résulter d'altérations d'autres fonctions de XPD. Des lignées cellulaires CRISPR-Cas9 portant des mutations pathogènes ont été analysées. La microscopie confocale a permis d'analyser les effets des mutations sur la mitose, Le mécanisme de réparation a été évalué par irradiation UV, et un séquençage haut débit a permis d'analyser le mécanisme de transcription des lignées générées. Les résultats suggèrent que la perte d'activité hélicase n'affecte ni la localisation mitotique de XPD ni la ségrégation des chromosomes, mais altère la réparation UV. En transcriptomique, les mutations induisent des profils d'expression génique distincts. Ces données révèlent que les effets mutationnels sont spécifiques à chaque fonction, insistant sur la variabilité phénotypique observée chez les patients.

Mots clés : XPD, Complex TFIIH, Xeroderma Pigmentosum, Syndrome de Cockayne, Tricothiodystrophie, Transcription, Réparation de l'ADN, Mitose

Abstract

XPD, a 5'-3' helicase in the TFIIH complex, is involved in transcription, UV damage repair (NER) and chromosome segregation. Mutations in XPD are associated with rare recessive disorders such as XP, XP/CS and TTD. Long attributed to NER defects, these diseases may also result from alterations in other XPD functions. CRISPR-Cas9 cell lines carrying pathogenic mutations were analysed. Confocal microscopy was used to analyse the effects of mutations on mitosis, the repair mechanism was evaluated by UV irradiation, and high-throughput sequencing was used to analyse the transcription mechanism of the generated lines. The results suggest that the loss of helicase activity does not affect the mitotic localisation of XPD or chromosome segregation, but does alter UV repair. In transcriptomics, the mutations induce distinct gene expression profiles. These data reveal that the mutational effects are function-specific, emphasising the phenotypic variability observed in patients.

Keywords : XPD, TFIIH complexe, Xeroderma pigmentosum, Cockayne syndrome, Tricothiodystrophy, Transcription, Nucleotide excision repair, Mitosis